The Influence of Ocean Dynamics on the Air-Sea Flux of Carbon Dioxide and Nutrient Transport

February 1999

Abstract

The Influence of Ocean Dynamics on the Air-Sea Flux of Carbon Dioxide and Nutrient Transport

Alison McLaren

Two aspects of the influence of the ocean circulation on the air-sea CO_2 flux are investigated. The ability to use the surface heat flux to infer the dynamically driven component of the air-sea flux of CO_2 is examined. Two relationships between the air-sea fluxes of CO_2 and heat are derived for different timescales using contrasting assumptions, and are tested in a series of model experiments. A heat flux out of the ocean is expected to be related to a CO_2 flux into the ocean, due to the temperature dependency of the solubility of CO_2 gas. The various models show that this relationship holds on the large scale, and the heat flux can provide a useful upper and lower limit on the physical CO_2 uptake for an ocean region. However, the heat flux is unable to give accurate local predictions of the CO_2 flux everywhere due to the longer exchange timescale of carbon relative to heat. Monthly surface heat flux and atmospheric carbon concentration data are used to predict an upper and lower limit on the variability of the CO_2 uptake of the North Atlantic during 1960 and 1993. The natural variability dominates over the anthropogenic variability, with the upper limit being 0.15 Gt C yr^{-1} (2σ) for natural variability and 0.08 Gt C yr^{-1} for anthropogenic variability (over the region 14°N to 65°N). The upper and lower limit on the total CO_2 uptake variability are predicted to be 0.03 and 0.13 Gt C yr^{-1} for the subtropical gyre and 0.02 and 0.10 Gt C yr^{-1} for the subpolar gyre. The CO_2 uptake in the subpolar gyre is higher during the positive phase of the North Atlantic Oscillation (NAO+).

The air-sea CO_2 flux is also indirectly affected by the ocean circulation through the dynamical supply of nutrients which help to sustain the biological carbon pump. The dynamical nutrient supply is explored in an idealised ocean basin model, which highlights the importance of the lateral transfer of both inorganic and organic nutrients into a subtropical gyre. The model investigation also reveals that export production is affected by variability in the convective mixing and advective supply of nutrients associated with a phase of the NAO. The anomalous advective and convective nutrient supplies both act to increase or decrease export production in the subpolar gyre, whereas they oppose each other in the subtropical gyre. A method is devised to infer the variability in the Ekman transfer of nitrate into the North Atlantic subtropical gyre, using monthly surface heat flux and climatological nitrate data. The Ekman nitrate flux into the subtropical gyre region is found to vary by up to 40% from the climatological mean, with a stronger transfer in NAO+ years. This implies a variability of 0.03 Gt C yr^{-1} for the biological pump. The idealised model results suggest that this Ekman flux variability will reduce the effect of anomalous convective mixing on export production over short timescales, and will become more influential if the NAO remains in the same phase for several years.

Acknowledgements

Contents

Nomenclature

a	$\left(\frac{\partial C}{\partial T}\right)_{pCO_2}$
B	buoyancy flux
c_p	heat capacity
C	total inorganic carbon concentration
C^*	pseudo atmospheric total inorganic carbon concentration
f	Coriolis parameter
F_{CO_2}	air-sea flux of CO_2
F_{CO_2} upper	air-sea flux of CO_2 inferred from heat flux $\left(\frac{a}{\rho c_p}F_h\right)$
F_{CO_2} lower	air-sea flux of CO_2 inferred from heat flux $\left(\frac{\mathcal{K}_C}{\mathcal{K}_T}F_{CO_2}\text{ upper}\right)$
F_h	air-sea flux of heat
F_w	air-sea flux of freshwater
h	mixed layer depth
h_e	euphotic zone depth
$\mathcal{K}_T$	inverse exchange timescale for the air-sea heat flux
$\mathcal{K}_C$	inverse exchange timescale for the air-sea heat flux
N	Brunt-Väisälä frequency
$\mathcal{N}$	total inorganic nitrogen
pCO_2	partial pressure of CO_2
pCO_2^{atmos}	partial pressure of atmospheric CO_2
r	inverse timescale for remineralisation of DON
S	salinity
S_c	Schmidt number
S_{DON}	biological source of DON
$S_{\mathcal{N}}$	biological source of $\mathcal{N}$

t	time
T	temperature
TA	titration alkalinity
T^*	pseudo atmospheric temperature
u, v, w	velocity in the x, y and z direction
$\mathbf{u_h}$	horizontal velocity
u_w	wind speed
V	volume flux
$\mathbf{u_E}$	horizontal Ekman velocity
$\mathbf{U_E}$	horizontal Ekman volume flux
w_E	vertical Ekman velocity
w_{E0}	maximum vertical Ekman velocity
x, y, z	distance in the east, west and vertical directions
α	CO_2 solubility
β	Revelle buffer factor
γ	DON fraction of export production
κ	transfer velocity of CO_2 gas
κ_h, κ_v	horizontal and vertical diffusivity
$\kappa_1, \kappa_2, \kappa_w, \kappa_b$	chemical equilibrium constants for carbon, water and boron
λ	inverse timescale for photosynthesis
ν	kinematic viscosity of water
ρ	density
ρ_0	constant density value
$\sum B$	total boron concentration
$\sum CO_2$	total inorganic carbon concentration
τ	$\left(\frac{\partial lnpCO_2}{\partial T}\right)_C$
$\boldsymbol{\tau}$	wind stress
θ	inverse timescale of subduction

Chapter 1

Introduction

Since the beginning of the 19th century there has been an increase in the concentration of carbon dioxide (CO_2) in the atmosphere (e.g. Neftel *et al.*, 1985), caused by the activities of humankind. CO_2 is a greenhouse gas. In the lower troposphere, CO_2 absorbs outgoing long wave radiation and re-radiates the energy both upwards and downwards, which warms the Earth's surface. Callendar (1938) was the first to present evidence to suggest that rising CO_2 levels in the atmosphere were affecting the global climate. The possibility of climate change caused by humankind's activities has created a great amount of interest in the natural and anthropogenic carbon cycle of the Earth.

There are four carbon reservoirs on the Earth : the atmosphere, the oceans, terrestrial biosphere and the solid Earth. Figure 1.1 shows the sizes of the carbon reservoirs in a reconstruction of pre-industrial time. The oceans are the second largest carbon reservoir containing 65 times the amount of carbon that is stored in the atmosphere. Also shown on figure 1.1 are the fluxes of carbon between the reservoirs. The atmosphere is directly affected by fluxes from all the other three carbon reservoirs but on different timescales. The anthropogenic increase in atmospheric CO_2 is occurring on timescales of less than 1000 years. The reservoirs
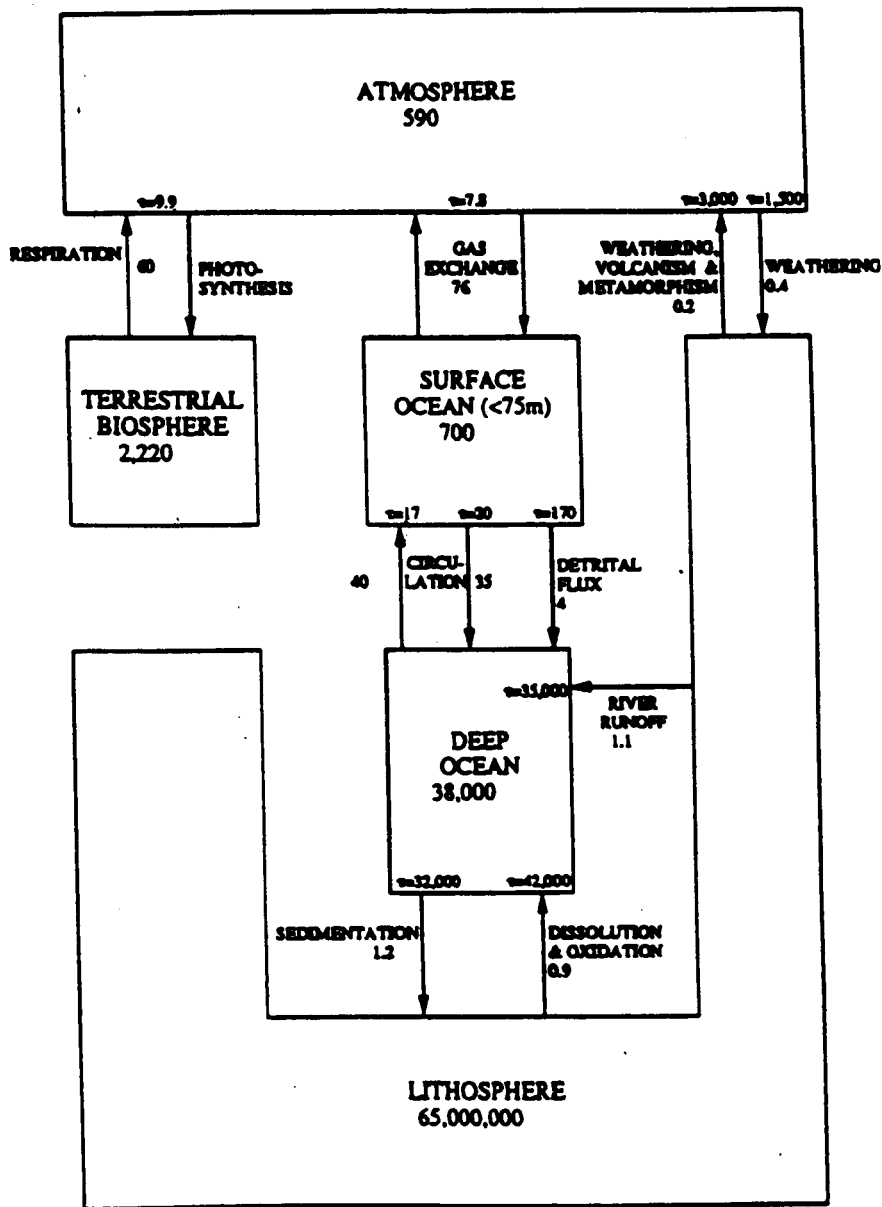
Figure 1.1: Diagram of the pre-industrial carbon cycle showing the size of the carbon reservoirs (gigatonnes of carbon, Gt C); carbon fluxes (Gt C yr^{-1}); and residence times (τ) in years. (Figure 1.2 of Najjar, 1990.) Refer to Najjar (1990) for sources.

that can affect the atmosphere on these timescales are the oceans and the terrestrial biosphere. Therefore the ocean is of current interest for two reasons: firstly, it is the second largest carbon reservoir of the Earth; and secondly, it can affect the atmospheric carbon concentrations on timescales of decades to centuries.

1.1   Objectives

The overall theme of this work is to examine the effect of the ocean circulation on the air-sea exchange of carbon caused by both physical and biological processes. The main objectives are:

- to investigate the relationship between the air-sea flux of heat and the dynamically driven CO_2 flux, and to determine whether the dynamically driven CO_2 flux can be inferred from the heat flux;

- to examine the dynamical supply of inorganic and organic nutrients that is required to sustain biological production and the biologically driven air-sea CO_2 flux;

- to determine the interannual variability of the dynamically driven air-sea CO_2 flux and the variability of the biological air-sea CO_2 flux caused by changes in the dynamical nutrient supply.

1.2   Structure

The plan of this thesis is as follows:

Chapter 2: A review of the ocean carbon cycle is given. The review is divided into three sections. The first describes the carbon chemistry of the ocean and the causes of air-sea CO_2 fluxes. The range of carbon models is reviewed in the

second section. Finally, the different methods used to estimate the air-sea flux of CO_2 are introduced and the atmospheric budget for the period 1980 to 1989 is discussed.

Chapter 3: The theoretical relationships between the air-sea fluxes of heat and CO_2 are derived. The relationships are then investigated in a series of elementary models, ranging from a one-dimensional model to an idealised three-dimensional ocean circulation model of an ocean basin.

Chapter 4: A general circulation model (GCM) is used to test the accuracy of predicting the non-biological air-sea CO_2 flux from heat fluxes. The knowledge gained using the simple models described in chapter 3, allows the results of the complex GCM to be understood. Observational heat flux data are then used to infer the physical air-sea flux of CO_2 for pre-industrial times. The interannual variability of the physical air-sea flux in the North Atlantic is also predicted for the period 1960 to 1993.

Chapter 5: The possible nutrient supply mechanisms to the ocean surface layer of a subtropical gyre are reviewed. An idealised three-dimensional model is used to investigate the physical supply of nutrients (in particular, dissolved organic nutrients) to the surface. The same model is used to examine the sensitivity of the biological production to changes in the dynamical nutrient supply caused by variability in the surface forcing of the ocean. Firstly, the steady state response of biological production to an increase in the wind strength is investigated. Secondly, the interannual variability of biological production caused by the variability of surface heat fluxes and wind strength is examined. Finally, a method is devised to quantify the interannual variability of the wind-driven supply of nutrients to the North Atlantic.

Chapter 6: This chapter contains a discussion of the important findings of the work and associated implications.

Chapter 7: The final chapter contains the main conclusions and suggestions for future work.

Chapter 2

Background

2.1   The Oceanic Carbon System

The oceanic carbon system is controlled by physical, biological and chemical processes. All three processes affect the air-sea flux of CO_2. In particular, CO_2 is chemically reactive with water. Therefore, CO_2 is different to other gases that are exchanged between the atmosphere and ocean basins (such as oxygen), which are nonreactive. On contact with seawater, CO_2 reacts to form other carbon components, which enables the ocean to contain 65 times more carbon than the atmosphere.

2.1.1   Carbon Chemistry in the Ocean

Carbon dioxide (CO_2) and water react together to form carbonic acid,

$$CO_2 + H_2O \;\rightleftharpoons\; H_2CO_3. \tag{2.1}$$
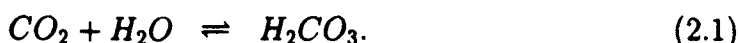
Carbonic acid then dissociates to bicarbonate (HCO_3^-) and carbonate (CO_3^{2-}) ions,

$$H_2CO_3 \;\rightleftharpoons\; H^+ + HCO_3^-; \tag{2.2}$$
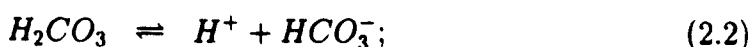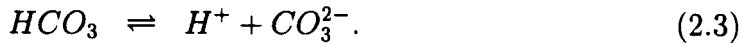
$$HCO_3 \ \rightleftharpoons \ H^+ + CO_3^{2-}. \tag{2.3}$$

Thus the inorganic carbon content of the ocean consists of four components :
CO_2 (dissolved gas), H_2CO_3, HCO_3^-, and CO_3^{2-}.

The total inorganic carbon concentration ($\sum CO_2$) is defined as

$$\sum CO_2 = [CO_2] + [HCO_3^-] + [CO_3^{2-}], \tag{2.4}$$

where [CO_2] is defined as the concentration of both CO_2 and H_2CO_3, because
it is difficult to distinguish between the two types. $\sum CO_2$ is dominated by the
bicarbonate ion with 90 - 95% of oceanic inorganic carbon in this form. Less
than $\sim 2\%$ of $\sum CO_2$ is in the form of dissolved CO_2 gas. However, the dissolved
CO_2 gas concentration is important as it determines the air-sea flux of carbon.

The reaction expressed in equation (2.1) reaches equilibrium in minutes (Baes,
1982). The other two reactions (equations 2.2 and 2.3) are instantaneous (Baes,
1982). The fast rate of the reactions allows equilibrium constants (k_1 and k_2) to
be used to the relate the concentrations of the quantities in these reactions:

$$k_1 \ = \ \frac{[HCO_3^-][H^+]}{[CO_2]}; \tag{2.5}$$

$$k_2 \ = \ \frac{[CO_3^{2-}][H^+]}{[HCO_3^-]}. \tag{2.6}$$

To calculate the air-sea flux of CO_2 it is necessary to calculate the partial
pressure of CO_2 of surface water. The partial pressure of a certain gas in a
mixture is defined as the pressure that gas would exert, if it alone occupied the
whole volume of the mixture at the same temperature. The partial pressure can
be related to the mass of the gas dissolved in a solvent and the solubility of the
gas using Henry's Law. Henry's Law states that the mass of a gas dissolved in a
given volume of solvent, at constant temperature, is proportional to the pressure
of gas in equilibrium with the solution. Henry's Law for the partial pressure of

CO_2 (pCO_2) of surface water is then,

$$pCO_2 = \frac{[CO_2]}{\alpha}, \tag{2.7}$$

where α, the proportionality constant, is called the solubility. The solubility of a gas increases for decreasing temperature and salinity and increasing pressure. Empirical relationships for the solubility as functions of temperature and salinity have been found through experiments (Weiss, 1974).

The above series of equations can be solved to find the concentrations of the individual carbon components, if two of the following measurable quantities are known: pCO_2; $\sum CO_2$; or pH ($\log_{10}[H^+]$). Other measurable quantities can be used to find the carbon components. The titration alkalinity is often used in solving for the three carbon components. The titration alkalinity (TA) is defined as the amount of acid required to bring the sea water from its initial pH to a pH where the conversion of bicarbonate and carbonate to carbonic acid is complete. This is expressed as,

$$TA = [HCO_3^-] + 2[CO_3^{2-}] + [X] + [OH^-] - [H^+], \tag{2.8}$$

where $[X]$ represents the concentrations of all the other species in sea water which react with acid. It is the carbon species that are the dominant contributors to TA and the other species are less important.

An Example of a Carbon Chemistry Scheme

One scheme to find the concentration of the individual carbon components was devised by Hoffert *et al.*(1979) and is used in the carbon models of this work. The scheme solves for pCO_2 and $[CO_2]$ using the knowledge of $\sum CO_2$, TA, total boron concentration ($\sum B$) and the equilibrium constants. The system is affected by boron and it is therefore included in the definition of the TA,

$$TA = [HCO_3^-] + 2[CO_3^{2-}] + [H_2BO_3^-] + [OH^-] - [H^+]. \tag{2.9}$$

The total boron concentration is defined as,

$$\sum B \;=\; [H_2BO_3^-] + [H_2BO_3]. \tag{2.10}$$

The scheme uses two additional equilibrium constants for the following reactions involving water and boron:

$$[H_2O] \;=\; [H^+] + [OH^-]; \tag{2.11}$$

$$[H_2BO_3] \;=\; [HBO_3^-] + [H^+]. \tag{2.12}$$

The equilibrium constants are defined as,

$$k_w \;=\; [H^+][OH^-]; \tag{2.13}$$

$$k_b \;=\; \frac{[HBO_3^-][H^+]}{[H_2BO_3]}. \tag{2.14}$$

The seven equations (2.4, 2.5, 2.6, 2.9, 2.10, 2.13 and 2.14) can be reduced to find a 5th order polynomial in $[H^+]$. The polynomial can be solved numerically for $[H^+]$ and then the other unknowns can be found. Lastly, the pCO$_2$ can be found using the calculated value of $[CO_2]$ in equation (2.7).

2.1.2 The Air-sea Flux of CO$_2$

The direction of the air-sea gas exchange is controlled by the difference of the partial pressures of the gas in the two media. The air-sea flux acts in the direction to reduce the partial pressure gradient. The equilibrium time for the air-sea CO$_2$ exchange is approximately one year (Broecker and Peng, 1974). The air-sea flux of CO$_2$, F_{CO_2}, can be expressed as

$$F_{CO_2} \;=\; \kappa\alpha(pCO_2^{\text{atmos}} - pCO_2), \tag{2.15}$$

where κ is the gas transfer velocity (or piston velocity), which is dependent on wind speed and other factors, and α is solubility of CO$_2$. pCO_2^{atmos} and pCO_2 are the partial pressure of CO$_2$ in the atmosphere and surface ocean, respectively.

The chemical carbon system of the ocean can be expressed simply by the buffer equation, which relates a change in $\sum CO_2$ to a change in oceanic pCO_2. When CO_2 is taken up by the ocean, both $\sum CO_2$ and pCO_2 increase. During the process, the carbon components are shifted to a new equilibrium such that pCO_2 increases approximately ten times the amount that $\sum CO_2$ increases. This is expressed in the buffer equation as

$$\frac{\Delta pCO_2}{pCO_2} \;=\; \beta \frac{\Delta \sum CO_2}{\sum CO_2}, \tag{2.16}$$

where β is the Revelle buffer factor and is typically 10, but varies from about 8 in warm water to 14 in cold water (Broecker and Peng, 1982).

This mechanism controls the uptake capacity of the ocean. The ocean contains about 65 times more carbon than the atmosphere, but at equilibrium the buffer mechanism means the ocean can only take up about 6.5 times as much additional carbon as the atmosphere (Siegenthaler and Sarmiento, 1993).

2.1.3   The Gas Transfer Velocity

To evaluate the air-sea flux from equation (2.15), the gas transfer velocity must be known. The gas transfer velocity is affected by a number of factors but is commonly parameterized as a function of wind speed.

The Schmidt Number

At the air-sea interface, vertical transport by turbulence is suppressed. Fluid is only vertically exchanged between the two media by molecular diffusion. Hence, the gas transfer velocity (κ) is a function of the molecular diffusivity of the gas (D). A range of models have been used to evaluate the relationship between D and κ (see review by Liss and Merlivat, 1986). Commonly, the Schmidt number

(S_c) is referred to instead of D, and is defined as,

$$S_c = \frac{\nu}{D}$$

where ν is the kinematic viscosity of water. The Schmidt number is affected by temperature and salinity.

In the gas exchange equation (2.15), κ is multiped by the solubility. Despite the relationship between S_c (and therefore κ) and temperature, the sensitivity of the rate of gas exchange on temperature is small. The effect of temperature on solubility closely counteracts the temperature effect on S_c (Wanninkhof, 1992). Many models make the assumption that $\kappa\alpha$ is independent of temperature (e.g. Tans *et al.*, 1990). However, Wanninkhof (1992) argues that although the assumption only causes small errors, the assumption will produce a systematic bias with temperature. This is caused by the air-sea CO_2 flux commonly being directed out of the ocean in warm water regions and into the ocean in cooler water areas.

Gas Transfer Velocity Measurements and Parameterizations

Broecker *et al.*(1985) used ^{14}C measurements to construct a global budget of ^{14}C. From this ^{14}C budget, Broecker *et al.*(1985) inferred a global average transfer velocity for CO_2 of approximately 20 cm hr^{-1}.

Deliberate tracer releases have also been used to measure the gas transfer velocity (e.g. Watson *et al.*, 1991a). At the global mean wind speed, these experiments give lower transfer velocities than the velocity inferred by Broecker *et al.*(1985) using the ^{14}C budget. The value of Broecker *et al.*(1985) is a long term average calculated over a wide range of wind speeds. In contrast, the tracer release estimates are measured over shorter time periods and a smaller wind speed range. Wanninkhof (1992) argues that the different range of wind speeds

will cause the estimates to differ. Wanninkhof (1992) also suggests that the differences may be caused by environmental factors other than wind speed that affect gas transfer, or by experimental uncertainties in the actual measurements.

There are several empirical relationships between wind speed and κ in the literature. Liss and Merlivat (1986) combined data from a SF_6 lake experiment (performed by Wanninkhof *et al.*, 1985) with wind tunnel experiments for higher wind speed values, to create a parameterization of κ as a function of wind speed. Wanninkhof (1992) proposed an alternate relationship of,

$$\kappa = 0.31 u_w^2 \frac{Sc}{660}^{-0.5} \qquad (2.17)$$

for steady wind conditions or instantaneous measurements, where u_w is the wind speed. This relationship is designed so that the long term average value of κ calculated over a range of global wind speeds using equation (2.17), is equal to the κ value found using the ^{14}C budget.

2.1.4 The Oceanic Uptake of Atmospheric CO_2

For CO_2 to be taken up by the ocean, the pCO_2 of the ocean surface must be reduced to less than the atmospheric pCO_2 . This is achieved either by the water being cooled or freshened and therefore increasing the solubility, or by decreasing the amount of total carbon in the mixed layer. The solubility in the surface water can be increased by the circulation advecting the water to regions of lower temperatures. However, if the surface water is not subducted into the thermocline, it will eventually circulate back to warmer regions and the water will lose any newly gained carbon (Follows *et al.*, 1996). Therefore, the main mechanism to allow oceanic uptake of CO_2 is the removal of carbon from the surface layer into the ocean interior. This removal is achieved by physical and biological processes and creates spatial and temporal variations in the pCO_2 of

the surface ocean. Atmospheric pCO_2 can be considered spatially homogeneous compared to the ocean. Therefore, it is the processes which affect the oceanic pCO_2 that control the air-sea flux of CO_2 and create the variations in the flux.

Volk and Hoffert (1985) were the first to define a carbon pump as a process which depletes the ocean surface of $\sum CO_2$ relative to the deep water. The $\sum CO_2$ in surface water is less than the $\sum CO_2$ of deep water everywhere in the ocean. A vertical gradient would be destroyed by diffusion if there were not processes restoring the gradient. These processes are the carbon pumps. There are three pumps: the solubility pump, the soft tissue pump and the carbonate pump. Each of these pumps will now be defined and discussed in turn.

The Solubility Pump

The solubility pump is the physical carbon pump. Atmospheric CO_2 enters the surface ocean where the temperature is cold and hence the solubility is high. The circulation then removes the newly gained carbon from the surface into the ocean interior. It is the dynamic removal of carbon from the surface layer that prevents a local equilibrium being reached and allows a net CO_2 uptake to occur (Follows *et al.*, 1996). The solubility pump is active in the subduction region of the subtropical gyres and in the regions of deep water formation where surface carbon is transferred into the deep ocean.

In subtropical gyres, warm water from the tropics is advected north in the western boundary current and loses heat to the atmosphere. This cooling causes an increase in CO_2 solubility and allows the water to take up atmospheric CO_2. The CO_2 uptake continues as the water enters the subduction region of the subtropical gyre (Follows *et al.*, 1996). Some of the surface water is then transferred into the main thermocline by subduction from the mixed layer at the end of winter. The subduction process leads to a net transfer of carbon from the atmo-

sphere to the deep ocean.

Deep water is formed in the regions of the Southern Ocean and the northern North Atlantic. In these regions, cold water is exported to depth by strong convective overturning. There is a corresponding transfer of carbon from the surface to depth, which drives a CO_2 flux from the atmosphere into the ocean. In the North Atlantic, the convective overturning is part of the thermohaline circulation. This circulation consists of a northwards flow at the surface of warm water in the North Atlantic. The warm water cools on its voyage north and absorbs CO_2 from the atmosphere. In small regions at high latitudes, the surface water, which is high in CO_2, becomes dense and sinks to eventually form North Atlantic Deep Water (NADW). The sinking water transports carbon from the surface to the deep ocean. The NADW flux is estimated to be 23 Sv by Broecker (1991), and has been calculated to transport a net 0.6 Gt C yr^{-1} from the northern to the southern hemisphere (Broecker and Peng, 1992).

The carbon that is transferred from the atmosphere to the deep ocean by the solubility pump will reach the ocean surface again at a later time. If this occurs in warmer regions, the carbon will be returned back to the atmosphere. A large outgassing of carbon occurs in the equatorial regions where deep water is upwelled. The water is warmed as it rises and carbon is lost to the atmosphere. This outgassing is necessary to create a steady state system.

The Soft Tissue Pump

The soft tissue pump is one of two biological pumps and describes the flux of organic carbon from the surface ocean into the deep ocean. Organisms in the surface ocean consume CO_2 during photosynthesis, converting inorganic carbon into organic carbon (CH_2O),

$$CO_2 + H_2O \rightleftharpoons CH_2O + O_2$$
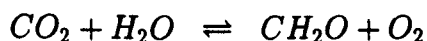
Respiration and decomposition reverse the reaction and release inorganic carbon.

Photosynthesis requires the presence of light, nutrients, CO_2 and certain trace metals (such as iron). The light requirement concentrates photosynthesis at the ocean's surface in a layer known as the euphotic zone. The depth of the euphotic zone varies from 30 m to 120 m in the North Atlantic. The organic material created by photosynthesis in the euphotic zone produces waste or dies, which causes a fallout of organic material through the water column. However, the majority of the organic matter does not leave the euphotic zone. Instead the organic matter is oxidised back into inorganic material within the euphotic zone and resupplies the surface with nutrients. These nutrients are termed recycled.

Between 10% to 30% of the organic matter created in the euphotic zone escapes the mixed layer (Doney, 1997) and is called export production. Below the euphotic zone, the sinking organic matter is oxidised back to inorganic carbon, thus transferring inorganic carbon from the surface to the deep ocean.

Primary productivity in the euphotic zone that uses nutrients that are new to the zone and not recycled is called 'new production' (Dugdale and Goering, 1967). New production reduces the surface pCO_2 and hence drives an oceanic uptake of atmospheric CO_2 . In a one-dimensional model, new production is equal to export production. However, in the three-dimensional ocean, the organic material created by new production can be horizontally advected, and therefore, new production will not locally equal the export production.

The oceanic nutrients required for soft tissue material are nitrogen (usually in the form of nitrate, NO_3^-) and phosphorus (such as phosphate, PO_4^{3-}). The chemical composition of organic soft tissue is relatively uniform. The ratio of the molar concentration of C, N and P in soft tissue is approximately C:N:P = 105:15:1 (Broecker and Peng, 1982) and is known as the Redfield Ratio. The Redfield Ratio does vary in different ocean regions, but the ratio can provide a

useful approximation. Export production removes both carbon and nutrients (in approximate Redfield Ratio proportions) from the euphotic zone. The carbon removed from the surface can be replaced from the atmosphere. In contrast, a continual supply of inorganic 'new' nutrients is required to balance the nutrients lost from the euphotic zone and sustain export production. The supply of nutrients to the euphotic zone is further discussed and investigated in chapter 5.

The Carbonate Pump

The carbonate pump is the second biological pump and is created by planktonic organisms forming calcium carbonate hard parts in the euphotic zone. The formation of calcium carbonate removes bicarbonate and calcium ions from solution,

$$Ca^{+2} + 2HCO_3^- \rightleftharpoons CaCO_3 + H_2O + CO_2. \qquad (2.18)$$
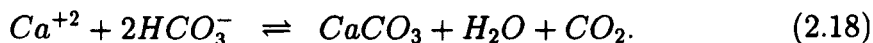
The organisms die and sink to the deep ocean. The deep ocean is under saturated with respect to calcium carbonate, which causes the calcium carbonate to dissolve. When the calcium carbonate dissolves, carbonate ions are released back into solution and increase the deep water $\sum CO_2$.

Although the carbonate pump transfers $\sum CO_2$ from the surface to depth, it does not cause an uptake of atmospheric CO_2. As shown in equation (2.18), the formation of calcium carbonate in the surface layer also produces CO_2. Therefore the carbonate pump actually increases the surface pCO_2.

2.1.5 Distributions of $\sum CO_2$ and pCO_2 in the Ocean

Figure 2.1 shows vertical profiles of $\sum CO_2$ for the seven regions of the world oceans. In all ocean regions, there is a clear increase in $\sum CO_2$ with depth in the
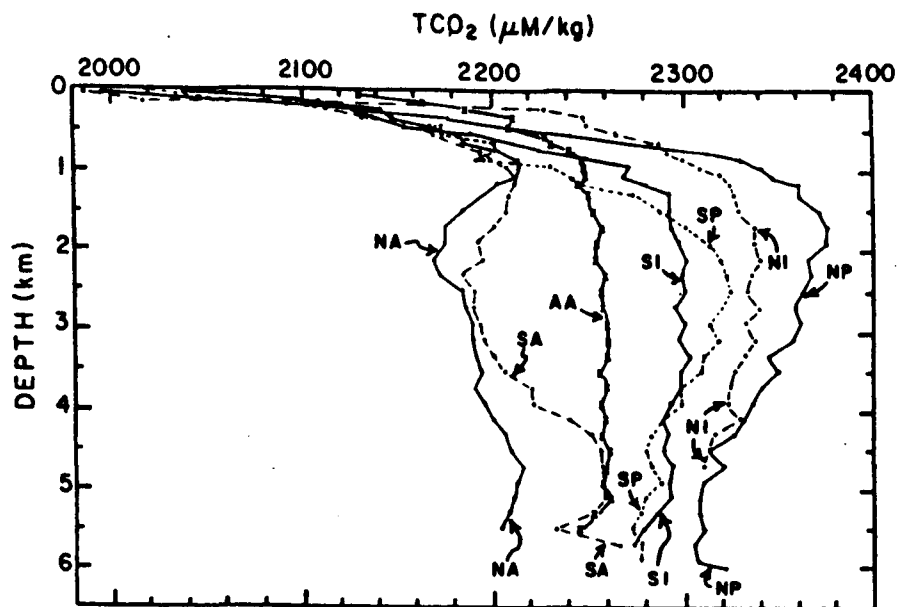
Figure 2.1: Vertical profiles of $\sum CO_2$ (μ M kg^{-1}) for the seven regions of the world oceans. NA = North Atlantic, SA = South Atlantic, NP = North Pacific, SP = South Pacific, NI = North Indian, SI = South Indian and AA = Antarctic region (south of 45 °S). Data from GEOSECS. (Figure 2.1 of Takahashi *et al.*, 1981.)

thermocline, with near constant values in the deep ocean. This structure is principally caused by the soft-tissue pump removing surface inorganic carbon during photosynthesis and returning the inorganic carbon at depth through respiration (Sarmiento *et al.*, 1995). The solubility and carbonate pumps also contribute to the vertical structure but are of minor importance relative to the soft-tissue pump. The solubility pump causes deeper water to have higher $\sum CO_2$ values as the deep water formation sites are at high latitudes where the solubility of CO_2 is high. Therefore the cold surface water is high in $\sum CO_2$ before it sinks to become deep water. The Pacific has higher values of $\sum CO_2$ at depth than the Atlantic because the Pacific deep water is older. Therefore, the Pacific water has had more carbon added to it through the biological pumps.

Tans *et al.*(1990) compiled available pCO_2 data for the oceans for the period 1972 to 1989 to produce maps of observed ΔpCO_2 (pCO_2^{ocean} - pCO_2^{atmos}) (figure 2.2). There are large areas of no data, especially in the southern hemisphere. The ΔpCO_2 distribution is caused by physical and biological processes occurring in the ocean. The equatorial and tropical regions have an implied flux of CO_2 out of the ocean in both seasons. Upwelling along the equator brings cold, high $\sum CO_2$ water to the surface. As the water rises, the temperature and pCO_2 increase causing a flux of carbon to the atmosphere. In the northern hemisphere subtropical gyres, the implied air-sea CO_2 flux is directed into the ocean in the winter, and out of the ocean in the summer. This is caused by the seasonal cycle of temperature. The subpolar gyre in the North Atlantic takes up atmospheric CO_2 all year, which is due to cold temperatures combined with biological drawdown. Overall, the broad features of the seasonal ΔpCO_2 maps can be explained by the temperature distribution.
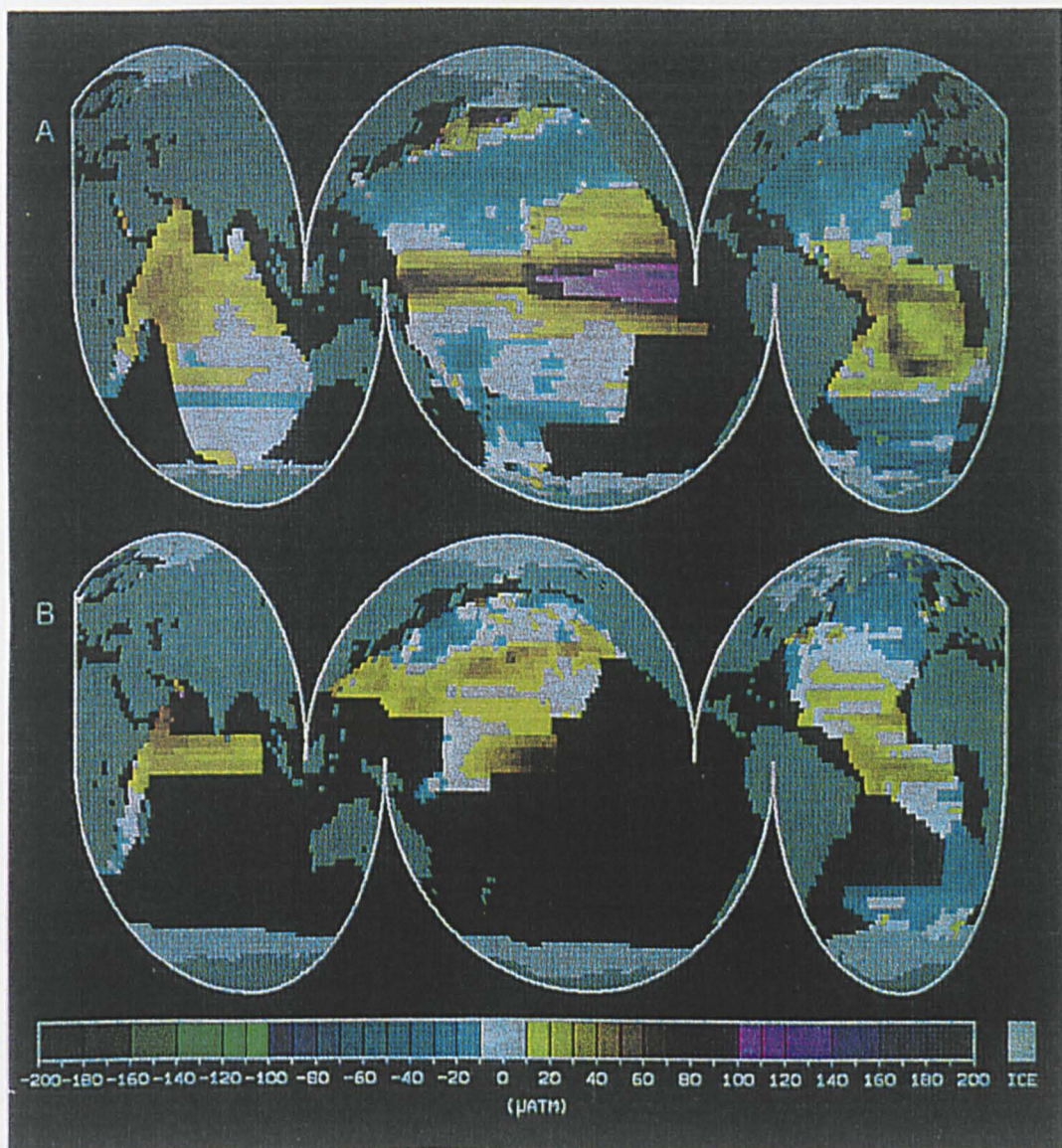
Figure 2.2: Maps of observed ΔpCO_2 (pCO_2^{ocean} - pCO_2^{atmos}) (in units of μ atmos) during two seasonal periods: A) January to April; and B) July to October. Equatorial Pacific data during El Niño years have been excluded. Areas of ice cover are shown in light grey. (Figure 3 of Tans *et al.*, 1990.)

2.1.6 The Oceanic Uptake of Anthropogenic Atmospheric CO_2

The rising level of CO_2 in the atmosphere is causing a net global flux of CO_2 into the ocean. There is evidence of the invasion of the anthropogenic CO_2 into the ocean (e.g. Kortzinger *et al.*, 1998 and Chen and Millero, 1979). Before any climate change predictions can be made, the amount of anthropogenic CO_2 entering the ocean must be evaluated.

The biological soft-tissue pump is vital in setting the steady state carbon distribution of the ocean. However, when estimating the anthropogenic CO_2 uptake by the ocean, it is commonly assumed that the biological pump has no ability to sequester anthropogenic CO_2. The biological pump is often limited by nutrient availability. So without changes in nutrient supply, the biological pump cannot become more efficient. Model investigations have also confirmed that the biological pump has a small effect if the circulation remains unchanged (Sarmiento *et al.*, 1995). Therefore, for models of the anthropogenic carbon cycle, only the solubility pump is usually included. However, it is possible that the efficiency of the biological pump may be altered by circulation changes associated with global warming which would affect the atmospheric CO_2 concentration (e.g. Sarmiento *et al.*, 1998).

2.2 Modelling the Oceanic Carbon System

Models of the oceanic carbon system are useful for understanding the complex processes involved in the carbon cycle. For example, models can be used to show which are the important processes in setting the observed carbon distribution or air-sea CO_2 fluxes. Models can also give useful predictions and many models have been used to evaluate the uptake of anthropogenic CO_2 by the ocean. The

existing models of the oceanic carbon system range from simple box models to three-dimensional general circulation models.

2.2.1 Box Models

Box models represent a carbon reservoir by a varying number of well mixed boxes which exchange carbon with each other. The exchange of carbon between two boxes is proportional to the carbon gradient between the boxes. Governing equations for the rate of change of carbon content in each box are obtained and solved to find the distribution of carbon in the different boxes.

The parameters required for the exchange (for example, the air-sea exchange parameter) are obtained by calibrating the box model with observations. Typically the calibration is made using the natural ^{14}C distribution or the bomb derived ^{14}C distribution (e.g. Oeschger et al., 1975). The natural ^{14}C cycle has a much longer timescale than bomb derived ^{14}C which has a timescale of a few decades. Some box models have difficulties in recreating both short and long timescale mixing (Oeschger et al., 1975). Therefore, some box model results are sensitive to whether natural or bomb ^{14}C distributions have been used in calibration (e.g. Siegenthaler, 1983).

Craig (1957) and Revelle and Suess (1957) where the first to use box models to examine the distribution of carbon between the atmosphere and ocean. These early box models represented the atmosphere, surface ocean and deep ocean as three separate well mixed boxes (figure 2.3). Only the surface mixed layer box exchanged carbon with the atmosphere. However, this three box model was found to produce an unrealistically high airborne fraction of anthropogenic CO_2 for 1959 to 1977 when the model was run with an increasing atmospheric carbon concentration (Björkström, 1986). This error indicates that this simple box model is not sufficient for modelling the atmosphere-ocean carbon system.
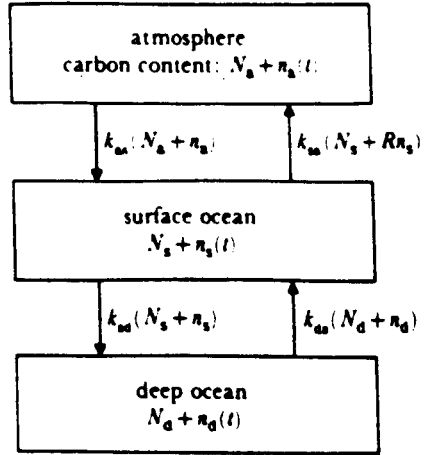
Figure 2.3: Diagram of a three box model. N_a, N_s and N_d represent steady-state pre-industrial carbon contents of the atmosphere, surface ocean and deep ocean respectively, and n_a, n_s and n_d man-made departures. k_{xy} is the first-order exchange coefficient for the carbon flux from box x to box y. R is the Revelle buffer factor. (Figure 2 of Crane, 1988.)
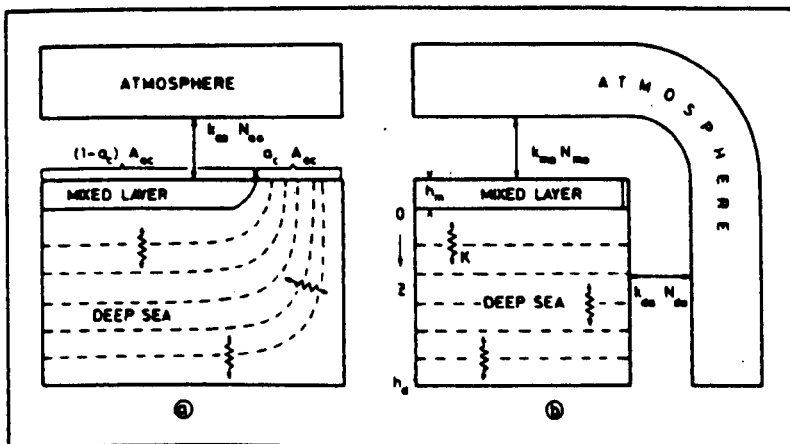
Figure 2.4: Diagram of the outcrop-diffusion model of Siegenthaler (1983): a) physical idea; and b) mathematical representation. (Figure 1 of Siegenthaler, 1983.)

The three box model was improved by Oeschger *et al.*(1975) who made the deep ocean diffusive (the box-diffusion model). This allowed the ocean to take up more atmospheric CO_2 than the non-diffusive three box model. But the airborne fraction of anthropogenic CO_2 was still found to be higher than observations (Björkström, 1986).

A major problem of the early box models was that carbon was only allowed to exchange between a warm mixed layer and the atmosphere. In the real ocean, isopycnals of deep cold water outcrop at high latitudes allowing exchange with the atmosphere and the deeper ocean (Siegenthaler, 1983). Siegenthaler (1983) included this mechanism of carbon exchange in a box-diffusion model by allowing layers of the deep ocean to outcrop at the surface (figure 2.4). The presence of the outcropping region caused the airborne fraction of anthropogenic CO_2 to decrease from 67% with no outcropping area, to 53-60% with the area of the outcrop box being 10% of the ocean's surface. Siegenthaler (1983) found that approximately half of the man-made CO_2 that entered the ocean, entered in the cold outcrop area. The warm mixed layer was very close to equilibrium as the air-sea exchange was limited by the rate at which vertical diffusion removed carbon from the mixed layer. However, the cold deep ocean was not at equilibrium with the atmosphere because the model assumed an infinitely fast mixing rate along isopycnals. Therefore carbon taken up from the atmosphere was diluted instantaneously into a large reservoir. Although the instantaneous mixing is unrealistic, the model does indicate the large potential of the cold water outcrop to take up CO_2 despite the relatively small surface area.

The next step in the development of box models was to add a crude representation of the circulation. For example, Sarmiento and Toggweiler (1984) used a box model which included a simplified circulation to investigate the rapid change in atmospheric CO_2 concentration that occurred at the end of the last ice age. The circulation is represented by water sinking from a high latitude box

into a deep ocean box (figure 2.5). The water then upwells into a low latitude box and the circulation is completed by a return flow from the low to the high latitude surface boxes. The biological soft tissue pump was also simply represented in these models. Sarmiento and Toggweiler (1984) found that atmospheric pCO_2 could be significantly altered by variations in the high latitude productivity or by changes in the circulation. An increase in the thermohaline circulation increases the amount of atmospheric CO_2 taken up by the ocean at equilibrium.

Box models are useful tools in understanding the coupled ocean-atmosphere carbon system. These simple models have highlighted the importance of the vertical transport of carbon into the deep ocean in controlling the air-sea CO_2 flux. Also the study of Siegenthaler (1983) has revealed the great importance of representing the formation of deep water and the subduction of water into the thermocline in carbon model. The box models involving the thermohaline circulation have shown the possible feedbacks between biological activity and the ocean circulation.

The advantages of box models are their simplicity and low computing costs, which allow the sensitivity of the system to be thoroughly examined. However, box models can be sensitive to the data used to calibrate them. This is a particular problem when modelling anthropogenic CO_2 as there is not a comparable measured tracer (Crane, 1988). Box models do not accurately represent the different physical processes of the ocean. In a box model all the physical processes such as advection along isopycnals are typically included in a vertical diffusion term (Bacastow and Maier-Reimer, 1990). Therefore, although box models can give a useful insight into the system, more complex models with a better representation of the dynamics are also needed.
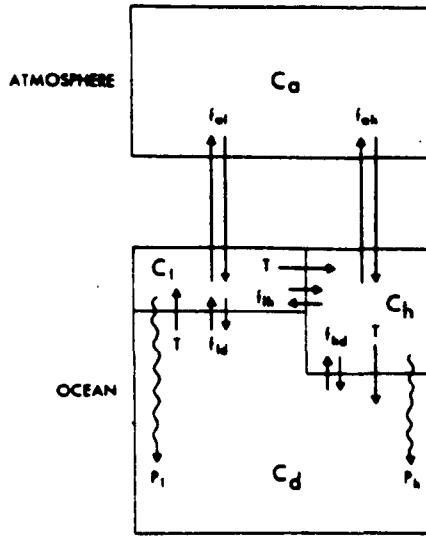
Figure 2.5: Diagram of the 4 box model of Sarmiento and Toggweiler (1984). f are fluxes between the difference reservoirs with subscripts: a = atmosphere; l = low latitude nutrient-depleted surface water; h = high latitude deep water formation regions; and d = deep ocean. T is the shallow thermohaline circulation. p is the particulate flux of organic and carbonate carbon. (Figure 2 of Sarmiento and Toggweiler, 1984.)

2.2.2 One-Dimensional Models

Follows *et al.*(1996) used a one-dimensional (1-D) Lagrangian ocean model to understand the solubility pump of carbon in a subtropical gyre. The model consists of a vertical column of water that circulates a subtropical gyre, exchanging carbon with the atmosphere. A seasonally varying mixed layer temperature and depth are imposed in the model. The column of water follows the geostrophic current and the vertical and horizontal Ekman currents subduct mixed layer water into the main thermocline. The carbon concentration of the mixed layer is affected by: air-sea exchange; entrainment as the mixed layer deepens; and Ekman advection.

Follows *et al.*(1996) found that CO_2 was taken up by the ocean in the Gulf Stream and in the northern subtropical gyre. The water is cooled in the Gulf Stream, which increases the CO_2 solubility and drives CO_2 into the ocean. In the northern gyre, deep cold winter mixed layers take up carbon which is then subducted into the main thermocline at the end of winter. The subduction of carbon away from the surface maintains the CO_2 flux into the ocean. In the tropics, CO_2 is lost to the atmosphere as the water warms and the mixed layer shallows. A model based on the 1-D model of Follows *et al.*(1996) is used and described in more detail in chapter 3.

The study of Follows *et al.*(1996) also investigates the importance of the seasonal cycle on the subduction of carbon. Although the seasonal cycle does not affect the air-sea flux CO_2 chemically because the equilibration time is about a year, the seasonal cycle does affect subduction (Follows *et al.*, 1996). The meridional slope of the base of the mixed layer is greatest at the end of winter which causes increased lateral advection (Marshall *et al.*, 1993). Also, it is the end of winter mixed layer properties that are subducted (Stommel, 1979). Although the amplitude of the seasonal cycle of mixed layer $\sum CO_2$ is heavily damped due

to the long equilibration time, there are still significant seasonal amplitudes in $\sum CO_2$. In the 1D model of Follows *et al.*(1996), the seasonal amplitudes in $\sum CO_2$ reached the order of 10 μ mol C kg^{-1}. Therefore, when subduction occurs at the end of winter, the subducted water has a higher $\sum CO_2$ than the annual mean value. Follows *et al.*(1996) found that a column of water with a seasonal cycle in mixed layer depth and temperature, absorbed 50% more carbon during one gyre circuit than a column with annual mean values.

Follows *et al.*(1996) have shown how a simple 1-D model can explain why carbon is absorbed by the ocean in different regions of a subtropical gyre. This simplified 1-D model is very useful tool to help understand the system. The knowledge gained from this simple model allowed Follows *et al.*(1996) to understand the results from a more complicated three-dimensional model.

2.2.3 Three-Dimensional Models

Three-dimensional (3-D) circulation models are needed to model the complex circulation that cannot be modelled in simple box and 1-D models. 3-D circulation models produce tracer distributions that essentially have no tunable parameters, unlike box models which are calibrated to observed tracer distributions (Maier-Reimer and Hasselmann, 1987). Instead 3-D models can use observations of tracers as an independent test of the ability of the model to produce realistic fields. Dynamical models can also include feedbacks that are believed to be important in the climate system. For example, Manabe and Stouffer (1993) using a 3-D model found that an increase in atmospheric CO_2 and the associated warming, could cause the thermohaline circulation to weaken or even collapse having a major impact on the carbon cycle.

Maier-Reimer and Hasselmann (1987) used a non biological 3-D model to investigate the oceanic uptake of anthropogenic CO_2. Initially the model was run
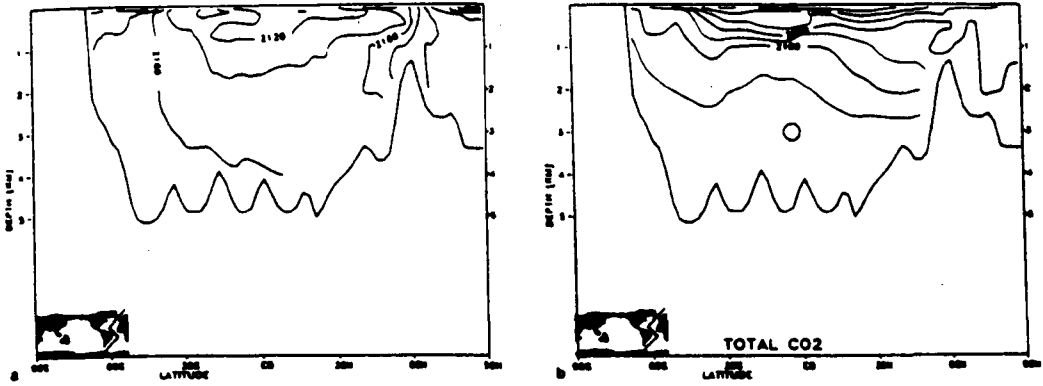
Figure 2.6: Cross section of $\sum CO_2 \, (\mu \, \mathrm{mol} \, l^{-1})$ along the Western Atlantic from the 3-D model of Maier-Reimer and Hasselmann (1987) for model runs: a) with no biota; and b) with biota. (Figures 16a and 16b of Maier-Reimer and Hasselmann, 1987.)
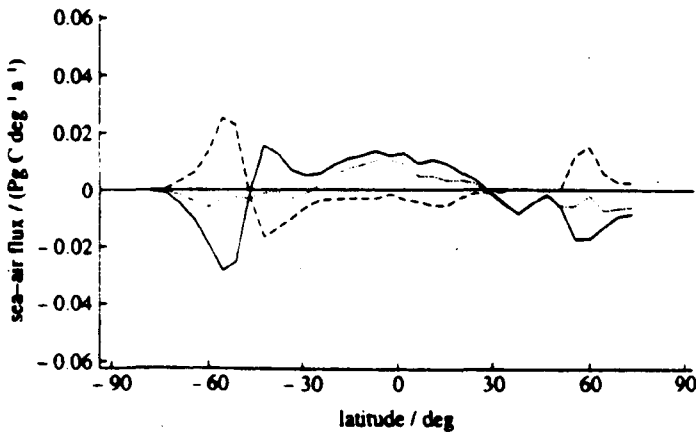
Figure 2.7: Zonally integrated sea-air CO_2 flux (Pg C deg^{-1} a^{-1}) in the North Atlantic from the 3-D model of Sarmiento et $al.$(1995). The total flux is shown by the dotted line, the flux caused by the solubility pump is the solid line and the dashed line shows the biological pump induced flux. (Figure 4 of Sarmiento et $al.$, 1995.)

until the oceanic carbon concentration was in equilibrium with a constant pre-industrial atmospheric carbon concentration. Figure 2.6a shows a cross section of the pre-industrial model carbon concentration in the North Atlantic. The solubility pump causes the carbon concentration to be greatest at depth and the high latitudes. The effect of biological processes on carbon is also included in the model as described in Bacastow and Maier-Reimer (1990). The impact of biology is to increase the vertical gradient in carbon concentration (figure 2.6b). In general, the model of Maier-Reimer and Hasselmann (1987) is reasonably successful in representing the present day carbon distribution especially the pCO_2 distributions. However, a problem with this particular circulation model is that not enough North Atlantic Deep Water is formed and too much convection occurs in the Southern Ocean (Maier-Reimer and Hasselmann, 1987). The underestimate of the NADW would be expected to cause an underestimation of the air-sea flux of CO_2 of the North Atlantic.

A 3-D global ocean circulation model was used by Sarmiento *et al.*(1995) to investigate the different impacts of the solubility pump and the biological pumps on the pre-industrial North Atlantic carbon distribution. To find the impacts of the different pumps, Sarmiento *et al.*(1995) ran the model with and without biology. The model was run until the ocean carbon concentration was in equilibrium with the atmospheric carbon concentration. The effect of the biological pump was assumed to be the difference between the two model runs. This assumes that the different pumps do not influence each other. Figure 2.7 shows the model zonally integrated sea-air CO_2 flux for the North Atlantic due to the different pumps. The solubility pump causes the ocean to take up CO_2 in the cold latitudes and lose CO_2 in the warm tropics. The inclusion of biology reduces the air-sea flux at the high latitudes. This is due to the increased deep water carbon concentrations in the biological model that are mixed back to the surface. The loss of CO_2 in the tropics is reduced with the presence of biology

as photosynthesis reduces the surface pCO_2.

Follows *et al.*(1996) used off-line velocity fields from a general circulation model of the North Atlantic to model the transport $\sum CO_2$. The study of Follows *et al.*(1996) concentrates on the affect of the solubility pump and no biology was included in the model. The diagnostics were made on the model after 250 years by which time the oceanic carbon concentrations was in equilibrium with the atmospheric CO_2 concentration. The model predicts an annual uptake of CO_2 in the subtropical gyre, with outgassing occurring in the warm tropics (figure 2.8). The overall uptake of the North Atlantic is balanced by the outflow of high $\sum CO_2$ water at depth through the open southern boundary of the model. This process is representative of the thermohaline circulation transporting carbon to the south. The 3-D model results agree with the predictions of the simple 1-D Lagrangian model of Follows *et al.*(1996).

Detailed analysis of the 3-D model by Follows *et al.*(1996) reveals the importance of the Ekman advection in causing an uptake of CO_2 in the tropics as is illustrated in figure 2.9. The figure shows the different rates of change of $\sum CO_2$ due to the geostrophic advection and the Ekman advection. In the northern subtropical gyre, the geostrophic advection reduces the local $\sum CO_2$ and causes the ocean to take up atmospheric CO_2. In the southern section of the subtropical gyre, the Ekman advection brings in low $\sum CO_2$ water from the tropics, allowing atmospheric CO_2 uptake. Observations in the North Pacific subtropical gyre show an overall oceanic uptake of CO_2 which is believed to be due to the horizontal Ekman transport (Winn *et al.*, 1994).

A variety of 3-D models have been used to investigate the carbon cycle of the ocean. They have given insight into how the solubility and biological pumps separately affect the carbon distribution. Analysis of the 3-D model results can also determine which physical processes are important in driving air-sea CO_2 fluxes. 3-D models have also been used to predict the oceanic uptake of
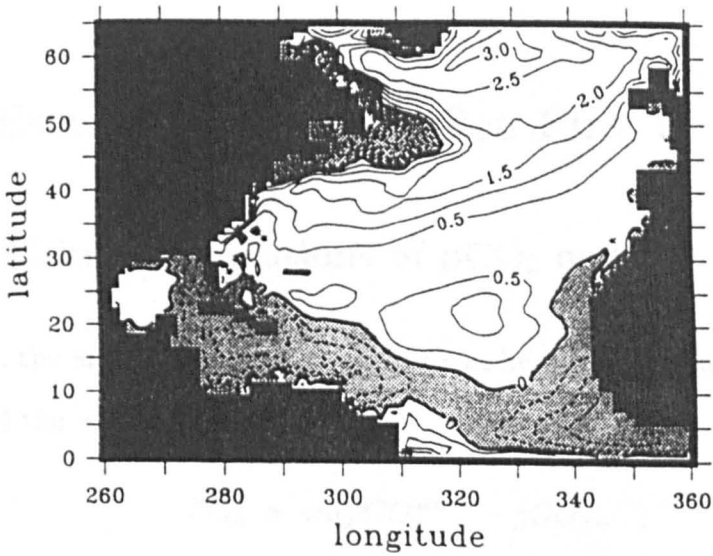
Figure 2.8: Annually integrated air-sea flux of CO_2 (mol m^{-2} yr^{-1}) in the North Atlantic for the non-biological 3-D model of Follows *et al.*(1996). Positive values indicate a flux into the ocean. (Figure 8 of Follows *et al.*, 1996.)
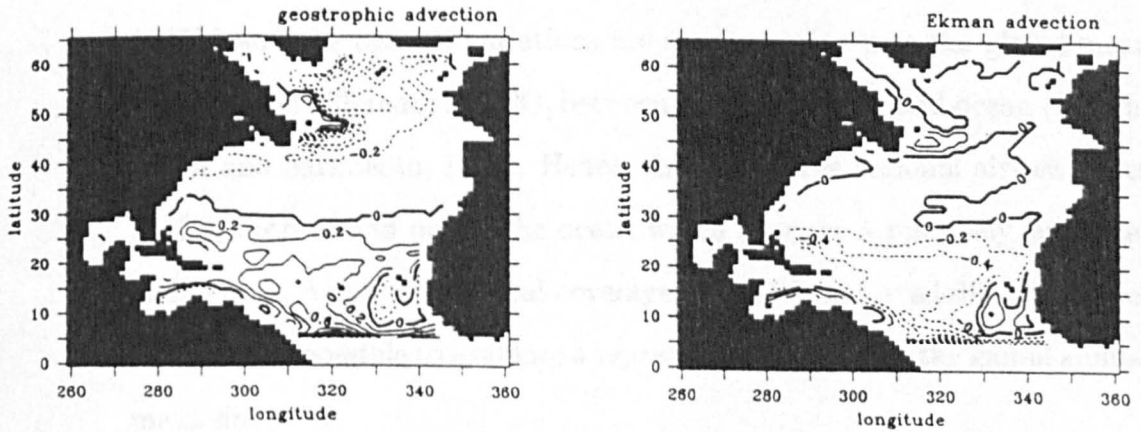
Figure 2.9: Annual average model tendencies (10^{12} mol kg^{-1} s^{-1}) due to a) geostrophic advection; and b) Ekman advection, over the upper 330 m of the non-biological 3-D model of Follows *et al.*(1996). Positive values indicate a tendency to increase $\sum CO_2$ locally. (Figure 12 of Follows *et al.*, 1996.)

atmospheric CO_2.

2.3 Estimating the Air-Sea Flux of CO_2

2.3.1 Using Observations of pCO_2 or Σ C

In theory, the air-sea exchange of carbon can be calculated using observations of pCO_2 and the air-sea flux equation

$$F_{CO_2} = \kappa\alpha(pCO_2^{atmos} - pCO_2).$$

The flux can then be integrated over time and space to obtain net fluxes for different regions. However, there are difficulties using this approach, especially to estimate the oceanic uptake of anthropogenic CO_2:

1. The gas transfer velocity is not accurately known as it depends on many variable factors such as wind speed;

2. pCO_2 varies greatly in time and space (Peng *et al.*, 1987; Watson *et al.*, 1991b) and the natural variations are much greater that the global mean values of the difference in pCO_2 between the atmosphere and ocean (Siegenthaler and Sarmiento, 1993). Hence, there are large regional air-sea fluxes of CO_2 both in and out of the ocean which produce a relatively small net global flux. At present, global coverage of data is not available and therefore it is not possible to evaluate a representative value for the global annual mean flux.

3. The local difference in atmospheric and ocean pCO_2 is a small difference between two large numbers; hence, it is very sensitive to experimental errors, such as the accuracy of the equilibrium constants used in the calculation of ocean pCO_2 (Siegenthaler and Sarmiento, 1993).

4. The present day flux is a combination of the natural and anthropogenic processes. To obtain the flux purely due to the increase in atmospheric CO_2, the pre-industrial flux must be known. Prior to the industrial revolution, the carbon cycle is believed to be in steady state. However, there was still an net flux of carbon from the ocean to the atmosphere, which was balanced by a flux of carbon into the ocean from rivers. The riverine flux drives an estimated outgassing of 0.4-0.7 Gt C yr^{-1} (Sarmiento and Sundquist, 1992).

The pCO$_2$ data coverage in the Northern Hemisphere is much better than the Southern Hemisphere. Lefèvre *et al.*(1999) used an objective analysis technique to produce seasonal maps of ΔpCO$_2$ for the Northern Hemisphere (north of 10°N). The Northern Hemisphere was found to be a net sink of carbon during the year, with an annual mean uptake of 0.86 ±0.61 Gt C yr^{-1}. The greatest uptake of 1.23 ± 0.40 Gt C yr^{-1} occurred during spring due to the strong biological drawdown. There are large error bounds associated with the estimates of Lefèvre *et al.*(1999) which are a result of the poor data coverage.

The anthropogenic flux of CO_2 into the ocean can be calculated from measurements of the increase in oceanic $\sum CO_2$ (e.g. Chen and Millero, 1979). In the past, this method has suffered from the experimental precision of the $\sum CO_2$ measurements. However, in a recent paper, Peng *et al.*(1998) argue that $\sum CO_2$ measurements are now precise enough to allow the anthropogenic flux of CO_2 to be determined. Peng *et al.*(1998) develop a new method of using $\sum CO_2$ data measured at different times to infer the anthropogenic CO_2 uptake.

2.3.2 Using Observations of pCO$_2$ Combined with Models

There are problems in determining the air-sea flux of CO_2 directly from pCO$_2$ data. However, the data can be used in conjunction with models to gain

Zones	Net CO_2 flux (Gt C yr^{-1})
North of 50 °N	0.19 to 0.45
14 °N to 50 °N	0.33 to 0.72
14 °N to 14 °S	-0.46 to -1.04
14 °S to 50 °S	0.42 to 0.92
South of 50 °S	0.12 to 0.30

Table 2.1: Annual mean air-sea CO_2 flux for different ocean regions for 1990 (Takahashi *et al.*, 1997). A positive flux is directed into the ocean.

the oceanic flux.

Takahashi *et al.*(1997) used a lateral diffusive and advective transport interpolation scheme to produce a global map of the air-sea flux of CO_2 using the available observations. Takahashi *et al.*(1997) combined data from different years to produce a flux map for 1990 taking into consideration the increase in atmosphere pCO_2. The flux estimates of Takahashi *et al.*(1997) for different regions are presented in table 2.1. The range of estimates is created from the use of different parameterizations of the gas exchange coefficient and different methods for converting the data to 1990 values. The results shown in table 2.1 reveal that the tropical regions act as a source of atmospheric CO_2 and the subtropical and polar regions act as sink regions.

Tans *et al.*(1990) used a novel combination of a 3-D atmospheric transport model of CO_2 and the air-sea flux of CO_2 in the Northern Hemisphere (NH) calculated using pCO_2 observations. The data coverage in the NH is reasonable to allow this calculation. In regions of no data, pCO_2 is inferred from surface temperature. Tans *et al.*(1990) also used atmospheric observations of the observed global increase in CO_2 concentration and the inter-hemisphere atmospheric gradient in CO_2. As 95 % of the fossil fuel CO_2 is released in the NH (Siegenthaler and

Sarmiento, 1993), an inter-hemispheric gradient is created. However, as Tans *et al.*(1990) discovered, the observed gradient (3 ppm in 1980-87) is smaller than that predicted by their atmospheric model with no CO_2 sinks ($\sim$ 5 ppm). This result suggests that the CO_2 sinks must be larger in the NH. Tans *et al.*(1990) used a range of different sinks together with the observed NH ocean sink in the atmosphere model to create the observed atmospheric gradient. Tans *et al.*(1990) found the only way to match the model results with observations was to make the Southern Hemisphere (SH) oceanic uptake very small and create a large NH terrestrial sink (2-3.4 Gt C yr^{-1}). The global oceanic uptake estimated by Tans *et al.*(1990) was 0.3-0.8 Gt C yr^{-1} for the period 1981 to 1987, with the Southern Ocean actually acting as a source of CO_2.

The predicted global oceanic uptake of Tans *et al.*(1990) is much lower than model predictions of the anthropogenic uptake (see section 2.3.4). However the Tans *et al.*(1990) prediction has to be corrected for three reasons:

1. The mean surface ocean pCO_2 is overestimated by several ppm because the partial pressure was calculated using the bulk water temperature which is warmer than the skin temperature of the sea surface (Robertson and Watson, 1992). Robertson and Watson (1992) estimate that the Tans *et al.*(1990) uptake should be increased by 0.44 Gt C yr^{-1}.

2. To calculate the anthropogenic uptake of CO_2, the pre-industrial steady state air-sea flux must be removed from the Tans *et al.*(1990) estimate. As mentioned before, rivers add carbon to the ocean which is believed to cause a sea to air CO_2 flux. This CO_2 flux has been estimated by Sarmiento and Sundquist (1992) to be 0.4-0.7 Gt C yr^{-1} and must be added to the oceanic uptake estimate of Tans *et al.*(1990) to gain the anthropogenic flux.

3. There is a correction due to the transport of carbon monoxide, which is created mainly in the NH, that was not included in the Tans *et al.*(1990)

model. Assuming that the main sink for carbon monoxide is in the SH ocean, 0.3 Gt C yr^{-1} needs to be added to the Tans *et al.*(1990) estimate (Sarmiento and Sundquist, 1992).

These three corrections increase the Tans *et al.*(1990) estimate to 1.8 Gt C yr^{-1} which is in agreement with other models. However, these corrections cannot account for the observed hemisphere gradient which implies stronger sinks in the NH. The need for the stronger sinks in the NH is partly offset by the transport of carbon by the North Atlantic Deep Water (Broecker and Peng, 1992). Keeling and Heimann (1986) concluded, after studying atmospheric CO_2 data, that prior to the Industrial Revolution there was a inter hemispheric gradient in atmospheric CO_2. However, the pre-industrial gradient was in the opposite direction to the present day gradient. This would imply greater sinks in the NH. Broecker and Peng (1992) argued that this atmospheric transport from the SH to the NH was balanced by ocean transport of carbon in the NADW travelling from the NH to the SH. Broecker and Peng (1992) calculated the ocean transport from the NH to the SH to be 0.6 Gt C yr^{-1}. This amount accounts for about 60 % of the difference between the amount of carbon transported by the atmosphere to the SH and the observed increase in carbon in the SH (Broecker and Peng, 1992). Hence, if the estimated oceanic uptake is correct, there is still need for a NH land sink to be found, but it is much smaller than that predicted by Tans *et al.*(1990).

2.3.3 Using Other Observations

A variety of methods to infer the air-sea CO_2 flux using other observational data have been tried. In particular, much work has concentrated on inferring the air-sea flux of CO_2 in the North Atlantic. The North Atlantic is very important in the carbon cycle because of the thermohaline circulation which exports carbon

to the south (Broecker and Peng, 1992).

Heat fluxes

Watson *et al.*(1995) inferred the non-biological air-sea CO_2 flux for the North Atlantic from surface heat fluxes. As a volume of water is advected polewards in the North Atlantic, it cools and absorbs CO_2 as the CO_2 solubility increases. If the water is then removed from the surface, the ocean has gained net CO_2 and lost net heat to the atmosphere. Watson *et al.*(1995) used the measured northwards heat transport of the North Atlantic to predict the net uptake of CO_2 caused by temperature changes. Including the effect of biology, salinity and alkalinity changes, Watson *et al.*(1995) estimated an oceanic uptake of 0.48 Gt C yr^{-1} for the pre-industrial North Atlantic.

Within the method used by Watson *et al.*(1995), an assumption of equilibrium between the ocean and atmospheric CO_2 concentrations is made. The equilibrium timescale for the exchange of atmosphere and oceanic CO_2 is about one year. Therefore, this assumption may not be valid. Sarmiento *et al.*(1995) argues that the estimate of Watson *et al.*(1995) is an upper limit due to the assumption of equilibrium. The assumption also means that the present day air-sea flux cannot be inferred using the method of Watson *et al.*(1995). This method of inferring the air-sea flux of CO_2 from heat fluxes is further investigated in chapter 3.

Water Mass Properties

Keeling and Peng (1995) used observed properties of different water masses to estimate the air-sea flux of CO_2 , oxygen and heat due to the North Atlantic thermohaline circulation. Keeling and Peng (1995) were able to calculate air-sea fluxes with knowledge of the potential temperature, oxygen concentration and $\sum CO_2$ of each water mass and the size of return flow. They assumed water mass

conversion occurred only due to air-sea exchanges and the return flow properties were constrained by the phosphate conservation.

Keeling and Peng (1995) calculated that the pre-industrial CO_2 flux for the North Atlantic was 0.40 ± 0.18 Gt C yr^{-1}. This carbon uptake is equivalent to the net southwards transport of carbon by the North Atlantic. The value of Keeling and Peng (1995) for the pre-industrial transport is less than the estimate of Broecker and Peng (1992) of 0.6 Gt C yr^{-1}. However, Broecker and Peng (1992) used a greater value for the thermohaline volume transport (Keeling and Peng, 1995). Sarmiento et al.(1995) combined the various estimates for the southwards transport of carbon by the North Atlantic to get a result of 0.6 ± 0.3 Gt C yr^{-1}, which is also consistent with the result of Watson et al.(1995).

Sea Surface Temperature

Stephens et al.(1995) used sea surface temperature (SST) to infer maps of pCO_2 for the North Pacific. Ship data of SST and pCO_2 were used to find regression equations which were then used to infer pCO_2 maps from satellite SST data. pCO_2 is controlled by temperature, total inorganic carbon concentration, alkalinity and salinity. In the North Pacific, Stephens et al.(1995) argue that seasonal changes in alkalinity and salinity are small and temperature and $\sum CO_2$ have the dominant effect on pCO_2. Stephens et al.(1995) found the method of inferring pCO_2 from only temperature worked better in the subtropics than the subpolar regions. In the subtropics, temperature is the primary control on pCO_2. In contrast, in the subpolar region, changes in $\sum CO_2$ caused by biology, mixing and air-sea exchange are important. These changes in $\sum CO_2$ are not explicitly included in the method of Stephens et al.(1995) for inferring pCO_2. Also to calculate the actual air-sea flux of CO_2 by this method, the gas transfer velocity still needs to known.

Atmospheric Oxygen Content

A novel method of inferring the anthropogenic oceanic uptake of CO_2 from atmospheric oxygen measurements has been proposed by Keeling and Shertz (1992). CO_2 is released into the atmosphere by fossil fuel burning and changes in land use, which also produces a stoichiometrically linked sink of atmospheric oxygen. The sinks of atmospheric CO_2 are the ocean and terrestrial biota. The land sink is associated with a corresponding oxygen source, however, the uptake of CO_2 by the ocean does not involve oxygen. Unlike carbon, the oceans do not significantly buffer the change in atmospheric CO_2 because of the low solubility of oxygen in seawater. Therefore, with accurate atmospheric CO_2 and O_2 measurements and knowledge of fossil fuel emissions, it is possible to calculate the oceanic uptake of CO_2 .

Keeling and Shertz (1992) used the available time series to calculate an oceanic sink of 3.0 ± 2.0 Gt C yr^{-1} for 1989 to 1991. The current timeseries of atmospheric O_2 measurements is not yet long enough to give a more accurate estimate using this method (Keeling and Shertz, 1992).

Isotopic Carbon Concentrations

The $\delta^{13}C$ value (the ratio $^{13}C/^{12}C$) of CO_2 produced by fossil fuel burning or deforestation is less than the $\delta^{13}C$ value of atmospheric CO_2 . Therefore, during the last 300 years, the $\delta^{13}C$ value of atmospheric CO_2 has decreased (Friedli et al., 1986). This atmospheric decrease in turn has led to a decrease in the oceanic $\delta^{13}C$. Quay et al.(1992) used changes in atmospheric CO_2 concentration together with changes in $\delta^{13}C$ of atmospheric CO_2 and oceanic $\sum CO_2$, to estimate the oceanic CO_2 uptake. For the period 1970-90, Quay et al.(1992) predicted an oceanic CO_2 uptake of 2.1 ± 0.75 Gt C yr^{-1} . The error margins of the estimate are mainly due to the lack of $\delta^{13}C$ measurements in the ocean, which is

a disadvantage of the method.

2.3.4   Using Models

Ocean models have also been used to evaluate the anthropogenic global air-sea flux of CO_2 . Sarmiento *et al.*(1992) used a 3-D global ocean circulation model to calculate an ocean uptake rate of 1.9 Gt C yr^{-1} for 1980-1989. The model is described as a perturbation model and assumes that the natural cycling of carbon remains the same in the presence of anthropogenic CO_2 . Box models also predict similar uptake rates for the decade 1980-89. The box-diffusion model predicts an uptake of 2.4 Gt C yr^{-1} (Siegenthaler, 1983). The outcrop-diffusion model of Siegenthaler (1983) estimates a higher uptake rate of 3.6 Gt C yr^{-1} .

Table 2.2 summarises the various estimates of the oceanic uptake of atmospheric CO_2 that have been discussed.

2.3.5   The Atmospheric CO_2 Concentration Budget

Much work has been done on evaluating the industrial atmospheric CO_2 budget. Fossil fuel emissions are known with reasonable accuracy, and estimates can be made for the emissions due to changes in land use. The atmospheric CO_2 budget can then be calculated for a certain period, such that the increase in atmospheric CO_2 concentration should equal the emissions minus the amount removed by sinks. The International Panel on Climatic Change (IPCC) produced a budget for the period 1980-89 using the best estimates available (Watson *et al.*, 1990). This budget is shown in table 2.3. The rate of anthropogenic emissions into the atmosphere is greater than the accumulation of anthropogenic CO_2 in the atmosphere. Therefore, some of the man-made CO_2 emissions have been removed from the atmosphere.

Table 2.2: Summary of the various estimates of the oceanic uptake of atmospheric CO_2.

Author	Method	Area	Time	CO_2 Uptake (Gt C yr^{-1})
Watson et al.(1995)	Heat flux	North Atlantic	Pre-industrial	0.48
Keeling and Peng (1995)	Water mass properties	North Atlantic (thermohaline circulation)	Pre-industrial	0.40± 0.18
Broecker and Peng (1992)	$\sum CO_2$ data	North Atlantic (thermohaline circulation)	Pre-industrial	0.6
Stephens et al.(1995)	SST data	North Pacific	Present day	0.02 to 0.07
Lefèvre et al.(1999)	pCO_2 data	North of 10°	Present day	0.86±0.61
Takahashi et al.(1997)	pCO_2 data + model	North of 15°	Present day	0.52 to 1.17
Keeling and Shertz (1992)	O_2 data	Global	Anthropogenic	3.0±2.0
Quay et al.(1992)	$\delta^{13}C$ data	Global	Anthropogenic	2.1±0.75
Tans et al.(1990) (plus corrections detailed in Siegenthaler and Sarmiento, 1993)	pCO_2 + model	Global	Anthropogenic	~ 1.8
Siegenthaler (1983)	1-D model	Global	Anthropogenic	2.4
Siegenthaler (1983)	1-D Outcrop model	Global	Anthropogenic	3.6
Sarmiento et al.(1992)	3-D GCM	Global	Anthropogenic	1.9

Emissions from fossil fuels	+	5.4 ± 0.5
Land use change	+	1.6 ± 1.0
Accumulation in atmosphere	-	3.4 ± 0.2
Uptake by ocean	-	2.0 ± 0.8
Missing sink	-	1.6 ± 1.4

Table 2.3: Atmospheric CO_2 budget in Gt C yr^{-1} for 1980-1989 from Watson *et al.*(1990)

The oceanic uptake estimate of 2.0 ± 0.8 Gt C yr^{-1} represents the results of the range of methods used to evaluate the uptake which have been discussed. The budget for 1980-89 suggests that more than a third of the anthropogenic emissions of CO_2 have entered the ocean.

As shown in table 1, the budget is not balanced with only the ocean sink and therefore if the figures are accurate there must be a another sink. The other sink, which is unaccounted for, has been named the 'missing sink'. It is believed to be associated with northern hemisphere land biota (Tans *et al.*, 1990). In a recent controversial work, Fan *et al.*(1998) calculated the terrestrial uptake in the Northern hemisphere for the period of 1988 to 1992 to be 1 - 2.2 Gt C yr^{-1} with the dominant sink being in North America.

2.3.6 Summary

There are many aspects of the carbon cycle that are still not fully understood. A range of different methods involving models and available observations give similar oceanic uptake values, but there is still a large error margin. Methods that estimate the air-sea CO_2 flux suffer from the lack of oceanic pCO_2 measurements. Therefore, methods which infer the air-sea flux from other more sampled data are very useful.

In the next chapter, the suggestion of Watson *et al.*(1995) that the air-sea heat flux can be used to infer the non-biological CO_2 flux is investigated. The relationship between air-sea fluxes of heat and CO_2 is potentially very useful for several reasons:

1. There are many more observations of the air-sea heat flux than the CO_2 flux. For example, in the North Atlantic, approximately 30,000 pCO_2 measurements were available for the study of Lefèvre *et al.*(1997) for the period 1978 to 1993. In comparison, Bunker (1976) used some 8,000,000 temperature measurements for the period 1941 to 1972 to diagnose the air-sea heat fluxes.

2. There are enough heat flux measurements to fully resolve the seasonal cycle of the heat flux. Observations of $\sum CO_2$ and pCO_2 tend to be biased towards the summer, hence, methods involving $\sum CO_2$ and pCO_2 data do not always account for the full seasonal cycle.

3. If the air-sea CO_2 flux can be inferred accurately from the heat flux, the CO_2 flux could be evaluated without knowledge of the poorly known gas transfer velocity of CO_2 ; and

4. If there is a strong relationship between local air-sea fluxes of heat and CO_2 , then maps of the air-sea flux of CO_2 could be produced in addition to calculating the net flux of a region.

Chapter 3

Air-Sea Fluxes of Heat and CO_2

- Idealised Experiments

There is a relationship between the air-sea fluxes of heat and CO_2 that is caused by the temperature dependency of the solubility of CO_2 gas. The solubility increases with decreasing temperature. Therefore, a heat flux into the ocean is expected to coincide with a carbon flux out of the ocean, in the absence of any other factors influencing the carbon flux. This idea is illustrated in figure 3.1. A volume of water enters an ocean basin at the surface and moves polewards. The water will start to lose heat to the atmosphere and the water temperature will decrease. The reduction in temperature will cause the CO_2 solubility to increase and drive a flux of CO_2 into the ocean. The volume of water is then converted into dense cooler water and exported out of the ocean basin at depth. The transfer from the surface to depth is through subduction or deep convection. Overall, the volume of water will have lost heat to the atmosphere but gained atmospheric CO_2 .

Watson *et al.*(1995) used the net heat flux of the North Atlantic to infer the net CO_2 uptake caused by temperature changes. Using a northwards heat trans-
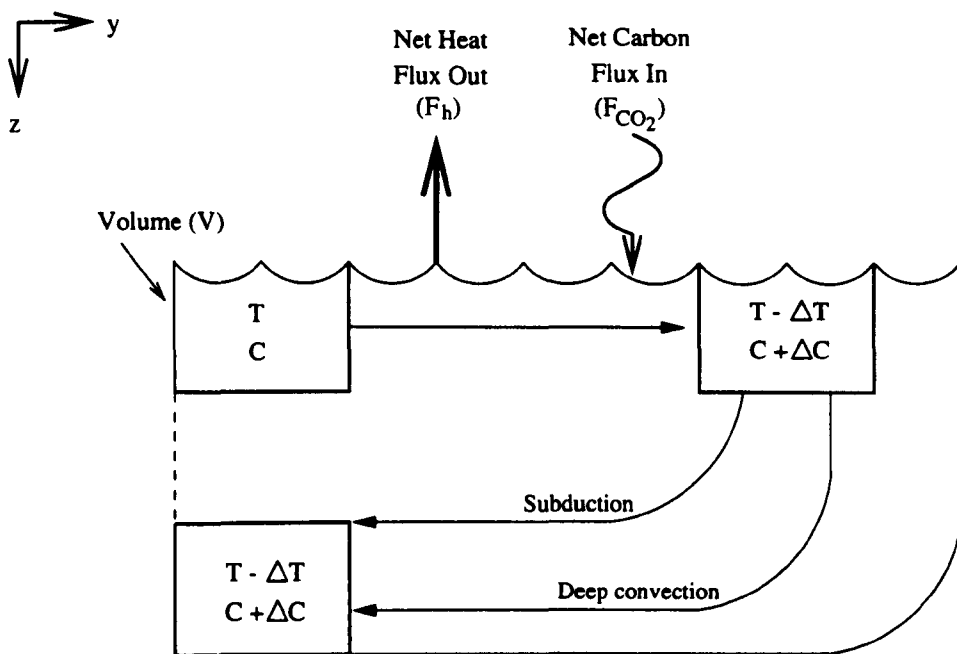
Figure 3.1: Diagram to illustrate the relationship between air-sea heat and CO$_2$ fluxes. ΔT and ΔC are both positive quantities.

port of 10^{15}W across 24°N reported by Isemer *et al.*(1989), Watson *et al.*(1995) inferred a net CO_2 uptake of 0.75 Gt C yr^{-1} caused purely by the solubility pump. However, the air-sea CO_2 flux is also affected by salinity, alkalinity and biological processes. Watson *et al.*(1995) added the CO_2 flux associated with these other factors to the solubility pump estimate and calculated that the pre-industrial net air-sea flux of CO_2 for the North Atlantic was 0.48 Gt C yr^{-1}.

The relationship between heat and CO_2 air-sea fluxes can be derived starting from the governing equations for temperature and carbon, which are described in the following section.

3.1 Theory

The governing equations for temperature and total inorganic carbon concentration (ignoring biological processes) for a mixed layer of thickness, h are,

$$\frac{DT}{Dt} = \frac{F_h}{\rho c_p h},$$ (3.1)

$$\frac{DC}{Dt} = \frac{F_{CO_2}}{h}.$$ (3.2)

T is the mixed layer temperature which is changed with time (t) by a surface heat flux (F_h); ρ and c_p are the mixed layer density and the heat capacity, respectively. C is defined as the total inorganic carbon concentration (normally denoted by $\sum CO_2$) and F_{CO_2} is the air-sea flux of CO_2.

The air-sea flux of CO_2 is driven by the difference in partial pressures of CO_2 (pCO_2) between the atmosphere and surface ocean,

$$F_{CO_2} = \kappa \alpha (pCO_2^{atmos} - pCO_2),$$ (3.3)

where α is the CO_2 solubility and κ is the gas transfer velocity.

It is possible to parameterize the right hand side of equation (3.1) in a similar style to equation (3.3),

$$\frac{F_h}{\rho c_p h} = \mathcal{K}_T(T^* - T), \qquad (3.4)$$

where T^* is a pseudo atmospheric temperature that gives the correct air-sea heat flux. $\mathcal{K}_T$ is the inverse timescale associated with the air-sea flux of heat. Williams (1988) found that an anomalous surface temperature of $\pm 2^{\circ}$C caused air-sea heat fluxes of -58 Wm^{-2} and 80 Wm^{-2}. These heat flux magnitudes imply a value of approximately 2 months for $1/\mathcal{K}_T$, for a mixed layer thickness of 50m.

3.1.1   Air-Sea CO₂ Flux Estimates

Before investigating the relationship between the heat and CO₂ fluxes, it is helpful to define some chemical quantities. pCO₂ is principally controlled by temperature, total inorganic carbon concentration, salinity and alkalinity (Takahashi et al., 1993). Hence, the following quantities can be defined and evaluated,

$$\tau = \left(\frac{\partial ln pCO_2}{\partial T}\right)_C \qquad (3.5)$$

$$\beta = \left(\frac{\partial ln pCO_2}{\partial ln C}\right)_T. \qquad (3.6)$$

τ has been found experimentally to be 0.0423°C^{-1} by Takahashi et al.(1993) for a range of typical ocean temperatures and salinities. β is the Revelle buffer factor as defined earlier in equation (2.16). β has a global average value of approximately 10 (Broecker and Peng, 1982). τ and β can be used to express the change in total inorganic carbon concentration with temperature as follows,

$$a = \left(\frac{\partial C}{\partial T}\right)_{pCO_2} = -C\frac{\tau}{\beta}. \qquad (3.7)$$

Using a typical C value of 2000 μ mol kg^{-1}, gives a value of -6.5 $\times 10^{-6}$ mol kg^{-1} $^{\circ}$C^{-1} for a.
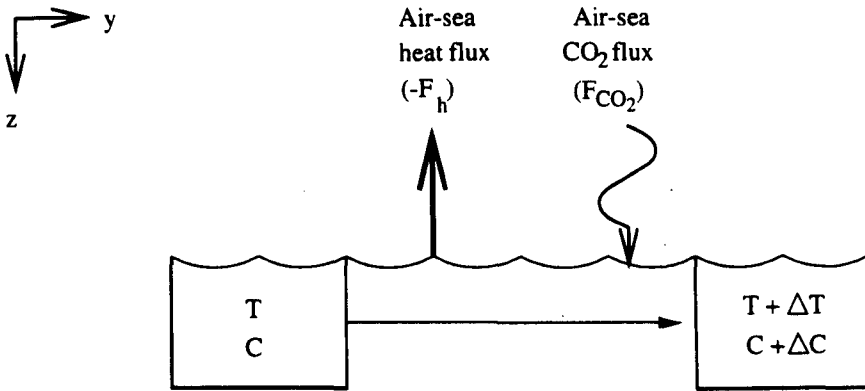
Figure 3.2: Diagram to illustrate the situation used to derive the first heat flux estimate of the CO_2 flux.

In the work presented in this section, it is only the effect of temperature on the air-sea CO_2 flux that is investigated. The effect of biological processes, salinity and alkalinity on the air-sea CO_2 flux are not discussed. Watson *et al.*(1995) found that the uptake of CO_2 by the North Atlantic was principally driven by temperature.

Two methods of obtaining an estimate of the CO_2 flux from the heat flux are found. These methods are derived by considering a moving volume of water that exchanges heat and carbon with the atmosphere.

First Estimate

Initially, the volume of water has a temperature T and carbon concentration C (figure 3.2). As the water moves, the temperature changes by ΔT as the water exchanges heat with the atmosphere. The change in temperature over time Δt

is expressed using equation (3.1) as,

$$\Delta T = \frac{F_h}{\rho c_p h} \Delta t. \tag{3.8}$$

The change in temperature will cause a change in the CO_2 solubility. This will affect the pCO_2 of the water. A change in pCO_2 will drive an air-sea flux of CO_2 in an attempt to stay in equilibrium with the atmosphere. Hence, a change in C will occur. The air-sea flux of CO_2 causes the carbon concentration to change by ΔC which is defined as,

$$\Delta C = \frac{F_{CO_2}}{h} \Delta t. \tag{3.9}$$

ΔC can be related back to the temperature change that caused the air-sea CO_2 flux using the quantity a (defined in equation 3.7) which gives,

$$\Delta C = a \Delta T. \tag{3.10}$$

In using the quantity a, it is assumed that the ocean stays in equilibrium with the atmosphere such that pCO_2 remains constant. This expression for ΔC can be substituted into equation (3.9) to give,

$$a \Delta T = \frac{F_{CO_2}}{h} \Delta t. \tag{3.11}$$

Finally, ΔT can be replaced using equation (3.8) to give an estimate of the air-sea CO_2 flux using the heat flux,

$$F_{CO_2}{}^{\text{upper}} = a \frac{F_h}{\rho c_p}. \tag{3.12}$$

This estimate of the air-sea CO_2 flux is named $F_{CO_2}{}^{\text{upper}}$ for a reason that will become apparent later. a is a negative quantity so an air-sea flux of heat into the ocean is associated with a flux of CO_2 out of the ocean. In obtaining this estimate of the air-sea CO_2 flux, it is assumed that the oceanic pCO_2 does not change during the change of temperature. This formula for a CO_2 flux estimate was first proposed by Watson et al.(1995).
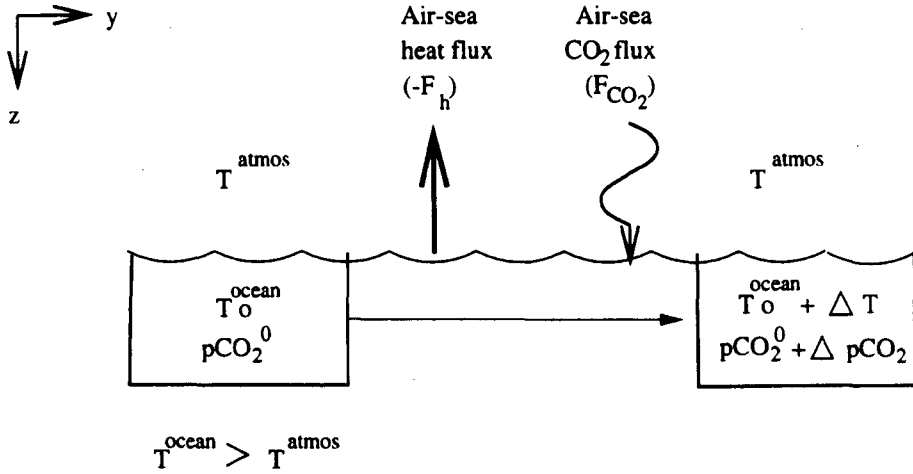
Figure 3.3: Diagram to illustrate the situation used to derive the second heat flux estimate of the CO$_2$ flux.

Second Estimate

The net air-sea CO$_2$ flux of an ocean region is controlled by the amount of carbon added to or removed from the surface mixed layer. Carbon is removed from the influence of the atmosphere during subduction. As the mixed layer deepens in the winter, entrainment will add carbon back to the surface layer. A net CO$_2$ uptake will occur if the subduction process removes more carbon than is supplied through entrainment. A volume of water circulating an ocean basin will experience several seasonal cycles, and, hence, several subduction periods will determine the overall atmospheric CO$_2$ uptake. To investigate the effect of the seasonal cycle further, the second estimate of the CO$_2$ flux is derived by considering a volume of water that experiences subduction only once. Therefore, the second estimate of the CO$_2$ flux is only appropriate for the seasonal timescale.

The similarity between the air-sea heat and CO$_2$ fluxes shown in equations (3.3) and (3.4) can be exploited to gain the second estimate of the CO$_2$ flux.

As before, a moving volume of water that changes temperature is considered (figure 3.3). Initially the volume of water has a water temperature of T^{ocean} which is different to the atmospheric temperature (T^{atmos}). The gradient in temperature across the air-sea boundary causes an air-sea heat flux which can be parameterized as in equation (3.4) as,

$$\frac{F_h}{c_p \rho h} = \mathcal{K}_T(T^{atmos} - T^{ocean}(t)).$$
(3.13)

The ocean temperature can be calculated at time t using,

$$\frac{\partial T^{ocean}}{\partial t} = \mathcal{K}_T(T^{atmos} - T^{ocean}(t))$$
(3.14)

which gives,

$$T^{ocean}(t) = T^{atmos} + (T_0^{ocean} - T^{atmos})\ e^{-\mathcal{K}_T t}$$
(3.15)

where T_0^{ocean} is the temperature of the ocean at time $t = 0$. The expression for $T^{ocean}(t)$ can then be substituted back into equation (3.13) to give,

$$\frac{F_h}{c_p \rho h} = \mathcal{K}_T(T^{atmos} - T_0^{ocean})e^{-\mathcal{K}_T t}$$
(3.16)

Using equation (3.15), the change in ocean temperature from the initial state is,

$$\Delta T = (T^{atmos} - T_0^{ocean})(1 - e^{-\mathcal{K}_T t})$$
(3.17)

The change in water temperature causes a change in water pCO₂ . The pCO₂ of the water is initially pCO_2^0 and changes by ΔpCO_2. This creates an air-sea flux of CO₂ which is expressed using equation (3.3) as,

$$
\begin{aligned}
F_{CO_2} &= \kappa\alpha(pCO_2^{atmos} - (pCO_2^0 + \Delta pCO_2)) \\
&= \kappa\alpha(pCO_2^{atmos} - pCO_2^0) - \kappa\alpha\Delta pCO_2.
\end{aligned}
$$
(3.18)

The CO₂ flux caused by the change in temperature (ΔT) is the second term on the right hand side of equation (3.18). This is the term that we are interested in. The first term on the right hand side of equation (3.18) is the initial air-sea

CO_2 flux and is assumed to be zero for the purposes of this derivation. A change in temperature will cause a change in the pCO_2 through changing the solubility of CO_2, which is expressed in τ (as defined in equation 3.5). Therefore, ΔpCO_2 can be expressed in terms of ΔT as,

$$\begin{aligned} \Delta pCO_2 &= \left(\frac{\partial pCO_2}{\partial T}\right)_C \Delta T \\ &= pCO_2\tau\Delta T \end{aligned} \tag{3.19}$$

In using the quantity τ, it is assumed that the change in the total carbon concentration is small and can be assumed to be zero. Equation (3.19) can then be substituted into equation (3.18) to give,

$$F_{CO_2} = -\kappa\alpha pCO_2\tau\Delta T. \tag{3.20}$$

ΔT in equation (3.20) can be replaced with equation (3.17) to give,

$$F_{CO_2} = -\kappa\alpha pCO_2\tau(T^{atmos} - T_0^{ocean})(1 - e^{-\mathcal{K}_T t}) \tag{3.21}$$

Averaging the air-sea fluxes of CO_2 and heat given in equations (3.21) and (3.16) over time from t=0 to t=t, gives

$$\begin{aligned} \overline{F_{CO_2}} &= -\frac{1}{t}\int_0^t F_{CO_2}dt \\ &= -\kappa\alpha pCO_2\tau(T^{atmos} - T_0^{ocean})\left(1 + \frac{e^{-\mathcal{K}_T t} - 1}{\mathcal{K}_T t}\right) \end{aligned} \tag{3.22}$$

$$\begin{aligned} \overline{F_h} &= -\frac{1}{t}\int_0^t F_h dt \\ &= \rho c_p h \mathcal{K}_T(T^{atmos} - T_0^{ocean})\frac{(1 - e^{-\mathcal{K}_T t})}{\mathcal{K}_T t}. \end{aligned} \tag{3.23}$$

$(pCO_2\tau)$ and T^{atmos} are assumed to remain constant in time.

Finally, equations (3.22) and (3.23) can be combined to give the second estimate of the CO_2 flux, which is named $F_{CO_2}{}^{lower}$,

$$\overline{F_{CO_2}}^{lower} = -\frac{\kappa\alpha}{h\theta}pCO_2\tau\frac{\overline{F_h}}{\rho c_p} \tag{3.24}$$

where

$$\theta^{-1} = \frac{t}{1 - e^{-\mathcal{K}_T t}} - \frac{1}{\mathcal{K}_T}. \tag{3.25}$$

θ has the units of t^{-1} and is therefore an inverse timescale. $\theta^{-1} \to t - 1/\mathcal{K}_T$ as $t \to \infty$. Therefore, the CO$_2$ flux estimate in equation (3.24) grows with time, which is due to the assumption of constant $\sum$CO$_2$. In reality, the CO$_2$ flux will reduce as $\sum$CO$_2$ reaches equilibrium with the atmospheric carbon concentration. τ is a positive quantity, hence, an air to sea flux of heat is associated with a sea to air flux of CO$_2$. In the derivation of $F_{CO_2}{}^{lower}$, it has been assumed that the change in carbon concentration is small.

3.1.2 Comparing the Two Estimates

Two contrasting expressions for estimating the air-sea CO$_2$ flux from the heat flux have been found. To compare the two estimates, the timescale of carbon exchange with the atmosphere is firstly derived. The air-sea flux of CO$_2$ (equation 3.3) can be expressed as a change in total carbon concentration as,

$$\frac{F_{CO_2}}{h} = \mathcal{K}_C(C^* - C) \tag{3.26}$$

$$\text{where} \quad \mathcal{K}_C = \frac{\kappa}{h} \alpha \beta \frac{pCO_2}{C}. \tag{3.27}$$

C^* is a pseudo carbon concentration that gives the correct air-sea flux and $\mathcal{K}_C$ is the inverse timescale of the exchange. To derive this equation, the buffer factor (β) has been used to convert the difference in pCO$_2$ to a difference in C as follows,

$$\frac{pCO_2^{atmos} - pCO_2}{pCO_2} = \beta \frac{(C^* - C)}{C}. \tag{3.28}$$

The carbon exchange timescale ($1/\mathcal{K}_C$) is equal to 8 months for a mixed layer depth (h) of 50m and the gas exchange velocity (κ) of 20 cm hr^{-1}. Therefore the timescale of carbon exchange is longer than the timescale associated with the air-sea heat flux.

Now, returning to the heat flux estimates of the air-sea CO_2 flux, the second estimate ($F_{CO_2}{}^{lower}$) can be written as,

$$F_{CO_2}{}^{lower} = \frac{k\alpha}{h\theta} \left(\frac{\partial pCO_2}{\partial C} \right)_T \left(\frac{\partial C}{\partial T} \right)_{pCO_2} \frac{F_h}{\rho c_p}.$$ (3.29)

Using the quantities a and β (as defined in equations 3.7 and 3.6), equation (3.29) can be written as,

$$
\begin{aligned}
F_{CO_2}{}^{lower} &= \frac{\kappa\alpha}{h\theta} \beta \frac{pCO_2}{C} a \frac{F_h}{\rho c_p} \\
&= \frac{\mathcal{K}_C}{\theta} a \frac{F_h}{\rho c_p}.
\end{aligned}
$$ (3.30)

Therefore,

$$F_{CO_2}{}^{lower} = \frac{\mathcal{K}_C}{\theta} F_{CO_2}{}^{upper}.$$ (3.31)

By comparing the estimates it can be seen that the timescale of carbon exchange is not considered in $F_{CO_2}{}^{upper}$. Hence, in $F_{CO_2}{}^{upper}$, the CO_2 exchange is (unrealistically) assumed to take place on the same timescale as heat exchange. As carbon exchange is a slower process than heat exchange, $F_{CO_2}{}^{upper}$ is expected to give better predictions over timescales of several years. The assumptions made during the derivations of $F_{CO_2}{}^{upper}$ also has implications for the estimate. $F_{CO_2}{}^{upper}$ is derived assuming that the water stays at the same pCO_2 as the atmosphere. As the carbon exchange equilibrium timescale is approximately one year, the water is unlikely to stay at equilibrium with the atmosphere.

For the estimate $F_{CO_2}{}^{lower}$, the timescale of carbon exchange has been taken into account. The heat flux is scaled by the ratio of the carbon timescale to the quantity θ in $F_{CO_2}{}^{lower}$. θ can be viewed as the inverse timescale of subduction. If the timescale of subduction is equal to the timescale of carbon equilibrium, the oceanic carbon concentration will have equilibrated with the atmosphere before subduction occurs. Hence, $F_{CO_2}{}^{lower}$ equals the equilibrium solution, $F_{CO_2}{}^{upper}$.

However, the timescale of subduction is the order of a season, and therefore $F_{CO_2}{}^{lower}$ will be less than $F_{CO_2}{}^{upper}$. $F_{CO_2}{}^{lower}$ is expected to give better predictions than $F_{CO_2}{}^{upper}$ over timescales of seasons.

In creating $F_{CO_2}{}^{lower}$, it was assumed that the change in total carbon concentration is small and can be ignored when calculating τ. Therefore, the assumptions used in $F_{CO_2}{}^{lower}$ are only valid over short timescales.

$F_{CO_2}{}^{upper}$ and $F_{CO_2}{}^{lower}$ only provide an estimate for the CO_2 flux caused by a change in temperature. CO_2 fluxes caused by changes in salinity, alkalinity or biological activity are not included in the heat flux estimates. Also any initial CO_2 flux that is present before the temperature change occurs will not be included in the estimates.

3.1.3 Summary

Two expressions relating the air-sea flux of heat and CO_2 have been found originating from the governing equations of temperature and carbon. These are summarised below.

$$
\begin{aligned}
F_{CO_2}{}^{upper} &= a\frac{F_h}{\rho c_p} \\[2mm]
F_{CO_2}{}^{lower} &= -\frac{\kappa\alpha}{h\theta}pCO_2\tau\frac{F_h}{\rho c_p} \\[2mm]
&= \frac{\mathcal{K}_C}{\theta}a\frac{F_h}{\rho c_p} \\[2mm]
\text{where } a &= \left(\frac{\partial C}{\partial T}\right)_{pCO_2} \\[2mm]
\text{and } \tau &= \left(\frac{\partial lnpCO_2}{\partial T}\right)_C
\end{aligned}
$$

The two estimates differ in the timescales used to predict the CO_2 flux and in the assumptions made to evaluate the derivatives in each expression. To understand the difference between the two CO_2 estimates and to investigate the accuracy of the estimates, a program of model experiments was designed.

3.2 Series of Model Tests

A series of progressively more complex models was used to investigate the ability of the heat flux estimates to predict CO_2 fluxes. The models were

1. a non-seasonal, one-dimensional model in which the ocean temperature was perturbed over one year;

2. a one-dimensional model with seasonally varying ocean temperature;

3. a fully seasonal, Lagrangian one-dimensional model of a column of water circulating around a subtropical gyre;

4. a three-dimensional planetary-geostrophic ocean model with and without seasonality; and

5. a three-dimensional general circulation ocean model.

The first three models were fundamental and were used to understand the differences between the air-sea fluxes of heat and CO_2. They were also used to examine how $F_{CO_2}{}^{upper}$ and $F_{CO_2}{}^{lower}$ differ. The planetary-geostrophic ocean model (PGOM) is an idealised three-dimensional model. PGOM was used to investigate how the relationship between heat and CO_2 fluxes differs in contrasting ocean regions. The effects of seasonality and the reaction of CO_2 with water were also analysed using PGOM. Finally, a complex general circulation model was used to accurately test the heat flux predictions of the CO_2 flux (which is described in the next chapter.)

In all the models, the solubility pump of carbon was included with **no** biological processes. Appendix C details how the air-sea flux of CO_2 was modelled in all of the carbon models used in this work.

3.3 Non-Seasonal One-Dimensional Model

3.3.1 Model Description

The model consists of a column of water that exchanges heat and carbon with the atmosphere. No other processes influence the water column. The evolution of the water temperature and carbon content are modelled. The model can be viewed as a simulation of a column of water exiting a western boundary current and adjusting to the new atmospheric conditions. The model experiment ends when the volume of water reaches equilibrium with the atmosphere.

The governing equations for temperature (T) and total inorganic carbon concentration (C) are,

$$\frac{DT}{Dt} = \mathcal{K}_T(T^* - T)$$
$$\frac{DC}{Dt} = \kappa\alpha(pCO_2^{atmos} - pCO_2).$$

$1/\mathcal{K}_T$, the timescale for heat exchange, is set at 2 months. pCO_2^{atmos} is equal to 278 μ atm and T^* is held at 15 °C throughout the model run. The method used to calculate pCO_2 is described in Appendix C.

The column of water is 50 m deep and initially has the same pCO_2 as the atmosphere. The water temperature is initially at 20 °C. Salinity is kept constant at 35. The model was run until the water returns to state of equilibrium with the atmosphere. The model CO_2 flux was then compared with estimates of the flux inferred using the model heat flux ($F_{CO_2}{}^{upper}$ and $F_{CO_2}{}^{lower}$). Mean values of τ and β calculated from the model results over the first three years were used in the calculation of $F_{CO_2}{}^{upper}$ and $F_{CO_2}{}^{lower}$.
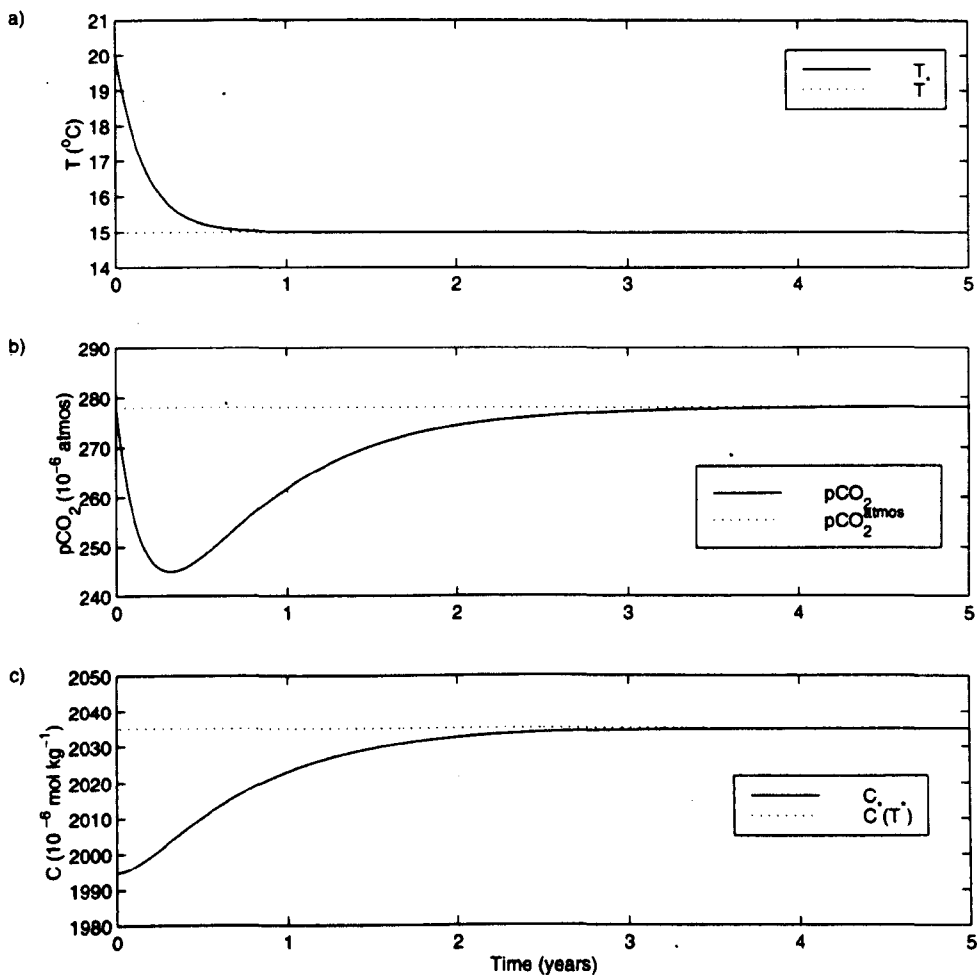
Figure 3.4: Results from the non-seasonal 1-D model. Time series of: a) temperature of the water column (solid line) and atmosphere (dotted line) (^{o}C); b) pCO$_2$ (solid line) and pCO$_2$^{atmos} (dotted line) (μ atm); c) total inorganic carbon concentration of the water column (solid line) and the carbon concentration in equilibrium with the atmospheric pCO$_2$ and atmospheric T (dotted line) (μ mol kg^{-1}).

3.3.2   Surface Fluxes

The time series of the temperature, carbon concentration and pCO$_2$ of the column of water are shown in figure 3.4. The difference in water and atmospheric temperature at the start of the model drives a heat flux out of the water. This causes the water temperature to decrease. After one year, the water temperature has reached equilibrium with the atmospheric temperature.

Over the first year, the decreasing water temperature causes the CO$_2$ solubility to increase and, hence, the pCO$_2$ of the water falls below the pCO$_2$ of the atmosphere (figure 3.4b). The gradient in partial pressures drives a carbon flux into the ocean from the atmosphere. The air-sea flux of CO$_2$ causes the carbon concentration of the water to increase (figure 3.4c). However, the air-sea flux of CO$_2$ is unable to restore equilibrium over the first few months and the pCO$_2$ continues to drop below the atmospheric pCO$_2$. After four months, the pCO$_2$ starts to increase as the air-sea flux continually drives CO$_2$ into the water. By the fourth year of the model run, the column of water has the same pCO$_2$ as the atmosphere and the air-sea flux of CO$_2$ ceases.

The actual and the equilibrium carbon concentrations are presented in figure 3.4c. The equilibrium carbon concentration (C^*) is the carbon concentration that the water would have if it remained in equilibrium with the atmospheric CO$_2$ content and atmospheric temperature. C^* remains constant throughout the model run as the atmospheric temperature is held constant. Figure 3.4c highlights the disequilibrium between the carbon concentration of the water and the atmosphere in the first three years of the model run.

The air-sea flux of heat (figure 3.5) is directed out of the ocean and has a maximum value of ~ 200 W m^{-2} at the start of the model run. The heat flux decreases over the model run as the water temperature approaches the atmospheric temperature. The heat flux approaches zero by the end of the first year.
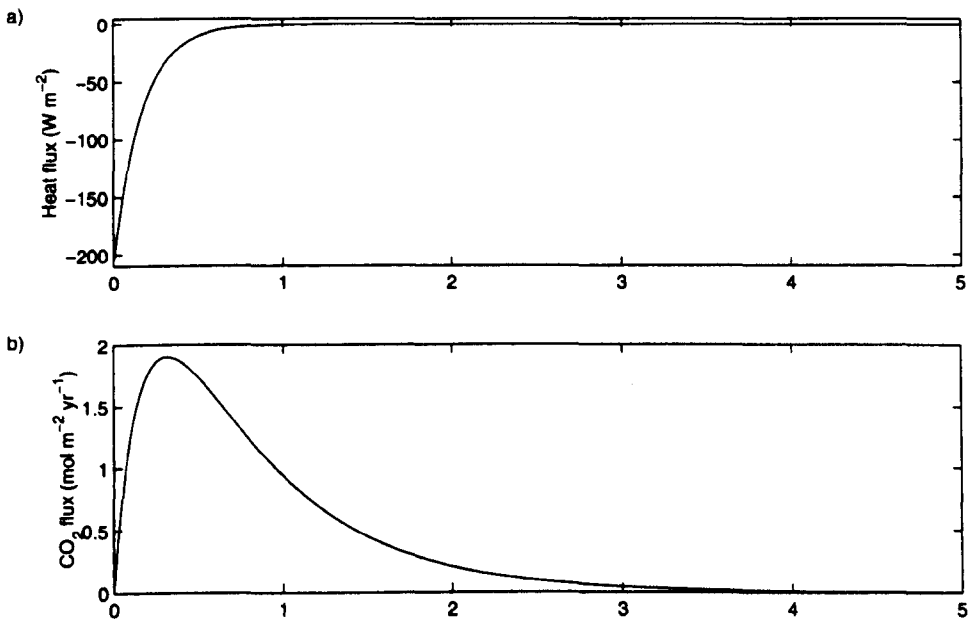
Figure 3.5: Results from the non-seasonal 1-D model. Time series of: a) the air-sea heat flux ($W\ m^{-2}$); and b) the model air-sea CO_2 flux ($mol\ m^{-2}\ yr^{-1}$). A positive flux is directed into the ocean.
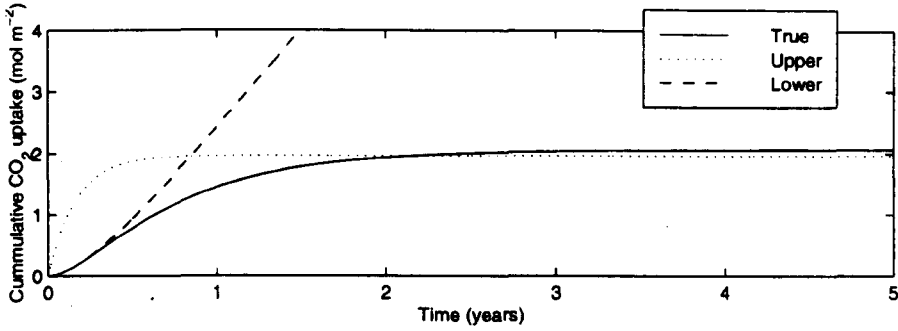
Figure 3.6: Results from the non-seasonal 1-D model. Time series of the cumulative CO$_2$ uptake (mol m^{-2}) (solid line). Also shown are the air-sea CO$_2$ fluxes inferred from the heat flux, F_{CO_2} ^{upper} (dotted line) and F_{CO_2} ^{lower} (dashed line).

The air-sea flux of CO$_2$ is in the opposite direction to the heat flux (figure 3.5b). The water loses heat and gains carbon from the atmosphere. The highest CO$_2$ flux of ~ 2 mol m^{-2} yr^{-1} occurs in the fourth month of the model run. The CO$_2$ flux eventually becomes zero during the fourth model year, three years after the heat flux becomes zero. This delay in carbon equilibrium is caused by the longer exchange timescale of carbon compared to the timescale of heat exchange.

3.3.3 Accuracy of F$_{CO_2}$ ^{upper}

The cumulative CO$_2$ uptake is shown in figure 3.6. The volume of water takes up 2 mol m^{-2} of carbon over the five year model run. Also presented in figure 3.6 are the heat flux estimates of the CO$_2$ uptake. F_{CO_2} ^{upper} initially overestimates the CO$_2$ uptake. However, after the second year, F_{CO_2} ^{upper} provides an accurate estimate of the actual CO$_2$ uptake, as the CO$_2$ flux has responded fully to the change in water temperature.

The change in carbon concentration (ΔC) of the volume of water is affected by the change in temperature (ΔT) and the change in pCO$_2$ (ΔpCO_2). This can
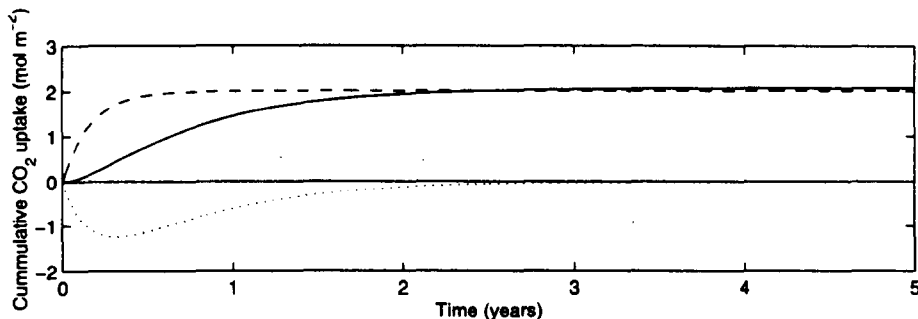
Figure 3.7: Time series of the cumulative ΔC (the air-sea CO$_2$ flux) (solid line) with the ΔT component (dashed line) and the ΔpCO_2 component (dotted line) as defined in equation (3.32).

be expressed as,

$$\Delta C = \left(\frac{\partial C}{\partial T}\right)_{pCO_2} \Delta T + \left(\frac{\partial C}{\partial pCO_2}\right)_T \Delta pCO_2 \qquad (3.32)$$

Figure 3.7 shows the individual terms of equation (3.32) for the model experiment. In the estimate $F_{CO_2}{}^{\text{upper}}$, the second term of equation (3.32) is assumed to equal zero. As shown in figure 3.7, the second term in not initially zero as pCO$_2$ is changing. Therefore, initially $F_{CO_2}{}^{\text{upper}}$ is an overestimate of the true uptake. However, as the volume of water approaches equilibrium, ΔpCO_2 becomes zero, and the second term in equation (3.32) disappears. So over the entire model run, $F_{CO_2}{}^{\text{upper}}$ gives an accurate estimate of the net uptake.

3.3.4   Accuracy of $F_{CO_2}{}^{\text{lower}}$

The cummulative CO$_2$ uptake predicted by $F_{CO_2}{}^{\text{lower}}$ is also included in figure 3.6. Over the first few months, $F_{CO_2}{}^{\text{lower}}$ gives a very accurate prediction of the cummulative uptake. However, $F_{CO_2}{}^{\text{lower}}$ then continues to increase exponentially due to the assumption of a constant total carbon concentration. However, $F_{CO_2}{}^{\text{lower}}$ is

71
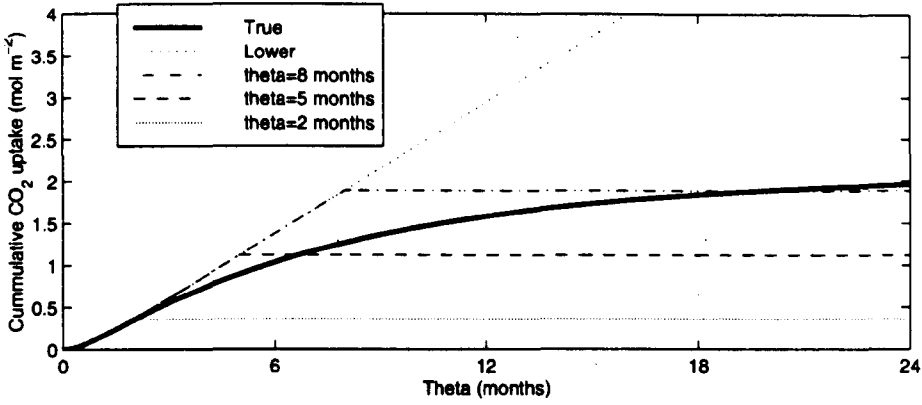
Figure 3.8: Results from the non-seasonal 1-D model. Time series of the cumulative CO_2 uptake (mol m^{-2}) (thick solid line) against the subduction timescale (θ^{-1}). Also shown is the air-sea CO_2 flux inferred from the heat flux using F_{CO_2} ^{lower}. The dotted line is F_{CO_2} ^{lower} with no subduction occurring. The grey, dashed and dash-dot line correspond to F_{CO_2} ^{lower} with subduction occurring when θ^{-1} is equal to 2 months, 5 months and 8 months respectively.

only intended to give an estimate of the CO_2 flux on the seasonal timescale prior to subduction. Figure 3.8 shows the true cummulative CO_2 uptake, togther with F_{CO_2} ^{lower} estimates where subduction occurs when θ^{-1} reaches certain times. If subduction occurs when θ^{-1} is equal to 2 months (i.e. $\mathcal{K}_T^{-1}$), F_{CO_2} ^{lower} provides an accurate estimate of the CO_2 uptake. Longer values of θ^{-1} cause the uptake to be overestimated. When θ^{-1} equal to 8 months, $\theta \sim \mathcal{K}_C$, and F_{CO_2} ^{lower} is approximately equal to F_{CO_2} ^{upper}.

These results of F_{CO_2} ^{upper} and F_{CO_2} ^{lower} are summarized in table 3.1.

3.3.5 Discussion

The air-sea flux of CO_2 responds to changes in temperature on a timescale slower than the heat flux. This causes the pCO_2 of the water to drop below the atmospheric pCO_2. F_{CO_2} ^{upper} responds to changes of temperature on the same timescale as the heat flux. F_{CO_2} ^{upper} also assumes that there are no changes in

Time period	F_{CO_2} actual	F_{CO_2} upper	F_{CO_2} lower (with θ^{-1}=2 months)
Over first 3 months	0.32	1.53	0.33
Over 1st year	1.44	1.98	0.36
Over all 5 years	2.07	1.98	0.36

Table 3.1: The actual and inferred net uptake of CO$_2$ by the water column over the first 3 months, the first year and over the whole 5 years of the model run (mol C m^{-2}).

pCO$_2$ and the water remains at equilibrium with the atmospheric CO$_2$ content. During the first year, there are changes in the water pCO$_2$, and therefore, F_{CO_2} upper overestimates the CO$_2$ flux. Over the whole five years, the carbon concentration of the water column is allowed to fully respond to the change of heat content on it's own timescale. Therefore, over the five year period there is no net change in pCO$_2$ and F_{CO_2} upper provides an accurate prediction of the CO$_2$ uptake over the whole of model run.

F_{CO_2} lower is intended to predict the CO$_2$ flux on the seasonal timescale and has been found in this experiment to give accurate results over the first few months, with θ equal to $\mathcal{K}_T$. After the initial months, the assumption of constant $\sum$CO$_2$ made in the derivation of F_{CO_2} lower becomes unrealistic, and F_{CO_2} lower overestimates the net uptake.

To summarize, this simple experiment reveals that F_{CO_2} lower gives good predictions of the net CO$_2$ uptake over the first few months and F_{CO_2} upper gives good predictions after two years.

This idealised experiment allows F_{CO_2} upper and F_{CO_2} lower to be investigated. However, the model experiment is unrealistic as the water temperature will con-

tinually be changing as the water moves around the ocean. $F_{CO_2}{}^{upper}$ gives a good estimate of the actual CO_2 uptake in this model experiment because the carbon system has been allowed to reach equilibrium. In the ocean where the temperature is constantly changing, this may not necessarily be true. Therefore, the results over the first year of the model run are probably more representative of the true situation.

3.3.6   Sensitivity Test

In the calculation of $F_{CO_2}{}^{lower}$ and $F_{CO_2}{}^{upper}$, the quantities τ, β and a (as defined in section 3.1.1) must be known. In the results quoted in the previous section, τ, β and a were calculated within the model and mean values were used in the calculation of $F_{CO_2}{}^{lower}$ and $F_{CO_2}{}^{upper}$ which were 0.0386 $^{o}C^{-1}$, 10.12 and - 7.72 $\times 10^{-6}$ mol kg^{-1} $^{o}C^{-1}$ respectively. In contrast, Watson et al.(1995) used typical values of β and C (10 and 2000 μ mol kg^{-1}) in the calculation of a to estimate the CO_2 uptake using $F_{CO_2}{}^{upper}$. A τ value of 0.0423 $^{o}C^{-1}$ found experimentally by Takahashi et al.(1993) was also used by Watson et al.(1995). The constants used by Watson et al.(1995) were used to calculate $F_{CO_2}{}^{upper}$ and $F_{CO_2}{}^{lower}$ for the 1-D model results. The choice of constants used in the CO_2 flux estimates was found not to significantly change the results and did not account for the inaccuracy of the estimates over the first year. Therefore, it is concluded that the CO_2 flux estimates, $F_{CO_2}{}^{upper}$ and $F_{CO_2}{}^{lower}$, are not significantly sensitive to the choice of τ, β and a.

3.3.7   Choice of θ in $F_{CO_2}{}^{lower}$

Throughout the rest of this work, $F_{CO_2}{}^{lower}$ will be evaluated using θ equal to $\mathcal{K}_T$. The timescale of heat exchange is 2-3 months which is an appropriate timescale for subduction. In the simple 1-D model, this choice of θ has provided accurate

results on the seasonal timescale. However, the predictions of $F_{CO_2}{}^{lower}$ can be rescaled with different values of θ if required.

3.4 One-Dimensional Model with Seasonally Varying Temperature

3.4.1 Model Description

The previous model experiment investigated the net uptake of CO_2 in a situation with a changing ocean temperature but a constant atmospheric temperature. In this seasonally varying model, the atmospheric and ocean temperature change seasonally. The model consists of the same volume of water as the first model experiment, except that it remains stationary and there is no net temperature change over one year. A seasonal cycle is imposed on the atmospheric temperature. The governing equations are,

$$\frac{\partial T}{\partial t} = \mathcal{K}_T(T^* - T)$$
$$\frac{\partial C}{\partial t} = \kappa\alpha(pCO_2^{atmos} - pCO_2).$$

$1/\mathcal{K}_T$, the timescale for heat exchange, is set to 2 months and the atmospheric pCO_2 (pCO_2^{atmos}) is equal to 278 μ atm. A sinusoidal wave was used to model the seasonal variation of T^* (dotted line in figure 3.9a). The model was run until a steady repeating seasonal cycle was achieved with no net air-sea fluxes of heat or CO_2 during a year. As before, the model air-sea CO_2 flux was compared with the values inferred from the heat fluxes. The values used for τ, β and C in the calculation of $F_{CO_2}{}^{lower}$ and $F_{CO_2}{}^{upper}$ were values of 0.0423 ^{o}C $^{-1}$, 10 and 2000 μ mol kg^{-1} respectively as assumed by Watson *et al.*(1995). In $F_{CO_2}{}^{lower}$, θ is set equal to $\mathcal{K}_T$.

3.4.2 Surface Fluxes

Figure 3.9 shows the temperature, heat and CO_2 fluxes over a 2 year period after the cycles have become steady. The coldest temperature of the water column occurs during March lagging the atmospheric temperature by 2 months. The air-sea heat flux is directed into the water during summer and out of the water during winter. The summer influx of heat balances the loss of heat during winter. The air-sea flux of CO_2 is generally in the opposite direction to the heat flux, with the water gaining carbon in the winter and losing the newly gained carbon in the summer. However, there is a time lag of $\sim$ 3 months between the heat and CO_2 fluxes changing direction which is seen in figure 3.9b.

The CO_2 fluxes inferred from the instantaneous heat fluxes are presented in figure 3.9c. $F_{CO_2}{}^{lower}$ captures the amplitude of the CO_2 flux seasonal cycle accurately but with the incorrect phase. $F_{CO_2}{}^{upper}$ greatly overestimates the seasonal variation of the CO_2 flux.

The reason that $F_{CO_2}{}^{lower}$ predicts the seasonal variation of the instantaneous CO_2 flux well can be investigated by considering the relationship between the seasonal change in temperature and carbon concentration. If the seasonal change in C is related to the seasonal change in temperature (ΔT) by,

$$\frac{\partial C}{\partial t} = \mathcal{K}_C\, a\, \Delta T. \qquad (3.33)$$

Then using $\Delta T = T^{seas}\, sin(\omega t)$ and integrating equation (3.33) gives,

$$C = -\frac{\mathcal{K}_C a}{\omega}\, T^{seas}\, cos(\omega t) + \mathcal{D}, \qquad (3.34)$$

where $\mathcal{D}$ is a constant of integration. The seasonal cycle of C predicted using the model temperature and equation (3.34) is a reasonable approximation of the true seasonal variation of the model C (as shown in figure 3.10). The seasonal cycle of C is 90° out of phase with the temperature cycle. The magnitude of

76
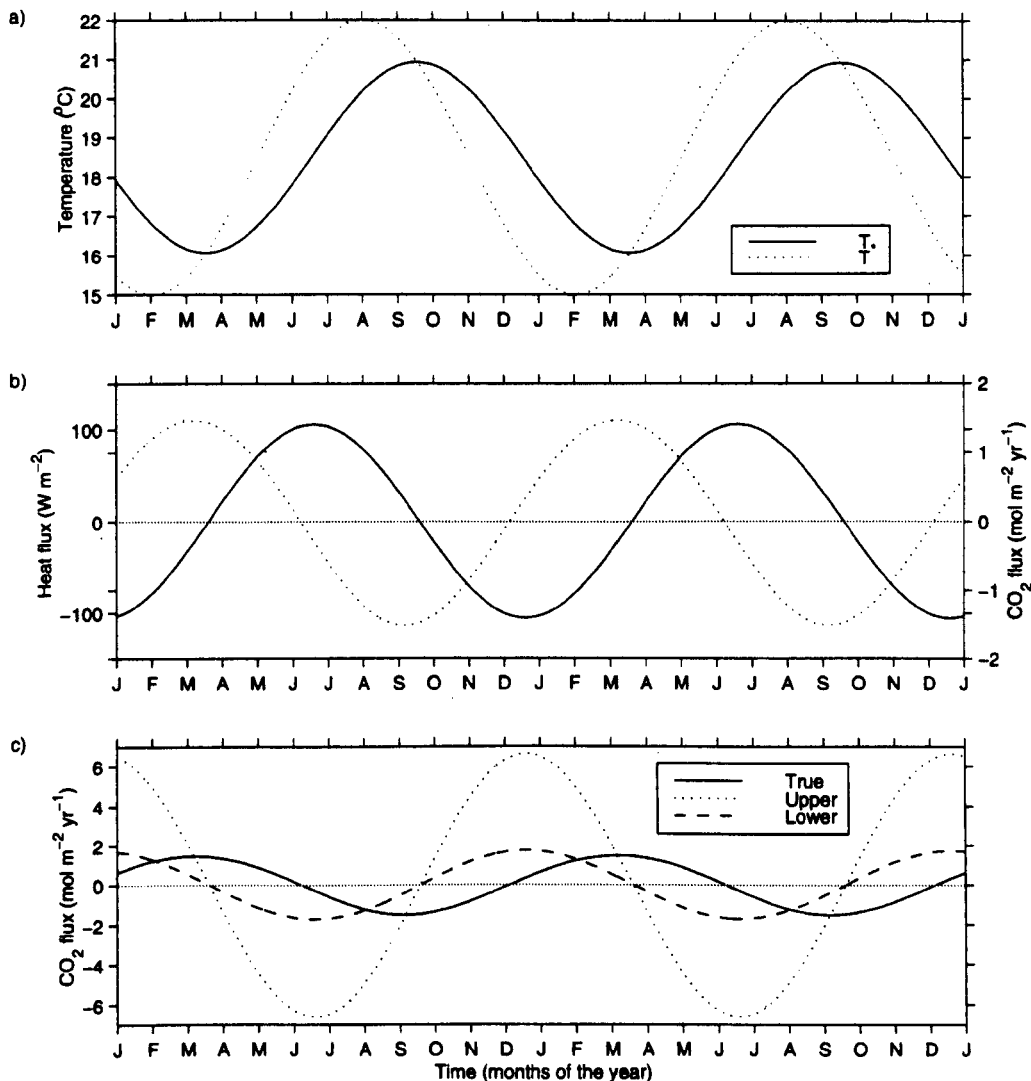
Figure 3.9: 2 year time series of the seasonal temperature 1-D model of: a) water temperature (solid line) and atmospheric temperature (dotted line) (^{o}C); b) air-sea heat flux (solid line, W m^{-2}) and air-sea CO$_2$ flux (dotted line, mol C m^{-2} yr^{-1}); and c) model air-sea CO$_2$ flux (solid line) and estimates of the CO$_2$ fluxes inferred from heat fluxes, F_{CO_2} ^{upper} (dotted line) and F_{CO_2} ^{lower} (dashed line) (mol C m^{-2} yr^{-1}). Positive fluxes are directed into the ocean.
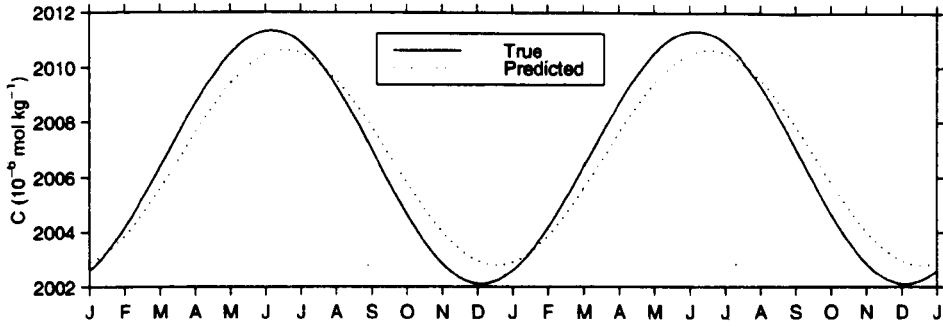
Figure 3.10: 2 year time series of the seasonal temperature 1-D model of model total carbon concentration (solid line) and total carbon concentration evaluated from the temperature and equation (3.34) (dotted line) (10^{-6} mol^{-1} kg^{-1}).

the seasonal C cycle is equal to the magnitude of the temperature seasonal cycle scaled by $\mathcal{K}_C\, a/\omega$. $F_{CO_2}{}^{lower}$ scales the heat flux by the quantity $\mathcal{K}_C\, a/\theta$. As ω (1.9 months^{-1}) is approximately equal to the choice of θ used in this experiment (2 months^{-1}) then $F_{CO_2}{}^{lower}$ has the correct scaling for the seasonal cycle of C. Therefore, $F_{CO_2}{}^{lower}$ correctly predicts the magnitude of the seasonal CO₂ flux variations. However, $F_{CO_2}{}^{lower}$ does not have the correct phase for the seasonal cycle of the CO₂ flux as the C cycle is 90° out of phase with the T cycle.

3.4.3 Discussion

The seasonal temperature variations are very rapid and occur on a timescale shorter than the air-sea CO₂ flux. Therefore, the timescale of $F_{CO_2}{}^{upper}$ is too short to accurately predict the seasonal variations of the air-sea CO₂ flux. In contrast, $F_{CO_2}{}^{lower}$ gives very good predictions of the amplitude of the seasonal air-sea CO₂ fluxes as $F_{CO_2}{}^{lower}$ has the correct timescale.
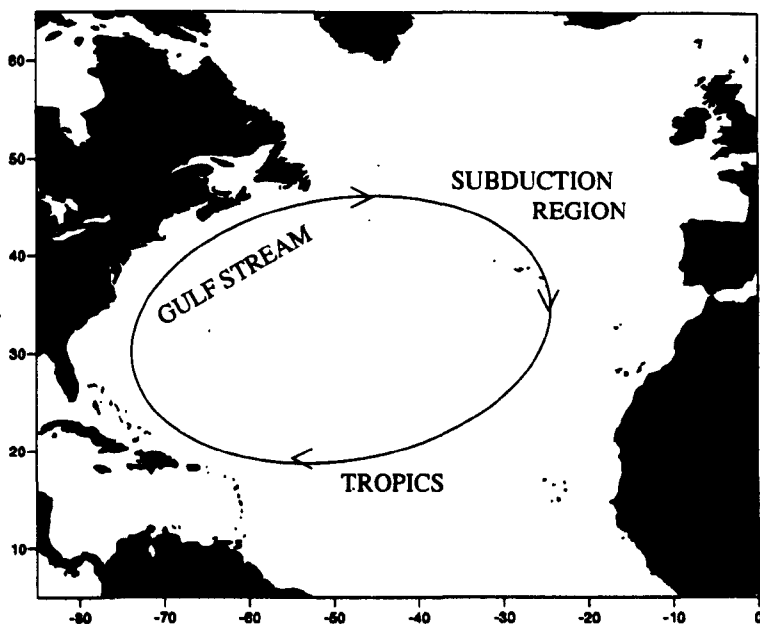
Figure 3.11: Sketch of the path of the Lagrangian model of Follows *et al.*(1996) around a subtropical gyre.

3.5 Fully Seasonal One-Dimensional Lagrangian Model

3.5.1 Model Description

The one-dimensional model was made fully seasonal by adding a varying mixed layer depth. To make the temperature and mixed layer depth changes realistic, the model was based on the Lagrangian one-dimensional model used in Follows *et al.*(1996). The model mimics a column of water travelling around a subtropical gyre (figure 3.11) which exchanges heat and carbon with the atmosphere. A full circuit of the gyre takes 12 years. The temperature and carbon concentration of the column of water are solved for using the model governing equations. The mixed layer depth and the air-sea heat flux are imposed.

Heat and carbon are exchanged across the sea surface and are entrained from below the mixed layer. The governing equation for T is,

$$\frac{DT}{Dt} + w\frac{\partial}{\partial z}T + \frac{\partial}{\partial z}\overline{w'T'} = \frac{1}{\rho C_p}\frac{\partial I}{\partial z}. \qquad (3.35)$$

D/Dt is defined as the Lagrangian derivative $(\partial/\partial t + \mathbf{u_h}.\nabla)$ where $\mathbf{u_h}$ is the horizontal velocity that advects the column around the gyre. I is the penetrating solar radiation. Following the water column, the mixed layer temperature is changed by vertical advection (2nd term in equation 3.35), by turbulent fluxes caused by surface forcing and entrainment (3rd term) and by solar heating (1st term on right-hand side).

Equation (3.35) can be integrated over the mixed layer thickness (h) to give,

$$h\frac{DT_m}{Dt} + \overline{w'T'}_{z=0} - \overline{w'T'}_{z=-h} = \frac{1}{\rho C_p}I(0). \qquad (3.36)$$

neglecting the solar heat flux at the base of the mixed layer. The surface turbulence flux and entrainment fluxes are parameterized to give the following equation for the temperature in the mixed layer,

$$h\frac{DT_m}{Dt} = \frac{F_h}{c_p\rho} - \bigwedge\left(w + \frac{Dh}{Dt}\right)(T_m - T_{th}), \qquad (3.37)$$

where $F_h = I(0) - \rho C_p\overline{w'T'}_{z=0}$ and

$$\bigwedge = 1 \quad \text{if} \left(w + \frac{Dh}{Dt}\right) > 0$$

$$\bigwedge = 0 \quad \text{if} \left(w + \frac{Dh}{Dt}\right) \leq 0.$$

The subscript m indicates the mixed layer and th the thermocline. The first term on the right hand side of equation (3.37) is the air-sea flux of heat. The second term is the entrainment of heat from the underlying thermocline. The entrainment rate ($w + Dh/Dt$) is equal to the vertical advection at the base of the mixed layer plus the rate of mixed layer deepening (following Denman, 1973). Entrainment is switched on and off by the Heaviside function, $\bigwedge$.

In this simple model, Ekman advection is ignored, although the model of Follows *et al.*(1996) includes the Ekman velocity component. Thus, the governing equation for the temperature of a mixed layer following the geostrophic flow is,

$$h\frac{DT_m}{Dt} = \frac{F_h}{c_p\rho} - \bigwedge\frac{Dh}{Dt}(T_m - T_{th}).$$

(3.38)

The lack of Ekman advection in the model causes no water to be permanently subducted into the main thermocline over the circuit of the gyre. Therefore, there are no net air-sea fluxes of heat or carbon over one complete 12 year cycle. Total inorganic carbon (C) was modelled in a similar manner to T with the following governing equation

$$h\frac{DC}{Dt} = \kappa\alpha(pCO_2^{atmos} - pCO_2) - \bigwedge\frac{Dh}{Dt}(C_m - C_{th}).$$

(3.39)

The model had the mixed layer depth and the air-sea heat flux imposed using the values shown in figure 3.12. The column of water spends 8 years in the 'subduction region' where there is an annual heat flux into the ocean. The mixed layer is very deep in the winter and shallows sharply every spring. The water column is then advected into the 'tropics' where there is little net heat exchange over a year and shallow winter mixed layers. After leaving the tropics, the water column is rapidly advected northwards in the Gulf Stream and loses heat to the atmosphere. The winter mixed layer deepens dramatically. The water column only spends 1 year in the 'Gulf Stream' region before recirculating back into the subduction region. There is no net air-sea heat flux during the cycle, so the heat gained by the water column whilst in the subduction region is lost during the short passage in the Gulf Stream.

Values of 0.0423 °C $^{-1}$, 10 and 2000 μ mol kg^{-1}were used for τ, β and C respectively in the calculation of F_{CO_2} $^{\text{upper}}$ and F_{CO_2} $^{\text{lower}}$.
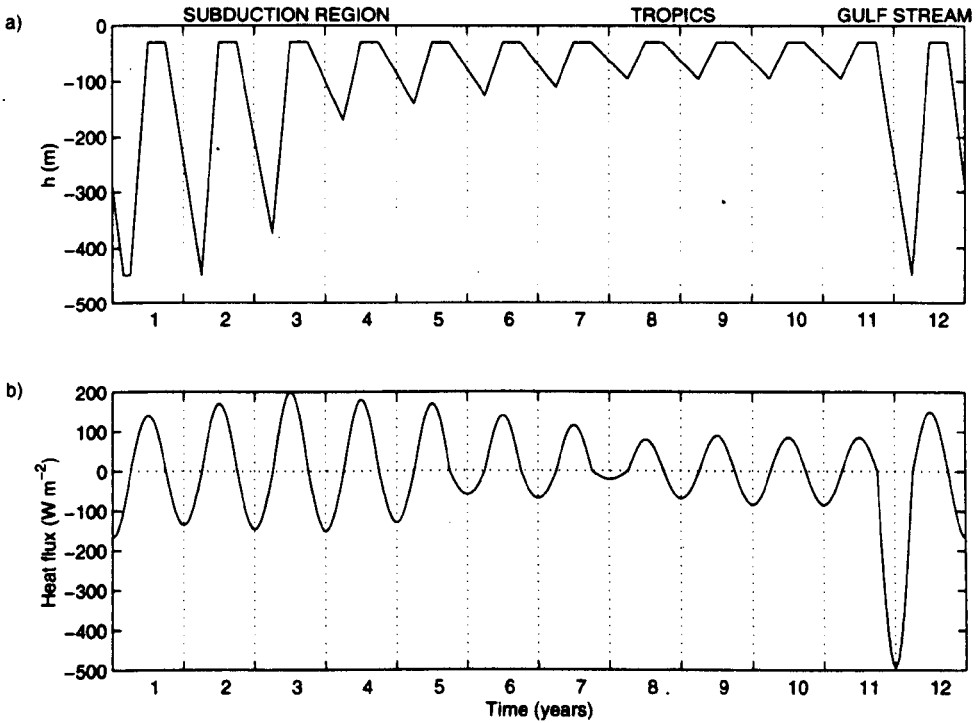
Figure 3.12: The cycle of: a) the imposed mixed layer depth (m); and b.) the imposed air-sea heat flux (W m^{-2}) used in the Lagrangian 1-D seasonal model. A positive heat flux is directed into the ocean.
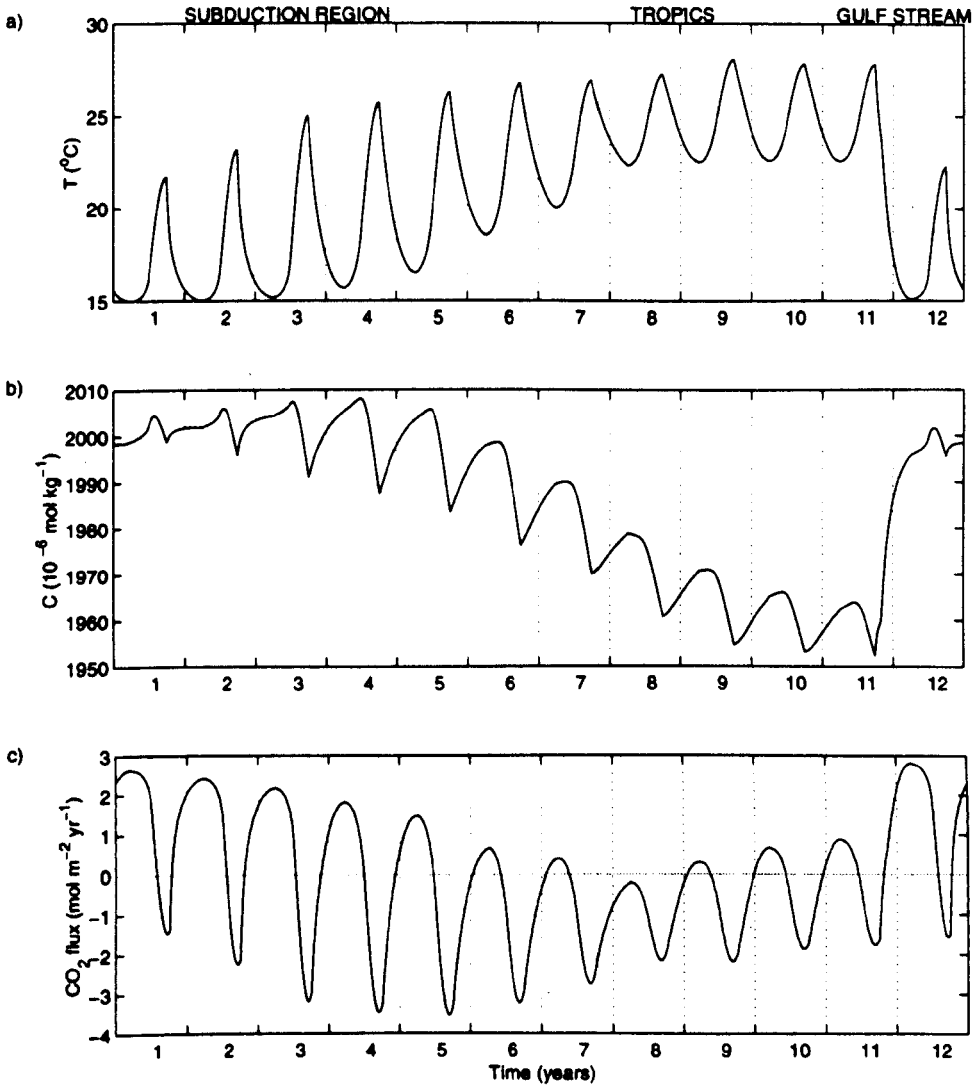
Figure 3.13: Time series of: a) mixed layer temperature (^{o}C); b) mixed layer carbon concentration (10^{-6} mol kg^{-1}); and c) the air-sea flux of CO$_2$ (mol m^{-2} yr^{-1}) for the Lagrangian 1-D seasonal model. A positive CO$_2$ flux is directed into the ocean.

3.5.2 Surface Fluxes

The time series of temperature (figure 3.13a) has a pronounced seasonal cycle with a variation of 5 to 10 °C. The temperature increases in the subduction region as the annual air-sea heat flux is directed into the ocean. In the tropics, temperature has a regular repeating seasonal cycle. In the autumn of the eleventh year, the column of water experiences large changes as it enters the Gulf Stream. The temperature drops quickly during the winter as heat is lost to the atmosphere. The column of water then cycles back into the subduction region.

There is little seasonal variation in the carbon concentration during the first years of the passage through the subduction region (figure 3.13b). The lack of seasonal variation is caused by the deep mixed layers which increase the carbon exchange timescale. During years 4 to 7, there is a stronger seasonal cycle as the winter mixed layers are shallower and the CO_2 flux can respond quicker to the seasonally varying temperature. In the tropics, the ocean loses carbon to the atmosphere as the temperature increases. The carbon concentration during the winter increases despite the weak sea-air flux due to entrainment of richer carbon water from below. In the Gulf Stream region, the temperature decrease causes the water to take up carbon and the carbon concentration rapidly increases during years 11 and 12. However, after leaving the Gulf Stream, the carbon concentration is still not in equilibrium with the new environmental conditions. There is a delayed reaction of the CO_2 flux to the large decrease in temperature and the deepening mixed layers that occurs in the Gulf Stream. Therefore, the ocean continues to take up CO_2 for the first few years while in the subduction region.

The annual mean air-sea heat and CO_2 fluxes are compared in figure 3.14. The annual mean heat flux is in the opposite direction to the CO_2 flux for the majority of years. In the tropics, the water gains heat and loses CO_2 . In the
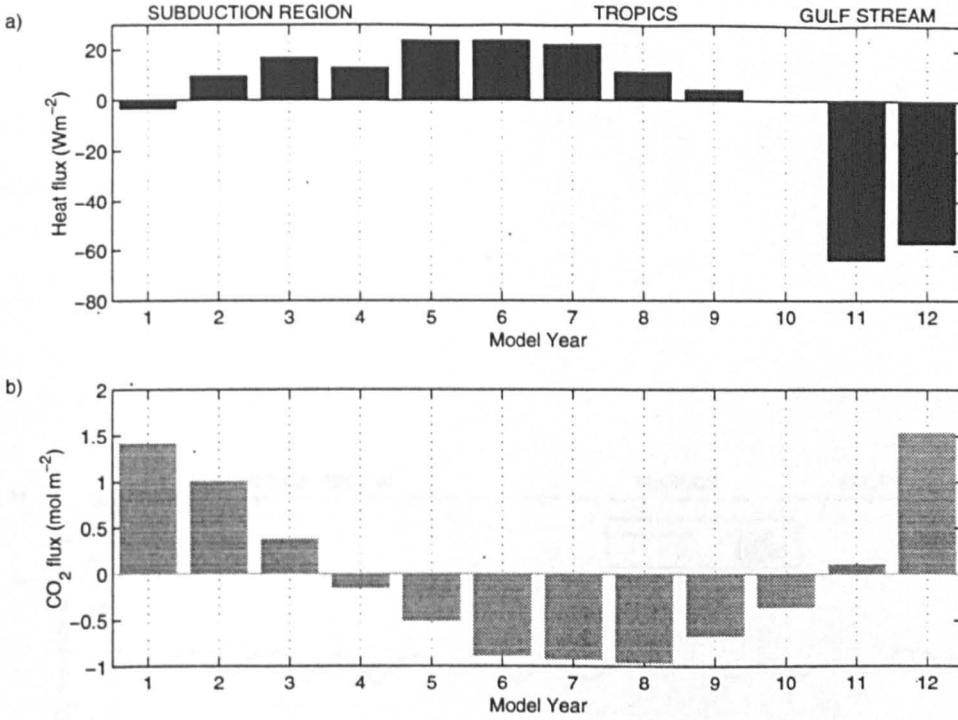
Figure 3.14: Time series of: a) annual mean air-sea heat flux (Wm^{-2}); and b) annual mean air-sea CO_2 flux (mol m^{-2} yr^{-1}). A positive flux is directed into the ocean.

Gulf Stream, the water loses heat very quickly but gains CO_2 at a slower rate. The delayed reaction of the CO_2 flux to the rapid temperature decrease in the Gulf Stream, causes the CO_2 uptake to continue into the subduction region. In years 2 and 3, the air-sea heat and CO_2 fluxes are in the same direction as the CO_2 flux is still reacting the large temperature decrease in the Gulf Stream.

Inferred CO_2 Fluxes

The CO_2 fluxes inferred from the heat flux are presented in figure 3.15. In the F_{CO_2} ^{lower} calculation for this model, the median carbon timescale of 10.8 months is used and a subduction timescale (θ^{-1}) of 2 months.

As in the previous model, F_{CO_2} ^{upper} overestimates the seasonal variation of the CO_2 flux (figure 3.15a). The large heat flux in the Gulf Stream region is not matched with an exceptionally large CO_2 flux. Instead the CO_2 flux remains high
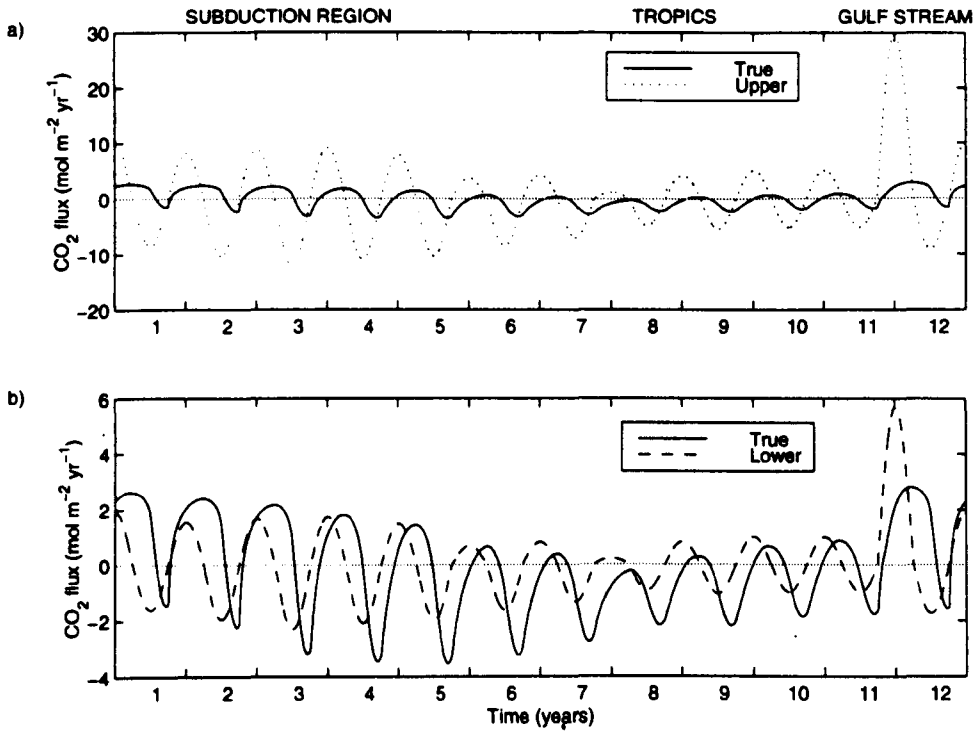
Figure 3.15: Time series of inferred and actual air-sea CO_2 fluxes (mol m^{-2} yr^{-1}) for the Lagrangian 1-D seasonal model: a) actual flux (solid line) and $F_{CO_2}{}^{upper}$ (dotted line); and b) actual flux (solid line) and $F_{CO_2}{}^{lower}$ (dashed line). A positive CO_2 flux is directed into the ocean.

over a longer time than the heat flux. $F_{CO_2}{}^{\text{lower}}$ captures the magnitude of the seasonal variation better than $F_{CO_2}{}^{\text{upper}}$ (figure 3.15b). However, the phase lag between the heat and CO₂ fluxes is apparent.

Cumulative CO₂ Uptake

The estimates of $F_{CO_2}{}^{\text{upper}}$ and $F_{CO_2}{}^{\text{lower}}$ are intended to give the net uptake of CO₂ over a period. The cumulative CO₂ uptake of the volume of water is calculated from two starting locations. Figure 3.16 presents the cumulative uptake starting in year 11 as the volume of water enters the Gulf Stream. There is no net air-sea CO₂ exchange over the 12 year cycle, as the model is at steady state with no net subduction occuring during the cycle. $F_{CO_2}{}^{\text{lower}}$ gives good predictions of the CO₂ uptake initially but then underestimates the net uptake. $F_{CO_2}{}^{\text{upper}}$ overestimates the initial CO₂ uptake associated with the passage through the Gulf Stream. However, after 6-7 years when the volume of water has travelled to the subduction region, $F_{CO_2}{}^{\text{upper}}$ provides a good estimate of the net uptake. When the temperature is changing quickly (such as in the Gulf Stream), $F_{CO_2}{}^{\text{upper}}$ gives better predictions over larger spatial scales as the different timescales of heat and carbon exchange have less of an impact on the estimate.

Figure 3.17 shows the cumulative CO₂ uptake starting in year 7 as the volume of water begins to enter the tropical region. In the tropics, the volume of water loses carbon and the cumulative CO₂ uptake is negative. Initially, $F_{CO_2}{}^{\text{lower}}$ gives a good prediction of the true outgassing. After one year, $F_{CO_2}{}^{\text{lower}}$ underestimates the true flux. $F_{CO_2}{}^{\text{upper}}$ gives a good prediction of the outgassing in the tropical region. In the tropics, the volume of water is moving slowly and the carbon system is able to stay in closer equilibrium with the atmosphere. Hence, $F_{CO_2}{}^{\text{upper}}$ is accurate over shorter spatial scales in the tropics relative to the Gulf Stream region.
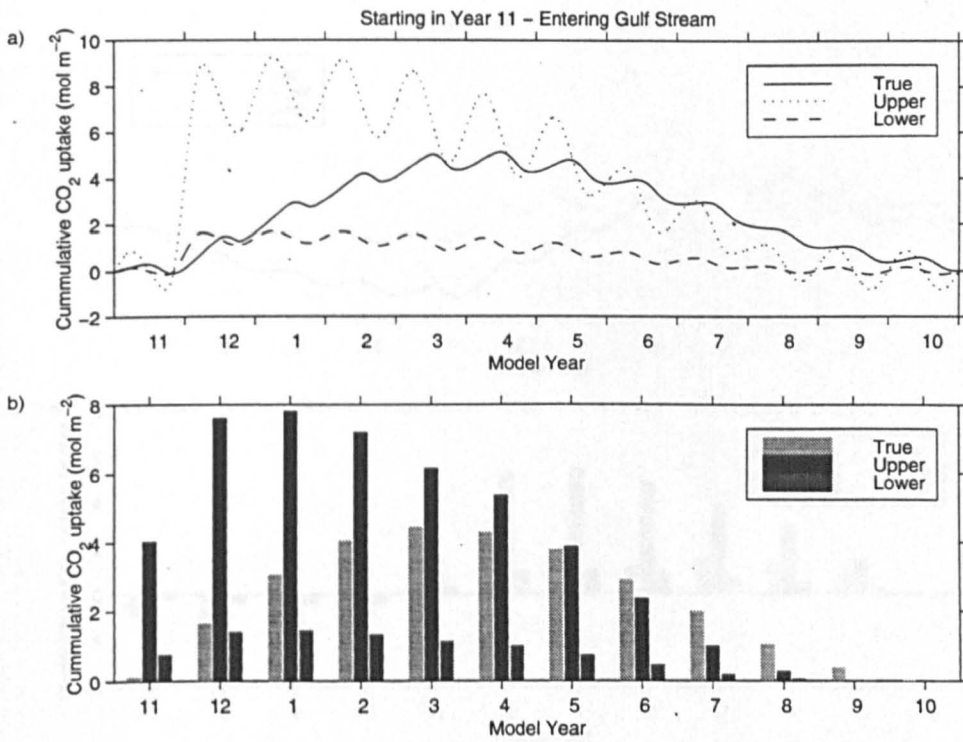
Figure 3.16: The cumulative uptake of CO_2 (mol m^{-2}) starting in year 11 (passage through the Gulf Stream). a) Time series of the true CO_2 uptake (solid line) and the heat flux estimates, F_{CO_2} upper (dotted line) and F_{CO_2} lower (dashed line); and b) annual values of the true uptake (light grey), F_{CO_2} upper (black) and F_{CO_2} lower (dark grey).
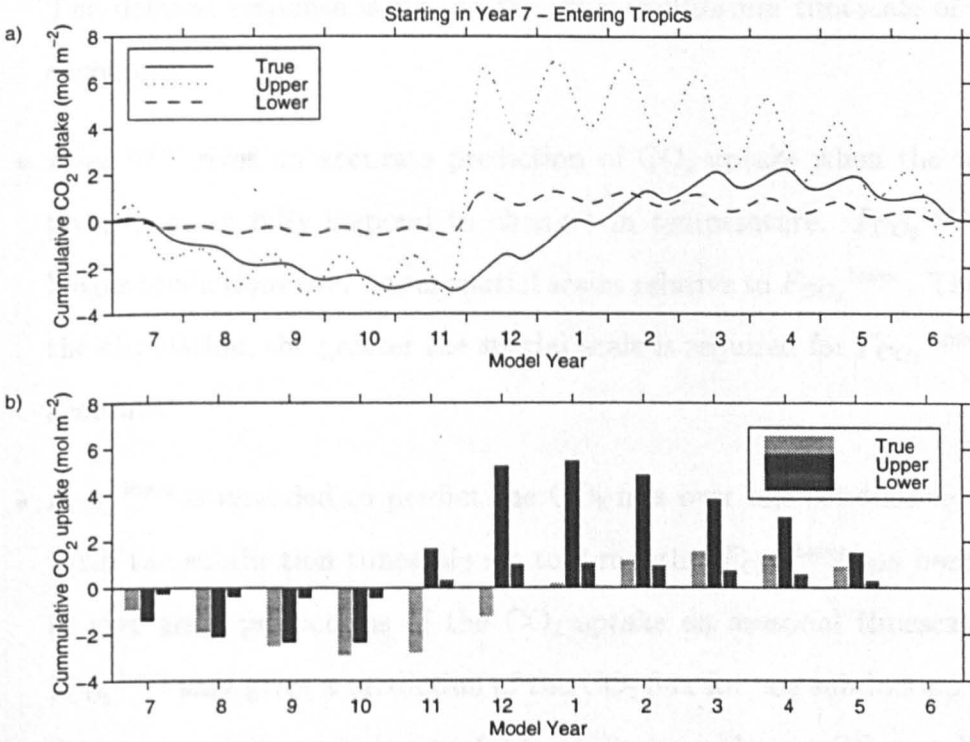
Figure 3.17: The cumulative uptake of CO_2 (mol m^{-2}) starting in year 7 (passage through the Tropics). a) Time series of the true CO_2 uptake (solid line) and the heat flux estimates, F_{CO_2} upper (dotted line) and F_{CO_2} lower (dashed line); and b) annual values of the true uptake (light grey), F_{CO_2} upper (black) and F_{CO_2} lower (dark grey).

3.6 Conclusions of the One-Dimensional Model Results

- In general, the air-sea heat flux is in the opposite direction to the air-sea CO$_2$ flux. However, there is a delayed reaction of the CO$_2$ flux to changes in temperature, which can cause the fluxes to be in the same direction. This has been found to occur as the water exits a western boundary current. The delayed response is due to the long equilibrium timescale of carbon exchange.

- F_{CO_2} ^{upper} gives an accurate prediction of CO$_2$ uptake when the water is given time to fully respond to changes in temperature. F_{CO_2} ^{upper} gives better predictions over larger spatial scales relative to F_{CO_2} ^{lower}. The faster the circulation, the greater the spatial scale is required for F_{CO_2} ^{upper} to be accurate.

- F_{CO_2} ^{lower} is intended to predict the CO$_2$ flux over one subduction period. With the subduction timescale set to 2 months, F_{CO_2} ^{lower} has been found to give good predictions of the CO$_2$ uptake on seasonal timescales. As F_{CO_2} ^{lower} only gives a prediction of the CO$_2$ flux for one subduction period, it can potentially provide a useful lower limit on the net CO$_2$ uptake of an ocean basin. In reality, a water column is expected to experience several subduction periods whilst circulating an ocean basin which will increase the CO$_2$ uptake.

The one-dimensional models have revealed some of the strengths and weaknesses of the two methods of estimating the CO$_2$ uptake from the heat flux. However, the first two one-dimensional models did not included subduction and convective mixing processes, and in the final Lagrangian model, there was no

net subduction over a gyre circuit. Subduction and deep convective mixing determine the amount of carbon removed from the surface layer, therefore, they determine the net air-sea CO_2 flux over a whole ocean basin. A more complex model is required to investigate the accuracy of predicting the net flux over an ocean basin from the heat flux.

3.7 Three-Dimensional Simplified Model

3.7.1 Model Description

The Planetary-Geostrophic Ocean Model (PGOM) of Samelson and Vallis (1997b) consists of a rectangular closed basin with no realistic bottom topography or coastlines. The velocities are near-geostrophic, which simplifies the governing equations of the model. The model is forced with a specified wind stress and interacts with an atmosphere with a meridional temperature gradient. A subtropical and a subpolar gyre are created with a thermohaline circulation associated with deep water formation in the high latitudes. The PGOM can simulate the time-mean transport of carbon in an ocean basin and the model is simplified enough that the results can be easily interpreted. The model is described in more detail in appendix A.

I added total inorganic carbon, C, to the PGOM. C is governed by the following equation in the interior,

$$\frac{\partial C}{\partial t} + \nabla \cdot (\mathbf{u}C) = \kappa_v \frac{\partial^2 C}{\partial z^2} + \kappa_h \nabla_h^2 C, \qquad (3.40)$$

where $\mathbf{u}$ is the velocity and κ_v and κ_h are the vertical and horizontal diffusivities and $\nabla_h^2 = \frac{\partial^2}{\partial x^2} + \frac{\partial^2}{\partial y^2}$. The diffusivities for carbon are equal to the diffusivity values used for temperature. Equation (3.40) is the same as the temperature governing equation except for the lack of biharmonic diffusion. The biharmonic

diffusion term is not required in equation (3.40), as C must satisfy only one lateral boundary condition, unlike temperature which must satisfy two (see appendix A). The boundary conditions for carbon are no flux through the lateral and bottom boundaries. In the Ekman layer, C is governed by the same equation as temperature with the air-sea flux of CO_2 prescribed as,

$$F_c = \kappa\alpha(pCO_2^{atmos} - pCO_2).$$

pCO_2^{atmos} is set equal to 350 μ atm. The method of solving for oceanic pCO_2 is described in appendix C. There were no biological processes included in the model. The maximum Ekman pumping $(we0)$ was set to 1×10^{-6} ms^{-1} in PGOM for the carbon model experiments. PGOM was run for 3000 years without carbon to obtain a steady state circulation. Carbon was then added to PGOM and the model was run for a further 3000 years.

3.7.2 Model Fields

The model circulation is shown in figure 3.18. The surface circulation is dominated by a wind driven subtropical gyre at the centre of the basin, with a strong western boundary current. North of the subtropical gyre, half of a subpolar gyre is created. At depth, a cyclonic gyre forms with an intense southwards current at the western boundary current. The density driven circulation consists of downwelling water at the northern boundary which upwells over the rest of the basin (figure 3.19). The thermohaline circulation is completed by the return of surface water to the deep water formation site by the western boundary current. (Temperature and salinity fields of the model are presented and discussed in Appendix A.)

The vertical structure of C in the model is shown in figure 3.20 with the model density field. The smallest values of C occur in the warm surface tropical

a) Base of Ekman layer
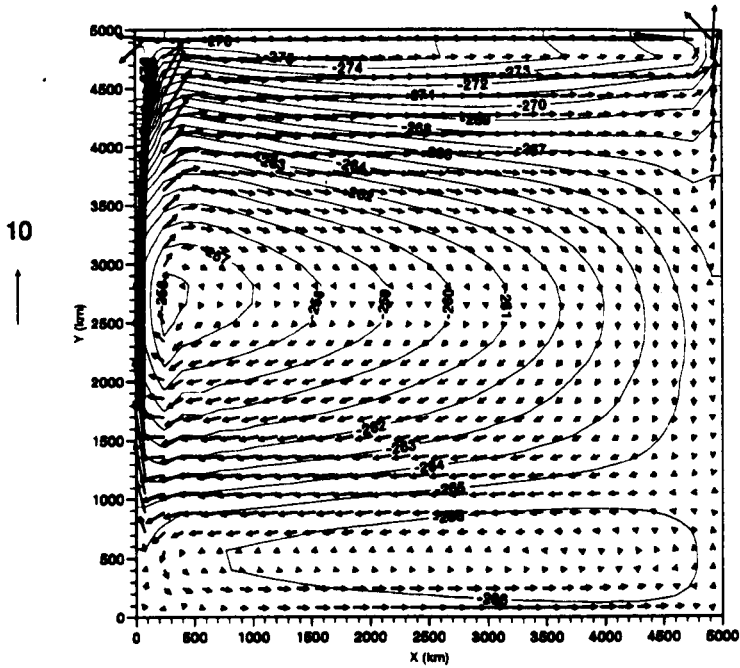
b) Deep ocean
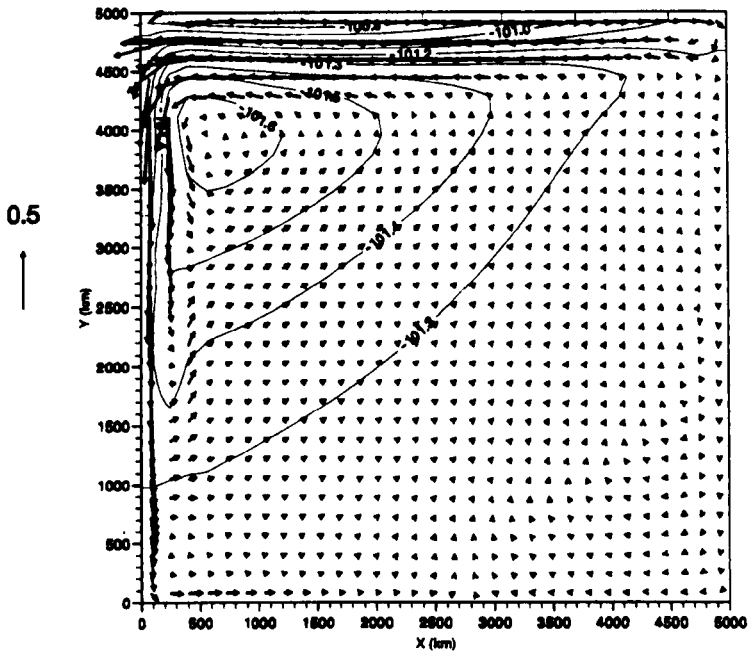
Figure 3.18: Pressure contours (nondimensional) and velocity vectors (10^{-2} ms^{-1}) at a depth of: a) z=25 m (base of Ekman layer); and b) z=1550 m (deep ocean).
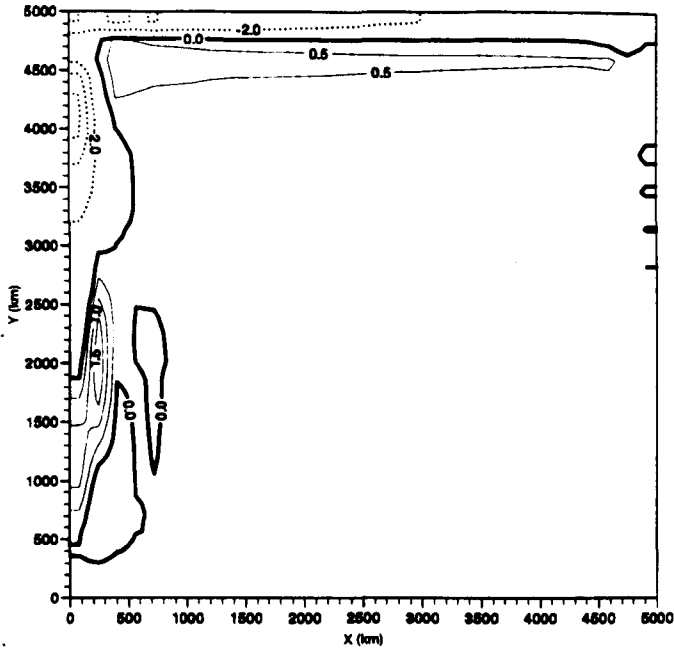
Figure 3.19: Vertical velocity (10^{-6} ms^{-1}) at a depth of 1550 m (deep ocean). Positive values indicate upwelling.

water where CO_2 solubility is lowest. The deep ocean has the highest C values (greater than 2120 μ mol kg^{-1}). The high solubility of the cold waters in the north causes atmospheric CO_2 to be absorbed into the ocean. The carbon is then transferred into the deep ocean by the circulation. In the real ocean, C reaches concentrations of 2250 μ mol kg^{-1} which is much higher than the model concentrations. The difference is caused by the lack of biology in the model as the biological pump is the dominant process in setting the vertical gradient in carbon (Sarmiento *et al.*, 1995).

The surface fields of pCO_2 and C (figure 3.21) reveal the importance of the temperature field in setting the surface carbon values. The lowest pCO_2 values occur in the coldest latitudes where the solubility is high. This allows the water to hold a large amount of carbon. In the warm tropics, the solubility is low, hence the water can hold less carbon relative to the colder latitudes.
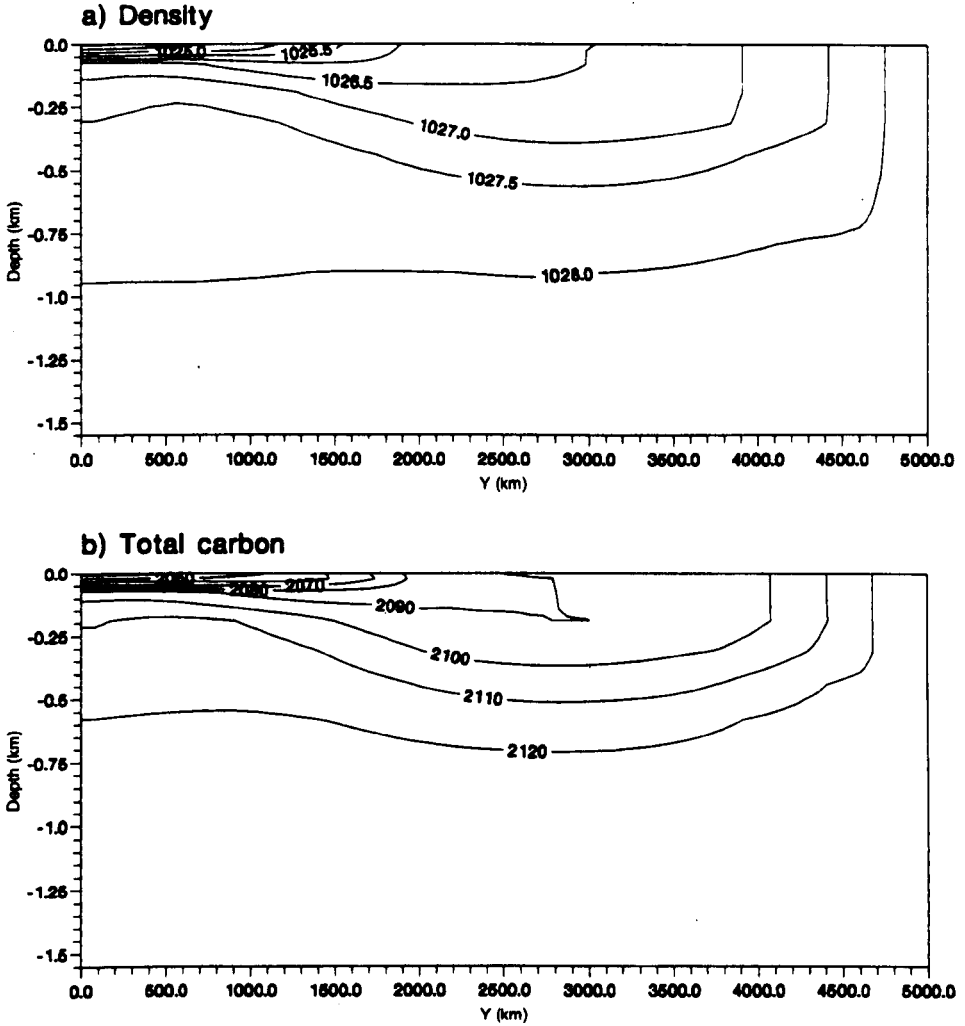
Figure 3.20: Meridional cross sections at the central longitude of the PGOM (x=2500 km) of: a) density (kg m^{-3}); and b) C (μ mol kg^{-1}).

a) Partial pressure

b) Total carbon
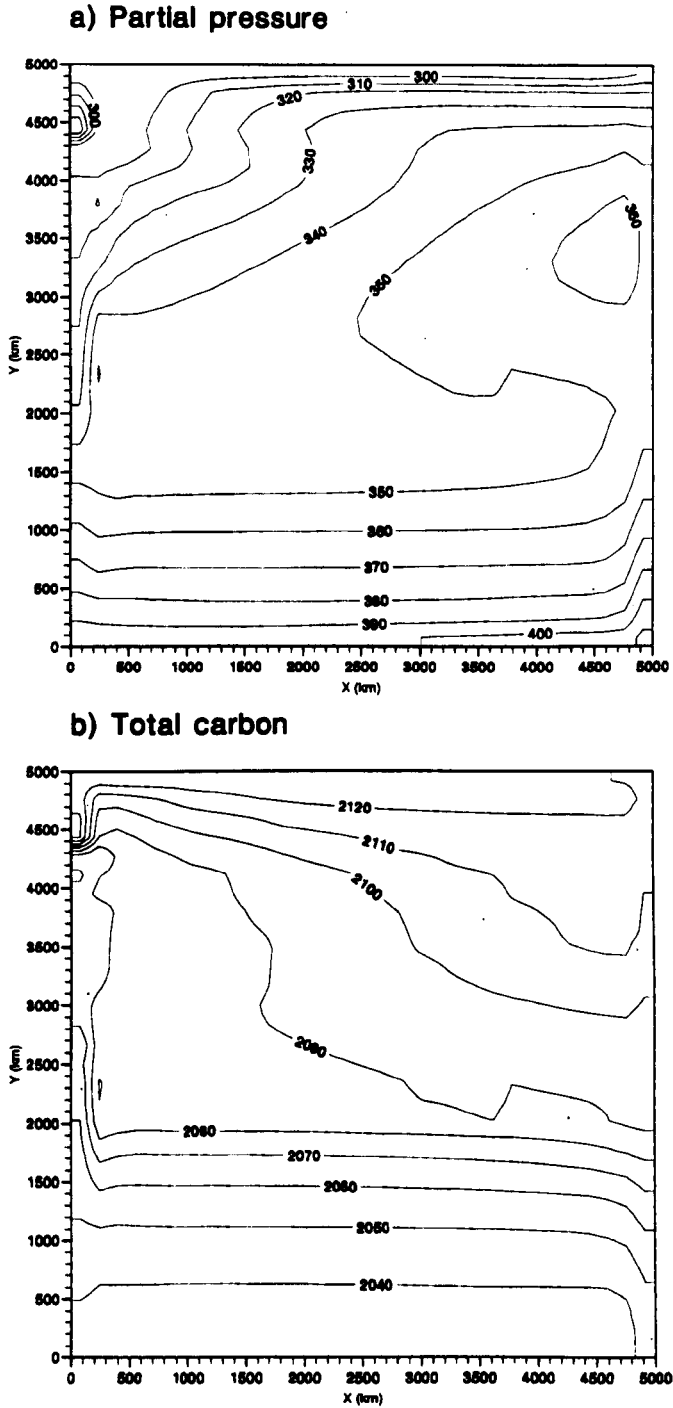
Figure 3.21: Surface distributions from PGOM during March of: a) pCO$_2$ (μ atm); and b) C (μ mol kg^{-1}).

3.7.3 Model Experiments

Four experiments were performed using the PGOM to investigate the relationship between the physical air-sea flux of CO_2 and the heat flux:

1. a seasonal run with variable salinity, but a constant salinity value of 35 was used in the calculation of the carbon chemistry constants;

2. the same as model experiment 1 except that CO_2 was not allowed to react with water i.e. no carbonate or bicarbonate was formed;

3. a seasonal run with variable salinity used in the calculation of the carbon chemistry constants; and

4. the same as model run experiment 1 except that the model was non-seasonal.

In the first model experiment, only changes in temperature caused air-sea fluxes of CO_2. This model experiment was used to analyse how the relationship between heat and CO_2 fluxes differs in different parts of an ocean basin. The second model experiment investigated the effect of the reactivity of CO_2 in sea water on the air-sea CO_2 flux. The effect of salinity was investigated with the third model experiment and the fourth experiment examined the impact of seasonality on the CO_2 flux.

3.7.4 Surface Fluxes

Maps of the air-sea fluxes of heat and CO_2 for the first model experiment are shown in figure 3.22. As expected, the spatial distributions of the fluxes are similar but with opposing sign (correlation coefficient of -0.75). In the tropics, cold high $\sum CO_2$ water upwells to the surface where it gains heat and loses CO_2 to

the atmosphere. As the water travels northwards towards the subtropical gyre, the air-sea fluxes of CO_2 and heat reduce as the ocean equilibrates with the atmosphere.

The water continues to move north in the western boundary current where the ocean loses heat and gains CO_2 from the atmosphere. The colder temperatures and deeper mixed layers cause the strongest uptake of CO_2 to occur at the northern end of the western boundary current. In the northern boundary, the cold water allows the ocean to take up CO_2 from the atmosphere. The transfer of high carbon water to the deep ocean by convection causes the continual uptake of atmospheric CO_2 . Over the northern subtropical gyre, the ocean takes up carbon from the atmosphere which is subducted into the ventilated thermocline.

The net air-sea heat and CO_2 fluxes over the region north of y = 1370km ($\sim$ 24 °N) for the four model experiments are shown in table 3.2. Also the net CO_2 flux inferred from the heat flux using F_{CO_2} ^{upper} is included in table 3.2. The model heat flux in the most northern and eastern row of grid points is not included in the calculation of F_{CO_2} ^{upper} , due to the large unrealistic heat flux in the northeastern corner. There is no air-sea CO_2 flux associated with this large heat flux. This lack of a CO_2 flux is due to the exclusion of the biharmonic diffusion term in the carbon governing equation, which creates different boundary conditions for temperature and carbon.

As discussed in appendix A, the northwards heat transport of the model is lower than observations of the North Atlantic suggest (table 3.2, model experiment 1). Hence, the inferred CO_2 flux is smaller than the estimate of 0.75 Gt C yr^{-1} made by Watson *et al.*(1995) using the observed northwards heat transport. The unrealistic low heat transport will cause a corresponding low net air-sea CO_2 flux in the model. However, the model is still useful for testing the relationship between heat and CO_2 as both variables are affected by the same conditions.

a) Heat

b) Carbon
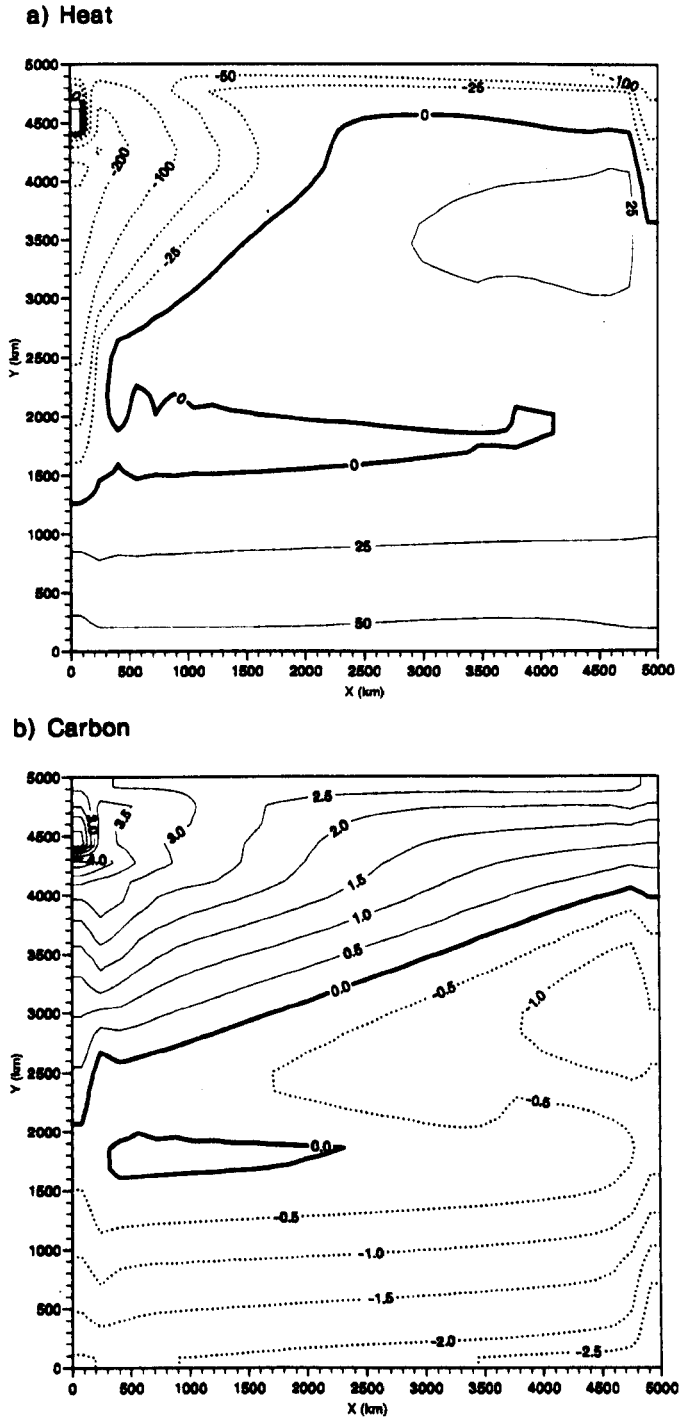
Figure 3.22: The annual air-sea flux of: a) heat (W m^{-2}); and b) CO_2 (mol m^{-2} yr^{-1}) for PGOM experiment 1. Positive values indicate a flux from the atmosphere into the ocean.

Model Experiment	Heat Flux	CO$_2$ Flux (Gt C yr^{-1})	
	(10^{15}) W	Actual	F_{CO_2} upper
1. Constant S used in chemistry	0.219	0.0925	0.1231
2. Non-reactive CO$_2$	0.219	0.0055	0.0049
3. Variable S used in chemistry	0.219	0.0751	0.1231
4. Non-seasonal	0.179	0.0844	0.0895

Table 3.2: The annual mean net air-sea flux of heat and CO$_2$ over the region north of $\sim 24^0 N$. Also the heat flux estimate of the CO$_2$ uptake, F_{CO_2} upper, is shown. The most northern and eastern row of grid points were not used in the net CO$_2$ flux calculation. $C_p = 4000 \mathrm{J\,kg^{-1}\,K^{-1}}$ was used in all calculations. In the calculation of F_{CO_2} upper, the values used for τ, β and C in model experiments 1, 3 and 4 were 0.0423 ^{o}C , 10 and 2000 μ mol kg^{-1}respectively. For model experiment 2, a mean value for a (defined in equation 3.7) of 3.4×10^{-4} mol m^{-3} ^{o}C $^{-1}$ was used which was calculated within the model.

Heat Flux Estimates of the CO$_2$ Fluxes

The results from the first model experiment reveal that the F_{CO_2} upper prediction overestimates the net CO$_2$ flux by one third (table 3.2). To explain the discrepancy, a map of the inferred flux is shown in figure 3.23a. F_{CO_2} upper greatly overestimates the influx of carbon occurring in the western boundary current. F_{CO_2} upper also predicts the incorrect sign of the flux in the northern subtropical gyre. In the northern section of the gyre, both the heat and the CO$_2$ flux are directed into the ocean.

The spatial differences between the air-sea heat and CO$_2$ fluxes can be understood using the results from the 1-D Lagrangian models described in the section 3.5. In the western boundary current, the temperature of the water reduces very rapidly as the ocean responds to the cooler atmosphere. The ocean starts to gain CO$_2$ but not as quickly as it loses heat. Hence, the CO$_2$ flux inferred using F_{CO_2} upper is too high. A proportion of the northwards moving water recirculates
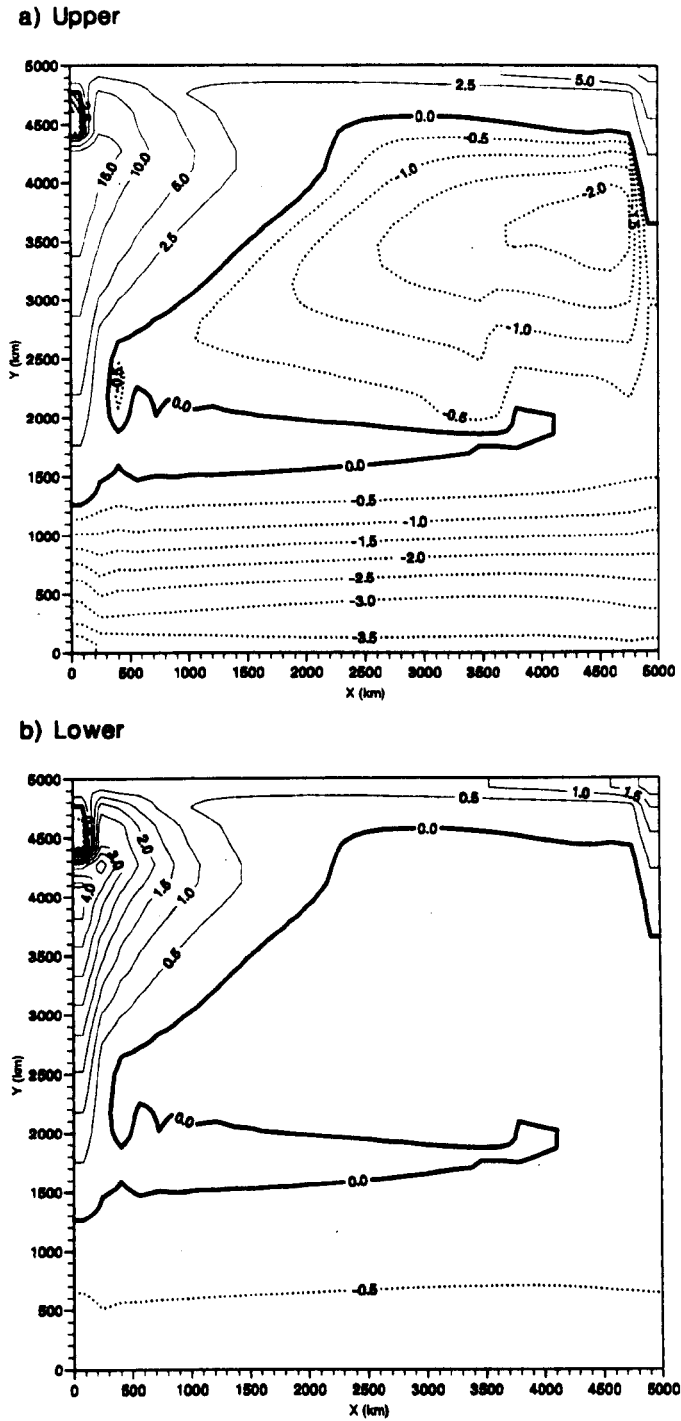
Figure 3.23: The annual air-sea flux of CO$_2$ (mol m^{-2} yr^{-1}) for PGOM experiment 1 inferred from the heat flux: a) F_{CO_2} ^{upper} ; and b) F_{CO_2} ^{lower} .

towards the south in the gyre. The heat flux changes direction as the ocean starts taking up heat from the atmosphere. However, the ocean is still undersaturated in carbon from the rapid transport in the western boundary current. Hence, the ocean continues to take up CO$_2$ even though the heat flux is also into the ocean.

When the net CO$_2$ uptake of the whole region is calculated using $F_{CO_2}{}^{upper}$, the underestimation of the uptake in the northern subtropical gyre, is partially offset by the overestimation of the uptake in the western boundary current. This finding agrees with the results from the 1-D models which show that in the western boundary regime, $F_{CO_2}{}^{upper}$ gives more accurate results over larger spatial scales. However, the net air-sea CO$_2$ flux over the region north of 24°N is still overestimated by $F_{CO_2}{}^{upper}$.

$F_{CO_2}{}^{lower}$ was also computed using the model heat fluxes. The temperature relaxation timescale (19 days) was used for θ^{-1}. The map of the inferred flux $F_{CO_2}{}^{lower}$ (figure 3.23b) reveals that $F_{CO_2}{}^{lower}$ provides a good estimate of the maximum fluxes in the western boundary current region. The Lagrangian 1-D model described in section 3.4, illustrated that in the western boundary, $F_{CO_2}{}^{lower}$ gave better predictions than $F_{CO_2}{}^{upper}$ over shorter spatial scales. Therefore, the local fluxes derived from $F_{CO_2}{}^{lower}$ in the western boundary current are more accurate from those calculated using $F_{CO_2}{}^{upper}$. However, in the other ocean regions where the circulation is slower, the accuracy of $F_{CO_2}{}^{upper}$ improves on shorter spatial scales. Therefore, the accuracy of the fluxes in the tropics calculated using $F_{CO_2}{}^{upper}$ is comparable to the fluxes calculated using $F_{CO_2}{}^{lower}$.

The net CO$_2$ uptake for the region north of 24°N calculated using $F_{CO_2}{}^{lower}$ is 0.03 Gt C yr^{-1}. This estimate is less than 30 % of the true uptake. The estimate is especially low due to the short temperature relaxation timescale used in the model. To conclude, the net uptake of CO$_2$ over the region north of 24°N is overestimated by $F_{CO_2}{}^{upper}$ and underestimated by $F_{CO_2}{}^{lower}$.

3.7.5 The Effect of the Reactivity of CO$_2$ in Water

The long equilibrium timescale of CO$_2$ is caused by the reactivity of CO$_2$ in water, as the water can hold more carbon. This effect is shown in the second model experiment. CO$_2$ is not allowed to react with water, hence, in model experiment 2, $C = [CO_2]$, rather than $C = [CO_2] + [HCO_3^{2-}] + [CO_3^-]$. The net CO$_2$ uptake of the nonreactive model experiment is only 6 % of the uptake of the first model experiment (table 3.2). This highlights the importance of the reactivity of CO$_2$ in water which allows the ocean to hold more carbon. The mean C for model experiment 2 is only 12 μ mol kg^{-1} compared to 2038 μ mol kg^{-1} for model experiment 1. The spatial distribution for the actual and the inferred CO$_2$ flux (F_{CO_2} ^{upper}) for the second model experiment are presented in figure 3.24. Not surprisingly F_{CO_2} ^{upper} now reproduces the distribution and magnitude of the real flux very accurately. In particular, the prediction of the CO$_2$ flux in the western boundary current region is greatly improved in the second model experiment. Also, the location of the zero air-sea flux contours are predicted well.

The net CO$_2$ uptake inferred by F_{CO_2} ^{upper} is accurate to within 10% of the true model uptake. In contrast to the results of model experiment 1, the inferred uptake is actually an underestimate of the actual flux for the 2nd model experiment (table 3.2). The CO$_2$ transfer velocity of 20 cm hr^{-1} is faster than the surface temperature relaxation rate (5.4 cm hr^{-1}). Therefore, the equilibrium timescale of carbon is now artificially shorter than that of heat, due to the removal of the carbon chemistry. This leads to the actual flux of CO$_2$ being greater than the flux inferred from the heat flux using F_{CO_2} ^{upper}. If model experiment 2 is repeated but with equal transfer velocities for temperature and CO$_2$, the F_{CO_2} ^{upper} overestimates the true flux by only 3%.
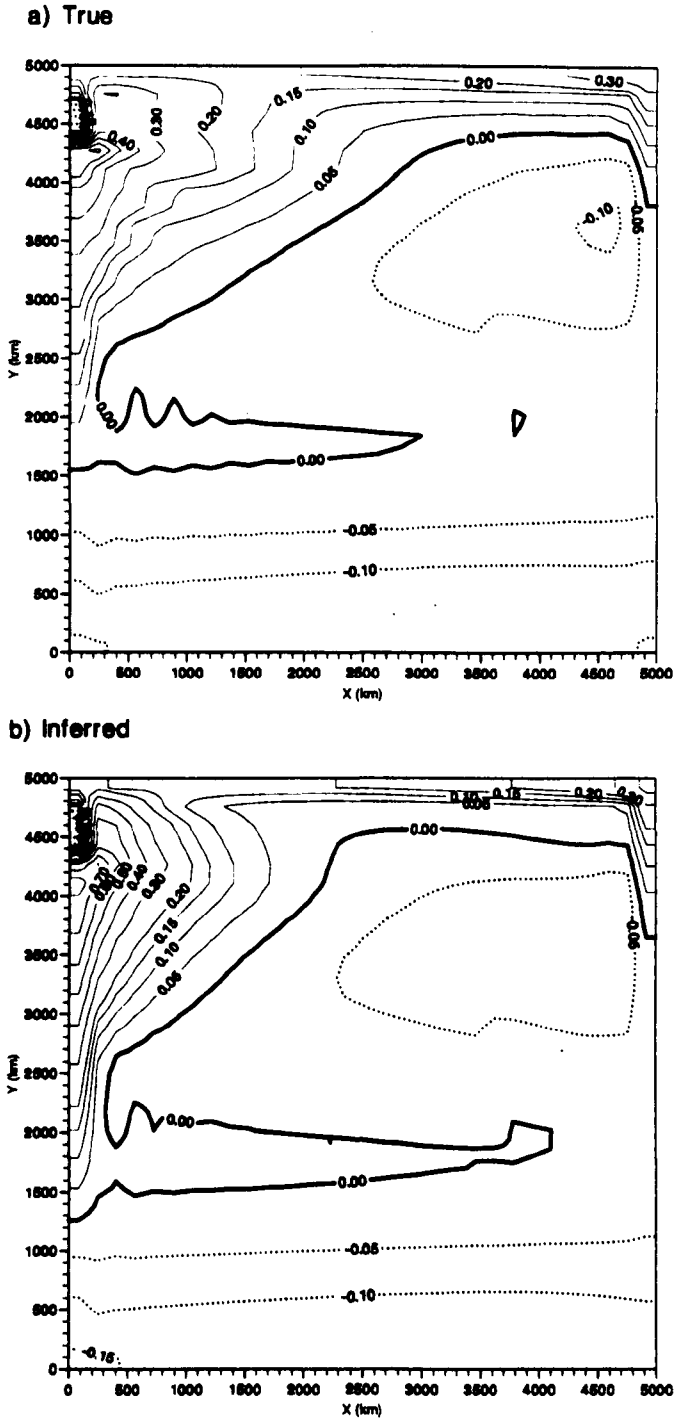
a) True

b) Inferred

Figure 3.24: The annual air-sea flux of CO_2 (mol m^{-2} yr^{-1}) for PGOM experiment 2 (the non-reactive CO_2 experiment) : a) true model flux; and b) flux inferred from heat flux using $F_{CO_2}{}^{upper}$.

3.7.6   The Effect of Salinity

In model experiment 3, changes in salinity in the carbon chemistry are investigated. Comparing the results of model experiments 1 and 3 in table 3.2, reveals that using the true salinity in the calculation of the carbon chemical system reduces the net air-sea flux of CO_2 by 19%. The solubility of CO_2 increases with decreasing salinity. The surface salinity reduces to the north across the subtropical gyre, hence the solubility of CO_2 will increase. Therefore, the inclusion of variable salinity in the model would be expected to increase the net air-sea CO_2 flux. But in comparing model experiments 1 and 3, this has not occurred.

The apparent contradiction is caused by using a constant value of salinity of 35 in the model experiment 1. The lowest value of surface salinity in the model experiment is 35 at the northern boundary. Hence, in model experiment 1, the solubilities used in the carbon chemistry are always higher than in model experiment 3. This causes a greater uptake of atmospheric CO_2 to occur in model experiment 1 than in model experiment 3. Therefore, although using a constant salinity value in the carbon chemistry does not create air-sea fluxes of CO_2, the chosen salinity value does affect the magnitude of the exchange.

3.7.7   The Effect of Seasonality

Model experiment 4 investigates the effect of seasonality on the air-sea fluxes of heat and CO_2. The northwards heat transport of the model is 20% smaller in the non-seasonal version of the model than the seasonal version. The net CO_2 uptake is reduced by 9% when seasonality is removed from the model.

Seasonality in the model causes a wider range of temperatures and deeper mixed layer depths in the winter. This increases the rate of subduction and deep water formation leading to enhanced net fluxes of both heat and CO_2. Also the
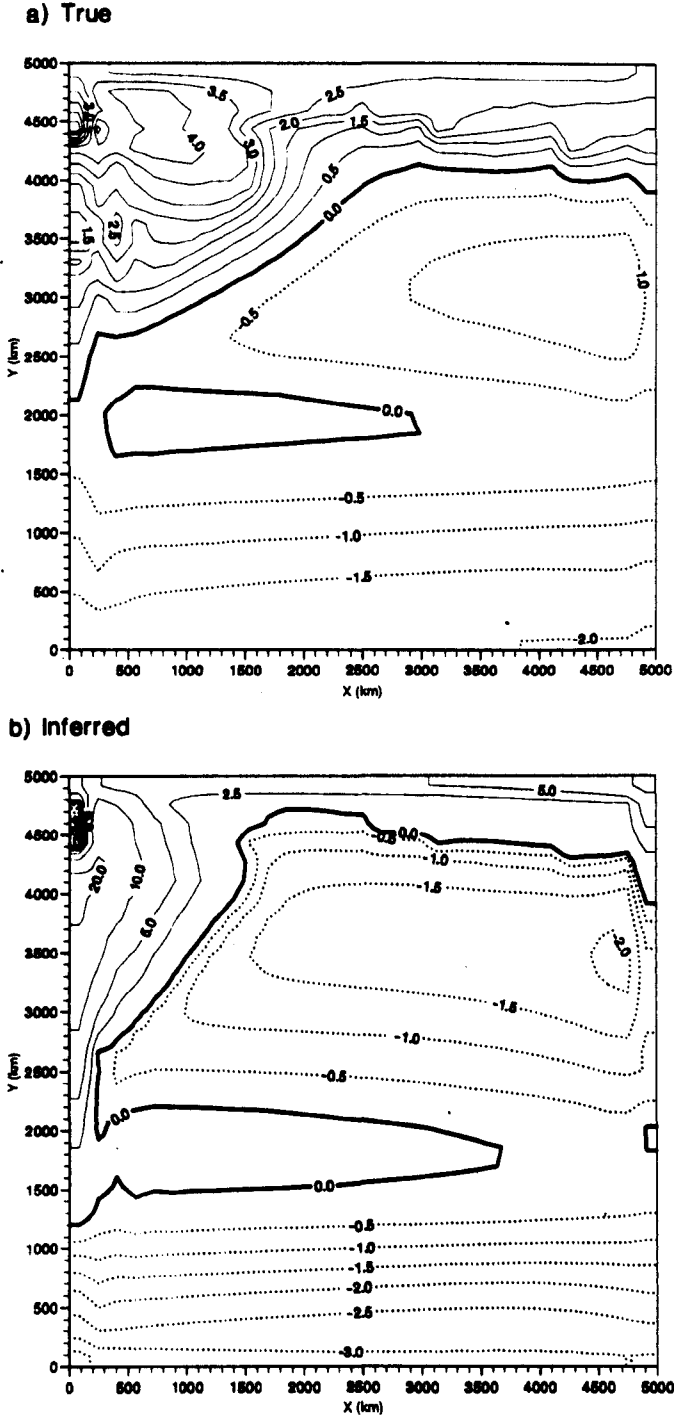
a) True

b) Inferred

Figure 3.25: The air-sea flux of CO_2 (mol m^{-2} yr^{-1}) for PGOM experiment 4 (non-seasonal model experiment): a) true model flux; and b) flux inferred from heat flux using F_{CO_2} ^{upper}.

water in the thermocline and deep ocean is colder in the seasonal model than in the non-seasonal model, which will increase CO_2 uptake. However, the equilibrium timescale for CO_2 air-sea exchange is longer than one season. Therefore, seasonality affects the heat flux more than the CO_2 flux.

The lack of seasonality in the model greatly improves the accuracy of the inferred F_{CO_2} ^{upper} estimate (table 3.2). Figure 3.25 shows the actual and the inferred air-sea flux (F_{CO_2} ^{upper}) of CO_2 for the non-seasonal model experiment 4. F_{CO_2} ^{upper} overestimates the true flux in the western boundary layer and underestimates in the northern subtropical gyre. However, unlike the seasonal results, these two errors cancel out each other when calculating the net flux.

3.7.8 Conclusions

PGOM has been successfully used to model the carbon transport in an ocean basin. The model region north of 24°N is a source of heat to the atmosphere and a sink for atmospheric CO_2. In the tropics (south of 24°N), heat is gained from the atmosphere and CO_2 is lost to the atmosphere, such that there are no net heat or CO_2 exchange over the whole model basin during a year.

A model experiment has confirmed that the longer exchange timescale of CO_2 relative to other gases is caused by the reaction of CO_2 with seawater. If the reaction is blocked, the equilibrium timescale of carbon is comparable to heat.

The net heat flux of the model is found to be more affected by seasonality than the net CO_2 flux, due to the shorter equilibrium timescale of the heat exchange. The seasonal cycle of mixed layer depths and surface temperatures increases the difference in the responses of the air-sea heat and CO_2 fluxes. The heat flux is able to respond more to deep cold mixed layers during the winter period compared to the CO_2 flux. Therefore, the removal of the seasonal cycle, eliminates some of the differences between the heat and CO_2 fluxes.

The results from the PGOM experiments on the accuracy of $F_{CO_2}{}^{upper}$ and $F_{CO_2}{}^{lower}$ agree with the findings of the 1-D models. The heat flux estimates of the CO_2 uptake, $F_{CO_2}{}^{upper}$ and $F_{CO_2}{}^{lower}$, bound the true uptake of the model basin north of 24°N. In the PGOM, the integrated estimate over the basin north of 24°N found using $F_{CO_2}{}^{lower}$ is exceptionally low due to the short air-sea heat flux timescale used in the model. The heat flux timescale used to create the seasonal temperature cycle is unrealistically short in the model. This aspect could be improved by increasing the heat flux timescale in the model and changing the pseudo atmospheric temperature to create the same seasonal temperature cycle.

$F_{CO_2}{}^{lower}$ provides a better estimate of the CO_2 flux in the western boundary regime than $F_{CO_2}{}^{upper}$. Elsewhere in the model, the fluxes estimated using $F_{CO_2}{}^{lower}$ and $F_{CO_2}{}^{upper}$ have a similar accuracy. The 1-D models of the previous section revealed that $F_{CO_2}{}^{upper}$ gives better estimates over longer timescales as the differing timescales of heat and CO_2 exchange become less important. Therefore, $F_{CO_2}{}^{upper}$ is more accurate over longer spatial scales in regions where the circulation is fast. Whereas the accuracy of $F_{CO_2}{}^{upper}$ is improved over shorter spatial scales in regions where the circulation is slow.

The lack of seasonality improves the accuracy of $F_{CO_2}{}^{upper}$, as seasonality accentuates the differences between the heat and CO_2 fluxes. Also, $F_{CO_2}{}^{upper}$ is found be very accurate when the reaction of CO_2 with water is blocked, because this reaction increases the exchange timescale of CO_2.

3.8   Summary

Two theoretical relationships between heat fluxes and CO_2 fluxes have been investigated, using a range of idealised models. Firstly, several 1-D models were used to gain a basic understanding of the differences between the air-sea fluxes

of heat and CO_2. The basic 1-D models also provided an idealised situation to test the accuracy of the heat flux estimates of the CO_2 flux. The knowledge gained from the 1-D models allowed the results of the more complex 3-D model (PGOM) to be explained.

The first heat flux estimate of the CO_2 flux, $F_{CO_2}{}^{upper}$, assumes that the ocean stays in equilibrium with the atmospheric CO_2 concentration at all times. However, the exchange timescale for heat is shorter than the exchange timescale for carbon. This leads to temperature changes occurring at a faster rate than changes in carbon concentration. The accuracy of $F_{CO_2}{}^{upper}$ is found to be dependent on the time and spatial scales involved in the prediction. $F_{CO_2}{}^{upper}$ is more accurate over longer timescales, as the different equilibrium timescales of heat and CO_2 become less important. Therefore, the local accuracy of $F_{CO_2}{}^{upper}$ is dependent on the speed of the circulation. $F_{CO_2}{}^{upper}$ provides better local estimates in slow moving regions of the ocean than in faster moving areas. Although the accuracy of $F_{CO_2}{}^{upper}$ is improved when used over larger spatial scales, $F_{CO_2}{}^{upper}$ still overestimates the net CO_2 uptake of an ocean basin due to the assumption of equilibrium with the atmosphere.

The second heat flux estimate of the CO_2 flux, $F_{CO_2}{}^{lower}$, has the correct timescale of CO_2 exchange but is only valid on seasonal timescales. Therefore, $F_{CO_2}{}^{lower}$ is found to give accurate estimates over a few months and captures the seasonal variation of the CO_2 flux well. $F_{CO_2}{}^{lower}$ also provides better local flux estimates in regions of a fast circulation than $F_{CO_2}{}^{upper}$. In regions where the water is moving fast, the oceanic carbon concentration is generally not in equilibrium with the atmosphere, and therefore the equilibrium relationship ($F_{CO_2}{}^{upper}$) greatly overestimates the flux. The estimate $F_{CO_2}{}^{lower}$ predicts the CO_2 uptake caused by one subduction period. Therefore, $F_{CO_2}{}^{lower}$ provides a useful lower limit on the net uptake of an ocean basin as the net uptake will be determined by one or more subduction periods.

The model experiments have show that $F_{CO_2}{}^{lower}$ is appropriate for estimating the CO$_2$ flux over several months, whereas $F_{CO_2}{}^{upper}$ is appropriate for predicting the CO$_2$ flux over several years. The model results also suggest that $F_{CO_2}{}^{upper}$ and $F_{CO_2}{}^{lower}$ can provide an upper and lower limit on the annual net uptake of carbon of an ocean basin. This idea is further tested in a global 3-D model as described in the next chapter.

Chapter 4

Estimating the Physical Air-Sea CO_2 Flux from Heat Fluxes

The basic model experiments described in chapter 3 have shown that measurements of the air-sea flux of heat can potentially provide limits on the physical air-sea CO_2 flux. In this chapter, the accuracy of the CO_2 flux estimates made using the heat flux is investigated. The circulation field generated from a global general circulation model (GCM) is used to model the global air-sea flux of CO_2. The model CO_2 flux is then compared to the CO_2 flux estimates inferred from the air-sea heat flux of the GCM.

Finally, using the knowledge gained from the series of model experiments, observational heat flux data are used to infer the air-sea flux of CO_2 linked to the solubility pump. Climatological CO_2 flux maps are inferred from the heat flux. In addition, the interannual variability of the CO_2 flux in the North Atlantic is also predicted from the heat flux data.

4.1 Global Carbon Transport Model Experiment

4.1.1 Model Description

A global version of the carbon transport model of Follows *et al.*(1996) was used for the investigation. The carbon model was driven by monthly-mean fields generated by the MIT ocean circulation model (Marshall *et al.*, 1997a,b). The MIT model is a global general circulation model with realistic coastlines and bottom topography. The model is forced with observed winds, heat and freshwater fluxes from NCEP reanalysis. The MIT model was initialised with Levitus climatology and integrated for 150 years. The carbon model used temperature, salinity, velocity and convective index fields averaged over the final year of the GCM run. The velocity fields for January are presented in figure 4.1 and the temperature and salinity fields are shown in Appendix B.

The offline carbon model has a horizontal resolution of 2.8°x 2.8°with 15 vertical levels. Total inorganic carbon (C) is carried in the model and governed by the following equation,

$$\frac{\partial C}{\partial t} + \nabla \cdot (\mathbf{u}C) - \nabla \cdot (K \nabla C) \;=\; \kappa \alpha (pCO_2^{atmos} - pCO_2).$$

where $\mathbf{u}$ is the monthly mean velocity field from the GCM and K is the diffusion tensor. Convective mixing is included in the carbon model using a convective index generated from the GCM run. The atmospheric pCO_2 (pCO_2^{atmos}) was set to 278 μ atm. There were no biological effects included in the carbon model. The air-sea flux of CO_2 was modelled as detailed in appendix C. In contrast to the previous carbon models of this work, the gas transfer velocity was parameterized as a function of wind speed using the parameterization of Wanninkhof (1992) (see section 2.1.3).
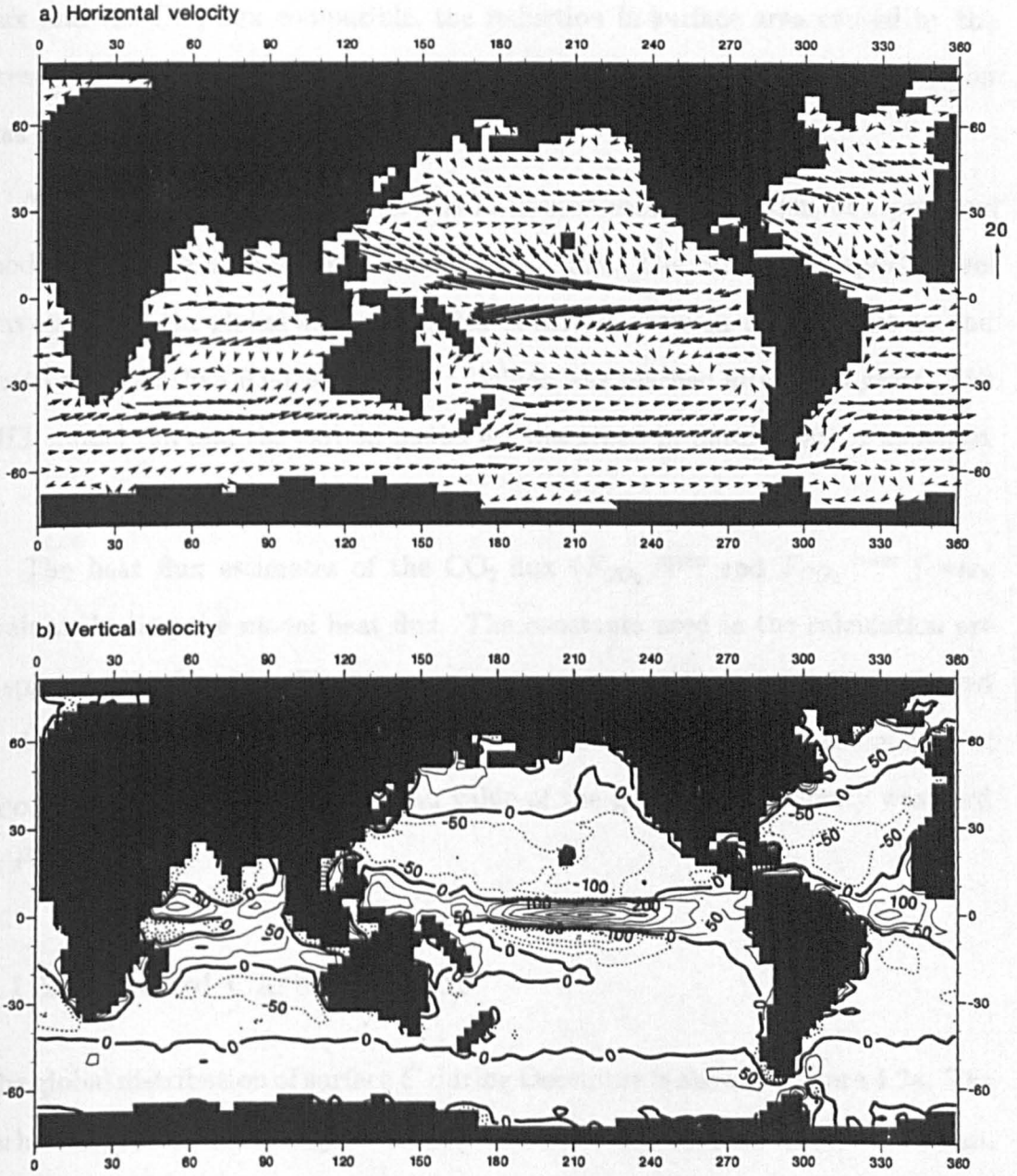
Figure 4.1: Monthly mean surface velocity fields from the MIT GCM for January: a) horizontal velocity (10^{-2} ms^{-1}); and b) vertical velocity (m yr^{-1}) (positive values indicate upwelling).

The effect of ice cover blocking the air-sea exchange is included in the carbon model using climatological ice fields. The air-sea heat flux in the GCM is not affected by ice as ice cover was not included in the GCM. To make the heat flux and the CO_2 flux compatible, the reduction in surface area caused by the presence of ice was taken into account when the net heat flux of an ocean region was calculated.

The carbon field of the model was initialised using the output of a previous model run which used different model parameters. The carbon transport model was run until the global annual net flux of carbon between the atmosphere and ocean was less than 0.0025 Gt C yr^{-1}, which was reached after 1200 years. The MIT model run and the carbon model are described in more detail in appendix B.

The heat flux estimates of the CO_2 flux (F_{CO_2} ^{upper} and F_{CO_2} ^{lower}) were evaluated using the model heat flux. The constants used in the calculation are displayed in table 4.1. The temperature relaxation timescale of 75 days used in the MIT model run was used as the heat flux timescale in the calculation of F_{CO_2} ^{lower}. The global annual mean value of the gas transfer velocity was used in F_{CO_2} ^{lower}.

4.1.2 Model Carbon Fields

The global distribution of surface C during December is shown in figure 4.2a. The carbon concentration is highest in the North Atlantic and the Southern Ocean. The North Pacific has lower carbon concentrations than the North Atlantic due to the lower alkalinity in the North Pacific. The concentrations are lowest in the tropical regions. There is evidence of the high carbon content water being upwelled along the equator in the Pacific Ocean.

The cross section of C through the Atlantic Ocean (figure 4.2b) shows the

Parameter	Source	Value
$\left(\frac{\partial lnpCO_2}{\partial T}\right)_C (\tau)$	experimental value of Takahashi *et al.*(1993)	0.0423^oC^{-1}
Buffer factor (β)	typical ocean value (Broecker and Peng, 1982)	10
$\sum CO_2 (C)$	typical ocean value	2000μ mol kg^{-1}
Mixed layer depth (h)	depth of model surface layer	50 m
Gas transfer velocity (κ)	global annual mean model value (at 20 ^oC)	12.6 cm hr^{-1}
CO_2 solubility (α)	empirical relationship of Weiss (1974) at 20 ^oC	0.03241 mol kg^{-1} atm^{-1}
Partial pressure of CO_2 (pCO$_2$)	pCO_2^{atmos} of the model	278μ atm
Temperature exchange timescale $(\mathcal{K}_T^{-1})$	temperature relaxation timescale used in GCM	75 days
Carbon exchange timescale $(\mathcal{K}_C^{-1})$	$\left(\frac{\kappa}{h}\alpha\beta\frac{pCO_2}{C}\right)^{-1}$	~ 1 year
Subduction timescale (θ^{-1})	$\mathcal{K}_T^{-1}$	75 days

Table 4.1: Parameters used in the calculation of F_{CO_2} ^{upper} and F_{CO_2} ^{lower} for the global carbon transport model experiment.
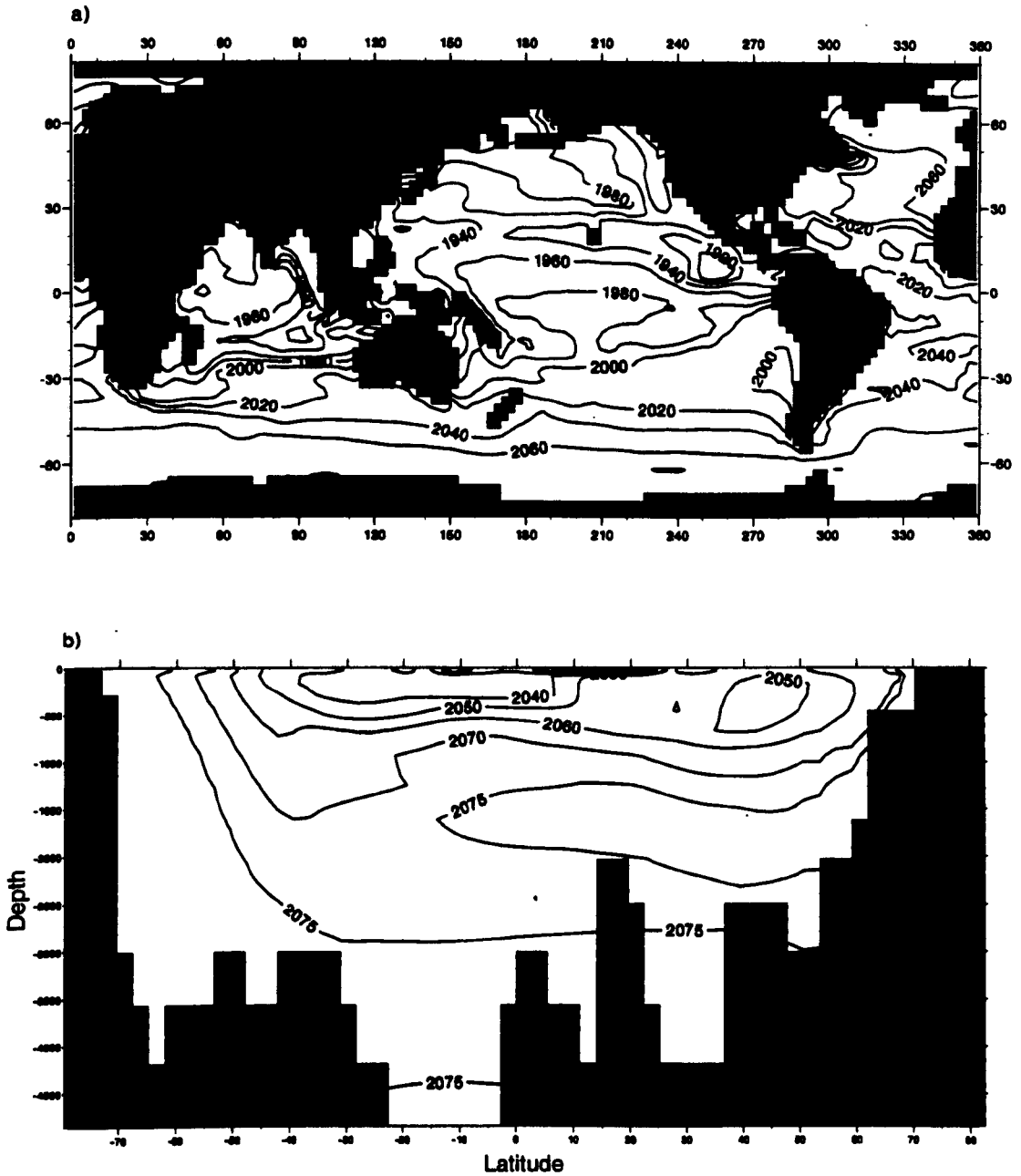
Figure 4.2: Carbon fields from the global abiotic carbon transport model driven by GCM circulation fields at the end of December: a) surface C (μ mol kg^{-1}); and b) a vertical cross section of C in the Atlantic along the longitude of 24°W (μ mol kg^{-1}).

116

increase of C with depth. The intrusion of the NADW with high carbon concentrations is also evident at a depth of 2km.

4.1.3   The Effect of Salinity on the CO_2 Flux

The CO_2 flux in the model is affected by changes in temperature and salinity. Changes in the model salinity cause CO_2 fluxes through changing the CO_2 solubility. However, Watson *et al.*(1995) calculated the change in salinity in the North Atlantic caused a CO_2 flux that was only 11 % of the flux caused by temperature changes.

The contribution of salinity changes to the model CO_2 flux is quantified using the freshwater air-sea fluxes of the GCM. Following the method of Watson *et al.*(1995) the CO_2 flux caused by changes in salinity can be expressed as,

$$F_{CO_2}{}^{sal} = V \Delta S \left(\frac{\partial C}{\partial S} \right)_{pCO_2} , \qquad (4.1)$$

where V is the volume flux of water entering the region and ΔS is the change in salinity. The derivative on the right hand side of equation (4.1) can be evaluated using the chemical scheme of Hoffert *et al.*(1979) as described in chapter 2. A mean value of -0.0037 mol m^{-3} psu^{-1} is found for $\left(\frac{\partial C}{\partial S} \right)_{pCO_2}$ using a range of typical ocean temperatures and salinities. $V \Delta S$ can be related to the model freshwater volume flux (F_w) as,

$$V \Delta S = -S_o F_w, \qquad (4.2)$$

where S_o is a reference salinity and set to 35.

Table 4.2 shows the freshwater fluxes for different regions of the model and the implied $F_{CO_2}{}^{sal}$ value. For a discussion on the model freshwater fluxes see Appendix B. Also shown on table 4.2 are the net CO_2 fluxes of the model. Generally, the salinity component of the CO_2 flux is small and it can be assumed

117

Region	Freshwater flux in km^3 day^{-1} (bracketed values are area averages in mm day^{-1})	F_{CO_2} sal (Gt C yr^{-1})	F_{CO_2} $model$ (Gt C yr^{-1})
N. Atlantic subarctic (north of 50 °N)	12.6 (1.4)	0.007	0.11
N. Atlantic gyre (14 °N to 50 °N)	-30.3 (-1.2)	-0.017	0.14
N. Pacific gyre (14 °N to 50 °N)	-37.0 (-0.8)	-0.021	0.08
Equatorial (14 °S to 14 °N)	-52.3 (-0.5)	-0.030	-1.06
Southern gyres (50 °S to 14 °S)	-107.2 (-1.0)	-0.060	0.51
Southern Ocean (south of 50 °S)	29.8 (0.7)	0.017	0.21

Table 4.2: Annual freshwater fluxes and the implied CO_2 uptake caused by the change in salinity (F_{CO_2} sal) for different ocean regions for the GCM experiment. Also shown is the true model CO_2 uptake (F_{CO_2} $model$) for the ocean regions from the carbon transport model. A positive value indicates a flux into the ocean.

that temperature changes are the main cause of air-sea CO_2 exchange in the model.

4.1.4   Air-Sea Fluxes of Heat and CO_2

Spatial Distribution

The annual mean air-sea heat flux of the MIT model is shown in figure 4.3. The annual heat flux is directed into the ocean in the equatorial region with the strongest heating occurring in the Equatorial Pacific. The Southern Ocean generally loses heat over a year with fluxes reaching 50 Wm^{-2}. The largest heat
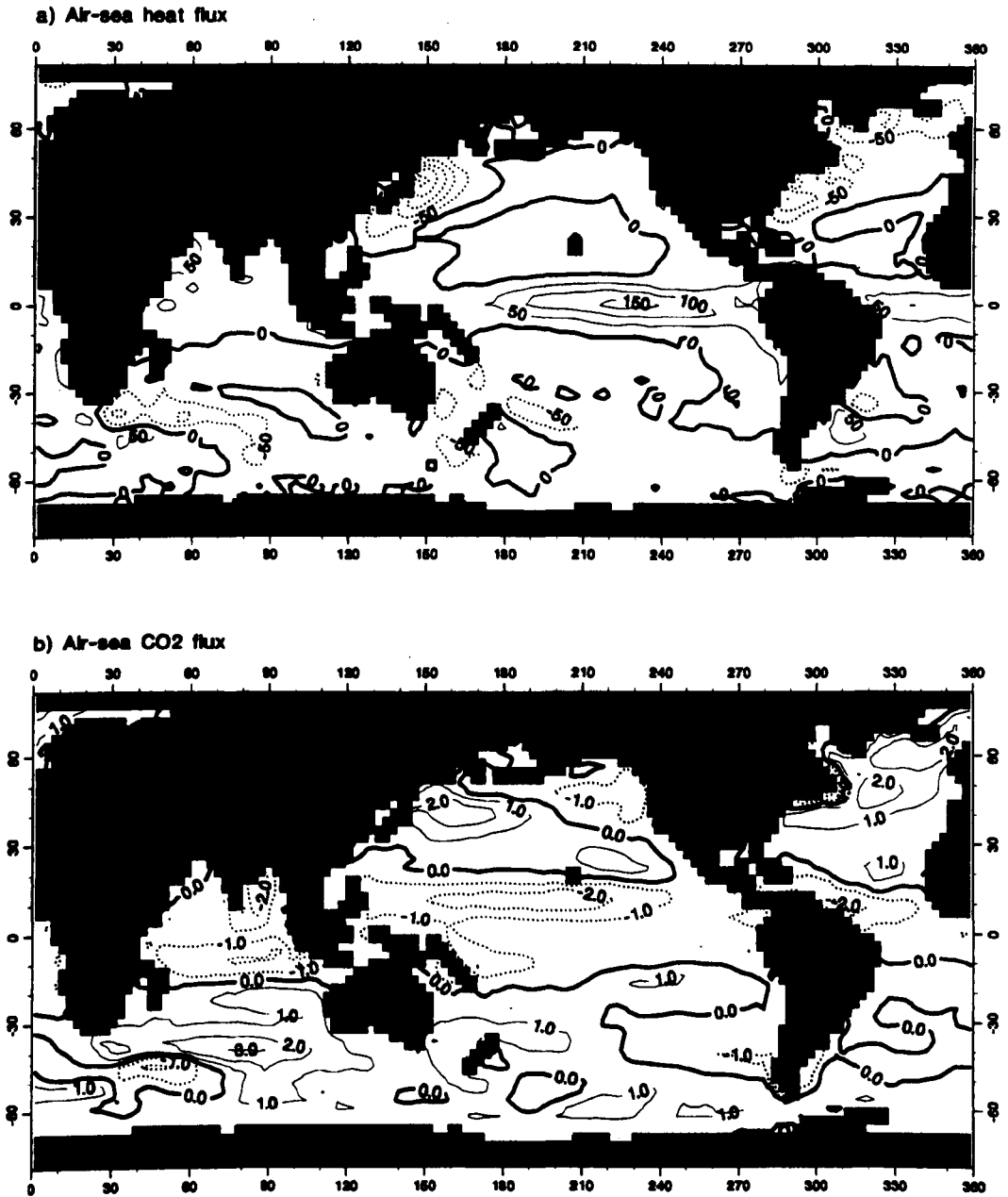
Figure 4.3: Annual mean air-sea fluxes: a) of heat (Wm^{-2}) from the GCM run; and b) of CO_2 $(mol\ C\ m^{-2}\ yr^{-1})$ from the global carbon transport model.

loss of the ocean occurs in the western boundary currents of the North Atlantic and Pacific. The heat loss reaches 150 Wm^{-2} in the Kurisho current.

Also shown on figure 4.3 is the annual mean air-sea flux of CO_2. In general, the CO_2 flux is in the opposite direction to the heat flux. In the tropical region, the ocean loses carbon to the atmosphere. Cold water that is high in carbon is upwelled along the equator, as shown in figure 4.1b. The water warms as it rises, and, gains heat from the atmosphere as it reaches the surface. The increase in temperature causes the CO_2 solubility to decrease and CO_2 is outgassed. The Southern Ocean and subtropical gyres generally take up CO_2 from the atmosphere. The strongest CO_2 uptake regions are the western boundary currents in the Northern Hemisphere and a section of the Antarctic Circumpolar Current (ACC) south west of Australia.

Maps of $F_{CO_2}{}^{upper}$ and $F_{CO_2}{}^{lower}$ calculated using the model heat flux are shown in figure 4.4. Comparing the heat flux predictions with the true model CO_2 flux reveals that the heat flux predictions are generally in the correct direction. However, there are some locations where the heat flux is in the same direction as the CO_2 flux. In the North Pacific, downstream of the western boundary current, both fluxes are directed into the ocean, which was also found in the idealised models in chapter 3. Also, there are regions in the tropics such as between 10°N and 20°N in the Pacific, where the heat flux and the CO_2 flux are both directed out of the ocean.

The magnitudes of the two heat flux estimates differ greatly. As has already been shown in the idealised models, $F_{CO_2}{}^{upper}$ tends to overestimate the air-sea CO_2 flux in fast moving regions of the ocean. In particular, $F_{CO_2}{}^{upper}$ estimates the outgassing in the strong upwelling region of the Equatorial Pacific to be five times too large. The uptake in the western boundary currents predicted by $F_{CO_2}{}^{upper}$ is similarly too great.
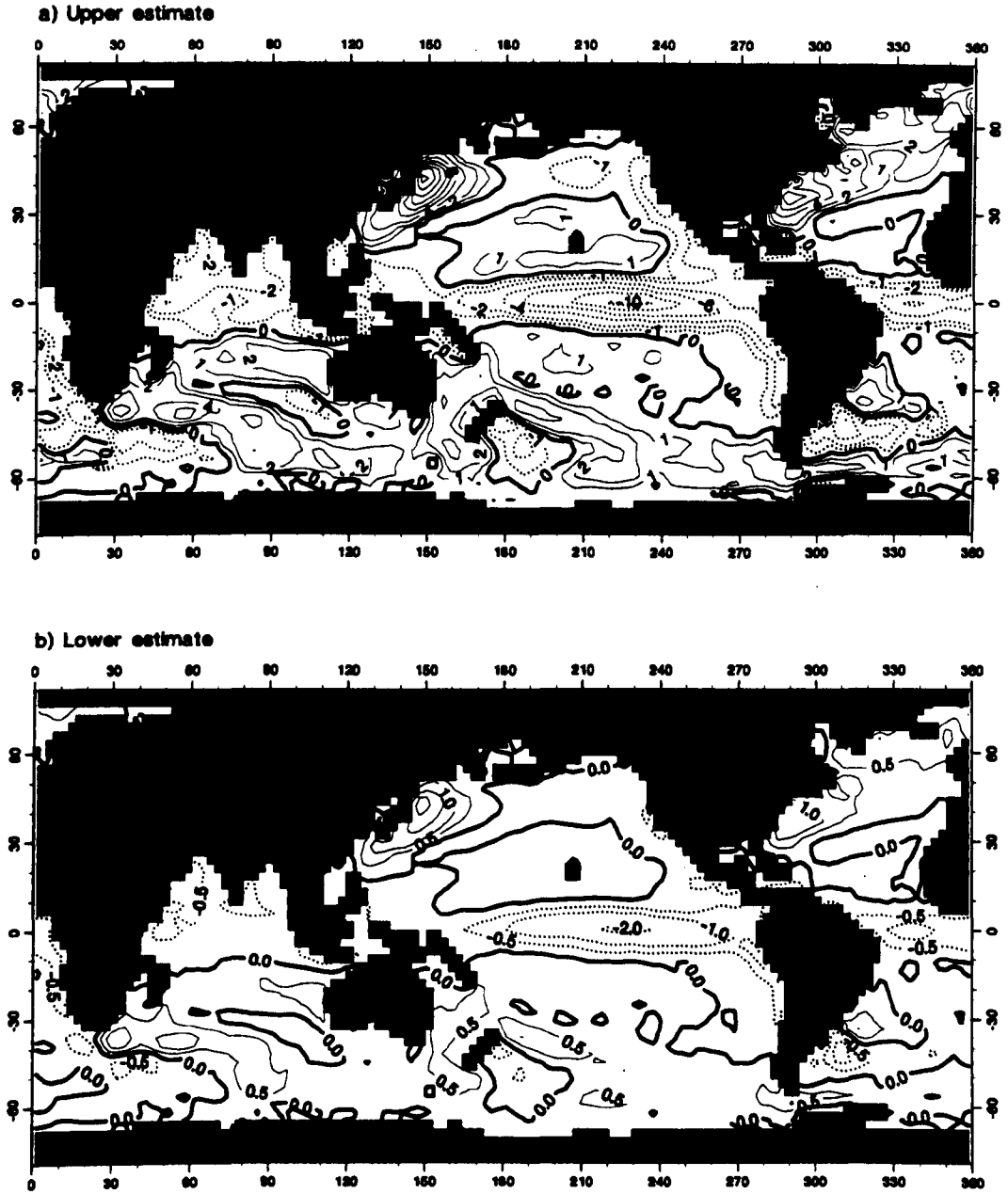
Figure 4.4: Annual mean air-sea CO_2 fluxes (mol C m^{-2} yr^{-1}) inferred from the air-sea heat flux of the GCM run: a) $F_{CO_2}{}^{upper}$; and b) $F_{CO_2}{}^{lower}$.

The idealised models showed that $F_{CO_2}{}^{lower}$ provided better estimates of the local flux than $F_{CO_2}{}^{upper}$ in fast moving regions. This is similarly found in the GCM experiment as illustrated in figure 4.4b. $F_{CO_2}{}^{lower}$ predicts the maxima and minima of the air-sea flux more accurately than $F_{CO_2}{}^{upper}$. The CO_2 uptake in the western boundary currents in the North Hemisphere is slightly underestimated by $F_{CO_2}{}^{lower}$. Also the strong uptake in the ACC west of Australia is predicted too low.

Net Fluxes

The net annual heat loss of the North Atlantic (north of 24°N) in the model is 6.5×10^{14} W. This heat loss is less than the value of $\sim 1 \times 10^{15}$ W calculated from observations (Isemer *et al.*, 1989). However, the GCM heat transport is an improvement on the heat transport of the idealised PGOM used in chapter 3. The net model CO_2 uptake for the North Atlantic (north of 24°N) is 0.25 Gt C yr^{-1}.

The model net CO_2 fluxes for different ocean regions are shown in table 4.3. The only model region not to gain atmospheric carbon over a year is the equatorial region. The outgassing of CO_2 in the equatorial region balances the net CO_2 uptake in the rest of the ocean. The largest uptake occurs in the southern gyres region which has the largest area. The strongest uptake per unit surface area occurs in the North Atlantic subarctic region.

Also shown in table 4.3 are the CO_2 flux values estimated by Takahashi *et al.*(1997) using available pCO_2 measurements and an advective-diffusive interpolation scheme. The values of Takahashi *et al.*(1997) are not directly comparable to the model values for two reasons. Firstly, the Takahashi *et al.*(1997) values are for the year 1990, and therefore, include the effect of the anthropogenic increase in atmospheric CO_2, whereas the model is for pre-industrial steady state times.

Secondly, the biological pump is not included in the model but the Takahashi *et al.*(1997) estimates involve biological effects.

The impact of the anthropogenic increase in atmospheric CO_2 will be to increase the uptake of CO_2 everywhere in the ocean. Hence, the outgassing in the Equatorial region will be reduced. The effect of biological processes on the CO_2 flux is less obvious. Although the soft-tissue biological pump reduces the surface pCO_2, it also greatly increases the deep water $\sum CO_2$ value. Therefore, upwelling and convective mixing will mix higher $\sum CO_2$ water back to the surface and reduce the efficiency of the solubility pump. Sarmiento *et al.*(1995) found that the inclusion of biological processes in a model reduced the CO_2 uptake in the North Atlantic north of 50°N (figure 2.7). However, the net CO_2 uptake between 14°N and 50°N was increased. The addition of biota in the model of Maier-Reimer and Hasselmann (1987) increased the outgassing in the Equatorial Pacific region. In contrast, biological processes decreased the outgassing of the Atlantic Equatorial region in the model of Sarmiento *et al.*(1995). Therefore, the effect of biological processes on the CO_2 uptake varies with region.

In the North Atlantic north of 50°N, the model CO_2 uptake value is less than the Takahashi estimate. The effect of biological and anthropogenic processes on the CO_2 flux are expected to oppose each other in this region. The model flux may be an underestimate because of the low northwards heat transport in the North Atlantic of the model. Alternatively, the uptake of anthropogenic CO_2 may have a greater effect on the Takahashi estimate than the inclusion of biological processes. The Takahashi estimate is expected to be larger than the model CO_2 uptake in the North Atlantic and Pacific gyre region as the effect of both biological and anthropogenic processes is to increase the uptake. The equatorial outgassing in the model is larger than the Takahashi *et al.*(1997) value, which might be explained by biological and anthropogenic factors. In the Southern Hemisphere, the model uptake values are within the range of the

Takahashi estimates.

Heat Flux Estimates of the Net CO_2 Flux

The heat flux estimates of the net air-sea CO_2 flux are shown in table 4.4. In all regions $F_{CO_2}{}^{upper}$ overestimates the net flux. In the North Atlantic, $F_{CO_2}{}^{upper}$ is twice as large as the real flux. $F_{CO_2}{}^{lower}$ underestimates the net exchange in all regions except the North Pacific. These findings are broadly in agreement with the idealised models described in chapter 3.

In the North Pacific, $F_{CO_2}{}^{lower}$ gives a good prediction of the low uptake while $F_{CO_2}{}^{upper}$ is a large overestimate. This can be explained by examining the spatial differences in the air-sea heat and CO_2 fluxes shown in figure 4.3. The equatorial band of CO_2 outgassing spreads across a wider latitude band than the corresponding heat flux into the ocean. After the water is upwelled at the equator, it moves polewards largely driven by the Ekman transport. On this poleward journey, the water equilibrates with the atmospheric temperature and CO_2 concentration. However, the longer exchange timescale of carbon, relative to heat, causes the air-sea heat flux to reach equilibrium and change direction before the CO_2 flux. Hence, the latitude band of CO_2 outgassing is wider than the band of heat uptake. The North Pacific region defined in table 4.4 is north of 14°N. At the latitude of 14°N, the air-sea heat flux is approximately zero. However, the air-sea CO_2 flux is still losing carbon after the northwards passage through the tropics. The heat flux that is causing this air-sea CO_2 flux is actually south of 14 °N and is therefore not included in the defined North Pacific. Hence, $F_{CO_2}{}^{upper}$ greatly overestimates the uptake in the North Pacific, as the true CO_2 uptake is reduced by outgassing that originates from the warming over the Equatorial region. This error highlights the need to choose the boundaries of the selected region carefully. $F_{CO_2}{}^{upper}$ and $F_{CO_2}{}^{lower}$ provide estimates of the CO_2 flux in a region, caused by the temperature changes within that region.

Region	Area (10^4 km^2)	$F_{CO_2}{}^{model}$ (Gt C yr^{-1})	Takahashi et al.(1997) (Gt C yr^{-1})
N. Atlantic subarctic (north of 50 °N)	927	0.11	0.19 to 0.45
N. Atlantic gyre (14 °N to 50 °N)	2432	0.14	0.33 to 0.72
N. Pacific gyre (14 °N to 50 °N)	4839	0.08	
Equatorial (14 °S to 14 °N)	10474	-1.06	-0.46 to -1.04
Southern gyres (50 °S to 14 °S)	10736	0.51	0.42 to 0.92
Southern Ocean (south of 50 °S)	4301	0.21	0.12 to 0.3

Table 4.3: The model area, model CO_2 uptake ($F_{CO_2}{}^{model}$) and the CO_2 uptake calculated using observational pCO_2 data by Takahashi et al.(1997) for different ocean regions.

Region	$F_{CO_2}{}^{model}$	$F_{CO_2}{}^{upper}$	$F_{CO_2}{}^{lower}$
N. Atlantic subarctic (north of 50 °N)	0.11	0.20	0.04
N. Atlantic gyre (14 °N to 50 °N)	0.14	0.28	0.06
N. Pacific gyre (14 °N to 50 °N)	0.08	0.47	0.10
Equatorial (14 °S to 14 °N)	-1.06	-2.36	-0.48
Southern gyres (50 °S to 14 °S)	0.51	0.66	0.14
Southern Ocean (south of 50 °S)	0.21	0.37	0.08

Table 4.4: CO_2 uptake (Gt C yr^{-1}) for different ocean regions for the global carbon transport model experiment: model values ($F_{CO_2}{}^{model}$) and values inferred from the heat flux ($F_{CO_2}{}^{upper}$ and $F_{CO_2}{}^{lower}$).

The initial air-sea CO$_2$ flux of the water entering the region is not predicted by F_{CO_2} ^{upper} or F_{CO_2} ^{lower} . If the region is defined to be north of 15ºS, then the CO$_2$ flux estimate inferred from the heat flux of -0.21 to -1.01 Gt C yr^{-1} does bound the model CO$_2$ flux of -0.53 Gt C yr^{-1} .

4.1.5   Conclusions

The results of the GCM experiment support the findings of the idealised models of chapter 3. The heat flux estimates, F_{CO_2} ^{upper} and F_{CO_2} ^{lower}, bound the true net fluxes for ocean regions. The model results have also shown that the accuracy of the heat flux estimates of the net CO$_2$ flux for a region is sensitive to the boundaries selected for the region. It is important that the heat flux that causes the CO$_2$ flux is present in the same region.

F_{CO_2} ^{lower} provides a better prediction than F_{CO_2} ^{upper} of the range of annual mean air-sea CO$_2$ fluxes present in the model. This is because the maxima and minima annual mean air-sea CO$_2$ fluxes occur in regions where the circulation is faster than average. The idealised model experiments revealed that F_{CO_2} ^{lower} gave better estimates of the local CO$_2$ flux in fast moving regions, as the oceanic pCO$_2$ is not close to equilibrium.

4.2   Observational Heat Flux Estimates

The model results show that the heat flux can be used to provide useful bounds on the air-sea flux of CO$_2$ caused by temperature changes. Next, observational heat flux data is used to infer the pre-industrial CO$_2$ flux caused by the solubility pump.

4.2.1 Heat Flux Data

The heat flux climatologies of Josey *et al.*(1996) and da Silva *et al.*(1994) were used to infer the climatological air-sea CO_2 flux. The annual mean heat fluxes calculated from the two climatologies are shown in figure 4.5. Both climatologies are derived from the Comprehensive Ocean Atmosphere Data Set (COADS), however, the methods used to calculate the net heat flux differ. In addition, Josey *et al.*(1996) combined the COADS with individual ship meteorological reports which allowed biases caused by variations in observing procedure to be corrected. The principal difference between the two heat flux climatologies is that the da Silva data is constrained to globally integrate to zero over a year whereas the Josey climatology is not constrained. Instead, there is a average heat gain by the ocean of 30 Wm^{-2} in the Josey climatology (Josey *et al.*, 1999). Josey *et al.*(1999) compared the climatology with buoy measurements and found that the accuracy of the climatology varied in different regions. In particular, the Josey climatology has been found to underestimate the net heat flux in regions including a western boundary current (Josey *et al.*, 1999). Therefore, Josey *et al.*(1999) argue that closure of the ocean heat budget requires regional scaling of the flux components as opposed to global scaling.

The da Silva heat flux data has been fine tuned using a simple linear inverse calculation to force the annual net heat flux between 65 °S to 65 °N to zero. The scaling is done globally which Josey *et al.*(1999) argue is not appropriate. In the polar regions (north of 65 °N and south of 65 °S), the data in the da Silva climatology is not constrained causing an global annual net heat flux of -0.05 PW.
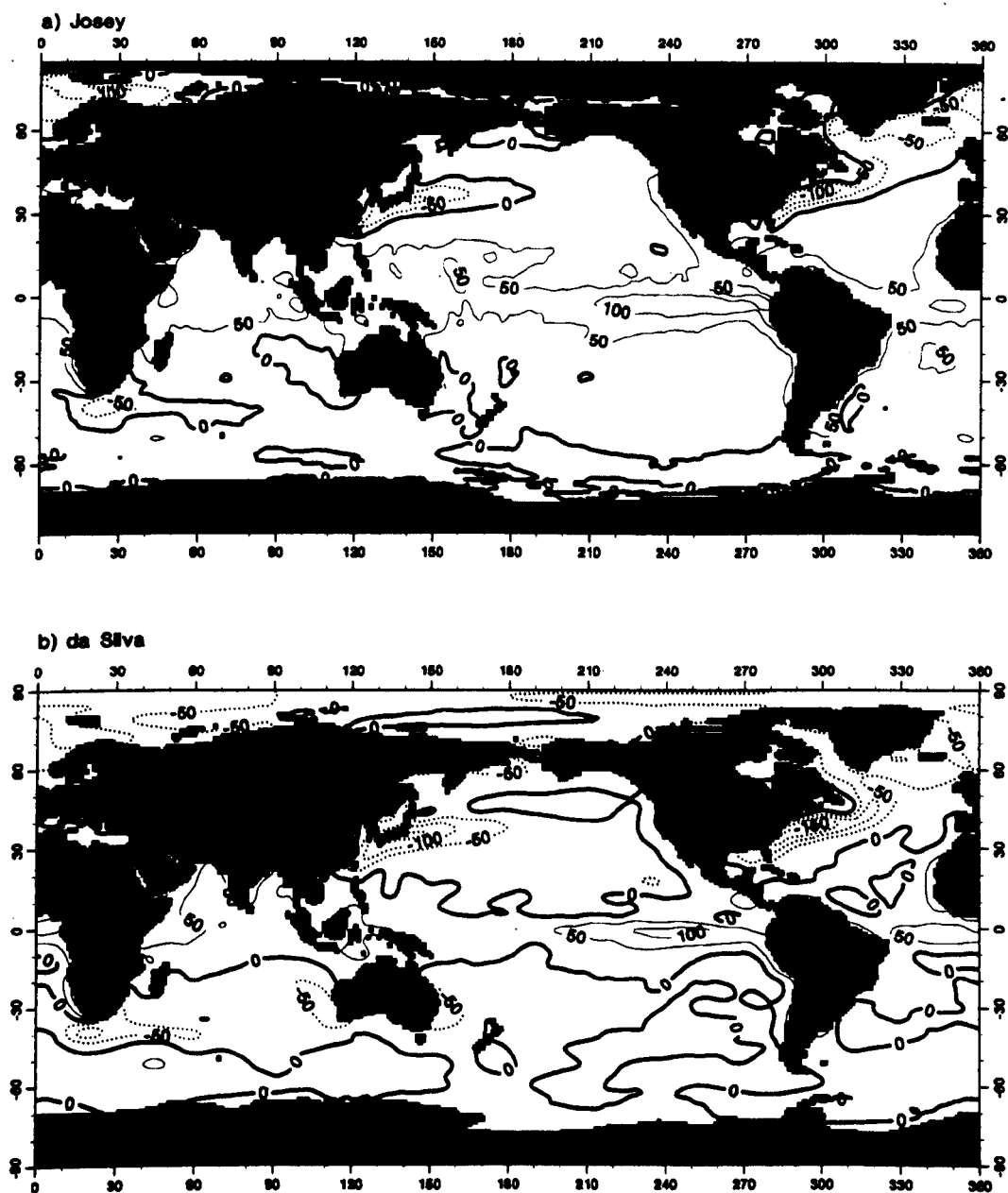
Figure 4.5: Annual mean air-sea heat fluxes (Wm^{-2}) from: a) the Josey *et al.*(1996) climatology; and b) the da Silva *et al.*(1994) climatology. A positive heat flux is directed into the ocean.

Parameter	Source	Value
$\left(\frac{\partial ln pCO_2}{\partial T}\right)_C$ (τ)	experimental value of Takahashi et $al.$(1993)	$0.0423^{\circ}C^{-1}$
Buffer factor (β)	typical ocean value (Broecker and Peng, 1982)	10
$\sum CO_2$ (C)	typical ocean value	$2000\ \mu\ mol\ kg^{-1}$
Mixed layer depth (h)	typical depth of surface layer	50 m
Gas transfer velocity (κ)	global mean value (Broecker et $al.$, 1985)	$20\ cm\ hr^{-1}$
CO_2 solubility (α)	empirical relationship of Weiss (1974) at 20 °C	0.03241 $mol\ kg^{-1}\ atm^{-1}$
Partial pressure of CO_2 (pCO_2)	pre-industrial pCO_2^{atmos} (Neftel et $al.$, 1985)	$278\ \mu\ atm$
Temperature exchange timescale $(\mathcal{K}_T^{-1})$	typical heat exchange timescale (see section 3.1)	60 days
Carbon exchange timescale $(\mathcal{K}_C^{-1})$	$\left(\frac{\kappa}{h}\alpha\beta\frac{pCO_2}{C}\right)^{-1}$	$\sim$ 8 months
Subduction timescale (θ^{-1})	$\mathcal{K}_T^{-1}$	60 days

Table 4.5: Parameters used in the calculation of $F_{CO_2}{}^{upper}$ and $F_{CO_2}{}^{lower}$ using climatological heat flux data.

	Region	CO_2 uptake
Heat flux (using da Silva)	25°N to 65°N	0.18 to 0.68
Heat flux (using Josey)	25°N to 65°N	0.02 to 0.09
Brewer et al.(1989,1991)	north of 25°N	0.41
Broecker and Peng (1992)	thermohaline circulation	0.6
Keeling and Peng (1995)	thermohaline circulation	0.4

Table 4.6: Estimates of the pre-industrial CO_2 uptake (Gt C yr^{-1}) of the North Atlantic inferred from the heat flux data of da Silva et al.(1994) and Josey et al.(1996). Also shown are estimates made using different methods by various authors.

4.2.2 Climatological Air-Sea CO_2 Flux

The annual mean air-sea CO_2 fluxes predicted from the heat flux data of Josey et al.(1996) are shown in figure 4.6. The parameters used in the calculation of $F_{CO_2}{}^{upper}$ and $F_{CO_2}{}^{lower}$ are displayed in table 4.5. $F_{CO_2}{}^{lower}$ has been found to give better estimates of the range of CO_2 fluxes using the model experiments. Therefore, using the $F_{CO_2}{}^{lower}$ map, the predicted range of physically driven CO_2 is a maximum uptake flux of 2 mol C m^{-2} yr^{-1} occurring in the Gulf Stream and -2 mol C m^{-2} yr^{-1} occurring in the Equatorial Pacific. The model experiments have also shown that the areas of CO_2 uptake associated with the western boundary currents are expected to be larger in reality than those predicted by $F_{CO_2}{}^{lower}$. The local CO_2 fluxes in the slower moving regions of the ocean tend to be bounded by the $F_{CO_2}{}^{upper}$ and $F_{CO_2}{}^{lower}$ estimates. Therefore the fluxes in these regions are typically less than 0.1 mol C m^{-2} yr^{-1}.

North Atlantic Uptake

The limits on the net CO_2 uptake for the North Atlantic inferred from the two heat flux climatologies are shown in table 4.6. The CO_2 uptake inferred from the
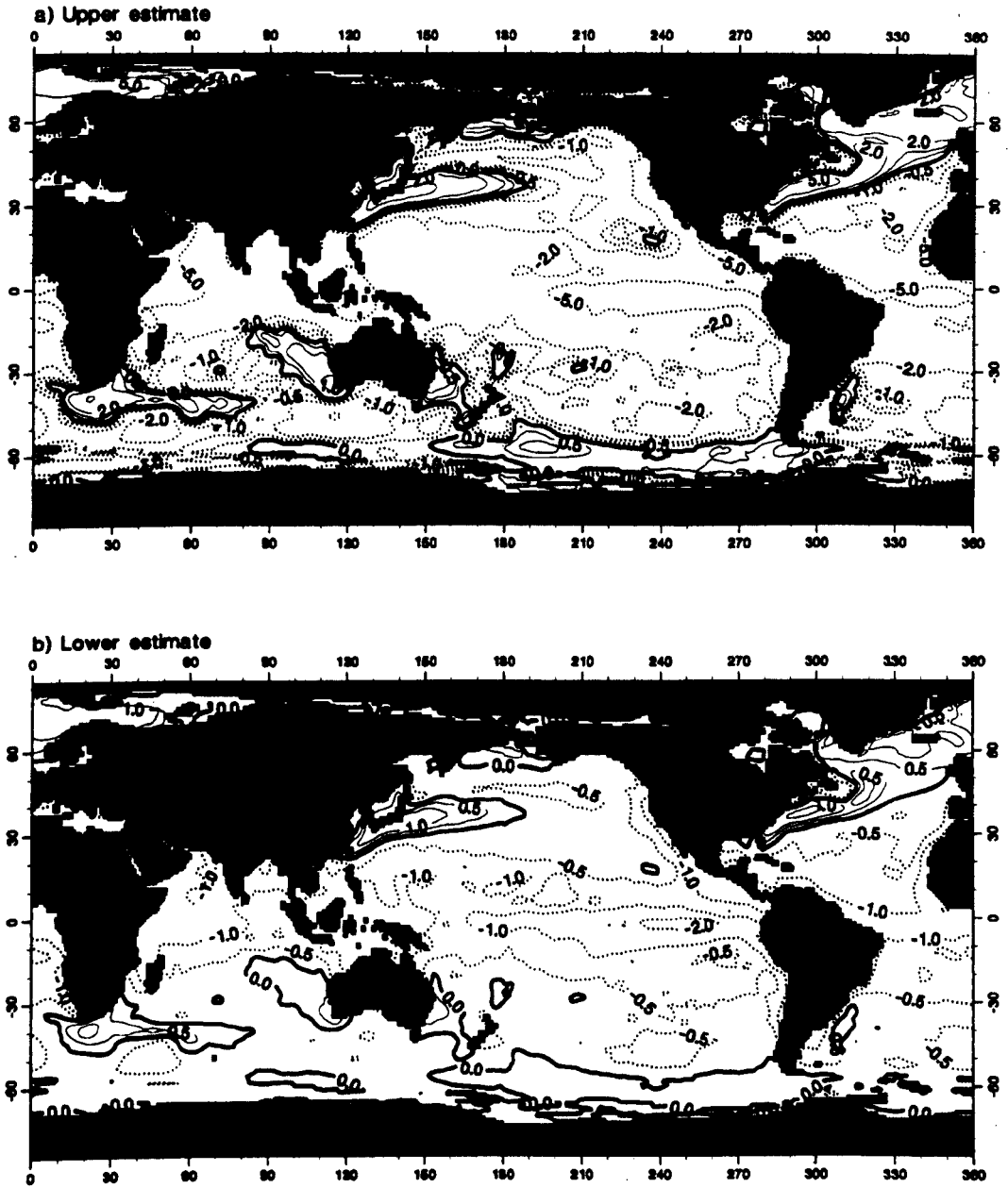
Figure 4.6: Annual mean CO$_2$ air-sea fluxes (mol C m^{-2} yr^{-1}) inferred from the heat flux climatology of Josey *et al.*(1996) using: a) F_{CO_2} ^{upper} ; and b) F_{CO_2} ^{lower} . Contour intervals for the upper plot are: -5, -2, -1, -0.5, 0, 0.5, 1, 2, 5; and for the lower plot: -2, -1, -0.5, 0, 0.5, 1, 2. A positive CO$_2$ flux is directed into the ocean.

Josey climatology is smaller than the value inferred from the da Silva data. The net heat loss from the North Atlantic (25°N to 65°N) calculated using the Josey climatology is only 0.12 PW, which is smaller than the observed northwards heat transport at 25°N of $\sim$ 1 PW. Josey et al.(1999) found that the climatology underestimated the heat loss in regions containing a western boundary current. The da Silva climatology gives a heat loss of 0.87 PW for the North Atlantic (25°N to 65°N) which is believed to be more realistic in this region.

The heat flux method using the da Silva data predicts the CO$_2$ uptake caused by the solubility pump to be between 0.18 to 0.68 Gt C yr^{-1} for the North Atlantic (25°N to 65°N) prior to the industrial revolution. The results of the MIT model suggest that the true uptake value is in the middle of the lower and upper limit ($\sim$ 0.43 Gt C yr^{-1}). Brewer et al.(1989, 1991) used $\sum$CO$_2$ to calculate that the net southwards transport of carbon across 25°N was 0.41 Gt C yr^{-1} for pre-industrial times. The southwards carbon transport due to the thermohaline circulation has been estimated to be 0.4 to 0.6 Gt C yr^{-1} (Keeling and Peng, 1995; Broecker and Peng, 1992) depending on the volume transport used in the calculation. Assuming that these southward carbon transports are balanced by the air-sea uptake of CO$_2$, the heat flux estimate encompasses these previous estimates of the net CO$_2$ uptake of the North Atlantic (as summarized in table 4.6). Therefore, the North Atlantic CO$_2$ uptake is dominated by the solubility pump as has been found previously by Watson et al.(1995) and Keeling and Peng (1995).

Global Uptake

The limits on the net physical CO$_2$ uptake of different oceans inferred from the heat flux climatologies of Josey et al.(1996) and da Silva et al.(1994) are displayed in table 4.7. The differing heat flux climatologies predict different directions of the CO$_2$ flux in the gyre regions. The Josey climatology is expected

Region	F_{CO_2} upper		F_{CO_2} lower		Takahashi et al.(1997)
	da Silva	Josey	da Silva	Josey	
N. Atlantic subarctic (north of 50 °N)	0.25	0.13	0.06	0.03	0.19 to 0.45
N. Atlantic gyre (14 °N to 50 °N)	0.38	-0.41	0.10	-0.11	0.33 to 0.72
N. Pacific gyre (14 °N to 50 °N)	0.88	-0.74	0.23	-0.19	
Equatorial (14 °S to 14 °N)	-2.22	-4.80	-0.58	-1.25	-0.46 to -1.04
Southern gyres (50 °S to 14 °S)	0.84	-1.69	0.22	-0.44	0.42 to 0.92
Southern Ocean (south of 50 °S)	-0.21	-0.22	-0.06	-0.06	0.12 to 0.30

Table 4.7: The upper (F_{CO_2} upper) and lower (F_{CO_2} lower) limit on the CO₂ uptake of different ocean regions inferred from the heat flux climatologies of da Silva et al.(1994) and Josey et al.(1996). Also shown are the CO₂ uptake estimates calculated using observational pCO₂ data by Takahashi et al.(1997).

to underestimate the CO_2 uptake in these gyre regions, as the heat loss is known to be underestimated (Josey *et al.*, 1999). Using the da Silva climatology, the North Atlantic and the North Pacific are both predicted to take up CO_2 , as heat is lost from these regions. The results from the global carbon transport model suggest that the range of the CO_2 uptake predicted for the North Pacific region is likely to be an overestimate. F_{CO_2} [lower] probably gives a more accurate estimate of the true uptake in the North Pacific region at 0.23 Gt C yr^{-1} . The Equatorial region is found to lose CO_2 and gain heat from the atmosphere using both heat flux climatologies. The net heat flux calculated for the Southern Ocean using either heat flux climatology is out of the ocean, which implies a predicted outgassing of CO_2 . This is a surprising result, and, in view of the lack of data available for the Southern Ocean, the result is not reliable.

The estimates of the CO_2 uptake for 1990 made by Takahashi *et al.*(1997) are again presented in table 4.7. The estimates of Takahashi *et al.*(1997) include the effect of biology and the anthropogenic increase in atmospheric CO_2 . In contrast, the CO_2 estimates made using the heat fluxes are for only the physical CO_2 flux in pre-industrial times. As already discussed in section 4.1.4, the impact of biological processes on the air-sea CO_2 flux is dependent on the region. In the Northern Hemisphere, the CO_2 uptake range found using the da Silva heat flux data overlaps with the range of estimates of Takahashi *et al.*(1997) (if the F_{CO_2} [lower] estimate is used for the North Pacific). The estimates for the range of the CO_2 uptake in the Southern gyres are also comparable. In the Equatorial region, the both heat flux climatologies predicts a greater efflux than the Takahashi *et al.*(1997) estimates, which was also found in the MIT model. This could be caused by the impact of anthropogenic and biological processes on the CO_2 flux. With the exception of the Southern Ocean, the comparison with the estimates of Takahashi *et al.*(1997) shows that the heat flux estimates of the CO_2 uptake made using the da Silva climatology are reasonable.
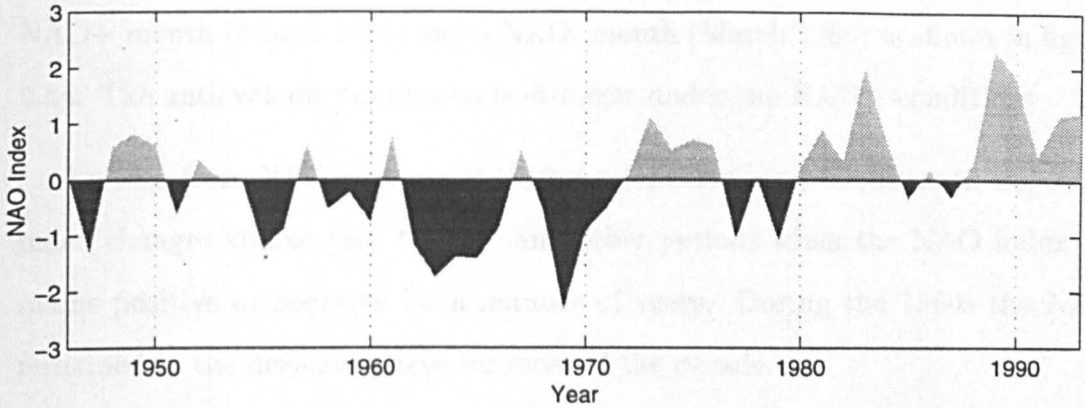
Figure 4.7: Time series of the North Atlantic Oscillation (NAO) index for the winter months (Hurrell, 1995). Light grey for NAO+ years and darker grey for NAO- years.

4.2.3 The North Atlantic Oscillation

Next, the method of obtaining limits of the CO_2 flux from the heat flux is used to infer the interannual variability of the CO_2 uptake of the North Atlantic. In order to explain the interannual variability of the CO_2 uptake it is useful to consider the variability of the atmosphere-ocean system. The dominant interannual variability of the sea-level pressure over the North Atlantic is known as the North Atlantic Oscillation (Wallace and Gulzter, 1981). The spatial pattern of the variability forms a dipole in the pressure field, with the anomalous pressure over Greenland and Iceland being inversely related to the anomalous pressure over the Azores to Portugal region. An index of the strength of the NAO for a specific time can be given by the difference in anomalous pressures between the dipole centres. The NAO index shown in figure 4.7 was defined by Hurrell (1995) and is equal to the difference in normalized sea level pressure between Lisbon, Portugal, and Stykkisholmur, Iceland. When the NAO index is positive (NAO+), the pressure is anomalously high in Portugal and low in Iceland, causing stronger westerly winds. When the NAO index is negative (NAO-), the meridional pres-

sure gradient is weaker than normal. The difference in wind stress between a NAO+ month (March 1989) and a NAO- month (March 1969) is shown in figure 4.8a. The anticyclonic circulation is stronger under the NAO+ conditions.

As seen from NAO time series (figure 4.7), there are periods when the NAO index changes almost year to year, and other periods when the NAO index remains positive or negative for a number of years. During the 1960s the NAO remained in the negative phase for most of the decade.

The NAO pattern of atmospheric variability has been related to oceanic variability. The NAO causes changes in the air-sea heat flux, and hence, changes in water mass formation. Figure 4.8b shows how the winter air-sea heat flux differs between NAO+ and NAO- conditions. During NAO+ periods, there is more heat lost to the atmosphere over the subpolar gyre. In contrast, there is less heat loss over the western and central subtropical gyre in NAO+ periods. The differing heat fluxes cause changes in the amount of convective mixing which affects water mass formation. The formation of Labrador Sea water is found to increase during NAO+ periods, while the production of 18 ^{o}water in the Sargasso Sea decreases (Dickson, 1997).

4.2.4   Interannual Variability of the CO_2 Uptake by the North Atlantic

In this section, the variability of the CO_2 uptake due to the solubility pump in the North Atlantic is quantified for the period 1960 to 1993. The variability of the solubility pump will have a 'natural' and an 'anthropogenic' component for this period. Firstly, the natural variability which is inferred from the heat flux is discussed. Secondly, the anthropogenic variability is evaluated using the increasing concentration of atmospheric CO_2 .

a) Wind stress difference

b) Air-sea heat flux difference
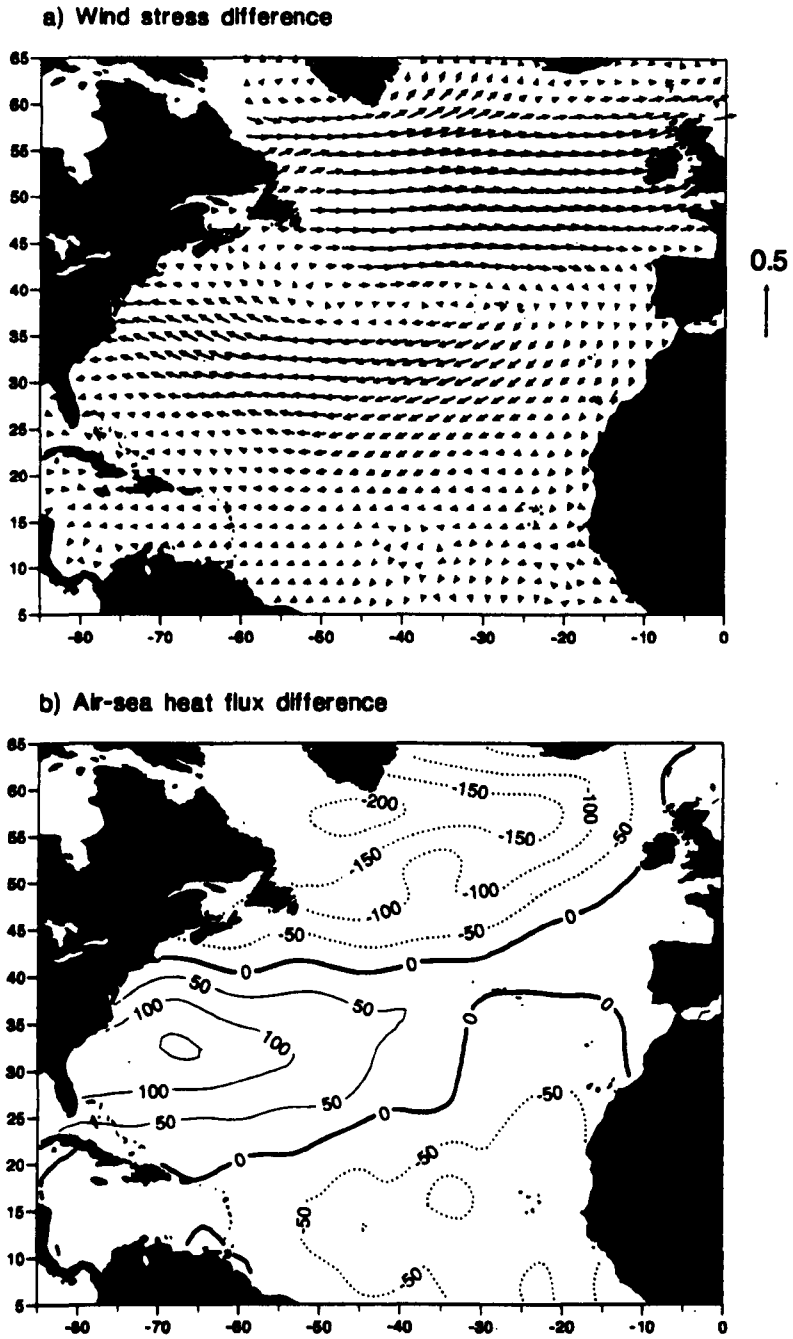
Figure 4.8: Difference between March 1989 (NAO+) and 1969 (NAO-) of: a) the wind stress (Pa); and b) the air-sea heat flux (W m^{-2}) (positive values indicate a reduced heat loss). Data from the da Silva *et al.*(1994) Atlas of Surface Marine Data.

137
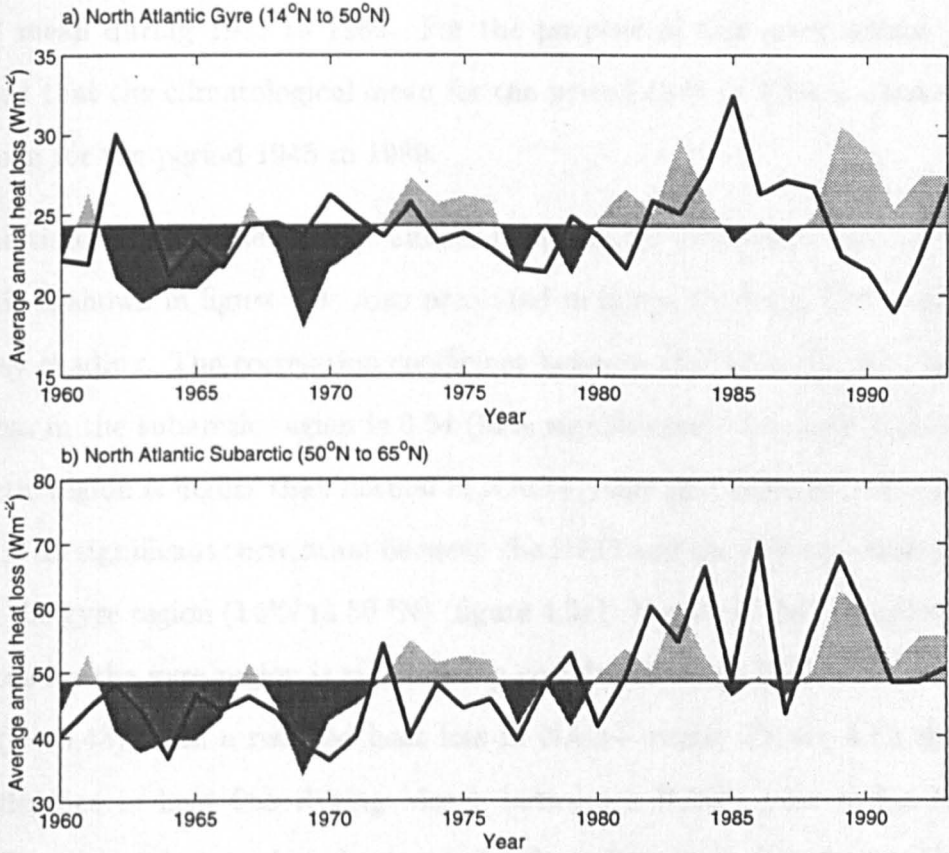
Figure 4.9: Time series of the annual mean heat loss to the atmosphere (Wm^{-2}) for 1960 to 1993 (black line) for: a) the North Atlantic Gyre (14°N to 50°N); and b) the North Atlantic Subarctic (50°N to 65 °N). The grey shading is the NAO index of Hurrell (1995) with light (dark) grey indicating NAO+ (NAO-) years. Heat flux data from the da Silva et al.(1994) Atlas of Surface Marine Data.

Natural Variability

The heat flux data from the da Silva *et al.*(1994) Atlas were used to infer the possible 'natural' interannual variability of the air-sea flux of CO_2 in the North Atlantic for the years 1960 to 1993. The heat flux anomalies in the da Silva *et al.*(1994) Atlas are available for the years 1945 to 1993 relative to the climatological mean during 1945 to 1989. For the purpose of this investigation, it is assumed that the climatological mean for the period 1945 to 1993 is identical to the mean for the period 1945 to 1989.

The time series of the average annual heat flux for two regions in the North Atlantic is shown in figure 4.9. Also presented in figure 4.9 is the NAO index in the grey shading. The correlation coefficient between the NAO and the average heat loss in the subarctic region is 0.54 (99% significance). The heat loss in the subarctic region is higher than normal in NAO+ years and lower in NAO- years. There is no significant correlation between the NAO and the average annual heat flux in the gyre region (14°N to 50 °N) (figure 4.9a). However, the average winter heat loss for the gyre region is significantly correlated at the 99% level with the NAO (r=-0.43), with a reduced heat loss in NAO+ years. Figure 4.8b showed the difference in heat flux during March between a NAO+ year and a NAO- year. The area of anomalous heat gain in the subtropical gyre during NAO+ conditions is confined to the Sargasso Sea in the southwest section of the defined 'subtropical gyre region'. The annual mean heat loss in the region 85°W to 40°W and 14°N to 40°N is significantly correlated to the NAO (r=-0.55), with greater heat loss occurring in NAO- years. Therefore, the lack of correlation between the annual heat flux in the entire subtropical gyre region and the NAO is due to correlation in the Sargasso Sea being cancelled out by the anomalies in the rest of the region.

The anomalous heat flux for each year is used to produce F_{CO_2} ^{upper} and
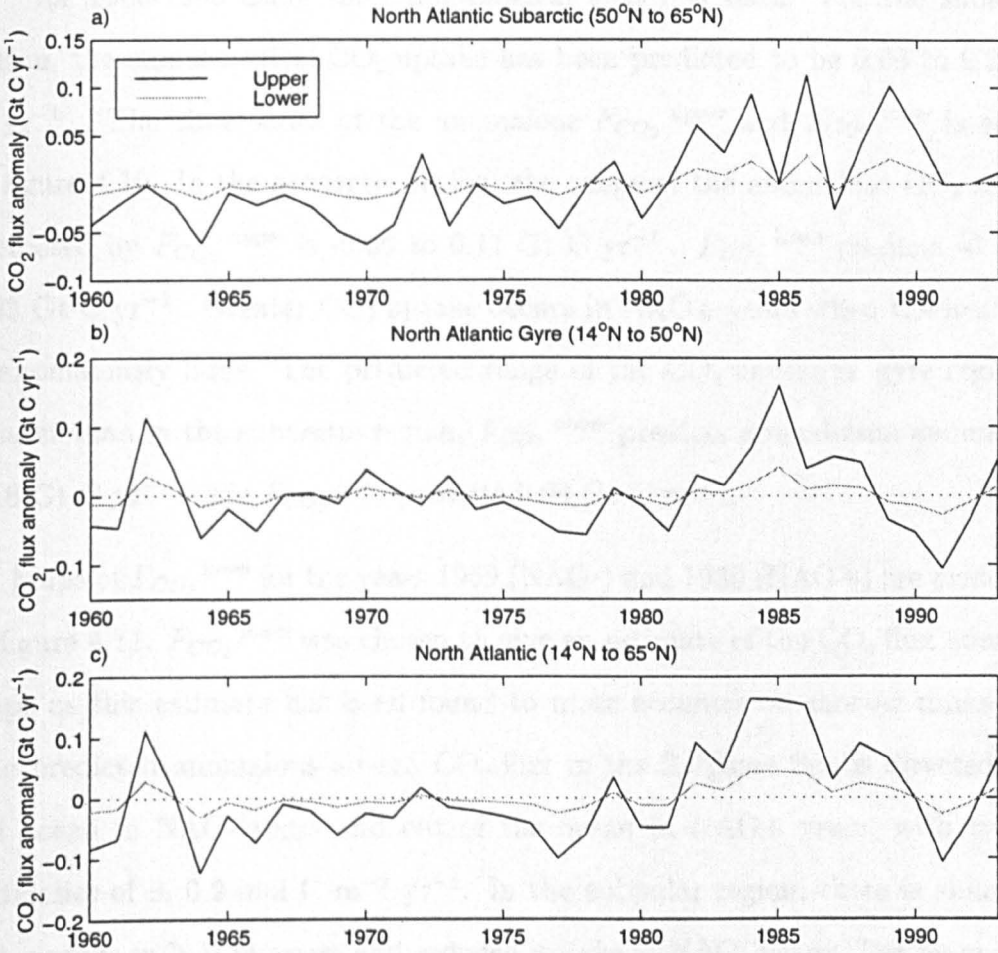
Figure 4.10: Time series of the natural anomalous CO_2 uptake (Gt C yr^{-1}) inferred from heat flux data relative the mean for 1960 to 1993 for the North Atlantic regions: a) 50°N to 65°N; b) 14°N to 50°N; and c) 14°N to 65°N. Upper limit (black line) is F_{CO_2} ^{upper} and lower limit (grey line) is F_{CO_2} ^{lower}. The pre-industrial climatological mean CO_2 uptake has been estimated to be between 0.06 to 0.25 Gt C yr^{-1} for the region 50°N to 65°N and between 0.06 and 0.25 for the region 14°N to 50°N. Heat flux data from the da Silva et al.(1994) Atlas of Surface Marine Data.

$F_{CO_2}{}^{lower}$, which are expected to give an upper and lower limit on the 'natural' variability of the physical CO_2 uptake. The climatological pre-industrial CO_2 uptake for the gyre region is estimated to be between 0.13 to 0.49 Gt C yr^{-1} for 1960-1993 using the climatological heat flux data. For the subarctic region, the climatological CO_2 uptake has been predicted to be 0.06 to 0.25 Gt C yr^{-1} . The time series of the anomalous $F_{CO_2}{}^{upper}$ and $F_{CO_2}{}^{lower}$ is shown in figure 4.10. In the subarctic region, the range of the anomalous CO_2 uptake predicted by $F_{CO_2}{}^{upper}$ is -0.06 to 0.11 Gt C yr^{-1} . $F_{CO_2}{}^{lower}$ predicts -0.02 to 0.03 Gt C yr^{-1} . Greater CO_2 uptake occurs in NAO+ years when the heat loss is anomalously large. The predicted range of the CO_2 uptake in gyre region is greater than in the subarctic region. $F_{CO_2}{}^{upper}$ predicts a maximum anomaly of 0.16 Gt C yr^{-1} while $F_{CO_2}{}^{lower}$ predicts 0.04 Gt C yr^{-1} .

Maps of $F_{CO_2}{}^{lower}$ for the years 1969 (NAO-) and 1989 (NAO+) are presented in figure 4.11. $F_{CO_2}{}^{lower}$ was chosen to give an estimate of the CO_2 flux anomaly maps as this estimate has been found to more accurate on shorter timescales. The predicted anomalous air-sea CO_2 flux in the Sargasso Sea is directed into the ocean in NAO- years and out of the ocean in NAO+ years, with typical anomalies of $\pm$ 0.2 mol C m^{-2} yr^{-1}. In the subpolar region, there is enhanced CO_2 uptake in NAO+ years and reduced uptake in NAO- years. The magnitude of the CO_2 flux anomalies are predicted to be greater in the subpolar gyre with anomalous fluxes reaching 0.6 mol C m^{-2} yr^{-1}in 1989. This magnitude is very significant when compared with the climatological maps of $F_{CO_2}{}^{lower}$ (figure 4.6b).

Figure 4.10c shows the variability in the CO_2 uptake over the whole North Atlantic. During the 1980s the CO_2 uptake was anomalously large due to a greater heat loss from both the subtropical and subpolar gyre. The CO_2 uptake is generally smaller than normal for the period 1964 to 1980, which is caused mainly by a reduced heat loss in the subpolar gyre.
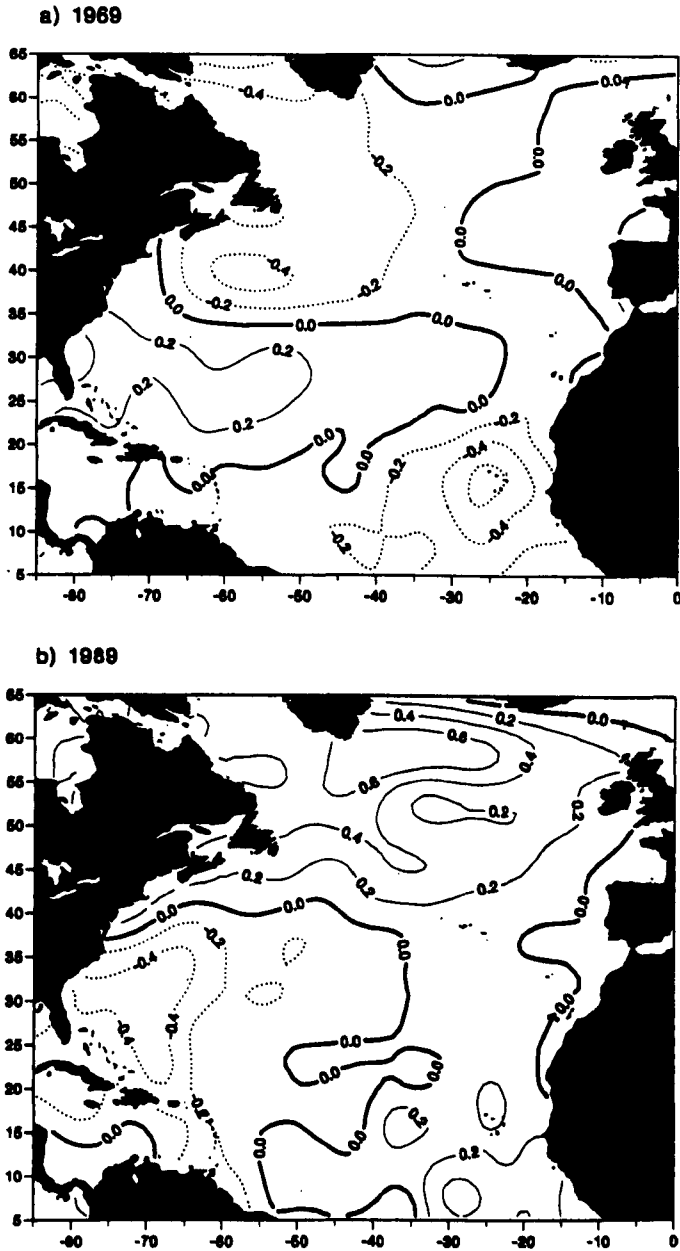
Figure 4.11: The anomalous annual mean air-sea CO_2 flux inferred from the heat flux using F_{CO_2} [lower] for: a) 1969 (NAO-); and b) 1989 (NAO+). A positive flux indicates a greater CO_2 flux into the ocean relative to the mean for the period 1960 to 1993. The anomalous values can be compared with the climatological maps presented in figure 4.6. Heat flux data from the da Silva et al.(1994) Atlas of Surface Marine Data.

Anthropogenic Variability

The variability of the CO$_2$ uptake of the North Atlantic due to the increasing atmospheric pCO$_2$ during 1960 to 1993 can be estimated using the air-sea CO$_2$ exchange equation. The equation can be split into a pre-industrial component and an anthropogenic component as follows:

$$\begin{aligned} F_{CO_2} &= \kappa\alpha(pCO_2{}^{atmos}(t) - pCO_2{}^{ocean}(t)) \\ &= \kappa\alpha(pCO_2{}^{atmos}(t) - \overline{pCO_2{}^{atmos}}) - \kappa\alpha(pCO_2{}^{ocean}(t) - \overline{pCO_2{}^{ocean}}) \\ &\quad + \kappa\alpha(\overline{pCO_2{}^{atmos}} - \overline{pCO_2{}^{ocean}}). \end{aligned} \tag{4.3}$$

where the horizontal bar indicates the time-mean pre-industrial value. The first two terms on the right hand side of equation (4.3) are the CO$_2$ flux caused by the anthropogenic increase in atmospheric and oceanic pCO$_2$. The third term on the right hand side of equation (4.3) is the pre-industrial ('natural') CO$_2$ flux which has been evaluated using the heat flux.

The ability to use equation (4.3) to calculate the anthropogenic CO$_2$ uptake of the North Atlantic was investigated in the PGOM. The PGOM was run for 3000 years with a pre-industrial atmospheric pCO$_2$ value of 280 μ atm. The atmospheric pCO$_2$ was then increased linearly for the period 1750 to 1990 as shown in figure 4.12a. The annual anthropogenic CO$_2$ uptake of the region north of 24°N is presented in figure 4.12b. The rate at which anthropogenic CO$_2$ is taken up by the ocean region increases with time. The maximum anthropogenic CO$_2$uptake value of $\sim$ 0.05 Gt C yr^{-1}in 1990 is half the pre-industrial CO$_2$uptake. The continual increase of the CO$_2$ uptake with time is caused by the increasing difference between the atmospheric CO$_2$ and the oceanic pCO$_2$ (figure 4.12a). The anthropogenic CO$_2$uptake calculated using equation (4.3) with annual mean oceanic pCO$_2$ values is found to compare well with the true model uptake.

To enable equation (4.3) to be used to estimate the variability of the
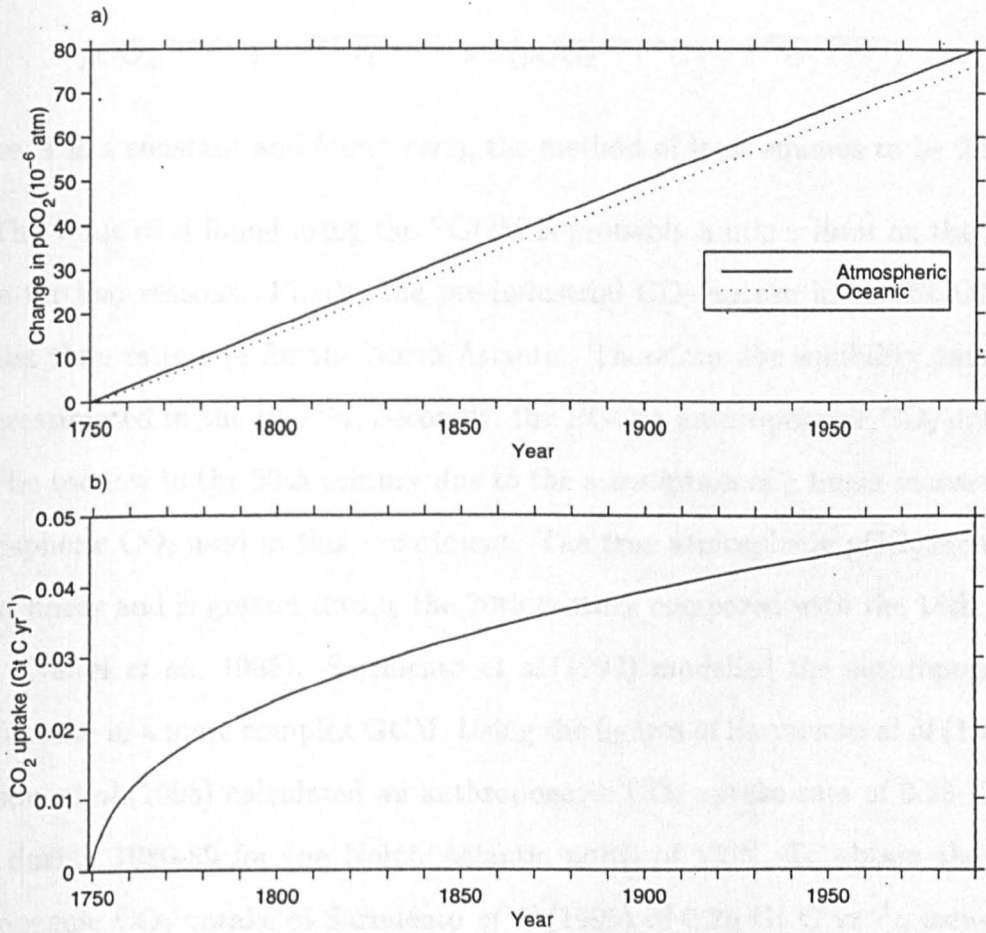
Figure 4.12: Results from the PGOM anthropogenic CO_2 experiment. a) Increase in atmospheric pCO_2 (solid line) and annual mean oceanic pCO_2 (over the region north of 24°N) from pre-industrial times. b) Oceanic uptake of anthropogenic CO_2 over time for the region north of 24°N (Gt C yr^{-1}).

CO_2 flux due to anthropogenic processes, a method must be devised to evaluate $pCO_2{}^{ocean}(t)$ from available data. In the PGOM experiment, a strong linear relationship between $(pCO_2{}^{ocean}(t) - \overline{pCO_2{}^{ocean}})$ and $(pCO_2{}^{atmos}(t) - \overline{pCO_2{}^{atmos}})$ was found for the period 1960 and 1990, such that,

$$pCO_2{}^{ocean}(t) - \overline{pCO_2{}^{ocean}} \approx A(pCO_2{}^{atmos}(t) - \overline{pCO_2{}^{atmos}}) \qquad (4.4)$$

where A is a constant and found using the method of least squares to be 0.98.

The value of A found using the PGOM is probably a upper limit on the true value for two reasons. Firstly, the pre-industrial CO_2 uptake in the PGOM is smaller than estimates for the North Atlantic. Therefore, the solubility pump is underestimated in the PGOM. Secondly, the PGOM anthropogenic CO_2 uptake may be too low in the 20th century due to the assumption of a linear increase in atmospheric CO_2 used in this experiment. The true atmospheric pCO_2 increase is not linear and is greater during the 20th century compared with the 18th and 19th (Neftel *et al.*, 1985). Sarmiento *et al.*(1992) modelled the anthropogenic CO_2 uptake in a more complex GCM. Using the figures of Sarmiento *et al.*(1992), Watson *et al.*(1995) calculated an anthropogenic CO_2 uptake rate of 0.25 Gt C yr^{-1} during 1980-89 for the North Atlantic north of 15°N. To obtain the anthropogenic CO_2 uptake of Sarmiento *et àl.*(1995) of 0.25 Gt C yr^{-1} , using an increase of atmospheric pCO_2 of 278 μ atm to 360 μ atm, implies A is 0.87. This value of A is an average value over ~1750 to 1990. A was found to increase in the PGOM experiment with time. Therefore, the value of 0.87 for A is expected to be lowxer limit for the period 1960 to 1990.

Equations (4.3) and (4.4) were used with atmospheric pCO_2 data to calculate the anthropogenic variability in the CO_2 flux for the period 1960 to 1993. For simplicity, a linear increase in atmospheric pCO_2 from 315 μ atm in 1960 to 360 μ atm in 1993 was used. An upper and a lower limit on the anthropogenic CO_2 flux variability were obtained using the two values of A, 0.87 and 0.98, implied from

the results of Sarmiento *et al.*(1992) and the PGOM experiment.

The time series of the anomalous CO$_2$ uptake due the anthropogenic flux for the two North Atlantic regions is shown in figures 4.13b and 4.14b. The variability caused by the anthropogenic flux is combined with the natural variability in figures 4.13c and 4.14c. The variability for the whole North Atlantic region is shown in figure 4.15.

In both the North Atlantic regions, the variability in the solubility pump tends to be dominated by the natural variability. In the gyre region, the maximum variability in the anthropogenic component is 0.05 Gt C yr^{-1} which is smaller than the maximum natural anomaly of 0.16 Gt C yr^{-1}. For the entire North Atlantic region (figure 4.15), the anthropogenic component enhances the natural variability with greater CO$_2$ uptake in the 1980s relative to the 1960s and 1970s. There are some years, such as 1992, where the natural variability is stronger and acts in the opposite direction to the anthropogenic component, causing an anomalous CO$_2$ outgassing relative to the climatological mean value.

4.2.5 Conclusions

Observational heat flux data has been used to predict the upper and lower limit of the physical air-sea CO$_2$ flux for pre-industrial times. The predictions are feasible when compared with estimates of Takahashi *et al.*(1997). The interannual variability of the CO$_2$ uptake caused by the solubility pump in the North Atlantic has also been quantified. The 'natural' variability was inferred from heat flux data. The CO$_2$ uptake in the gyre region of the North Atlantic (14°N to 50 °N) has a maximum natural anomaly relative to the climatological mean of 0.16 Gt C yr^{-1} during 1960 and 1993. (The pre-industrial climatological mean for the gyre region for this period is 0.13-0.49 Gt C yr^{-1}.) The maximum natural anomaly of the CO$_2$ uptake in the subarctic region of the North Atlantic (50°N to
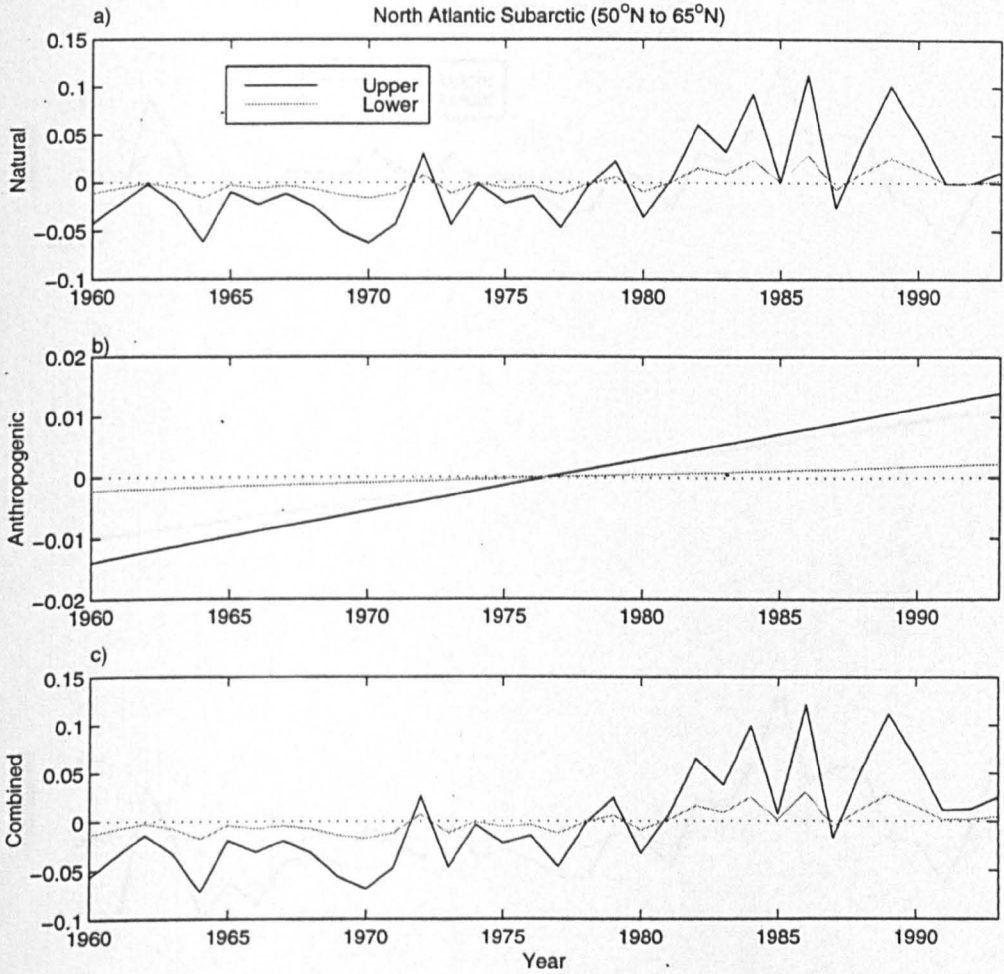
Figure 4.13: Time series of the anomalous CO_2 uptake caused by the solubility pump of the North Atlantic Subarctic (50°N to 65°N) relative the mean for 1960 to 1993: a) natural variability inferred from the heat flux, upper (black line) and lower (grey line) limit; b) anthropogenic variability inferred from atmospheric pCO_2 , upper (black line) and lower (grey line) limit; and c) total variability (natural plus anthropogenic variability), upper (black line) and lower (grey line) limit. The pre-industrial climatological mean CO_2 uptake has been estimated to be between 0.06 to 0.25 Gt C yr^{-1}. Heat flux data from the da Silva *et al.*(1994) Atlas of Surface Marine Data.
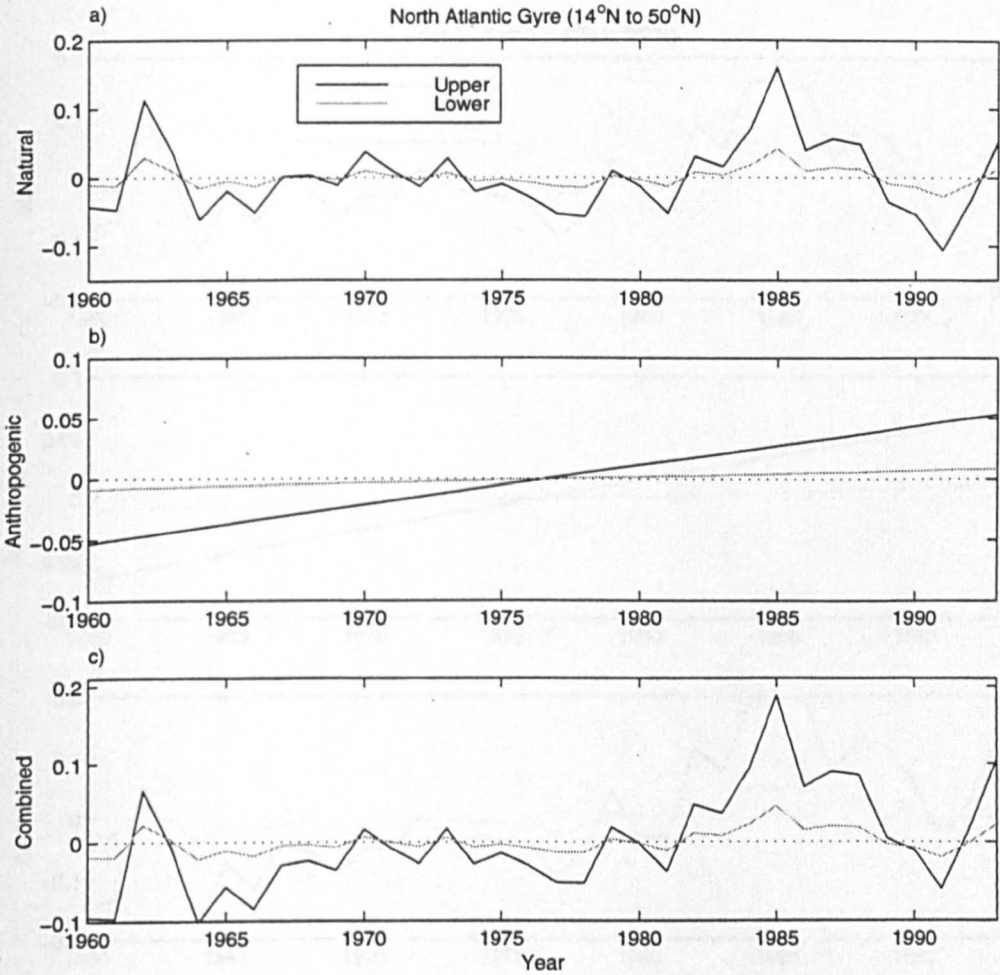
Figure 4.14: Time series of the anomalous CO_2 uptake caused by the solubility pump of the North Atlantic Gyre (14°N to 50°N) relative the mean for 1960 to 1993: a) natural variability inferred from the heat flux, upper (black line) and lower (grey line) limit; b) anthropogenic variability inferred from atmospheric pCO_2 , upper (black line) and lower (grey line) limit; and c) total variability (natural plus anthropogenic variability), upper (black line) and lower (grey line) limit. The pre-industrial climatological mean CO_2 uptake has been estimated to be between 0.13 to 0.49 Gt C yr^{-1} . Heat flux data from the da Silva et al.(1994) Atlas of Surface Marine Data.
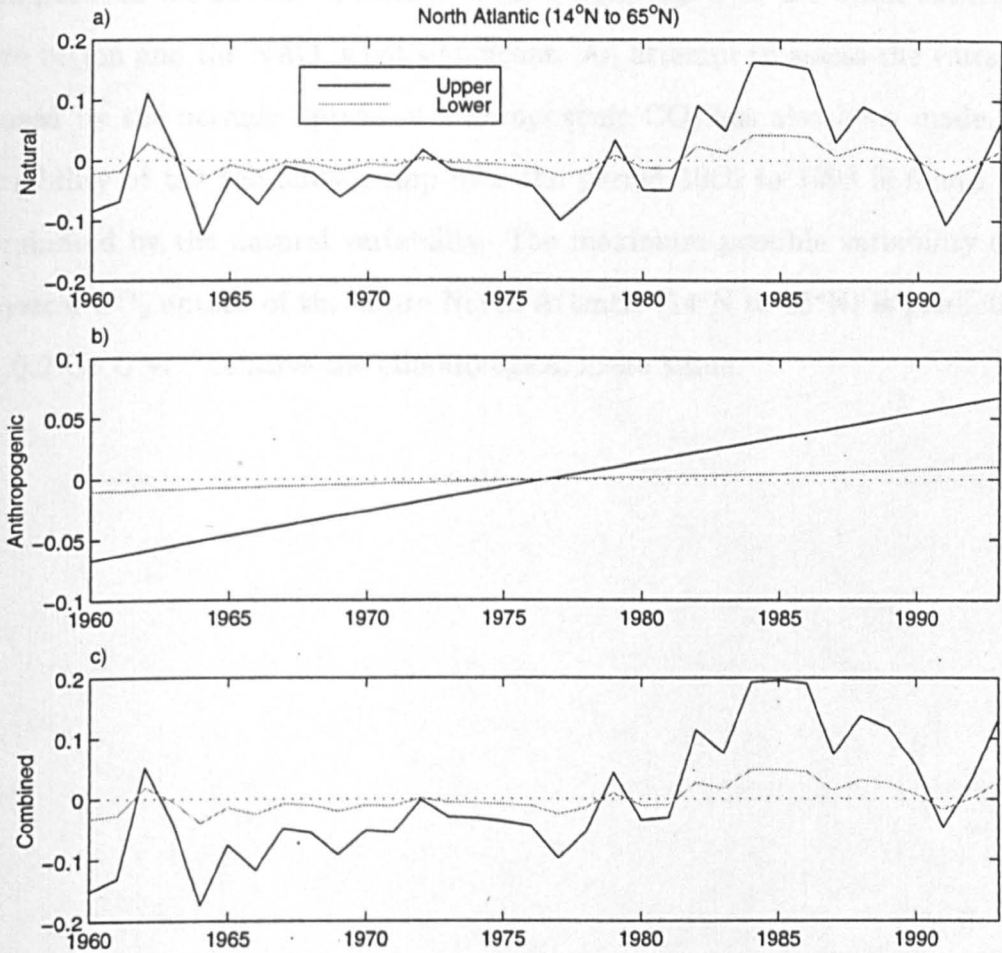
Figure 4.15: Time series of the anomalous CO_2 uptake for the North Atlantic (14°N to 65°N) relative the mean for 1960 to 1993: a) natural variability inferred from the heat flux, upper (black line) and lower (grey line) limit; b) anthropogenic variability inferred from atmospheric pCO_2 , upper (black line) and lower (grey line) limit; and c) total variability (natural plus anthropogenic variability), upper (black line) and lower (grey line) limit. The pre-industrial climatological mean CO_2 uptake has been estimated to be between 0.19 and 0.74 Gt C yr^{-1} . Heat flux data from the da Silva *et al.*(1994) Atlas of Surface Marine Data.

65 °N) is less at 0.11 Gt C yr^{-1}. However, the pre-industrial climatological mean CO$_2$ uptake is also smaller at 0.06 to 0.25 Gt C yr^{-1}. In the subarctic region, the CO$_2$ uptake is larger in NAO+ years and smaller in NAO- years. The correlation between the annual variability of the CO$_2$ uptake over the whole subtropical gyre region and the NAO is not significant. An attempt to assess the variability caused by the oceanic uptake of anthropogenic CO$_2$ has also been made. The variability of the solubility pump over the period 1960 to 1993 is found to be dominated by the natural variability. The maximum possible variability of the physical CO$_2$ uptake of the entire North Atlantic (14°N to 65°N) is predicted to be 0.2 Gt C yr^{-1} relative the climatological mean value.

Chapter 5

Dynamical Supply of Nutrients

The creation of organic carbon in the euphotic zone and the subsequent export of that organic material to the deep ocean causes air-sea fluxes of CO_2 as discussed in section 2.1.4. A continual supply of new nutrients into the euphotic zone is required to sustain this export production. In this section, the dynamical supply of nutrients to the euphotic zone is investigated. In particular, the dynamical supply of dissolved organic nutrients is examined. The variability of export production will affect the air-sea CO_2 flux. The variability of the dynamical nutrient supply and the effect on export production is investigated using an idealised model. Finally, the interannual variability of one of the dynamical nutrient supplies is quantified using available data. This work concentrates on the export production of the subtropical gyre.

5.1 Export Production in Subtropical Gyres

The supply of nutrients to the euphotic zone can limit biological production in some regions of the ocean. The largest rates of primary production are found to occur where there are large nutrient fluxes into the surface ocean. In regions of
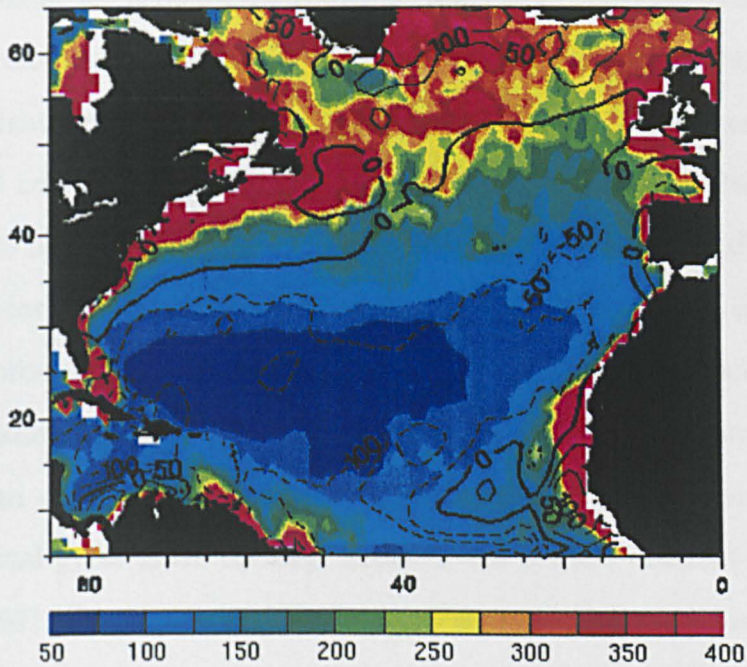
Figure 5.1: Annual net primary productivity (g C m^{-2} yr^{-1}) inferred from satellite observations of surface chlorophyll by Sathyendranath *et al.*(1995) (replotted here). Contours are the Ekman vertical velocity with positive contours for upwelling water. 50 g C m^{-2} yr^{-1} is equal to ~ 4 mol C m^{-2} yr^{-1}(Figure 1 of Williams and Follows, 1998b.)

upwelling, rates of primary productivity are very high as nutrients are advected vertically to the surface. This is seen in figure 5.1 in the upwelling regions off the west coast of Africa and in the subpolar gyre. In the subtropical gyres, where there is Ekman pumping, the rates of primary productivity are lower. The lack of upwelling in subtropical gyres has led to the subtropical gyres being viewed as oceanic 'deserts' with little export production.

However, measurements over the last 2 decades have shown that the level of export production in subtropical gyres is ~ 3 mol C m^{-2} yr^{-1} which is twice as high than previously thought (Jenkins, 1982). A wide range of techniques have been used to measure the export production. Jenkins (1982) inferred an export production rate in excess of 4 mol C m^{-2} yr^{-1}, by combining tritium dating with

oxygen measurements, for the eastern region of the North Atlantic subtropical gyre. Jenkins and Goldman (1985) used several methods including measurements of the oxygen utilization below the euphotic zone, the oxygen production in the euphotic zone and tritium measurements, to calculate the export production in the Sargasso Sea to be ~ 4 mol C m^{-2} yr^{-1}. Separate mass balances of dissolved oxygen, inorganic carbon and organic carbon were used by Emerson et al.(1997) to infer a export production rate of 2 mol C m^{-2} yr^{-1}for the North Pacific near Hawaii. These measured levels of export production in the subtropical gyres are still lower than other more productive regions such as the subpolar gyre. However, subtropical gyres make up large areas of the world's oceans (~ 60 %, Emerson et al., 1997). Consequently, if the measured production rates are typical of subtropical gyres, then these areas could contribute up to half of the global biological carbon pump.

To sustain export production, a supply of nutrients to the euphotic zone is required. Export production of 2-4 mol C m^{-2} yr^{-1}requires a nutrient supply of approximately 0.3-0.6 mol N m^{-2} yr^{-1}(using a Redfield ratio, C:N of 7:1). This estimate of the required nutrient supply is supported by the work of Jenkins (1988) who calculated the annual supply of nitrate to the euphotic zone of the North Atlantic subtropical gyre to be 0.6 ± 0.2 mol N m^{-2} yr^{-1}. The estimate of Jenkins (1988) was made by combining measurements of excess ^{3}He in the mixed layer with the observed correlation of ^{3}He and nitrate in the main thermocline. In the subtropical gyres, the necessary resupply of nutrients cannot be accomplished by the large scale, time-mean vertical motion. A variety of alternate nutrients sources have been suggested which are discussed next.

5.1.1   Vertical Diffusion

The traditional explanation of how nutrients are supplied to the euphotic zone is through vertical diffusion of nutrients across the bottom of the mixed layer. However, experiments in the open ocean have revealed that the diffusivity is too small in the thermocline (Ledwell *et al.*, 1993) to supply the amount of nutrients required to sustain the recent measured levels of export production. For example, measurements by Lewis *et al.*(1986) taken over a two week period in June in the eastern North Atlantic, only give a vertical diffusive nutrient supply of 0.05 mol N m^{-2} yr^{-1}. The vertical diffusivity is larger near the surface than in the ocean's interior, however, the vertical diffusion of nutrients remains small near the surface due to the low nutrient gradients.

5.1.2   Atmospheric Deposition

The atmosphere can supply fixed nitrogen to the surface by deposition. Knap *et al.*(1986) measured the supply by wet deposition in the Sargasso Sea to be 0.006-0.03 mol N m^{-2} yr^{-1}. The lower limit assumes that the organic N in the rainwater does not fuel new production. Hence, Knap *et al.*(1986) concluded that the nutrient supply to the open ocean from atmospheric deposition was insignificant.

5.1.3   Wintertime Convection

In the winter, the surface cooling creates deep mixed layers which mix nutrients back to the euphotic zone. If export production is defined with respect to the euphotic zone, then wintertime convection is a process that supports export production. Michaels *et al.*(1994) estimate a supply of 0.13 mol N m^{-2} yr^{-1} due to wintertime convection.

However, if export production is defined with respect to the mixed layer depth, then wintertime convection does not supply 'new' nutrients to the surface (Williams and Follows, 1998a). The nutrients that are supplied by convective mixing are recycled from the organic matter fallout from the mixed layer of the previous summer. The difference in definition is very significant. The uptake of atmospheric CO_2 is determined by the removal of CO_2 from the mixed layer to the main thermocline. Therefore to infer uptake rates of atmospheric CO_2, export production should be defined with respect to the mixed layer, in which convection does not supply nutrients.

5.1.4 Nitrogen Fixation

Approximately 95% of the nitrogen in the ocean is in the form of dissolved nitrogen gas (N_2). However, the majority of marine organisms require fixed nitrogen (e.g. nitrate) for photosynthesis. This is because only a few organisms (cyanobacteria) are capable of fixing N_2, thus converting N_2 into the nitrogen compounds needed for growth. Karl *et al.*(1997) used a variety of observations including isotopic nitrogen measurements, to calculate that up to half of the nitrogen required to sustain the observed export production at a site in the North Pacific was supplied by N_2 fixation. However, Karl *et al.*(1997) questioned whether their results were representative of the normal situation. Nitrogen fixation causes the Redfield ratio of nitrogen to phosphate to be higher than normal, which can be used as a signal to locate regions of nitrogen fixation. Gruber and Sarmiento (1997) made use of this signal to identify possible nitrogen fixation sites in the global oceans. The only subtropical gyre that showed signs of significant nitrogen fixation was the North Atlantic. By combining the observation of excess nitrate and the ventilation rate, Gruber and Sarmiento (1997) predicted a supply of new nitrogen through nitrogen fixation of 0.07 mol N m^{-2} yr^{-1}for the North Atlantic

subtropical gyre. Using available measurements of cyanobacteria abundance and nitrogen fixation rates, Lipschultz and Owens (1996) estimated a similar rate of new nitrogen supply by nitrogen fixation of 0.06 mol N m^{-2} yr^{-1} in the North Atlantic (between 0 °N and 30 °N).

Nitrogen fixation requires a larger supply of iron than normal biological feeding. Gruber and Sarmiento (1997) suggested the iron supply to the oceans other than the North Atlantic is insufficient to support nitrogen fixation.

5.1.5 Mesoscale Eddies

Cyclonic eddies upwell nutrients into the well-lit surface layer, which is rapidly utilised, thus supporting new production. Anticyclonic eddies remove nutrient poor surface water out of the well-lit region and do not affect biology. Therefore, the overall effect of mesoscale eddies is upwards advection of nutrients (McGuillicuddy and Robinson, 1997).

It is difficult to measure the nutrient flux caused by mesoscale eddies as they are by definition spatially and temporally intermittent. McGuillicuddy and Robinson(1997) have used a numerical model to estimate the nutrient fluxes associated with mesoscale eddies in the Sargasso Sea. They predicted the eddy annual flux of nutrients into the euphotic zone to be 0.35 ± 0.10 mol N m^{-2} yr^{-1}. Estimates of the eddy nitrogen flux from satellite data suggest an annual value of 0.19 ± 0.10 mol N m^{-2} yr^{-1} (McGuillicuddy et al., 1998).

Oschlies and Garçon (1998) assimilated satellite surface height data into an eddy-resolving numerical model to investigate new production in the North Atlantic. In some regions, such as Bermuda, observed levels of new production were predicted by the model. However, the model new production rates were too low in the southern subtropical gyre. They conclude that eddies cannot explain the observed level of new production everywhere in a subtropical gyre.

5.1.6 Horizontal Advection of Inorganic Nutrients

Although the large-scale vertical circulation acts to remove nutrients from the subtropical gyre, the horizontal circulation can supply nutrients. Williams and Follows (1998a) used climatological data to quantify the horizontal advection of nitrate by the Ekman transport. The horizontal Ekman flow can transport nutrients from the high nutrient subpolar gyre into the subtropical gyre (figure 5.2). The Ekman nitrate supply to the Ekman layer can be split into a horizontal and a vertical component,

$$-\int_{-he}^{0} \nabla \cdot (\mathbf{u_e} NO_3^-)dz = -\nabla_h \cdot (\mathbf{U_e} NO_{3m}^-) + w_e NO_{3m}^-. \qquad (5.1)$$

$\mathbf{u_e}$ is the Ekman velocity, w_e is the vertical Ekman velocity, U_e is the horizontal Ekman volume flux per unit length and NO_{3m}^- is the concentration of nitrate in the mixed layer. Equation (5.1) assumes that the Ekman layer is never deeper than the euphotic zone. The left-hand side of equation (5.1) can also be written as,

$$-\int_{-he}^{0} \nabla \cdot (\mathbf{u_e} NO_3^-)dz = -\mathbf{U_e} \cdot \nabla_h NO_{3m}^-.$$

using $\nabla_h \cdot \mathbf{U_e} = w_e$.

Figure 5.3 shows the vertical and horizontal components to the Ekman advection during April. The vertical component supplies nutrients to the upwelling regions in the subpolar gyre and off the east coast of Africa. Nutrients are fluxed out of the euphotic zone of the subtropical gyre by the Ekman pumping. The horizontal component supplies nutrients to most of the subtropical gyre, with especially high values at the gyre boundary. The total effect of the Ekman flux is to supply nutrients to large areas of the subtropical gyre (figure 5.3c).

The annual Ekman flux is show in figure 5.4. The largest supply is in the western subpolar gyre reaching 0.6 mol N m^{-2} yr^{-1}. The Ekman flux supplies
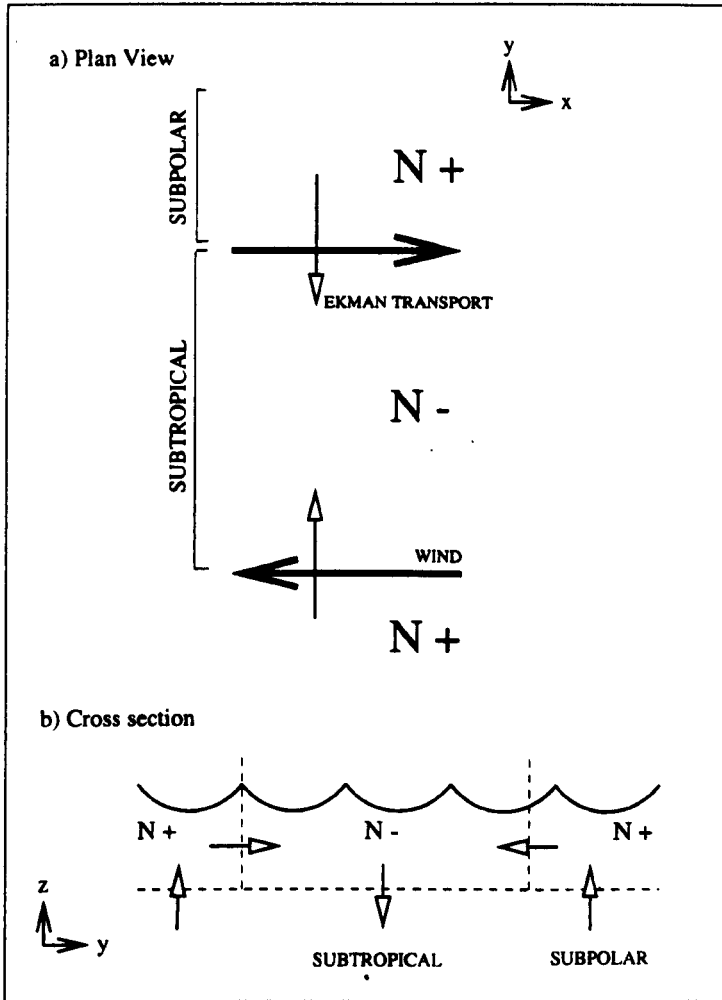
Figure 5.2: Diagrams showing the Ekman transfer of nutrients into the subtropical gyre: a) plan view; b) cross sectional view. The nutrient concentrations are high in the upwelling regions of the tropics and subpolar gyre. The nutrients from these regions are transferred into the subtropical gyre by the horizontal Ekman transport.
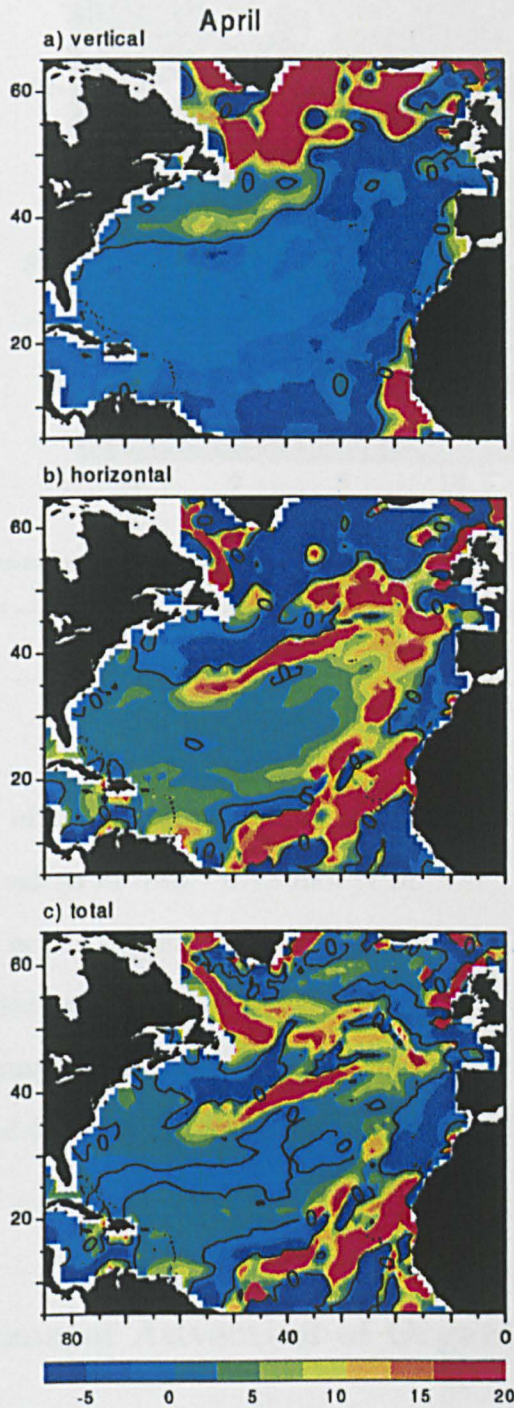
Figure 5.3: The Ekman supply of nitrate during April (10^{-9} mol N m^{-2} s^{-1}): a) the vertical Ekman nitrate flux; b) the convergence of the horizontal Ekman nitrate flux; and c) the convergence of the total Ekman nitrate flux. Positive values indicate a supply of nitrate to the Ekman layer. 10×10^{-9} mol N m^{-2} s^{-1} is equal to ~ 0.3 mol N m^{-2} yr^{-1}. (Figure 7 of Williams and Follows, 1998a.)

159
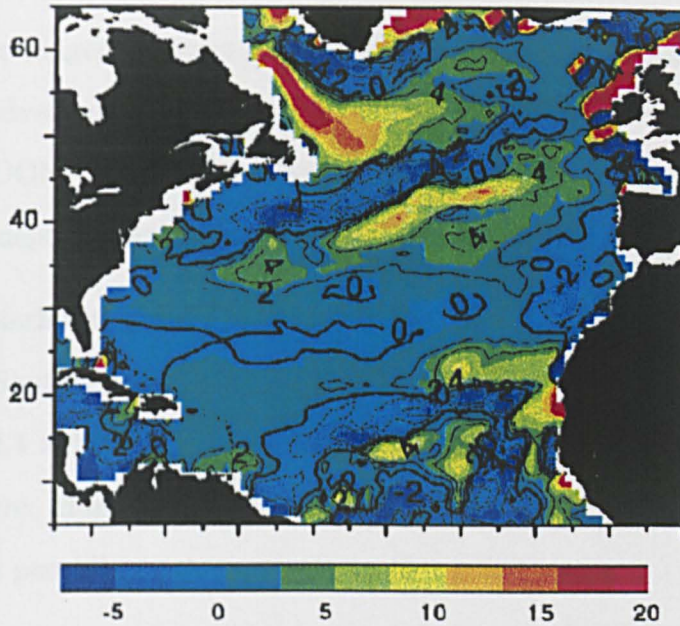
Figure 5.4: The annual mean Ekman flux of nitrate (10^{-9} mol N m^{-2} s^{-1}). 10×10^{-9} mol N m^{-2} s^{-1}is equal to ~ 0.3 mol N m^{-2} yr^{-1}. (Figure 8 of Williams and Follows, 1998a.)

nitrate to most of the subtropical gyre with the greatest flux occurring at the boundary with values of 0.06 - 0.12 mol N m^{-2} yr^{-1}. In the boundary region, the Ekman flux acts a significant source of new nutrients. However, the Ekman nitrate supply decreases towards the centre of the gyre as the nutrient concentration and Ekman volume flux reduces. When averaged over the whole North Atlantic (5 ^{o}N to 65 ^{o}N) the annual Ekman flux becomes 0.03 - 0.05 mol N m^{-2} yr^{-1}.

5.1.7 Horizontal Advection of Organic Nutrients

The horizontal advection of inorganic nitrogen cannot support the production observed in the centre of the gyre. But it is expected that dissolved organic nutrients will also be advected horizontally from the highly productive tropics and subpolar gyre into the subtropical gyre. Certain forms of dissolved organic

matter (DOM) have longer lifetimes than nitrate in the euphotic zone so DOM is expected to be advected further into the subtropical gyre. Indeed, dissolved organic nitrogen (DON) becomes the largest pool of reactive nitrogen in the surface of nutrient-depleted waters (Michaels *et al.*, 1996).

Hansell and Waterhouse (1997) took measurements of total organic nitrogen across the eastern South Pacific subtropical gyre. They calculated a horizontal Ekman transfer of 2.4×10^{12} mol N yr^{-1} in the form of organic material from the equator into the gyre. Hansell and Waterhouse (1997) argued that the organic matter transfer was providing new nutrients to the gyre.

Rintoul and Wunsch (1991) calculated the northwards of transport of nitrate at 24 °N and 36 °N. They found a pattern of transport that required a nitrate source between 24 °N and 36 °N of 3.5×10^{12} mol N yr^{-1}. A repeat analysis with recent WOCE data produced similar results (Ganachaud and Wunsch, 1998). Rintoul and Wunsch (1991) hypothesised that a southwards transport of DON into the region could be the nitrate source. Unfortunately, there are very few DON measurements and the hypothesis cannot yet be tested. Alternatively, nitrogen fixation could provide the source of nitrogen (Michaels *et al.*, 1996).

5.1.8   Summary

Table 5.1 reviews the dominant fluxes of new nitrogen into a subtropical gyre. If the predictions of the eddy fluxes are correct, then the budget is closed without the need to include DON advection or nitrogen fixation. However, as shown in the sophisticated modelling results of Oschlies and Garçon (1998), it is unclear whether the eddy flux is as large as McGuillicuddy and Robinson (1997) suggest everywhere in the subtropical gyre. Therefore it is still necessary to examine the alternative suggestions.

Process	Nitrate supply	Reference
Wintertime mixing	0.13 ± 0.05	Michaels *et al.*(1994)
Diapycnal diffusion	0.05 ± 0.01	Lewis *et al.*(1986)
Ekman flux of NO_3^-	0.03 ± 0.01	Williams and Follows (1998a)
Eddy upwelling	0.28 ± 0.10	McGuillicuddy and Robinson (1997) and McGuillicuddy *et al.*(1998)
Nitrogen fixation	0.07 ± 0.01	Gruber and Sarmiento (1997)
Horizontal advection of DON	??	
Total nitrate supply	0.56 ± 0.18	
Nitrate requirement	0.50 ± 0.14	Various (see text)

Table 5.1: Nitrate sources (mol N m^{-2} yr^{-1}) to the Sargasso Sea compared to the nitrate requirement. (Nitrogen fixation estimate is an average value for North Atlantic between 10°N and 50°N.) (Modified from McGuillicuddy *et al.*, 1998)

5.2 Model Investigation of the Nutrient Supply to the Euphotic Zone

I added a simple biological model to the Planetary Geostrophic Ocean Model (PGOM) of Samelson and Vallis (1997b) to investigate the sources of nutrients that sustain export production. In particular, the potential influence of dissolved organic matter on the system is examined. In view of the lack of DON measurements, it is not possible to give conclusive results. However, the idealised model allows the possible effect of DON on the system to be investigated. The PGOM is described in Appendix A.

5.2.1   Biological Model

It is assumed in the biological model that nitrogen is the limiting nutrient. There-
fore, only nitrogen is carried in the model. Total nitrogen is equal to $\mathcal{N}$ (total
inorganic nitrogen) plus PON (particulate organic nitrogen) and DON (dissolved
organic nitrogen). Total nitrogen is conserved in the model. Total inorganic ni-
trogen, $\mathcal{N}$, is defined as,

$$\mathcal{N} \;=\; NO_3^- + NO_2^- + NH_4.$$

Oceanic dissolved organic matter can be split into 3 pools: a) a labile pool
with a fast turnover time of days or less; b) a semi-labile pool with turnover
time of seasons; and c) a refractory pool with very long timescales of centuries
or more (Kirchman *et al.*, 1993). Only the semi-labile pool has a timescale that
will have an impact on new production. Therefore, only the semi-labile pool is
modelled.

$\mathcal{N}$ and DON are carried in the model and have the following governing equa-
tions,

$$\frac{\partial \mathcal{N}}{\partial t} + \nabla \cdot (\mathbf{u}\mathcal{N}) \;=\; \kappa_v \frac{\partial^2 \mathcal{N}}{\partial z^2} + \kappa_h \nabla_h^2 \mathcal{N} + S_\mathcal{N}$$

$$\frac{\partial DON}{\partial t} + \nabla \cdot (\mathbf{u}DON) \;=\; \kappa_v \frac{\partial^2 DON}{\partial z^2} + \kappa_h \nabla_h^2 DON + S_{DON}$$

$S_\mathcal{N}$ and S_{DON} are the biological sources of $\mathcal{N}$ and DON. The diffusivities are
equal to the temperature diffusivities.

The biological model is very similar to the scheme used by Williams and
Follows (1998a). Only the net effect of photosynthesis and respiration is mod-
elled. Hence, nutrients are consumed in the euphotic zone and remineralised
below. The organic material created in the euphotic zone is divided into PON
and DON. It is assumed that the PON falls through the water column with
no horizontal movement and is remineralised on a timescale smaller than one

163

model timestep. Therefore in the model, the amount of nitrogen transformed into PON in the euphotic zone is remineralised directly below the euphotic zone in the same timestep. DON is remineralised everywhere at a constant specified rate. The biological model is crude but successfully models the gross effect of biology in a simple manner. The model does not explicitly include the effect of mesoscale eddies nor does the biological model include nitrogen fixation.

In the Euphotic Zone

The biological export of inorganic nutrient in the euphotic zone is expressed as a function of depth (z) as,

$$S_{\mathcal{N}}(z) = -\lambda \mathcal{N}(z) + r \, DON(z).$$

$1/r$ is the timescale of DON remineralisation. $1/\lambda$ is the timescale for the consumption of $\mathcal{N}$ during photosynthesis and varies with latitude and season. The consumption timescale mimics the effect of light intensity on biology activity; the timescale is chosen to range from 2 weeks in the summer at southern latitudes to many years in the northern latitudes in winter.

The biological source of DON is,

$$S_{DON}(z) = \gamma \lambda \mathcal{N}(z) - r \, DON(z),$$

where γ is the fraction of new production that is converted into DON. The remainder of the new production is converted into PON and falls out of the euphotic zone.

Outside the Euphotic Zone

Remineralisation occurs below the euphotic zone. The source of inorganic nutrient caused by remineralisation is given by,

$$S_{\mathcal{N}} = -\frac{\partial F(z)}{\partial z} + r \, DON,$$

where $F(z)$ is the downwards flux of PON. $F(z)$ is assumed to decrease exponentially with depth from the euphotic zone, and vanishes at the sea floor,

$$F(z) \;=\; F(-he)\frac{e^{\left(\frac{he+z}{z^*}\right)} - e^{\left(\frac{he-D}{z^*}\right)}}{1 - e^{\left(\frac{he-D}{z^*}\right)}}$$

where $-he$ is the depth of the euphotic zone, D is the depth of the model and z^* is the scale height for remineralisation. The depth of the euphotic zone is set to 87.5 m. There is a range of estimates of the remineralisation scale height in the literature. Sediment trap observations of Lohrenz et al.(1992) suggest a scale height of a few hundred metres in the Sargasso Sea. Martin et al.(1987) estimated a scale height of ~ 400 m from sediment trap data in the northeast Pacific. Jenkins (1980) combined apparent oxygen utilisation measurements with ventilation ages (calculated using tritium and ^{3}He measurements) to evaluate a remineralisation scale height of about 350 m in the Sargasso Sea. However, Jenkins (1998) calculated a scale height of only 165 m in the eastern subtropical North Atlantic using velocities derived from tritium and ^{3}He measurements. The affect of mixing was also taken into account in the calculation of the scale height by Jenkins (1998). The work by Jenkins suggests that the scale height can vary by at least 200 m within the North Atlantic subtropical gyre.

The remineralisation scale height for the PGOM experiments was set at 400 m, which was also used in the modelling study of Follows et al.(1996). Sensitivity tests of the model results to the choice of remineralisation scale height were carried out and are described in sections 5.2.5 and 5.4.5.

The PON flux at the base of the euphotic zone, $F(-he)$, is equal to,

$$F(-he) \;=\; -(1-\gamma)\lambda \int_{-he}^{0} N(z)\,dz.$$

Below the euphotic zone, the only effect on the DON concentration is a loss due to remineralisation,

$$S_{DON} \;=\; -r\,DON.$$

There are few DON measurements on which to base the model values of γ and r. Yamanaka and Tajika (1997) found that using $\gamma = 2/3$ and $1/r = 6$ months in a GCM reproduced the available dissolved organic carbon (DOC) observations in the Pacific. Similarly, Archer *et al.*(1997) found that using $1/r = 1 - 6$ months in their model reproduced observations from the Equatorial Pacific. Carlson *et al.*(1994) found seasonal variability in DOC concentrations in the Sargasso Sea which supports $1/r$ being around 6 months. Bacastow and Maier-Reimer (1991) and Najjar *et al.*(1992) both used high values of γ (0.7 and 0.8 respectively) in their GCM investigations. Hansell and Carlson (1998) analysed measurements of DOC in the Sargasso Sea and found that 59-70 % of net community production was in the DOC form. However, after the spring bloom this percentage dropped dramatically, so that on a seasonal timescale the net DOC production was only 8% of the net community production. Using DOC data from two other contrasting ocean regions, Hansell and Carlson (1998) concluded that a global average of γ was $\sim$ 17%.

In view of the large range of estimates for γ, the model was run twice with $\gamma = 1/3$ and $2/3$. A value of $1/(6 \text{ months})$ for r was used in both model runs. A control model run with no DON ($\gamma=0$) was also carried out. The total amount of nitrogen in the model was the same in all model runs.

The vertical resolution of the PGOM was increased in the euphotic zone for the biological model runs, with vertical levels every 25 m. The PGOM was run for 3000 years before the biological model was included to obtain a steady circulation. The PGOM with the biological model was then run for a further 1000 years. The results presented in this section are from a model run with the maximum Ekman pumping (we0) set to 1.6×10^{-6} ms^{-1}. When the model was run with this we0 value, a steady oscillation occurs in the density and horizontal kinetic energy of the model with a period of 6 years. To remove this model dependent signal, the results were averaged over 6 years.
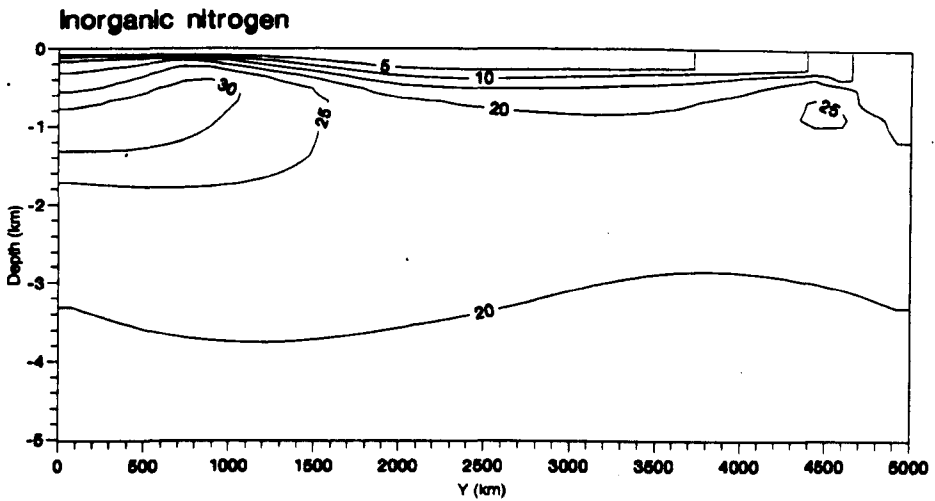
Figure 5.5: Meridional cross section at x=2500 km of the concentration of $\mathcal{N}$ (μ mol N kg^{-1}) during March. Results from model run with γ =0.

5.2.2 Nitrogen Budget of the Control Model Run

$\mathcal{N}$ Fields

The results presented in this section are from the control model run with no DON (γ=0). Figure 5.5 shows a cross section of the inorganic nitrogen concentration ($\mathcal{N}$) along the central longitude of the model during March. The lowest concentrations occur at the surface with the concentration increasing throughout the thermocline. The highest concentrations are below the highly productive tropical euphotic zone (see figure 5.7a). The high tropical concentrations are caused by the high level of export production and the upwelling of deep nutrient rich water.

The seasonal variation of surface $\mathcal{N}$ is shown in figure 5.6. The tropical surface concentration is below 0.1 μ mol N kg^{-1} for the entire year as the biota is active and consuming $\mathcal{N}$ all year round. In the subtropical and subpolar gyre, the concentrations are highest at the end of winter because photosynthesis in the

167
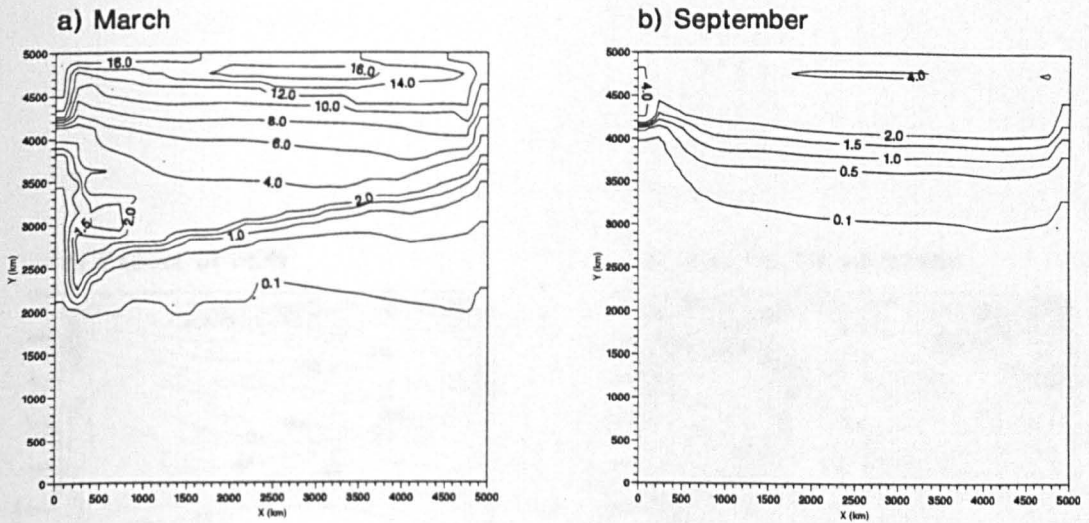
Figure 5.6: Surface concentrations of $\mathcal{N}$ (μ mol N kg^{-1}) during: a) March; and b) September. Results from model runs with $\gamma = 0$.

northern half of the model is limited by light in the winter.

Export Production

The fallout of PON from the euphotic zone (export production) is presented in figure 5.7a. Export production is highest in the subpolar gyre and tropical region reaching a maximum of 40×10^{-9} mol N m^{-2} s^{-1}(1.3 mol N m^{-2} yr^{-1}). The export of PON reduces towards the centre of the subtropical gyre with values becoming less than 1×10^{-9} mol N m^{-2} s^{-1}. The export production rates in the central subtropical gyre of the model are lower than the observed rates of 3 mol C m^{-2} yr^{-1}. The model value of 4×10^{-9} mol N m^{-2} s^{-1}is equal to ~ 1 mol C m^{-2} yr^{-1}(using a Redfield ratio, C:N of 7:1).
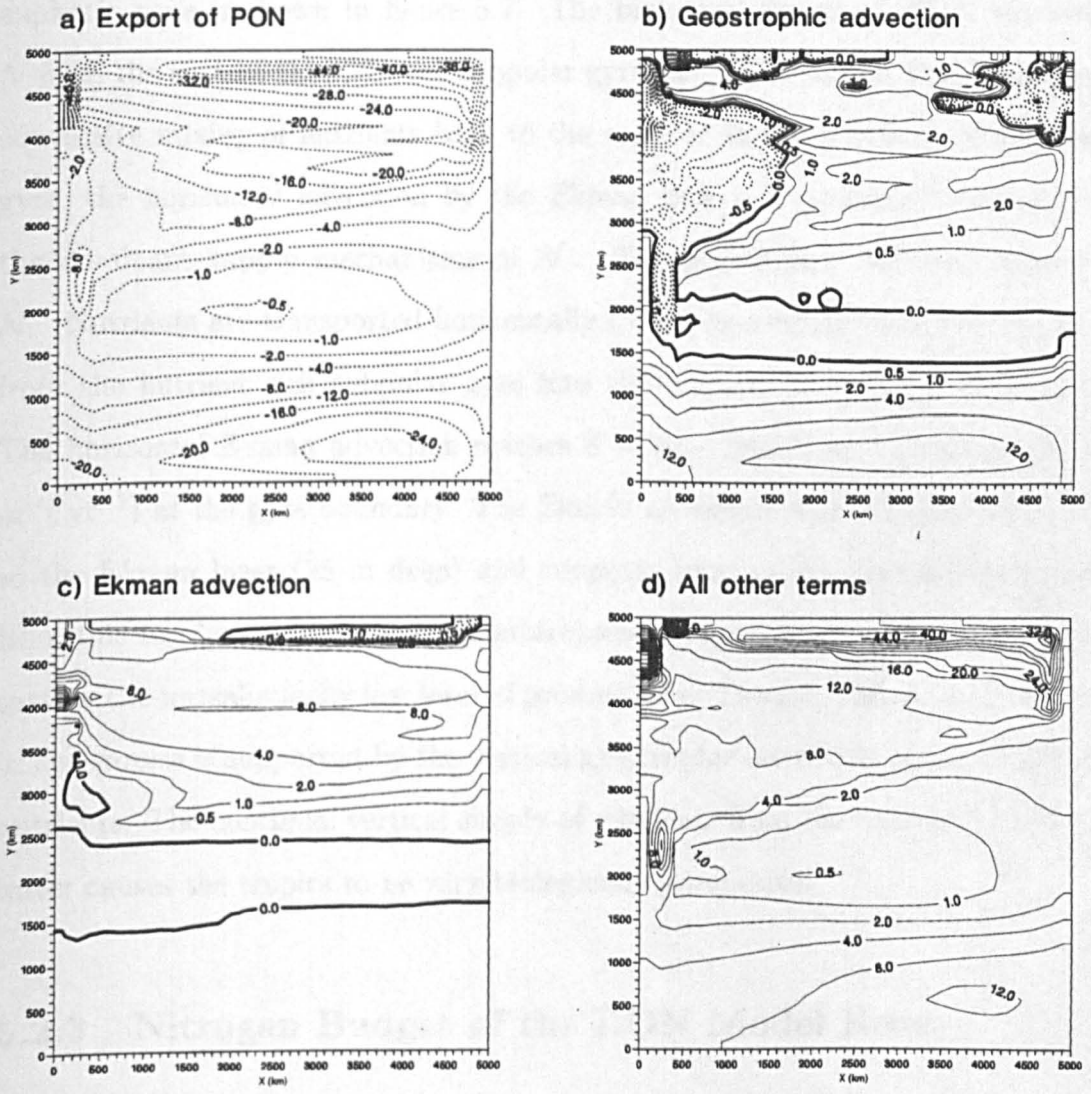
Figure 5.7: Annual mean supply of inorganic nitrogen to the euphotic zone (10^{-9} mol N m^{-2} s^{-1}) due to : a) export of PON; b) geostrophic advection; c) horizontal Ekman advection; and d) convective mixing and diffusion. Results from model runs with $\gamma = 0$. Positive values indicate a supply to the euphotic zone.

Euphotic Zone $\mathcal{N}$ Budget

The level of export production shown in figure 5.7a must be sustained by physical processes resupplying nutrients to the euphotic zone. The $\mathcal{N}$ budget for the whole euphotic zone is shown in figure 5.7. The biological export of PON removes $\mathcal{N}$ from the surface layer. In the subpolar gyre, the PON export is balanced by convective mixing of nutrients back to the surface. In the northern subtropical gyre, the horizontal advection by the Ekman flow and convective mixing are the dominant supply mechanisms of $\mathcal{N}$. The geostrophic flow also supplies $\mathcal{N}$. Nutrients are transported horizontally by the geostrophic and Ekman flow from the nutrient rich subpolar gyre into the nutrient poor subtropical gyre. The horizontal Ekman advection reaches 8×10^{-9} mol N m^{-2} s^{-1}(0.25 mol N m^{-2} yr^{-1}) at the gyre boundary. The Ekman advection only supplies nutrients to the Ekman layer (25 m deep) and supports most of the export production from this top layer. In the central subtropical gyre, vertical diffusion is able to sustain the unrealistically low level of productivity. The large export production in the tropics is supported by the vertical geostrophic advection and diffusion of nutrients. The continual vertical supply of nutrients from the nutrient rich deep water causes the tropics to be very biologically productive.

5.2.3 Nitrogen Budget of the DON Model Runs

$\mathcal{N}$ Fields

The presence of DON in the model increases the surface $\mathcal{N}$ concentration especially at the end of winter (figure 5.8). This is due to DON being remineralised in the surface. In the model with no DON, all organic matter is fluxed out of the euphotic zone in the form of PON and is remineralised below.

a) March - gamma = 1/3   **b) March - gamma = 2/3**
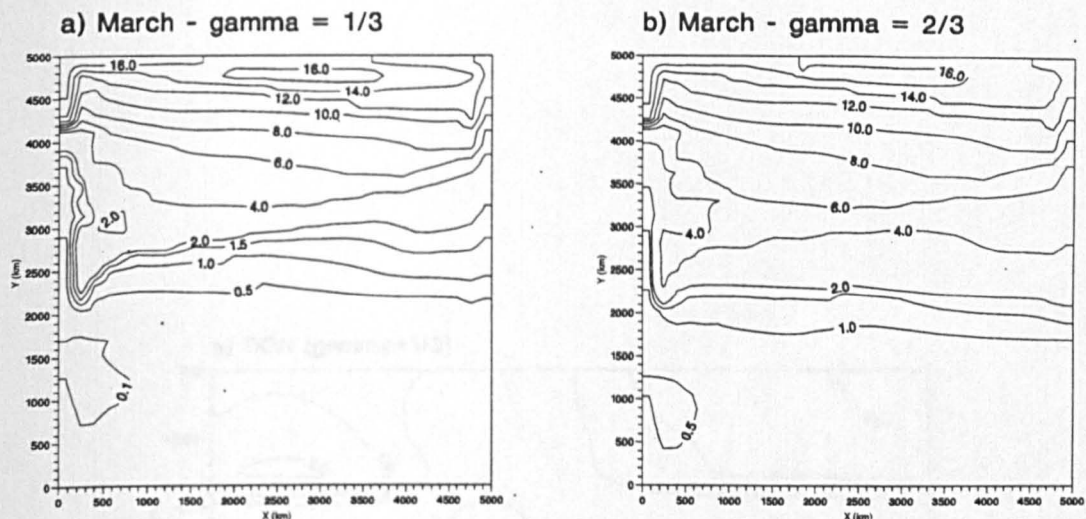
Figure 5.8: Surface concentrations of $\mathcal{N}$ (μ mol N kg^{-1}) during March for the model runs with: a) $\gamma = 1/3$; and b) $\gamma = 2/3$.

DON Fields

The magnitude of the DON concentration is very sensitive to the parameter that controls the DON fraction of new production (γ). However the general distribution pattern is unaffected by γ (figure 5.9). DON is concentrated in the surface where it is created. Deep concentrations are very low due to the short timescale of remineralisation of the semi-labile component. The highest values occur in the tropical euphotic zone. In the tropics, the high rate of biological production produces large concentrations of DON. In addition, upwelling water in the region stops the vertical removal of DON.

There are few observations of DON with which to compare the model results. Doval et al.(1997) measured DON in the Northeast Atlantic during September and found surface concentrations of ~ 6 μ mol N kg^{-1}. Hansell and Waterhouse (1997) found surface concentrations of total organic nitrogen to range between 4 and 7.5 μ mol N kg^{-1} in the Pacific. These DON measurements are for all
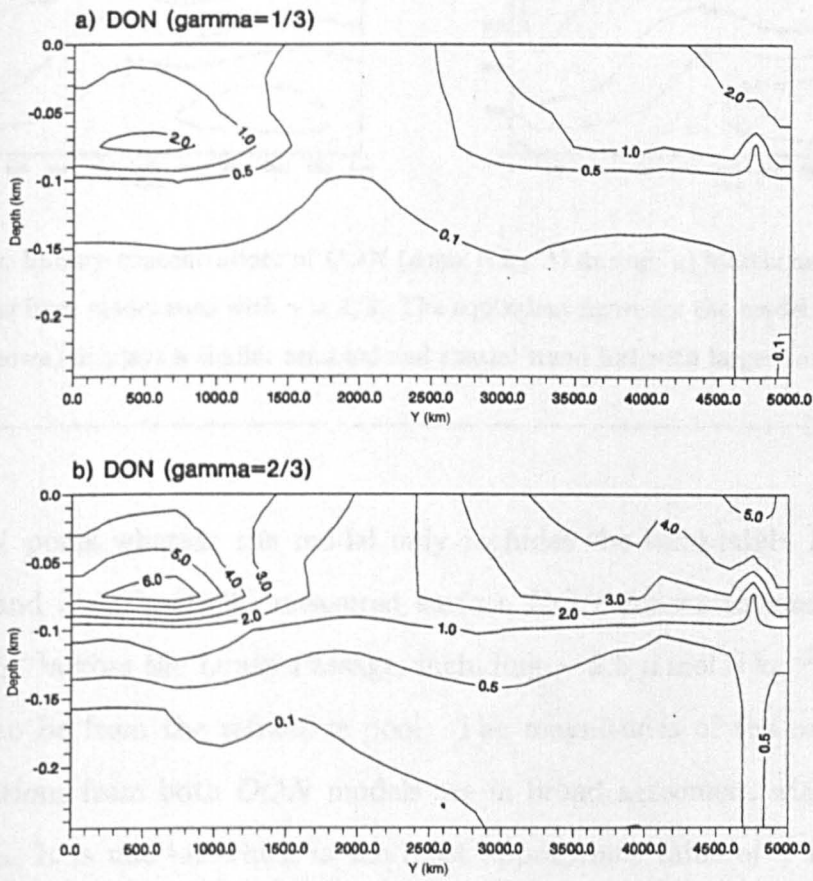
Figure 5.9: Meridional cross section at x=2500 km of the concentration of DON (μmol N kg^{-1}) during September for model runs : a) $\gamma = 1/3$; and b) $\gamma = 2/3$.
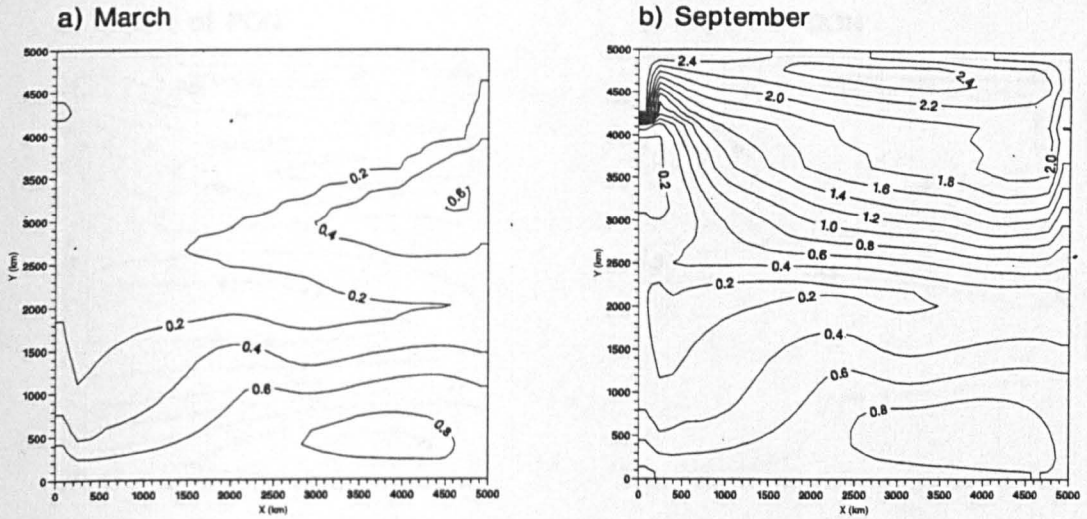
Figure 5.10: Surface concentrations of DON (μ mol N kg^{-1}) during: a) March; and b) September. Results from model runs with $\gamma = 1/3$. The equivalent figure for the model run with $\gamma = 2/3$ (not shown) displays a similar seasonal and spatial trend but with larger concentrations.

the DON pools whereas the model only includes the semi-labile DON pool. Sanders and Jickells (1999) measured surface DON concentrations of 3 - 7.5 μ mol N kg^{-1} across the Drake Passage, including $\sim$ 2.5 μ mol N kg^{-1} which they believed to be from the refractive pool. The magnitudes of the model DON concentrations from both DON models are in broad agreement with these observations. It is unclear which is the most appropriate value of γ with so few DON observations.

The surface DON concentrations have the opposite seasonal cycle to $\mathcal{N}$ with highest concentrations at the end of summer (figure 5.10). DON is produced during the spring and summer and has a lifetime of 6 months. Therefore, the highest concentrations occur at the end of summer. During the winter, DON is remineralised and the concentrations decrease. The highest DON concentrations coincide with the regions of high production (figure 5.11).

a) Export of PON **b) Export of DON**
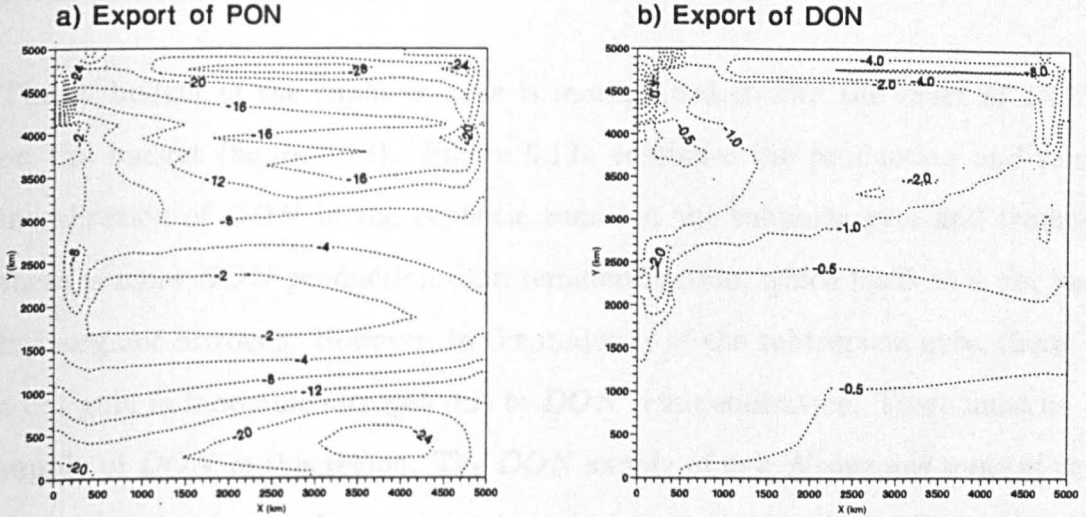
Figure 5.11: Annual mean export of organic nitrogen from the euphotic zone (10^{-9} mol N m^{-2} s^{-1}): a) in particulate form ; and b) in dissolved form. Results from model runs with $\gamma = 1/3$. Negative values indicate a loss from the euphotic zone.

Export Production

The export production of the DON models is equal to the removal of both PON and DON from the euphotic zone. The export of PON is shown in figure 5.11a for the model run with $\gamma = 1/3$. The largest production occurs in the subpolar gyre and the tropics, which is the same as the control model run with no DON. Figure 5.11b shows the export of DON due to vertical advection, vertical diffusion and convective mixing. The loss of organic material from the euphotic zone is largely dominated by sinking particulate matter. In the subpolar region, where the largest loss of DON from the euphotic zone occurs, the DON export is at most 40 % of the total export. Even in the model run with $\gamma = 2/3$, DON export contributes only approximately 25 % of the total model export. Similarly, Yamanaka and Tajika (1997) found that DOC export only contributed about 30 % to the total export production in their DOC model.

174

Euphotic Zone $\mathcal{N}$ Budget

The $\mathcal{N}$ budget of the euphotic zone is re-examined to find the effect of DON on the budget (figure 5.12). Figure 5.12b combines the production and remineralisation of DON in the euphotic zone. In the subpolar gyre and tropics, there is more DON production than remineralisation, which leads to a net loss in inorganic nitrogen. However, in the majority of the subtropical gyre, there is a net gain in inorganic nitrogen due to DON remineralisation. There must be a supply of DON in this region. The DON supply of new $\mathcal{N}$ sustains some of the export production in the central subtropical gyre, but vertical diffusion is still the dominant supply mechanism.

There must be a supply of DON to the subtropical gyre to cause the net remineralisation shown in figure 5.12b. Figure 5.13 shows the supply of DON to the euphotic zone by the different physical processes. Ekman advection is the main supplier of DON to the southern subtropical gyre. In the model run with $\gamma = 1/3$, the flux convergence reaches a maximum of 0.03 mol N m^{-2} yr^{-1}(0.8 $\times$ 10^{-9} mol N m^{-2} s^{-1}). In the model experiment with $\gamma = 2/3$, the maximum Ekman DON flux convergence increases to 0.10 mol N m^{-2} yr^{-1}. DON is formed in the highly productive tropics and advected northwards by the Ekman transport within the Ekman layer.

The geostrophic and Ekman circulation also advect DON formed in the subpolar gyre southwards into the subtropical gyre. The maximum horizontal DON advection in the northern subtropical gyre occurs away from the gyre boundary. This is in contrast to the horizontal advection of inorganic nitrogen which peaks at the boundary. This difference is caused by the longer lifetime of the semi-labile DON in the euphotic zone compared with inorganic nitrogen. This allows DON to be advected further into the subtropical gyre.

In the subpolar gyre, convective mixing redistributes DON which reduces the
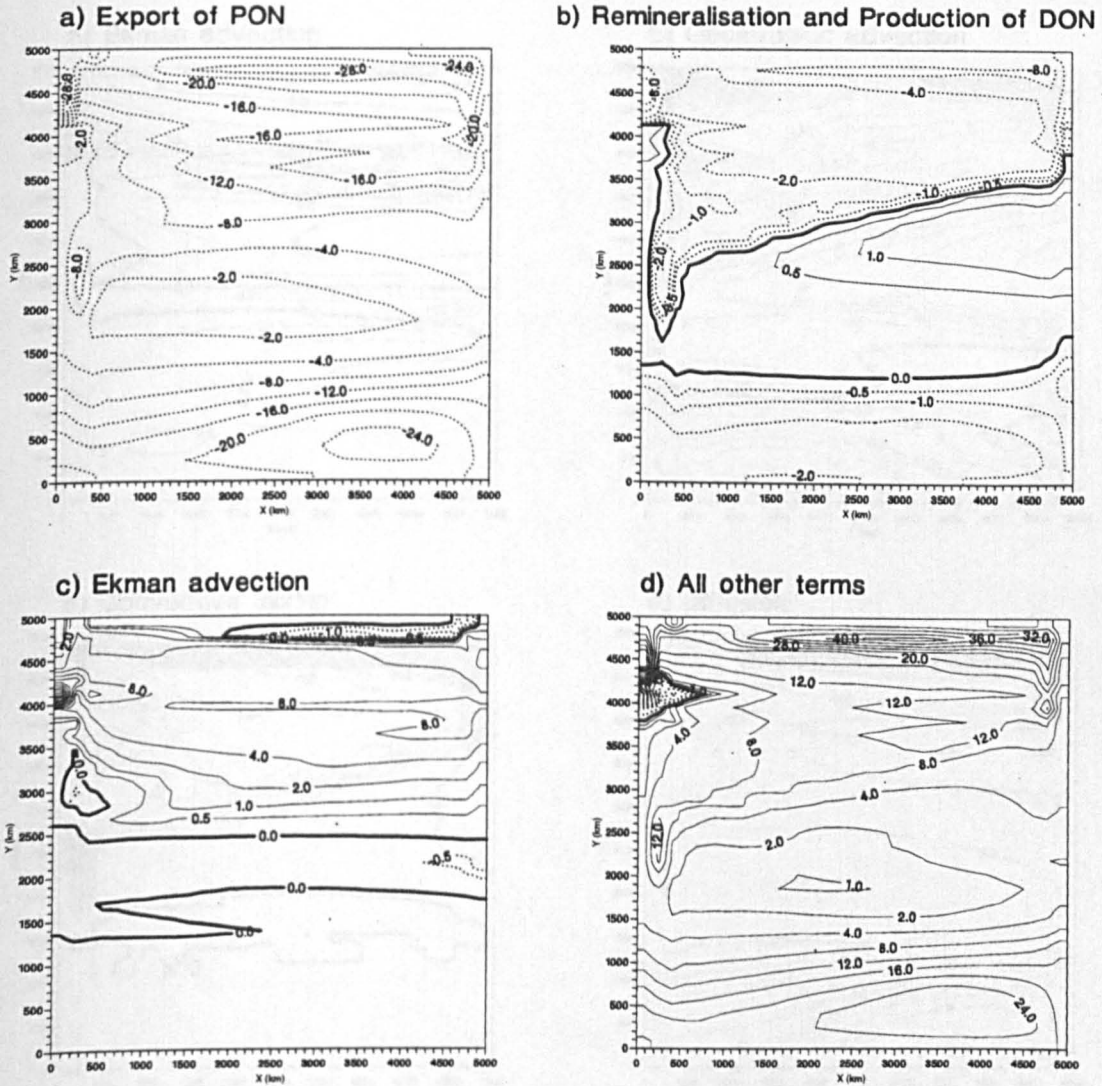
Figure 5.12: Annual mean supply of inorganic nitrogen to the euphotic zone (10^{-9} mol N m^{-2} s^{-1}) due to : a) export of PON; b) remineralisation and production of DON; c) horizontal Ekman advection; and d) all other sources (convective mixing, diffusion and geostrophic advection). Results from model runs with $\gamma = 1/3$. Positive values indicate a supply to the euphotic zone.
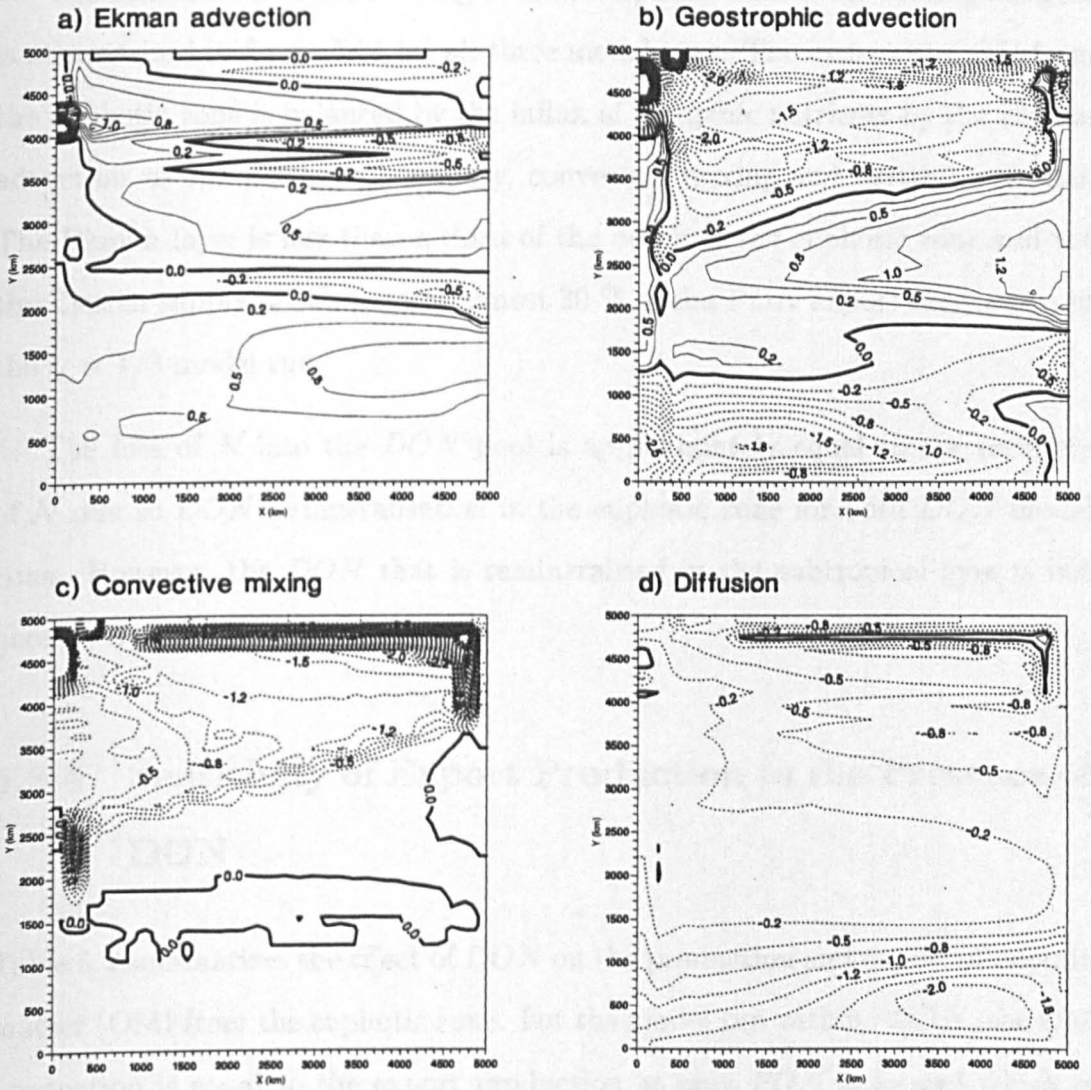
Figure 5.13: Annual mean supply of DON to the euphotic zone (10^{-9} mol N m^{-2} s^{-1}) due to : a) horizontal Ekman advection; b) geostrophic advection; c) convective mixing; and d) diffusion. Results from model runs with $\gamma = 1/3$. Positive values indicate a supply of DON to the euphotic zone.

concentration of DON in the euphotic zone. The DON formed in the euphotic zone is mixed to deeper levels where it remineralises. In the tropics, DON is removed by vertical advection and diffusion.

The annual mean nutrient budget for the euphotic zone of the subtropical gyre is summarized in figure 5.14 for all three model runs. The export of PON from the euphotic zone is balanced by the influx of inorganic nutrients by the Ekman advection at the northern boundary, convective mixing and vertical diffusion. The Ekman layer is less than a third of the depth of the euphotic zone and yet the Ekman supply of $\mathcal{N}$ supports almost 30 % of the PON export production in the $\gamma = 1/3$ model run.

The loss of $\mathcal{N}$ into the DON pool is approximately equal to the resupply of $\mathcal{N}$ due to DON remineralisation in the euphotic zone for both DON model runs. However, the DON that is remineralised in the subtropical gyre is not necessarily formed there.

5.2.4 Sensitivity of Export Production to the Presence of DON

Table 5.2 summarizes the effect of DON on the production and export of organic matter (OM) from the euphotic zone. For the model run with no DON, the OM production is equal to the export production as only PON is formed which is exported directly out of the euphotic zone. In the control model experiment with no DON, the subpolar gyre is the most productive despite the short growing season. The subtropical gyre is less than half as productive as the subpolar gyre even though the subtropical gyre is twice as large.

As γ increases, the different ocean regimes respond in different ways. In the tropics, the production of OM increases due to the larger surface $\mathcal{N}$ concentrations

a) Inorganic nitrogen

Subtropical gyre

S   N

0.2   EKMAN   EKMAN   5.5
(1.0)   N -> DON = - 9.5 (-44.2)   (8.0)
[0]   [4.2]
                               DON -> N = +9.5 (+41.0)

0   GEOSTROPHIC   GEOSTROPHIC   1.6
(-0.1)   (1.6)
[0]   [1.3]

                    PON EXPORT   GEOSTROPHIC   CONVECTION   DIFFUSION   Euphotic zone

z

y

         -19.2   -1.4   6.1   7.1
        (-22.1)   (-3.7)   (7.6)   (10.5)   Key: $\gamma = 1/3$
        [-16.0]   [-0.6]   [5.5]   [5.5]   ($\gamma = 2/3$)
                                                          [$\gamma = 0$]

b) DON

0.9   EKMAN   EKMAN   1.6
(5.0)   DON -> N = -9.5 (-41.0)   (4.2)

                               N -> DON = + 9.5 (+44.2)

0   GEOSTROPHIC   GEOSTROPHIC   0.3
(-0.2)   (-0.2)

                    GEOSTROPHIC   CONVECTION   DIFFUSION

         -1.1   -0.8   -1.0
        (-5.0)   (-2.7)   (-4.3)
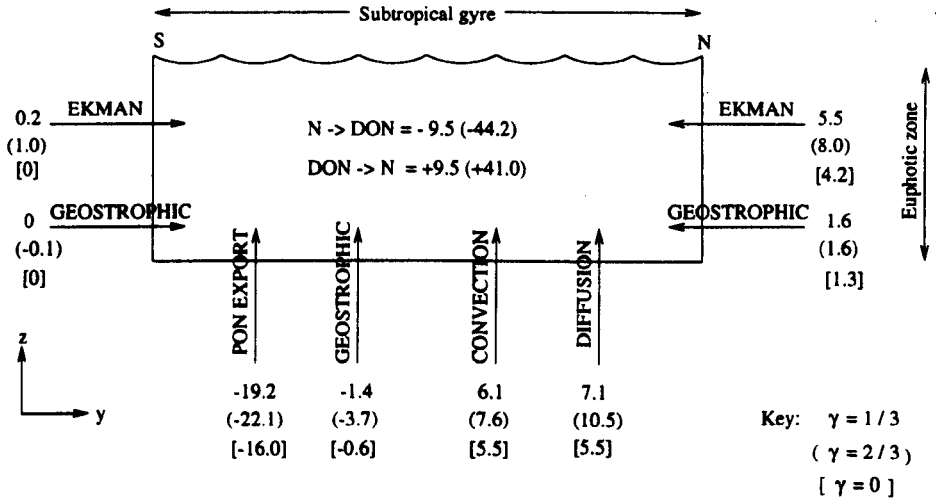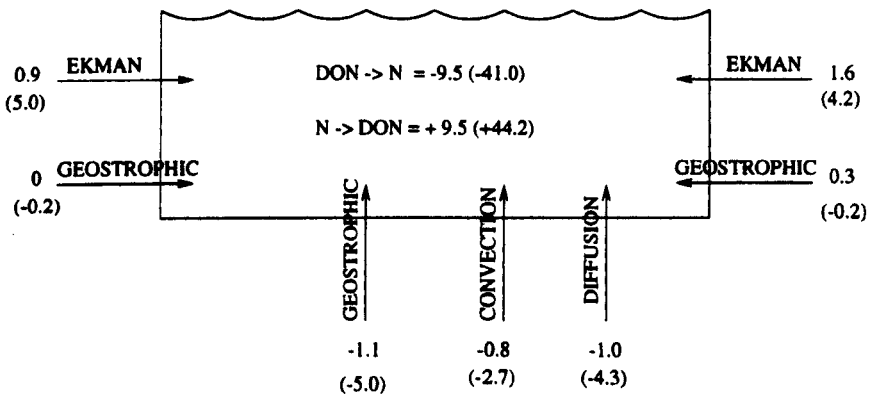
Figure 5.14: Annual mean budget of the subtropical gyre euphotic zone of: a) inorganic nitrogen; and b) DON. All values are fluxes in 10^{-2} Gt C yr^{-1} (1.2×10^{11} mol N yr^{-1}), with a positive flux acting to increase $\mathcal{N}$ or DON in the euphotic zone. 'N -> DON' is the flux of $\mathcal{N}$ caused by the transformation of $\mathcal{N}$ into DON. (Results from model run with $\gamma = 2/3$ are shown in round brackets and results from model run with $\gamma = 0$ are shown in square brackets.)

TROPICS	$\gamma=0$	$\gamma = 1/3$	$\gamma = 2/3$
Production of OM	0.26	0.39	0.69
Export of OM	0.26	0.27	0.25
SUBTROPICAL GYRE			
Production of OM	0.16	0.29	0.66
Export of OM	0.16	0.22	0.32
SUBPOLAR GYRE			
Production of OM	0.43	0.46	0.53
Export of OM	0.43	0.35	0.27

Table 5.2: Annual production of organic matter (OM) and export of organic matter from the euphotic zone for the tropics, subtropical gyre and the subpolar gyre (Gt C yr^{-1}) for the three model experiments. Note that in the model, the defined tropical and the subpolar region are both half the size of the subtropical gyre region.

as seen in figure 5.8. OM production only slightly increases in the subpolar gyre as the region is not nutrient limited (shown by the presence of nutrients in this region in September in figure 5.8). Therefore, an increase in nutrient concentrations has little effect on the subpolar region.

The greatest increase in OM production caused by the presence of DON occurs in the subtropics (with OM production being four times greater in the model run with $\gamma=2/3$ than with $\gamma =0$). This is caused by the increased fluxes of $\mathcal{N}$ into the region due to the higher $\mathcal{N}$ concentrations (as seen in figure 5.14). The increase in subtropical production is also caused by the flux of DON into the surface subtropical gyre. Figure 5.14b shows the DON budget for the subtropical gyre. There is net DON production in both the subpolar gyre and the tropics over the whole euphotic zone. Some of this excess DON is advected by the horizontal Ekman transport into the subtropical gyre as illustrated in figure 5.14b. Therefore horizontal advection supplies DON that is remineralised in

the subtropical gyre and creates new $\mathcal{N}$. DON is also vertically removed from the subtropical gyre euphotic zone by vertical geostrophic transport, convective mixing and vertical diffusion.

The inclusion of DON decreases the export production of the subpolar gyre. As the value of γ increases, more of the production is converted into DON which is then transported by the circulation and does not simply fall out of the euphotic zone as PON does in the model. The same is true for the tropics where despite the increase in OM production, the export of OM does not change with the value of γ. The presence of DON in the model increases the amount of export production in the subtropical gyre, especially in the central gyre region (comparing figures 5.11 and 5.7a). The export production in the central subtropical gyre is approximately 5 times as large in the model run with $\gamma = 2/3$ compared to the model run with no DON. In the subtropical gyre, the downwelling circulation ensures that DON is exported to the deep ocean. Therefore, the downwelling circulation and the major increase in production of OM, causes the export production in the subtropical gyre to increase with the inclusion of DON.

5.2.5   Sensitivity Test

The sensitvity of the PGOM results to the choice of remineralisation scale height (z^*) was investigated by carrying out two additional model runs with z^* equal to 200 m and 800 m. The results from these model runs were then compared with the model run with z^*=400 m. λ was set equal to 1/3 in these model runs. The effect of decreasing z^* is to increase export production from the euphotic zone (figure 5.15) which was also found by Follows *et al.*(1996). The export production in the subtropical gyre with $z^* = 200$ m is approximately double the export production with $z^* = 800$ m. Decreasing z^* causes a greater proportion of nutrients to be remineralised within the seasonal boundary layer. Convective

Figure 5.15: Export production from the subtropical gyre (Gt C yr^{-1}) against remineralisation scale height, z^* (m). Results from model run with $\gamma = 1/3$.
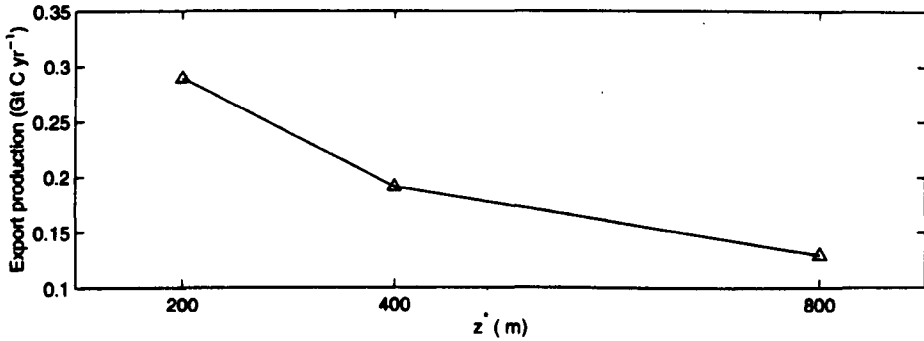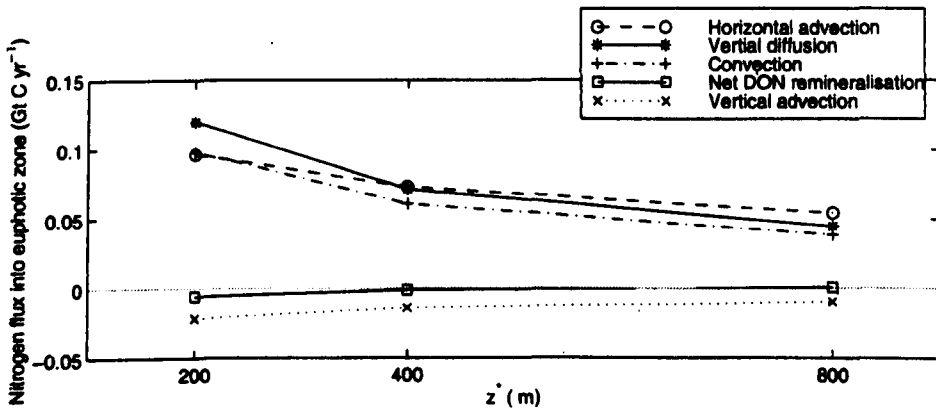

Figure 5.16: Dominant nutrient supply mechanisms to the euphotic zone of the subtropical gyre (Gt C yr^{-1}) against remineralisation scale height, z^* (m). Results from model run with $\gamma = 1/3$. These nutrient supplies support the rate of export production shown in figure 5.15.

mixing during the winter then redistributes the remineralised nutrients and increases the nutrient concentration in the euphotic zone. Although the absolute magnitude of the nutrient supply mechanisms to the euphotic zone are sensitive to z^*, the dominant balances remain unaffected (figure 5.16). Export production in the subtropical gyre is principally supported by the transport of nutrients due to horizontal advection, convective mixing and vertical diffusion regardless of the choice of z^*. Therefore, the sensitivity test shows that the main balances in the nutrient budget of the euphotic zone found in the PGOM are not sensitive to the choice of z^*.

5.2.6 Discussion

A biological model has been successfully added to the PGOM and allows the budget of inorganic nitrogen to be investigated in different ocean regimes. There are not enough DON observations available to accurately compare the model DON fields with real data. Therefore the model was run with different DON parameters and the results of all the model runs were considered.

The export production in the subtropical gyre is supported mainly by the horizontal Ekman advection of nutrients from the subpolar gyre and convective mixing. The horizontal Ekman flow transports inorganic and organic nutrients at a rate which is 37-50% of the total export production for the DON model experiments. The horizontal advection supplies nutrients that are truly external to the subtropical gyre. Convective mixing supplies a mixture of recycled and new nutrients. In the subtropical gyre, the sources of the nutrients that are supplied to the euphotic zone by convective mixing are: recycling of PON (54%); recycling of DON (19%); and advection of new nutrients (29%).

Export production is found to increase in the subtropical gyre with the inclusion of DON, principally due to an enhanced nutrient supply. The export

production in the tropics and subpolar gyre does not increase with the presence of DON, as DON is advected horizontally out of these regions. These model results highlight the potential importance of DON on the system.

While incorporating DON increases the amount of export production in the subtropical gyre, the level of export production in the central subtropical gyre is still lower than observed rates. This underestimate may be due to the lack of nitrogen fixation or the low resolution of the model that excludes the explicit representation of mesoscale eddies. The unrealistically low export production could also be due to the simplified model circulation.

5.3 The Effect of Wind Strength on Export Production

The Ekman supply of nutrients into a subtropical gyre has been shown to be significant. This Ekman supply would suggest that the amount of export production in a subtropical gyre is sensitive to the strength of the wind field. This sensitivity is now investigated with the PGOM.

5.3.1 Model Experiments

The PGOM was run with three different wind strengths, which was achieved by setting the maximum Ekman vertical velocity ($we0$), to 1.2, 1.6 and 2.0 $\times10^{-6}$ ms^{-1}. These maximum values correspond to average Ekman pumping values in the subtropical gyre of 24, 32 and 40 m yr^{-1} respectively. This range of average Ekman pumping values is seen in the North Atlantic (figure 5.17).

The PGOM was run for 3000 years without the biological model to allow the circulation to reach steady state. The biological model was then added to the
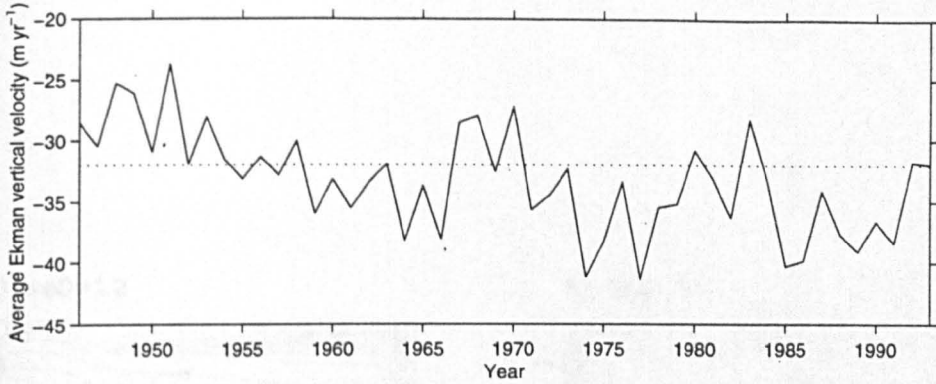
Figure 5.17: Time series of the average winter Ekman vertical velocity (m yr^{-1}) in the North Atlantic subtropical gyre (20-35 °N). Calculated using the wind stress data from the da Silva *et al.*(1994) Atlas of Surface Marine Data for the months October to April inclusive.

model and run for 1000 years. When the model was run with the higher wind speeds of we0 = 1.6 and 2.0 $\times 10^{-6}$ ms^{-1}, a steady oscillation occurred in the model with a period of 6 and 5 years respectively. To remove the effect of this oscillation, the results presented were averaged over the period of the oscillation.

5.3.2 Export Production

The export production for the different model experiments is presented in figure 5.18. Export production increases with wind strength in the subtropical gyre. There is a large increase in export production along the flanks of the subtropical/subpolar gyre boundary. Values increase from typically 12×10^{-9} mol N m^{-2} s^{-1}to 20×10^{-9} mol N m^{-2} s^{-1}between the model runs with the lowest and the highest wind speed. Values in the centre of the subtropical gyre more than double as the wind speed increases. The minimum value increases from 1.3×10^{-9} mol N m^{-2} s^{-1}to 3.0×10^{-9} mol N m^{-2} s^{-1}as we0 increases from 1.2 to 2.0×10^{-6} ms^{-1}. The net export production over the subtropical gyre is plotted against the wind strength in figure 5.19 and shows the strong relationship between export
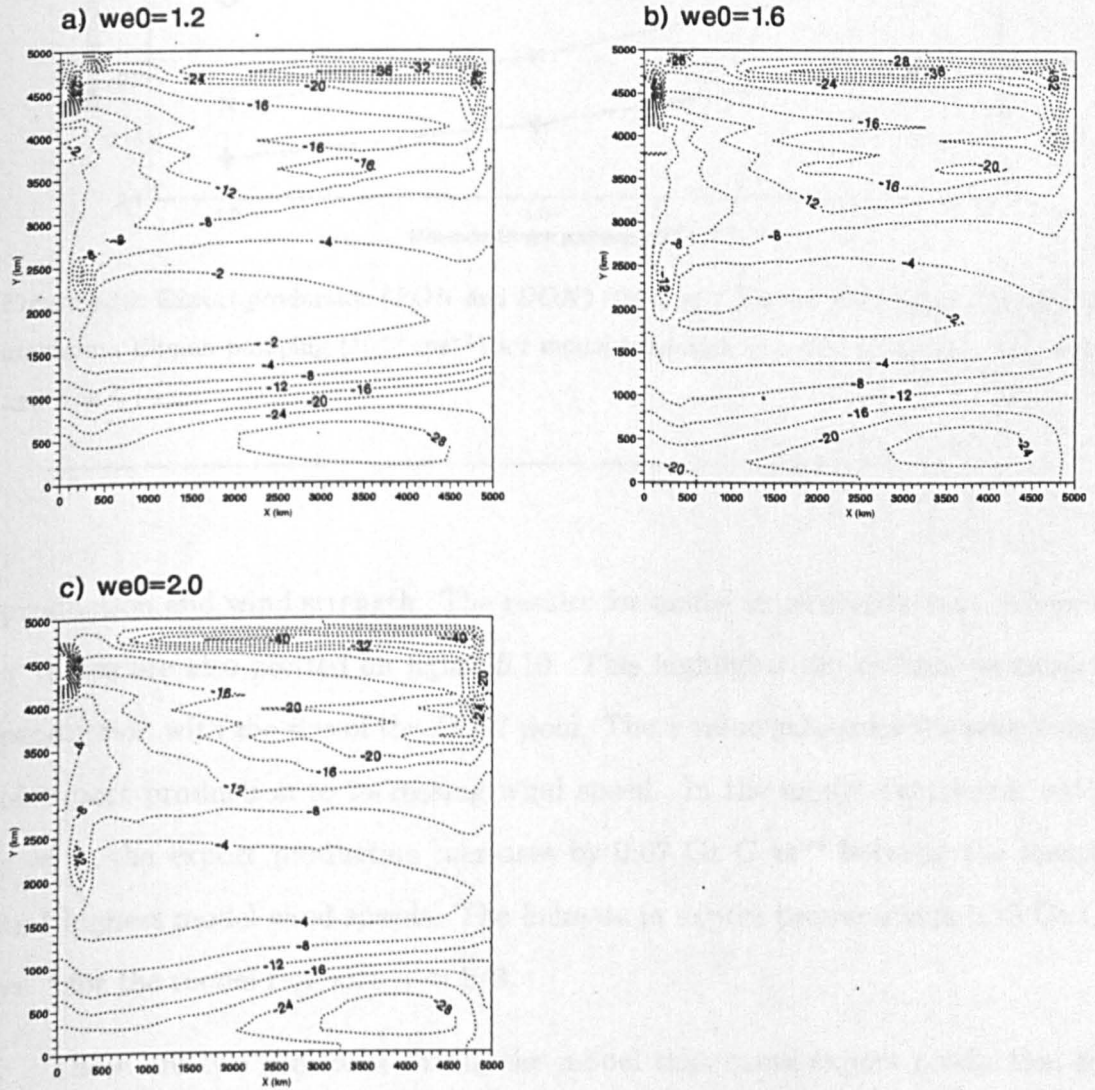
Figure 5.18: Export production (of PON and DON) (10^{-9} mol N m^{-2} s^{-1}) for model runs with the maximum Ekman pumping equal to: a) 1.2×10^{-6} ms^{-1}; b) 1.6×10^{-6} ms^{-1}; and c) 2.0×10^{-6} ms^{-1}. Results from model run with $\gamma = 1/3$.
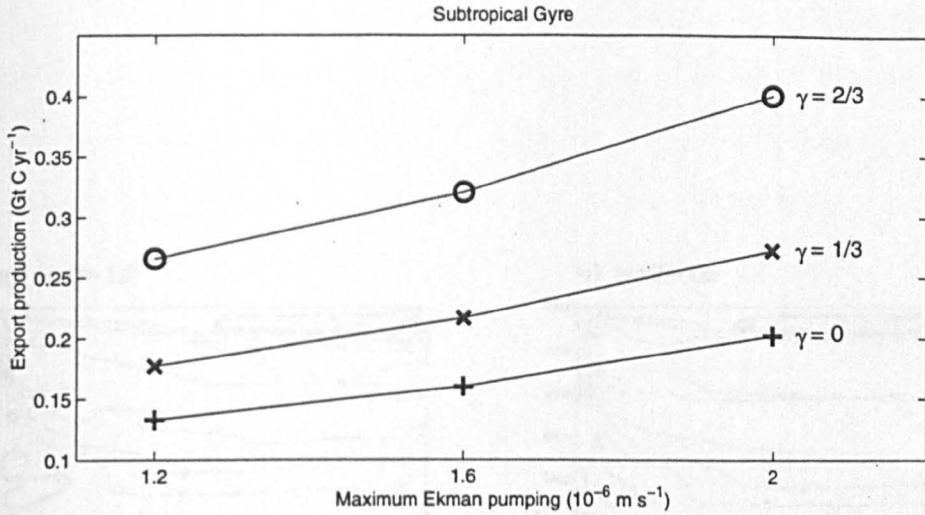
Figure 5.19: Export production (PON and DON) (Gt C yr^{-1}) in the subtropical gyre against maximum Ekman pumping (10^{-6} ms^{-1}) for model runs with $\gamma = 2/3$ (circles), $\gamma = 1/3$ (x) and $\gamma = 0$ (+).

production and wind strength. The results for model experiments with different γ values are also plotted on figure 5.19. This highlights the increase in export production with the size of the DON pool. The γ value influences the sensitivity of export production to increasing wind speed. In the model experiment with $\gamma = 0$, the export production increases by 0.07 Gt C yr^{-1} between the lowest and highest model wind speeds. The increase in export production is 0.13 Gt C yr^{-1} for the model run with $\gamma = 2/3$.

There are two processes within the model that cause export production to increase with wind strength. The first is the increase of N and DON supplied to the subtropical gyre by Ekman advection (figure 5.20). The Ekman advection of N and DON at the subtropical/subpolar gyre doubles as the maximum Ekman pumping is increased from 1.2 to 2.0 $\times$ 10^{-6} ms^{-1}.

The second reason for the relationship between export production and wind strength is the change in the convective mixing supply of N. A similar result was
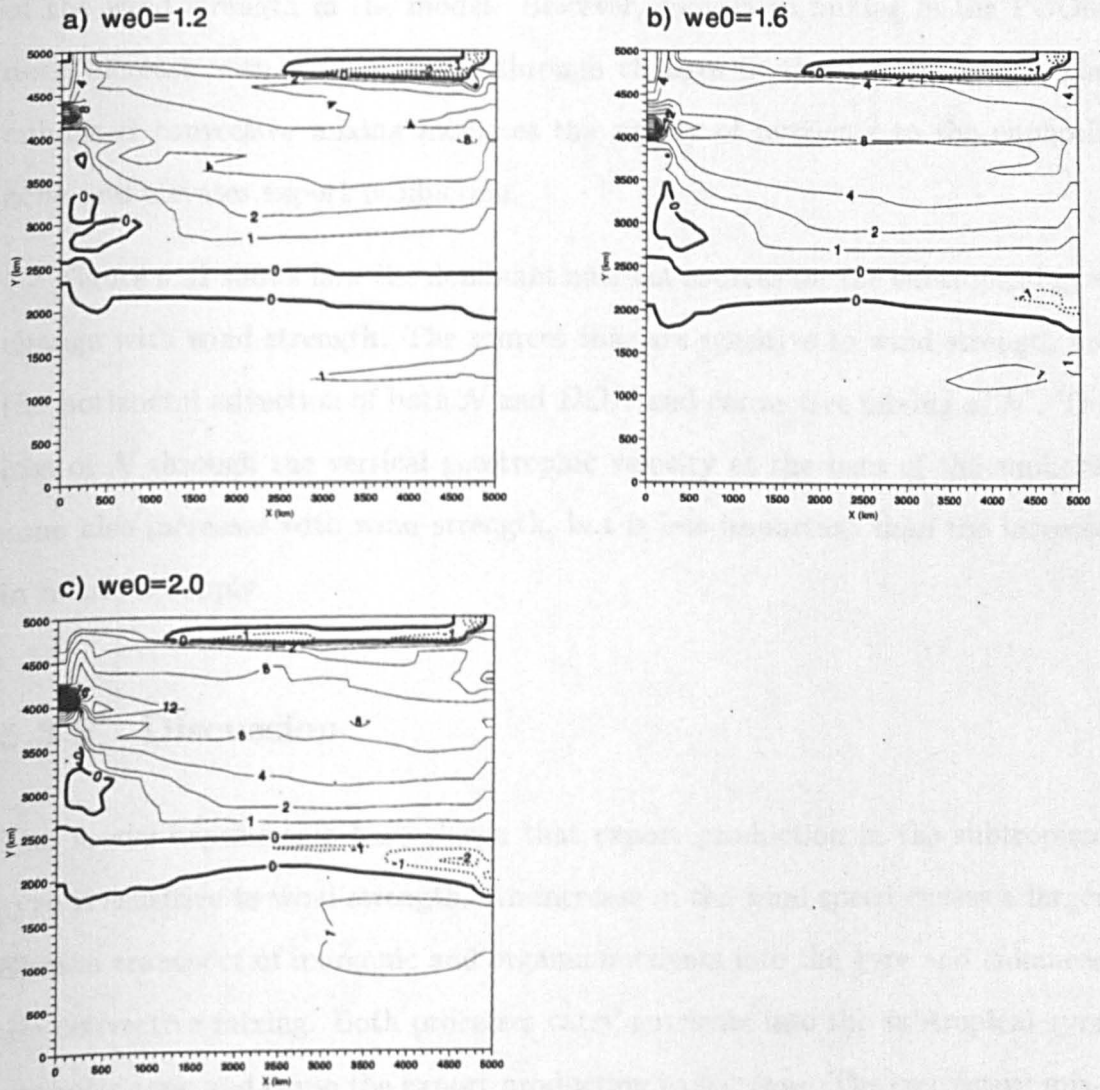
Figure 5.20: Horizontal Ekman advection of N and DON (10^{-9} mol N m^{-2} s^{-1}) for model runs with the maximum Ekman pumping equal to: a) 1.2×10^{-6} ms^{-1}; b) 1.6×10^{-6} ms^{-1}; and c) 2.0×10^{-6} ms^{-1}. Model run with $\gamma = 1/3$.

found by Follows and Marshall (1999) in a model investigation of the interannual variability of North Atlantic export production. The export production was found to vary with the North Atlantic Oscillation due to the changes in convective supply of nutrients. In the PGOM, convective mixing is not an explicit function of the wind strength in the model. However, convective mixing in the PGOM does increase with wind strength through changes in the density fields. The enhanced convective mixing increases the supply of nutrients to the euphotic zone and elevates export production.

Figure 5.21 shows how the dominant nutrient sources for the subtropical gyre change with wind strength. The sources that are sensitive to wind strength are the horizontal advection of both $\mathcal{N}$ and DON and convective mixing of $\mathcal{N}$. The loss of $\mathcal{N}$ through the vertical geostrophic velocity at the base of the euphotic zone also increases with wind strength, but is less important than the increase in nutrient supply.

5.3.3 Discussion

The model experiments have shown that export production in the subtropical gyre is sensitive to wind strength. An increase in the wind speed causes a larger Ekman transport of inorganic and organic nutrients into the gyre and enhances the convective mixing. Both processes carry nutrients into the subtropical gyre euphotic zone and cause the export production to increase. The convective mixing in the PGOM is not an explicit function of wind strength. The change in convective mixing with wind strength in the PGOM is a side effect of the system reaching a steady state with the different wind strength. An anomalous air-sea heat flux is expected to have more impact on convective mixing than an anomalous wind field.

The model experiments reveal the steady state response of export production
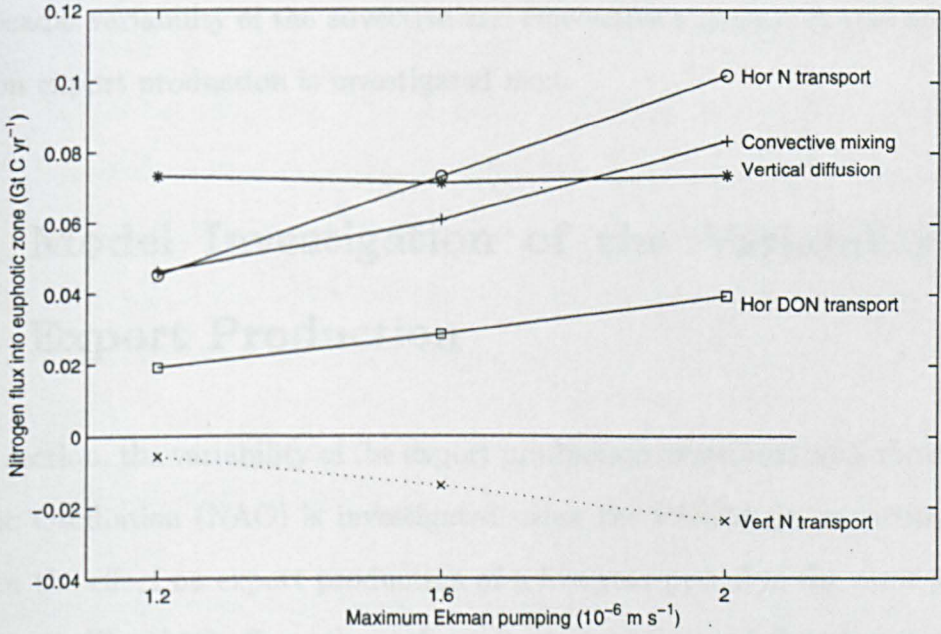
Figure 5.21: Dominant nitrogen supply mechanisms to the euphotic zone of the subtropical gyre (Gt C yr^{-1}) against maximum Ekman pumping: horizontal transport of $\mathcal{N}$ (o); convective mixing of $\mathcal{N}$ (+); vertical diffusion of $\mathcal{N}$ (*); horizontal transport of DON (□); and vertical transport of $\mathcal{N}$ (x). Results from model run with $\gamma = 1/3$. These nutrient supplies support the rate of export production shown in figure 5.19.

to changes in wind strength. Therefore, these results are only applicable to the real ocean for periods of anomalous wind strength that are long enough for the system to reach a steady state. The variability of the export production on annual and decadal timescales is of current interest due to the possible impact on the uptake of anthropogenic CO_2. The results of these steady state model experiments suggest that any variability in the advective and convective supply of nutrients will affect the variability of export production. The interannual and interdecadal variability of the advective and convective nutrients supply and the effect on export production is investigated next.

5.4 Model Investigation of the Variability of Export Production

In this section, the variability of the export production associated with the North Atlantic Oscillation (NAO) is investigated using the PGOM. In particular, we focus on the effect on export production of a five year period of the same phase of the NAO. The NAO affects the surface air-sea heat flux and the wind strength of the North Atlantic (as discussed in section 4.2.3). Anomalous heat fluxes are expected to alter the convective supply of nutrients. The anomalous wind strengths will affect the advective nutrient supply.

Follows and Marshall (1999) have used a GCM to show that export production in the subtropical gyre generally decreases in NAO+ conditions and increases during NAO- conditions. In contrast, in the subpolar gyre, the export production increases in NAO+ conditions and decreases in NAO- conditions. Follows and Marshall (1999) found that the export production sensitivity was caused by the variability of the convective mixing of nutrients. During NAO+ conditions, the anomalous surface heat fluxes cause the convective activity in the subtropical

gyre to decrease, while mixing increases in the subpolar gyre.

However, if the level of anomalous convective mixing is maintained for several years, the induced change in export production is expected to reach a constant level. For example, if the convective supply of nutrients is increased through deeper mixing, the export production will increase. The increased level of export production will supply more recycled nutrients to the winter mixed layer. These extra recycled nutrients are then convected back to the euphotic zone during the winter. Therefore to a first approximation, a closed cycle is formed with the extra export production balancing the additional convective supply of nutrients. Unless the actual amount of mixing changes, the anomalous export production is expected to remain at the same level. In contrast to the convective supply of nutrients, changes in the advective supply of nutrients could potentially cause the export production to continually increase or decrease with time.

5.4.1 Model Experiments

Three experiments were designed to investigate the effect a five year period of NAO+ conditions on the export production. To create the NAO+ conditions, the surface forcing of the PGOM was altered. The results from these experiments were then compared to a control model run with no anomalous surface forcing. Three complementary model experiments investigating NAO- conditions were also carried out.

The first NAO+ experiment was intended to isolate the effect of the changing convective mixing during NAO+ conditions. To create the change in convective mixing, the air-sea heat flux was altered (see table 5.3) by changing the temperature relaxation timescale (used in the model air-sea heat flux) during the months of October to March. To imitate NAO+ conditions, the surface heat loss during winter was increased in the subpolar gyre and decreased in the subtropi-

Model run	Max. Ekman pumping ($we0$) (10^{-6}ms^{-1})	January Mean Heat Flux (Wm^{-2})	
		Subtropical gyre	Subpolar gyre
Control	1.2	-80	-223
1. NAO+ (NAO-) heat flux only	1.2 (1.2)	-70 (-87)	-266 (-176)
2. NAO+ (NAO-) winds only	1.3 (1.1)	-80 (-79)	-223 (-224)
3. NAO+ (NAO-) heat flux and wind	1.3 (1.1)	-70 (-86)	-265 (-177)

Table 5.3: The change in the model surface forcing used to create NAO+ conditions for the three experiments. NAO- conditions are shown in brackets. A negative heat flux is directed out of the ocean. (Note that the heat flux is altered by changing the temperature relaxation scale in the air-sea heat flux equation. In model experiment 2, the temperature relaxation scale was not altered from the control run and the small change in heat flux in the NAO- experiment is caused by the circulation reacting to the anomalous wind strength.)

cal gyre relative to the control run (figure 5.22). The abnormal heat fluxes cause variations in the mixed layer depth (figure 5.23). The mixed layer in the subtropical gyre is deeper during NAO- conditions compared to NAO+ conditions and shallower in the subpolar gyre.

The objective of the second model NAO+ experiment was to investigate the sole effect of the anomalous advection caused by anomalous wind strengths during the NAO+ phase. The wind strength in the PGOM is controlled by the maximum Ekman pumping, which was increased to create NAO+ conditions (as detailed in table 5.3) and held at a constant value for the five year period.

Finally, the last NAO+ experiment combined the impact of both the anomalous convection and advection on export production during NAO+ conditions. For model experiment 3, the anomalous forcing used in model experiments 1 and 2 was combined to give the full NAO+ conditions.

DON was included in the biological model with $\gamma = 1/3$. As before, the
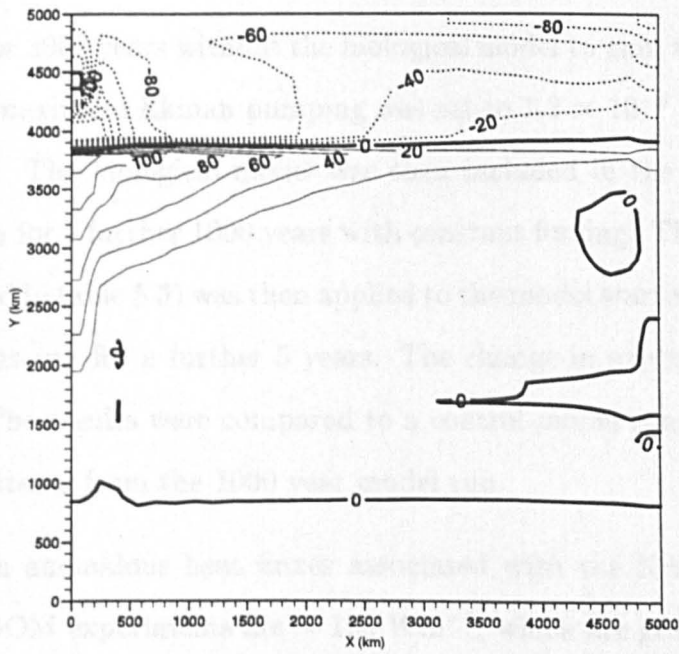
Figure 5.22: Anomalous mean air-sea heat flux (Wm^{-2}) during January for NAO+ conditions. These results were obtained during the first winter of the model experiment 1 (anomalous heat fluxes only). A positive value indicates a reduced heat loss relative to the control run.
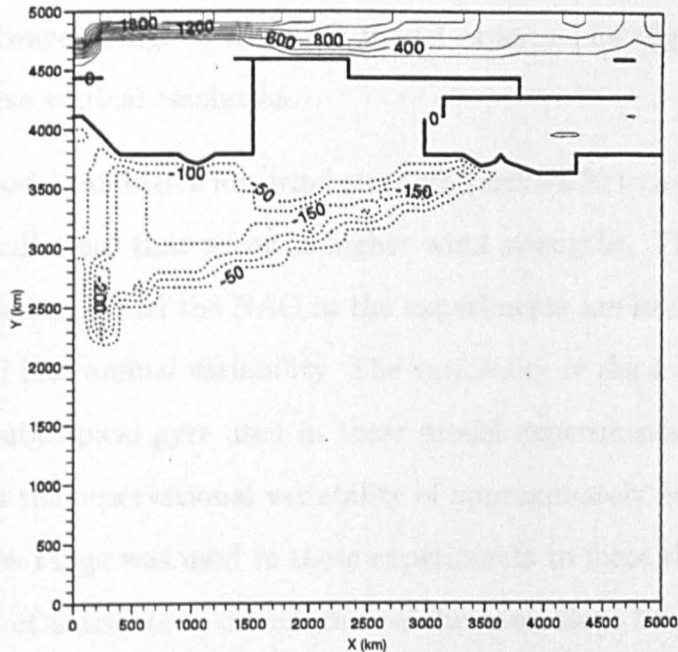
Figure 5.23: The difference between the deepest mixed layer depth during NAO+ conditions and NAO- conditions. These results were obtained from the first winter of the model experiments 1 (anomalous heat fluxes only). A positive value indicates a deeper mixed layer in NAO+ conditions relative to NAO- conditions.

PGOM was run for 3000 years without the biological model to gain a steady state circulation. The maximum Ekman pumping was set to 1.2×10^{-6} ms^{-1} for this initial model run. The biological model was then included in the PGOM, and the model was run for a further 1000 years with constant forcing. The anomalous forcing (as detailed in table 5.3) was then applied to the model starting in October and the model was run for a further 5 years. The change in export production was monitored. The results were compared to a control model run in which the forcing was not altered from the 1000 year model run.

The maximum anomalous heat fluxes associated with the NAO conditions created in the PGOM experiments are $\sim$ 100 Wm^{-2}, which are greater than the values of 30 Wm^{-2} typically found in observational data (Follows and Marshall, 1999). The larger model heat flux anomalies are necessary to force a change in the mixed layer. However, in the southern subtropical gyre, the mixed layer depth does not always change in the NAO model experiments (figure 5.23) due to the rather coarse vertical resolution.

The control model run uses a low wind strength ($we0$=1.2) to avoid the problems of steady oscillations that occur at higher wind strengths. The anomalous wind strengths used to model the NAO in the experiments are less than the observed wind speed interannual variability. The variability of the average Ekman pumping in the subtropical gyre used in these model experiments is 4 m yr^{-1}. This is lower than the observational variability of approximately 10 m yr^{-1} (figure 5.17). This low range was used in these experiments to force the anomalous convective supply of nutrients to dominate over the anomalous advective supply during the first year of the model experiments; this ensures agreement with the more realistic modelling study of Follows and Marshall (1999). Therefore, the quantitative results from these model experiments are not reliable. However, the experiments allow the trends in export production to be examined.

Process	Subtropical gyre supply	Subpolar gyre supply
Advection	0.94	1.88
Convective mixing	0.47	5.72
Diffusion	0.00	0.13
Production of PON	-1.63	-6.72
Production of DON	-0.82	-3.36
Remineralisation of DON	1.03	2.35

Table 5.4: The annual mean supply of inorganic nutrients to the Ekman layer by different physical and biological processes for the subtropical and subpolar gyre (10^{-9} mol N m^{-2} s^{-1}). Results from the control run.

5.4.2 Nitrogen Budget for the Control Model Run

The inorganic nutrient budget for the subtropical gyre and subpolar gyre for the control run is shown in table 5.4. Under control conditions, the export production in the subtropical gyre is principally maintained by the advection of nutrients. In contrast, the convective supply term is the most important in the subpolar gyre.

5.4.3 Anomalous Export Production in the Subtropical Gyre

The time series of the annual mean export production from the subtropical gyre Ekman layer for each model experiment is shown in figure 5.24. The anomalous forcing starts in year 1. The effect of changing the air-sea heat flux to NAO+ conditions is to rapidly decrease export production in the subtropical gyre by 9% during the first year (figure 5.24a). The export production remains at the same level during the second year and then gradually increases over the final 3 years of the model run. After 5 years, the export production is still lower than
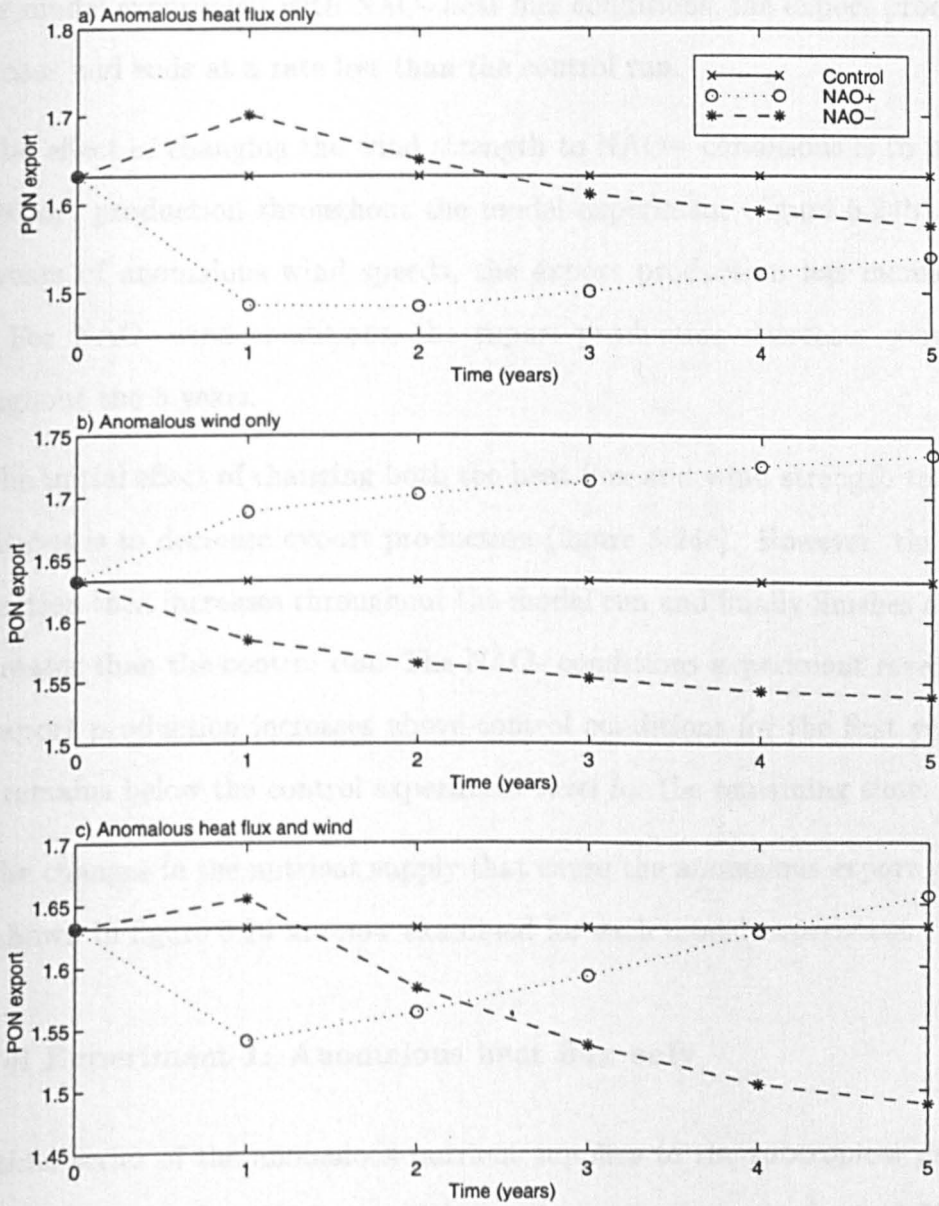
Figure 5.24: Time series of the annual export of PON from the Ekman layer of the subtropical gyre (10^{-9} mol N m^{-2} s^{-1}) for the model experiments: a) with NAO+ (circles) and NAO- (stars) heat flux conditions (model experiment 1); b) with NAO+ (circles) and NAO- (stars) wind conditions (model experiment 2); and c) with NAO+ (circles) and NAO- (stars) heat flux and wind conditions (model experiment 3). The control model results are shown by crosses. The anomalous conditions start during year 1.

the control run. When the air-sea heat flux is changed to NAO- conditions, the export production increases during the first year. Over the remaining 4 years of the model experiment with NAO- heat flux conditions, the export production decreases and ends at a rate less than the control run.

The effect of changing the wind strength to NAO+ conditions is to increase the export production throughout the model experiment (figure 5.24b). After five years of anomalous wind speeds, the export production has increased by 6%. For NAO- wind conditions, the export production decreases continually throughout the 5 years.

The initial effect of changing both the heat flux and wind strength to NAO+ conditions is to decrease export production (figure 5.24c). However, the export production then increases throughout the model run and finally finishes at a rate 2% greater than the control run. The NAO- conditions experiment reveals that the export production increases above control conditions for the first year, but then remains below the control experiment level for the remaining time.

The changes in the nutrient supply that cause the anomalous export production shown in figure 5.24 are now examined for each model experiment.

Model Experiment 1: Anomalous heat flux only

The time series of the anomalous nutrient supplies to the subtropical gyre Ekman layer for the first NAO+ model experiment is shown in figure 5.25. The initial change in export production is caused by a change in the convective supply of nutrients. The reduced heat loss over the subtropical gyre in NAO+ conditions decreases the amount of convective mixing. In contrast, convective mixing increases in NAO- conditions due to the enhanced heat loss.

The change in convective mixing is presented in figure 5.26, which shows that the amount of anomalous convective mixing does not stay constant during the
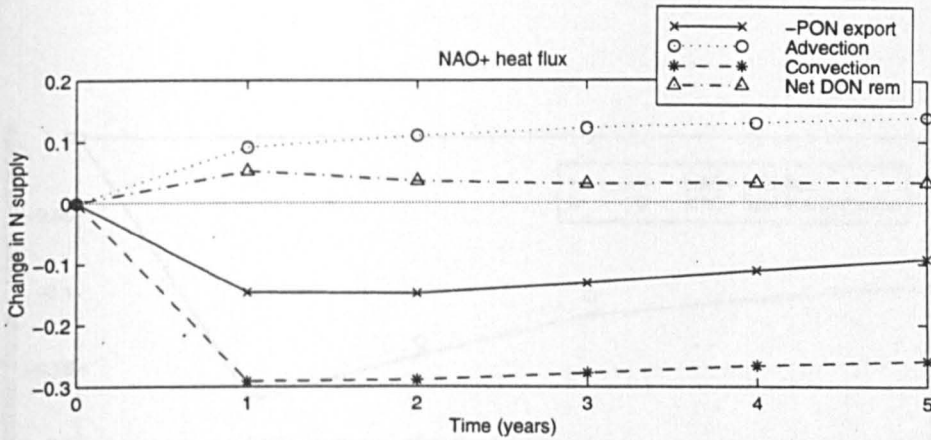
Figure 5.25: Time series of the change in the annual mean nutrient supply to the subtropical gyre Ekman layer (10^{-9} mol N m^{-2} s^{-1}) for NAO+ heat flux conditions (model experiment 1) by: advection (circles); convection (stars); net DON remineralisation (triangles); and -export of PON (crosses) relative to the control model run. Net DON remineralisation is defined as the amount of nutrients gained through remineralisation minus the amount of nutrients lost to DON production.

model experiment. The model circulation reacts to the changing surface forcing such that the amount of convective mixing changes during each year. During the NAO+ heat flux experiment, the amount of convective mixing always remains below the level of mixing in the control run. However, the greatest anomaly in convective mixing occurs during the first year and the anomaly decreases throughout the model run. This causes the anomalous convective supply of nutrients to decrease relative to the first year in the heat flux experiment (figure 5.25).

The advective supply of nutrients also changes in the heat flux experiments. The advective supply increases in NAO+ conditions and decreases in NAO- conditions. The change in advective supply is caused by anomalous nutrient concentrations in the subpolar gyre. The greater heat loss over the subpolar gyre in the NAO+ experiment causes greater convective mixing which increases the surface nutrient concentration (figure 5.27). The higher nutrient concentrations in the
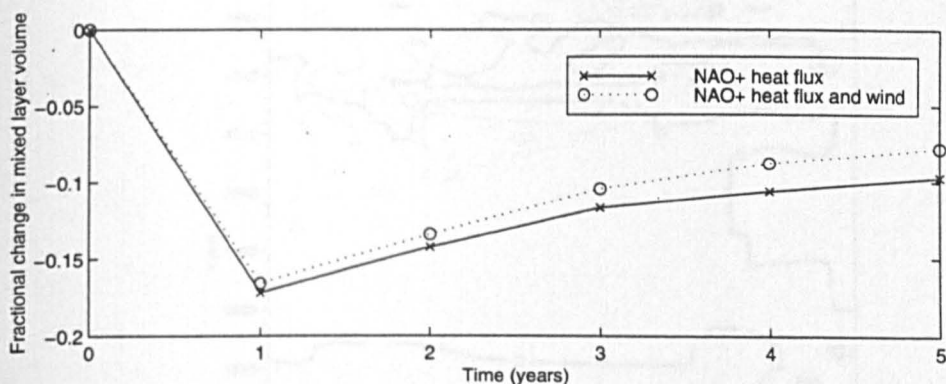
Figure 5.26: Time series of the fractional change in the volume of the deepest mixed layer in the subtropical gyre for NAO+ model experiment 1 (crosses) and NAO+ model experiment 3 (circles) relative to the control run.

subpolar gyre, increase the horizontal advection of nutrients into the subtropical gyre. The opposite situation occurs in NAO- conditions.

The anomalous advective nutrient supply has the opposite effect on export production than the anomalous convective supply during NAO conditions. In the NAO+ experiment, the anomalous convective supply is always greater than the anomalous advective supply, therefore, the export production remains lower than the control run. However, in the NAO- experiment, the anomalous advective supply becomes greater than the convective supply in year 3, and the export production becomes anomalously low.

The change in the nutrient supply due to net DON remineralisation for model experiment 1 is small relative to the change in convective and advective supply (figure 5.25). (Net DON remineralisation is defined as the amount of inorganic nutrients gained from DON remineralisation minus the amount lost due to DON production). For NAO+ model experiment 1, the amount of inorganic nutrients supplied through DON increases during the first year. This is due to the decrease
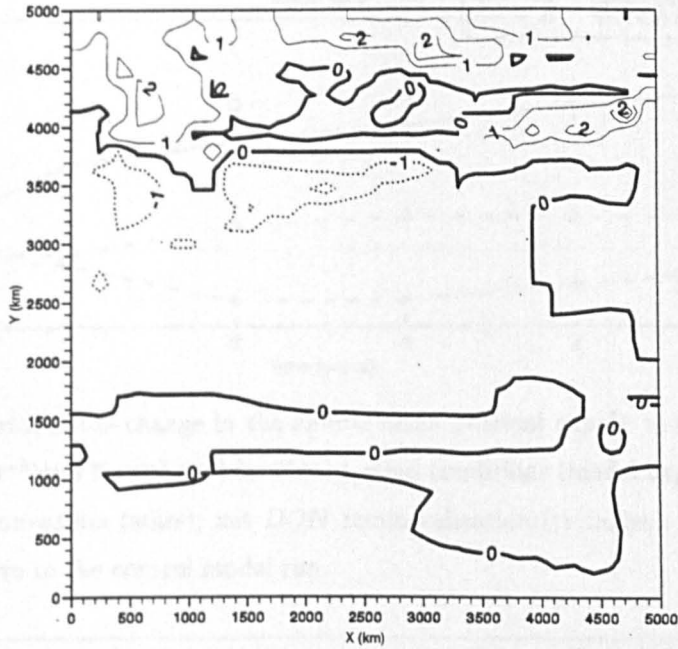
Figure 5.27: Difference in the surface nitrogen concentrations (μ mol N kg^{-1}) at the beginning of February for the first year of NAO+ model experiment 1 relative to the control run. A positive value indicates a higher nitrogen concentrations in NAO+ conditions.
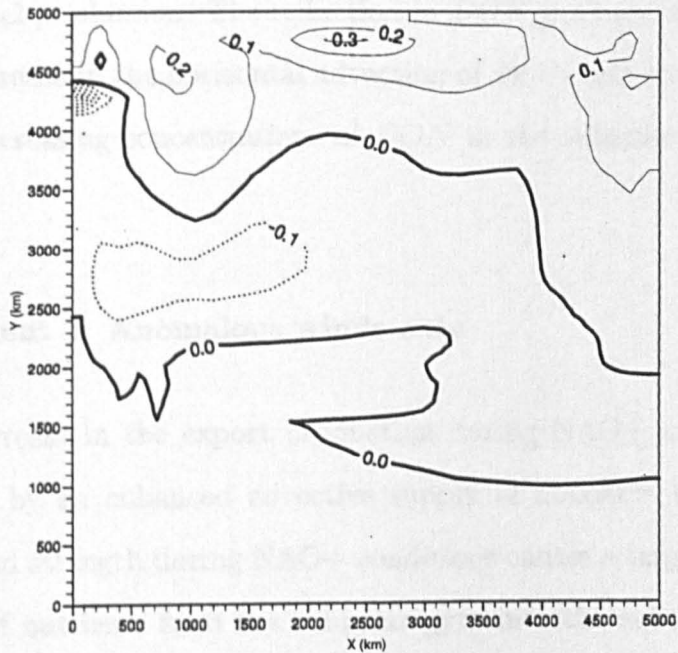
Figure 5.28: Difference in the surface DON concentrations (μ mol N kg^{-1}) at the beginning of September for the first year of NAO+ model experiment 1 relative to the control run. A positive value indicates a higher DON concentrations in NAO+ conditions.

Figure 5.29: Time series of the change in the annual mean nutrient supply to the subtropical gyre Ekman layer (10^{-9} mol N m^{-2} s^{-1}) for NAO+ wind conditions (model experiment 2) by: advection (circles); convection (stars); net DON remineralisation (triangles); and -export of PON (crosses) relative to the control model run.

in biological production causing less DON to be formed. However, after year 1, the nutrient supply due to DON remains approximately constant despite the change in biological production. The reduction in DON production is balanced by a continual increase in the horizontal advection of DON into the subtropical gyre caused by increasing concentrations of DON in the subpolar gyre (figure 5.28).

Model Experiment 2: Anomalous winds only

The continual increase in the export production during NAO+ model experiment 2 is caused by an enhanced advective supply of nutrients (figure 5.29). The increased wind strength during NAO+ conditions causes a larger horizontal Ekman transfer of nutrients from the subpolar gyre into the subtropical gyre. Similarly, there is an ongoing decrease in export production under NAO- wind conditions, caused by a decreasing advective nutrient supply.

The change in convective nutrient supply during the model experiment 2 is
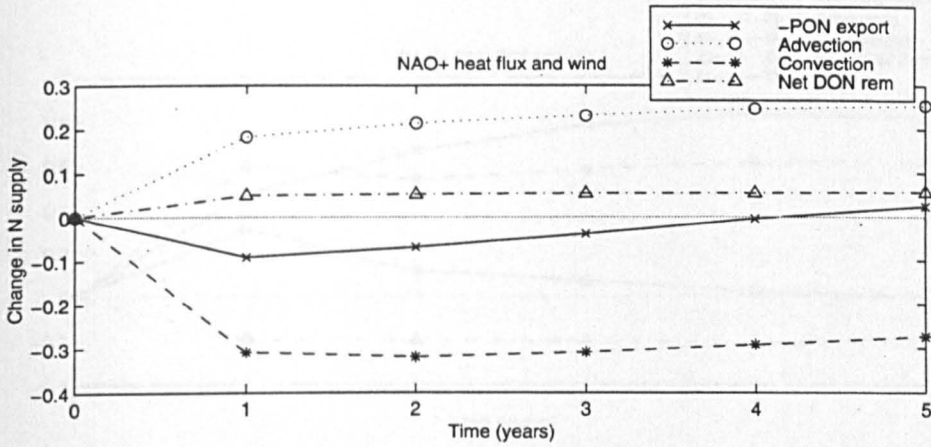
Figure 5.30: Time series of the change in the annual mean nutrient supply to the subtropical gyre Ekman layer (10^{-9} mol N m^{-2} s^{-1}) for NAO+ heat flux and wind conditions (model experiment 3) by: advection (circles); convection (stars); net DON remineralisation (triangles); and -export of PON (crosses) relative to the control model run.

small relative to the change in advective supply. The contribution of DON remineralisation is also small, but from year 2 onwards it acts in the same direction as the advective supply of inorganic nutrients. This is because the advective supply of DON from the subpolar gyre is similarly affected by the anomalous wind strength.

Model Experiment 3: Anomalous heat flux and winds

The change in export production during the first year is caused by anomalous convective mixing of nutrients (figure 5.30). The results for the first year therefore follow those of model experiment 1. The change in advective supply of nutrients opposes the change in convective supply. In the NAO+ conditions experiment, the convective supply slightly increases during years 2 to 5, relative to year 1, as the amount of convective mixing increases (figure 5.26). The advective supply continues to increase throughout the model run. In the final year, the advective supply causes the export production to be higher than the control run.
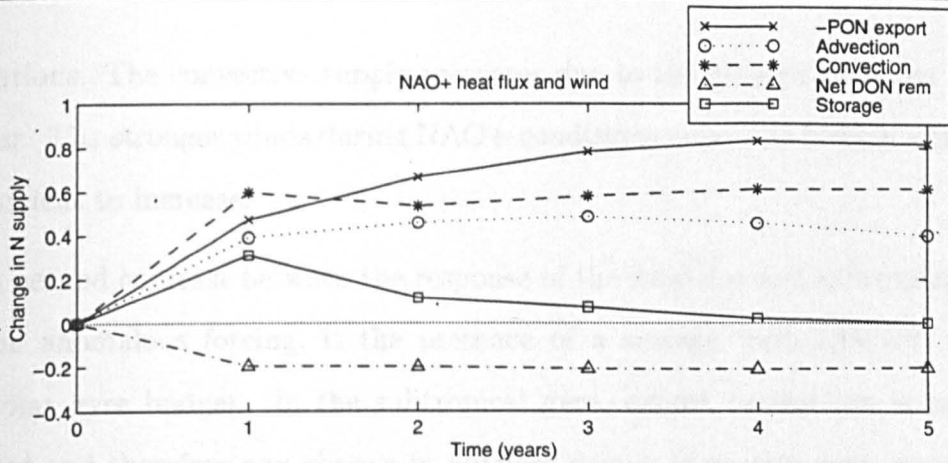
Figure 5.31: Time series of the change in the annual mean nutrient supply to the subpolar gyre Ekman layer (10^{-9} mol N m^{-2} s^{-1}) for NAO+ heat flux and wind conditions (model experiment 3) by: advection (circles); convection (stars); net $DON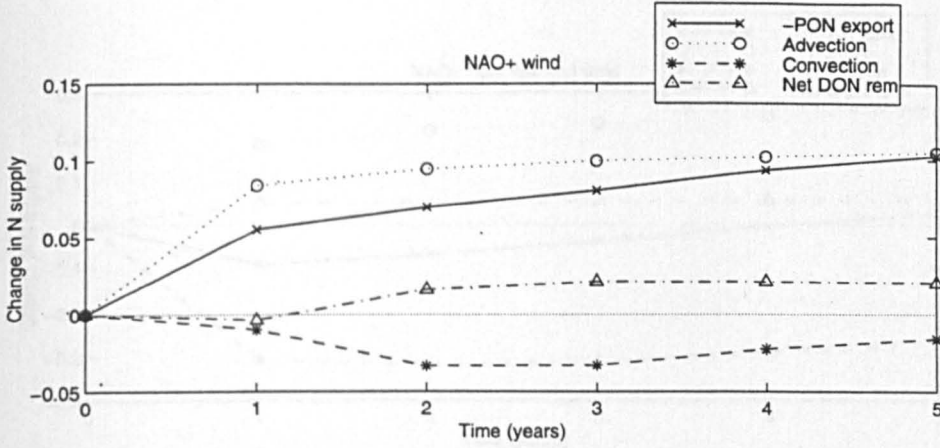$ remineralisation (triangles); and -export of PON (crosses) relative to the control model run. Also shown is the storage term ($\partial N / \partial t$) (squares).

In the NAO- conditions experiment, the anomalous convective mixing decreases during years 2 to 5 while the anomalous advection supply remains approximately constant. This leads to the export production becoming less than the control run in year 2.

5.4.4 Anomalous Export Production in the Subpolar Gyre

Only the results from model experiment 3 are discussed for the subpolar gyre. The export production of the subpolar gyre continually increases over the five year period during NAO+ conditions (figure 5.31) and continually decreases during NAO- conditions.

The change in nutrient supply to the subpolar gyre is shown in figure 5.31. Unlike the situation in the subtropical gyre, both the anomalous convective and advective supply of nutrients act to increase the export production during NAO+

conditions. The convective supply increases due to the greater heat loss during winter. The stronger winds during NAO+ conditions cause the Ekman upwelling of nutrient to increase.

A second contrast between the response of the subpolar and subtropical gyre to the anomalous forcing, is the presence of a storage term ($\partial \mathcal{N}/\partial t$) in the subpolar gyre budget. In the subtropical gyre, export production is nutrient limited and therefore any change in nutrient supply is exactly compensated by an immediate change in biological production. This does not occur in the first four years of the model run in the subpolar gyre. The increase in nutrient supply during the first year of NAO+ conditions, causes the export production and the total amount of nutrients in the Ekman layer to increase. Over the rest of the · model run, the system adjusts to the new conditions such that the storage term returns to zero.

The effect of DON on the nutrient supply under NAO+ conditions is to remove nutrients. The greater production of DON is larger than the remineralisation of DON. The increased loss in DON from the subpolar gyre contributes to the gain of inorganic nutrients in the subtropical gyre due to DON remineralisation.

Similar trends but in the opposite direction are found for the NAO- conditions model experiment.

5.4.5 Sensitivity Test

The model experiments with the variable surface forcings were repeated twice with different remineralisation scale heights to investigate the sensitivity of the results to the choice of z^*. The sensitivity tests were carried out with z^* equal to 200 m and 800 m. As discussed in section 5.2.5, a reduction in the remineralisation scale height causes the export production to increase as more nutrients are

remineralised and remain in the seasonal boundary layer. When the surface forcing is changed, the magnitude of the anomalous export production is found to be sensitive to the choice in z^*. For example, in the first year of model experiment 1, the export production from the subtropical gyre decreases from 2.60 to 2.36 $\times$ 10^{-9} mol N m^{-2} s^{-1} for $z^* = 200$ m , whereas for z^* the decrease is only from 1.08 to 0.99 $\times$ 10^{-9} mol N m^{-2} s^{-1}. However, the trends in the anomalous export production and nutrient supplies in the NAO experiments are not sensitive to z^*. As PGOM is an idealised ocean model, it is the trends that are of interest and not the absolute values of the results.

5.4.6 Discussion

The PGOM has been used to investigate how a 5 year period of the same NAO phase affects export production in a subtropical and subpolar gyre. In particular, the different effects of the changes in the convective and advection supply of nutrients have been investigated. The design of the model experiments is biased to create greater anomalies in the convective supply of nutrients than in the advective supply during the first year of anomalous forcing.

Model experiment 2 was successful in isolating the effect of changing advection on export production during NAO conditions. The horizontal advection of nutrients increases during NAO+ phases and supports a higher level of export production in the subtropical gyre. The export production continually increases for the 5 year period because the advective supply continues to increase. During the NAO- experiment, the advective supply continually decreases causing the export production to reduce throughout the 5 years.

The first model experiment had mixed success in investigating the sole effect of the changing convective supply. The initial response of the export production is controlled by the anomalous convective supply. During the NAO+ experiment,

the export production decreases due to less convective mixing over the first year. The advective supply of nutrients also changes during model experiment 1. The advective change is caused by anomalous nutrient concentrations in the subpolar gyre which are advected horizontally into the subtropical gyre. During NAO+ conditions, the nutrient concentration increases in the subpolar gyre due to the enhanced mixing. Therefore, the anomalous increase in the advective supply of nutrients in the subtropical gyre acts against the anomalous decrease in the convective supply during NAO+ conditions (this is summarized in figure 5.32).

After the first year of model experiment 1, the anomalous export production reduces. This is caused by the anomalous advective supply continuing to increase or remaining constant, while the anomaly in the convective supply decreases. This is what was predicted to happen. However, the convective anomaly decreases because the actual amount of anomalous convective mixing reduces. Therefore, it is unclear what would happen if the anomalous convective mixing stayed at the same level. Although the results of this dynamical model suggest that the ocean circulation will respond to the anomalous forcing and the situation of a constant level of anomalous convective mixing is unrealistic.

The effect of changing both the wind strength and heat flux combines the results from the first two model experiments. Although the initial change in the export production is caused by anomalous convective nutrient supply, the anomalous export production after 5 years is caused by the anomalous advective supply. This occurs despite the bias in the model design towards anomalous convective mixing. The anomalous nutrient supply caused by the presence of DON acts in the same sense as the advection of inorganic nutrients. An increase in the horizontal advection of inorganic nutrients also implies that the advection of DON into the subtropical gyre will also increase.

The increase during the first year of NAO- conditions is less than the decrease in export production during the first year of NAO+ conditions. This is because

NAO + Conditions

Subpolar gyre

Greater heat loss

Stronger winds

Subtropical gyre

Less heat loss

Tropics

y

x

Subpolar gyre

Convective N supply increases
Vertical advection of N increases

Horizontal advection
of N increases

Subtropical gyre

Convective N supply decreases

Tropics
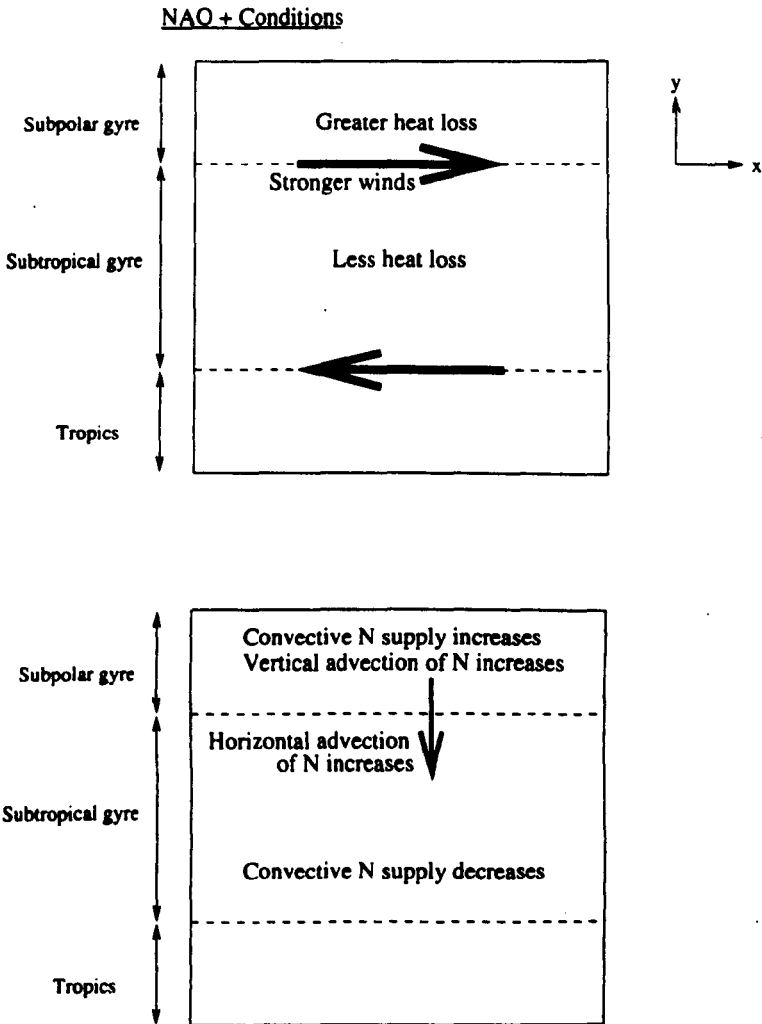
Figure 5.32: a) Schematic diagram of the changes that occur during the positive phase of the NAO: a) wind strength and air-sea heat flux; and b) the implied change in the convective and advective supply of nutrient to the euphotic zone. The opposite situation occurs during the negative phase of the NAO.

the anomalous convective mixing is greater in the NAO+ conditions experiment.

In the subpolar gyre, the anomalous advective and convective supply of nutrients are in phase with each other during NAO conditions. Both the advective and convective supply increase during NAO+ conditions and decrease during NAO- conditions (figure 5.32). The initial trend in export production is maintained for the rest of the model run. The biological production in the subpolar gyre is not nutrient limited. This causes a build up of inorganic nutrients in the Ekman layer during the first year of anomalous forcing for the NAO+ experiment. Over the remainder of the model run, the system adjusts such that the change in export production is equal to the change in nutrient supply.

5.4.7 Conclusions

The PGOM experiments suggest that any continual changes over several years in the export production of the subtropical gyre caused by the NAO will be driven by anomalous advection of nutrients. Short term changes in the subtropical gyre export production will be caused by changes in convective mixing. However, the short term impact of the anomalous convective mixing will be reduced by the anomalous advective supply which acts in the opposite direction.

5.5 Interannual Variability of the Ekman Supply of Nitrate

The interannual variability of the Ekman transport of nutrients has been shown to affect export production in a subtropical gyre. A method is now devised to calculate the time series of Ekman nitrate fluxes from available data. The method largely follows that of the climatological study of Williams and Follows

(1998a) and requires the mixed layer depth of the winter month to be known. The winter mixed layer depth cannot be obtained directly from density data for individual years, as there are only climatological density data available. To solve this problem, the mixed layer depths for the months October to April are inferred from the known heat fluxes. Two different methods are developed, one for deepening mixed layers and the second method for mixed layers that become more shallow. These methods are described next.

5.5.1 Inferring the Mixed Layer Depth - deepening mixed layers

The governing equation for density (ρ) in the mixed layer is,

$$\frac{\partial \rho}{\partial t} + \mathbf{u_h} \cdot \nabla_h \rho + w \frac{\partial \rho}{\partial z} = \frac{\rho_o}{g} \frac{\partial B}{\partial z} \tag{5.2}$$

where $\mathbf{u_h}$ is the horizontal velocity vector, w is the vertical velocity, ρ_o is a reference density and B is the buoyancy flux. Equation (5.2) is integrated with respect to z over the depth of the mixed layer (h) to give,

$$\int_{z=-h}^{0} \frac{\partial \rho}{\partial t} \, dz + \int_{z=-h}^{0} \mathbf{u_h} \cdot \nabla_h \rho \, dz = \frac{\rho_o}{g} B_0. \tag{5.3}$$

B_0 is the surface buoyancy flux and it is assumed that there is no buoyancy flux across the base of the mixed layer.

When equation (5.3) is integrated over an annual cycle, the time derivative of density must equal zero for a steady repeating annual cycle. Therefore the annual balance is,

$$\int_{year} \int_{z=-h}^{0} \mathbf{u_h} \cdot \nabla_h \rho \, dz \, dt = \int_{year} \frac{\rho_o}{g} B_0 \, dt. \tag{5.4}$$

On annual timescales, the surface buoyancy flux is balanced by horizontal advection. It is assumed that the horizontal advection is constant in time and depth

within the mixed layer. Following Williams (1987), this allows the horizontal advection to be parameterized using the annual budget expressed in equation (5.4) as,

$$\int_{z=-h}^{0} \mathbf{u_h} \cdot \nabla_h \rho \, dz = \frac{\rho_o}{g} \overline{B_0}.$$

where $\overline{B_0}$ is the annual mean surface buoyancy flux.

Therefore, equation (5.3) can be written as,

$$\int_{z=-h}^{0} \frac{\partial \rho}{\partial t} \, dz = \frac{\rho_o}{g} (B_0 - \overline{B_0}). \qquad (5.5)$$

Following the method of Follows (pers. comm.), the change in density is considered as the mixed layer deepens from $-h_1$ at time t_1 to a depth of $-h_2$ at time t_2 (figure 5.33). Firstly, equation (5.5) is integrated with respect to time between times t_1 and t_2 to give,

$$\int_{t=t_1}^{t_2} \int_{z=-h_2}^{0} \frac{\partial \rho}{\partial t} \, dz \, dt = \int_{t=t_1}^{t_2} \frac{\rho_o}{g} (B_0 - \overline{B_0}) \, dt$$

$$h_2 \rho_{m_2} - h_1 \rho_{m_1} - \int_{z=-h_2}^{-h_1} \rho(z, t_1) \, dz = \frac{\rho_o}{g} (B_0 - \overline{B_0}) \, \Delta t. \qquad (5.6)$$

ρ_{m_1} and ρ_{m_2} are the mixed layer densities at time t_1 and t_2 respectively and Δt is the time interval between t_2 and t_1.

Using the assumption that the density below the mixed layer varies linearly with depth, equation (5.6) can be rearranged to give,

$$\frac{h_2^2 - h_1^2}{\Delta t} = \frac{2}{N^2} (B_0 - \overline{B_0}), \qquad (5.7)$$

where N is the Brunt-Väisälä frequency and is defined as,

$$N^2 = -\frac{g}{\rho_o} \frac{\partial \rho}{\partial z}.$$

If $h_2 - h_1 \gg h_1$, then equation (5.7) becomes the well-known result for nonpenetrative deepening of a mixed layer (for example, Visbeck et al., 1996),

$$\frac{\partial h}{\partial t} = \frac{B_0}{N^2 h}.$$
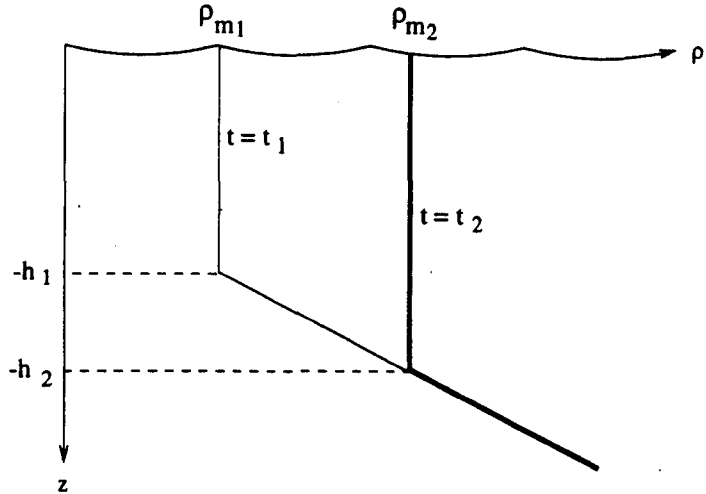
Figure 5.33: Diagram of the change in density profile from time t_1 to t_2. The thick line is the density profile at time, t_2.

For the purpose of this investigation, the surface buoyancy flux is assumed to consist purely of the air-sea heat flux and the freshwater flux is neglected,

$$B_0 = -\frac{g}{\rho_o}\frac{\alpha_T}{c_p}F_h$$

where α_T is the coefficient of thermal expansion. Therefore, equation (5.7) can be written in terms of the air-sea heat flux (F_h) as

$$\frac{h_2^2 - h_1^2}{\Delta t} = A(F_h - \overline{F_h}), \qquad (5.8)$$

where

$$A = \frac{2\alpha_T}{c_p \left(\frac{\partial \rho}{\partial z}\right)}.$$

In this study, equation (5.8) is used to predict the deepening of the mixed layer using knowledge of the surface heat loss, the stratification and an initial mixed layer depth.

5.5.2   Inferring the Mixed Layer Depth - shoaling mixed layers

Equation (5.8) becomes ill posed if there is net flux of heat into the mixed layer (i.e. the right hand side of equation 5.8 is negative). In April, large areas of the North Atlantic start to warm and the mixed layer begins to shallow. Therefore, it is necessary to be able to predict the mixed layer when there is a net heat flux into the ocean. When the mixed layer is becoming shallower, the mixed layer depth can be determined by,

$$h = 2\frac{u_*^3}{F_h/\rho c_p} \qquad (5.9)$$

(Kraus and Turner, 1967). u_*^3 is the net source of turbulent kinetic energy created by the wind and solar heating. If it is assumed that $T.K.E.$ source is constant over the summer months, then the mixed layer depth for one summer month can be inferred from the mixed layer depth of another summer month with knowledge of the heat fluxes. The mixed layer depth in July is unlikely to vary greatly from year to year, therefore, the mixed layer depth in April could be inferred from the climatological mean July mixed layer depth using

$$h^{April} = h^{July}\frac{F_h^{July}}{F_h^{April}}. \qquad (5.10)$$

This method was tested using the climatological heat flux data for April to predict April's climatological mixed layer depth. Unfortunately, the predictions were not accurate enough to be used in this analysis (as shown in figure 5.34). Therefore, it was decided that the climatological mixed layer depth would be used for points where the mixed layer shallows. The mixed layer only starts to shallow in the subtropical gyre at the end of March. Hence, this approximation will only have a small effect on the annual mean values.

a) True h - April   b) Predicted h - April
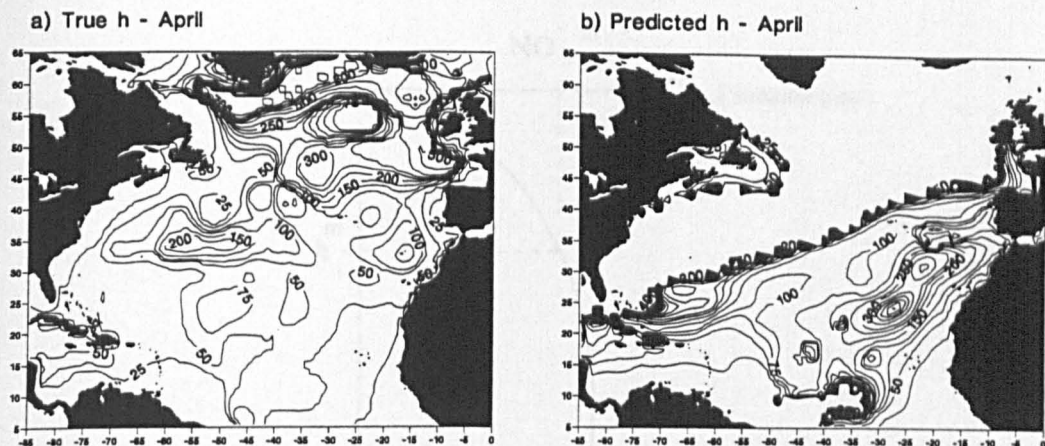
Figure 5.34: Depth of the mixed layer (m) in April: a) calculated directly from density data; and b) predicted from heat flux data using equation (5.10) where the mixed layer starts to shallow.

5.5.3   Method of Calculation

1. Monthly mixed layer depths were predicted for each winter month, October to April, for 1945 to 1993 using equation (5.8). h_1 was set equal to the climatological mixed layer depth in September. Therefore, it was assumed that the late summer mixed layer depth has no year to year variability. The monthly heat flux data was obtained from the da Silva *et al.*(1994) Atlas of Surface Marine Data. The stratification was calculated using the gradient in density across a distance of 50m below the climatological mixed layer depth. The stratification was evaluated using the climatological density data calculated using the salinity and temperature data of Levitus and Boyer (1994) and Levitus *et al.*(1994). The climatological mixed layer depth was defined as the depth where the potential density was 0.125 kg m^{-3} greater than the surface.

   If the ocean gained net heat from the atmosphere and horizontal advection, the mixed layer was set to the climatological value.

214
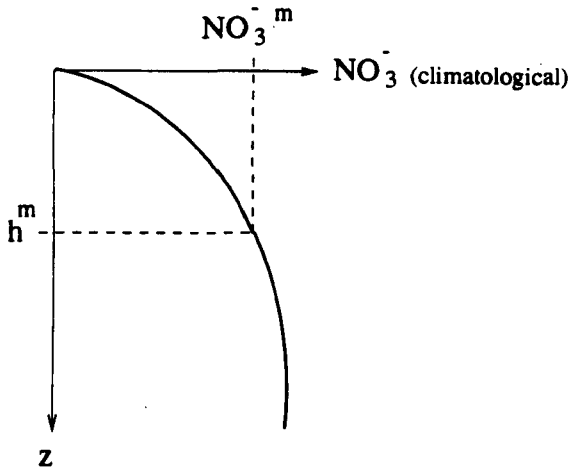
Figure 5.35: An illustration of the extrapolation method of Glover and Brewer (1988) which infers the mixed layer nutrient concentration from climatological nutrient profiles. The vertical profile is the climatological nitrate data which is biased towards summer values. h^m is the mixed layer depth during month m and $NO_3^{-\,m}$ is the inferred nitrate concentration for the mixed layer during month m.

2. The mixed layer concentrations of nitrate were obtained from the climatological data set of Conkright *et al.*(1994). These climatological nitrate data are biased to the summer months when most observations are taken. The winter mixed layer nitrate concentration was calculated from the summer-biased climatological data using the extrapolation method of Glover and Brewer (1988), where

$$NO_{3\,m}^-(x,y,t) = NO_{3\,\text{climatological}}^-(x,y,h(x,y,t)).$$

This method is illustrated in figure 5.35. The mixed layer nitrate concentration during March 1989 is shown in figure 5.36.

3. The Ekman volume fluxes were calculated from the monthly time series of wind stress from the da Silva *et al.*(1994) Atlas of Surface Marine Data.
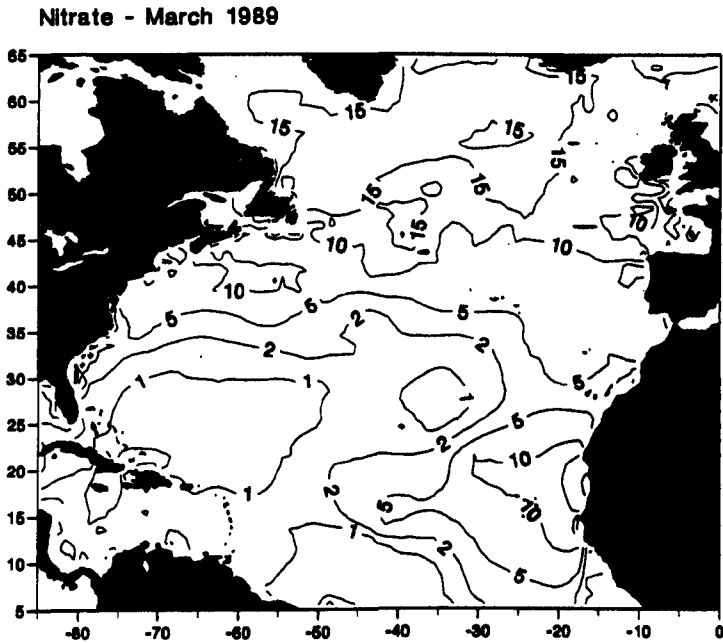
Figure 5.36: Mixed layer nitrate concentrations (μ mol N kg^{-1}) in March 1989. Calculated using the extrapolation method of Glover and Brewer (1988).

The horizontal Ekman volume flux ($\mathbf{U_e}$) is,

$$\mathbf{U_e} = (\mathbf{k} \times \boldsymbol{\tau})/(\rho_o f),$$

where f is the Coriolis parameter, $\mathbf{k}$ is the vertical unit vector, $\boldsymbol{\tau}$ is the wind-stress and ρ_o is a reference density.

The vertical Ekman velocity w_e is then given as the divergence of the horizontal flow,

$$w_e = \boldsymbol{\nabla} \cdot \mathbf{U_e} = (\mathbf{k}/\rho) \cdot \boldsymbol{\nabla} \times (\boldsymbol{\tau}/f).$$

The Ekman velocities are shown in figure 5.37 for March 1989.

4. The Ekman flux of nitrate was then calculated for each month on a 1^ox 1^ogrid. The depth of the Ekman layer was 30m. Upwind differencing was used in the vertical and centred difference in the horizontal.

5. The annual mean Ekman supply of nitrate for each year was calculated by summing the monthly contributions from October to April and dividing by 12. Thus the annual values are a lower estimate. Williams and Follows (1998a) argued that the surface nitrate concentrations are depleted in the summer and, therefore, there will be no flux..

5.5.4   Testing the Accuracy of the Method

Climatological Test

To test the accuracy of using equation (5.8) to predict the mixed layer depth, climatological heat fluxes were used to predict the climatological mixed layer depths. The predicted depths were then compared with mixed layer depths calculated directly from climatological density data ('true' depths).

a) Horizontal Ekman velocity
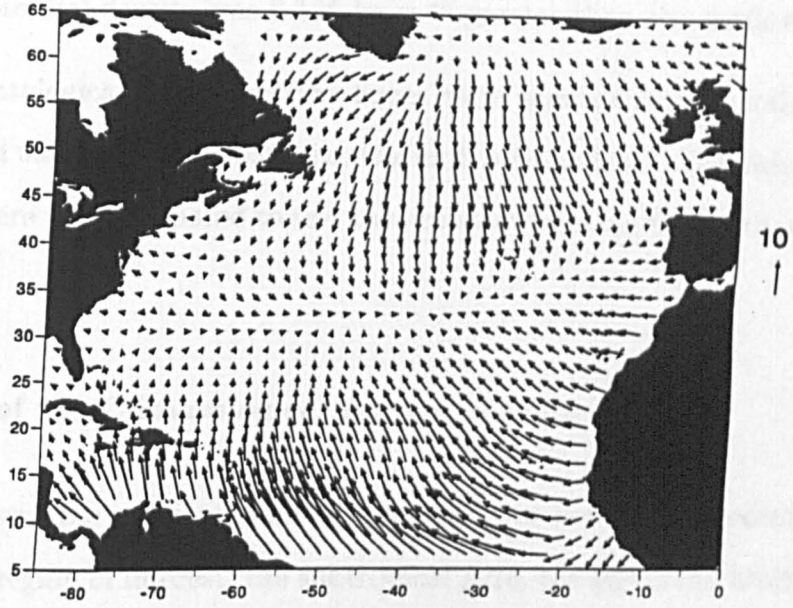
b) Vertical Ekman velocity
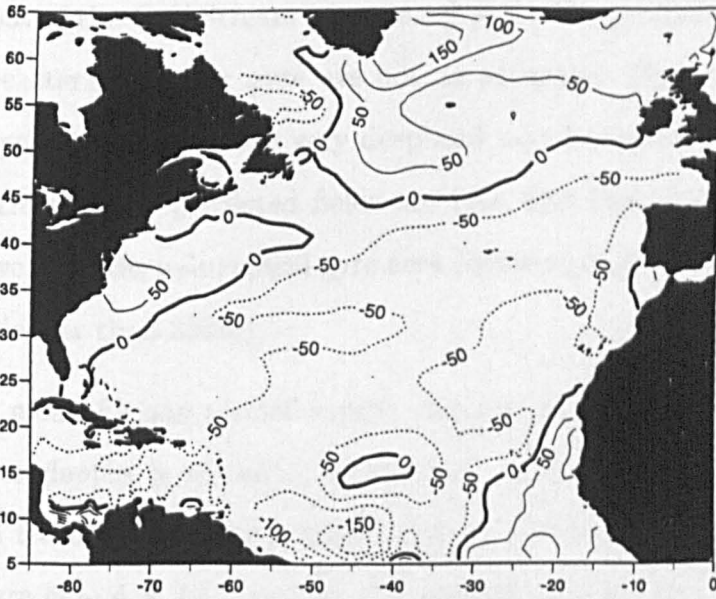
Figure 5.37: Ekman velocities for March 1989: a) horizontal component (10^{-2} ms^{-1}); and b) vertical component (m yr^{-1}).

The climatological mixed layer depths were calculated directly from the density data evaluated using the temperature and salinity data of Levitus and Boyer (1994) and Levitus *et al.*(1994). The mixed layer depth was defined as the depth where the potential density was 0.125 kg m^{-3} greater than the surface.

The climatological Ekman nitrate fluxes were then calculated following the above method using the predicted mixed layer depths and the 'true' mixed layers. The results were then compared to test the accuracy of using the predicted mixed layer depths.

Predictions of the Climatological Ekman Nitrate Flux

Figure 5.38 shows the predicted and true mixed layer depths for December and March. In the region of interest, the subtropical gyre, the predicted mixed layers are comparable with the true results. In March, the tongue of deeper mixed layers to the east of the Gulf Stream is captured well. The predicted mixed layer depths in the eastern subpolar gyre are not as accurate. However, the 'true' mixed layer depths in this area are very deep and may be unrealistic. The root mean square errors of the predicted fields are 28m and 78m in December and March respectively for the subtropical gyre area (ignoring points where the 'true' mixed layer is deeper than 300m).

The annual mean Ekman nitrate supply calculated using the predicted and true mixed layer depths is shown in figure 5.39. The predicted fields reproduces the main features of the true fields. The predicted flux at the subtropical/subpolar gyre is $\sim 4 \times 10^{-9}$ mol N m^{-2} s^{-1}which is comparable to the flux calculated using the true mixed layer depths. The predicted flux is underestimated northeast of Newfoundland where there are stronger horizontal gradients in the 'true' field. The meridional transport of nitrate by the Ekman flow is predicted well at the majority of latitudes (figure 5.40). The Ekman flow drives
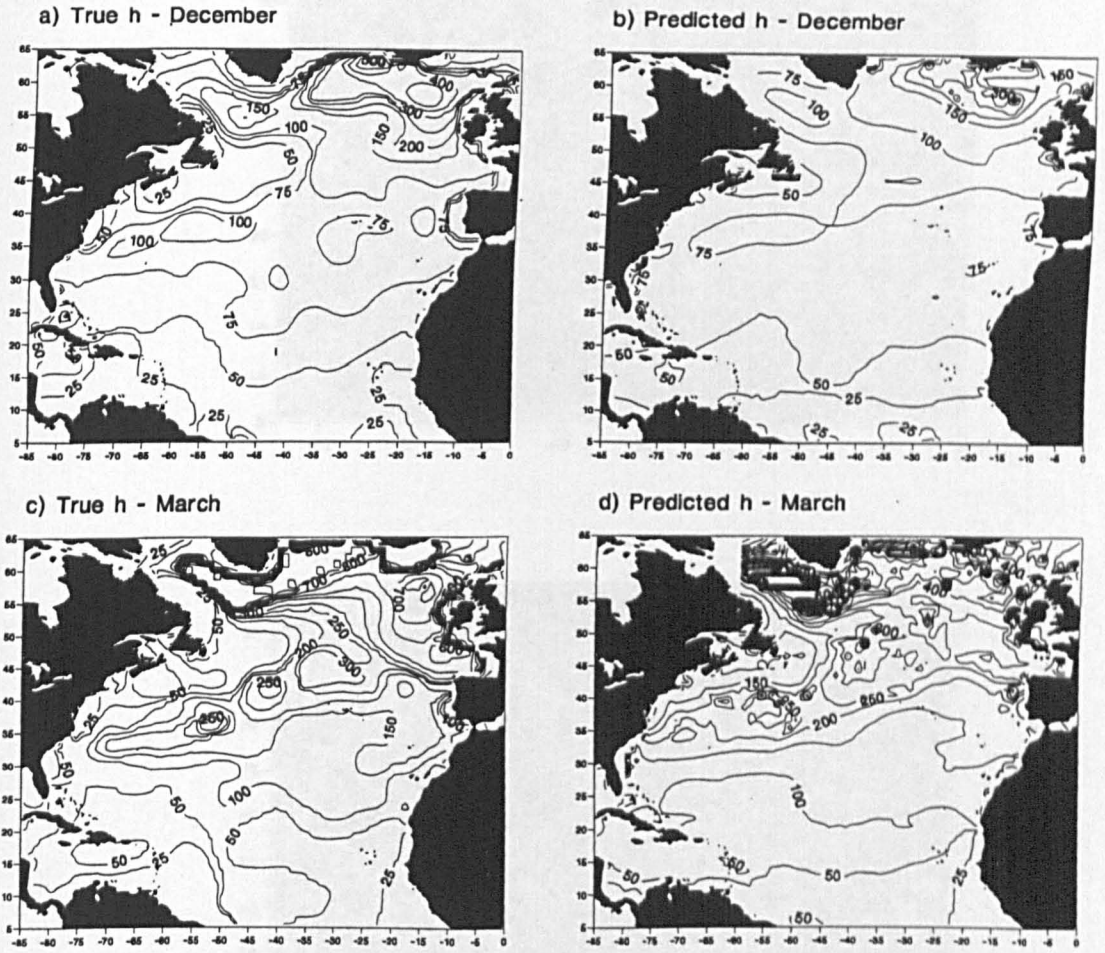
Figure 5.38: Depth of the mixed layer (m) calculated directly from density data (true depths) and predicted from heat flux data (predicted depths): a) and b) for December; and c) and d) for March.

a) Predicted

b) Actual
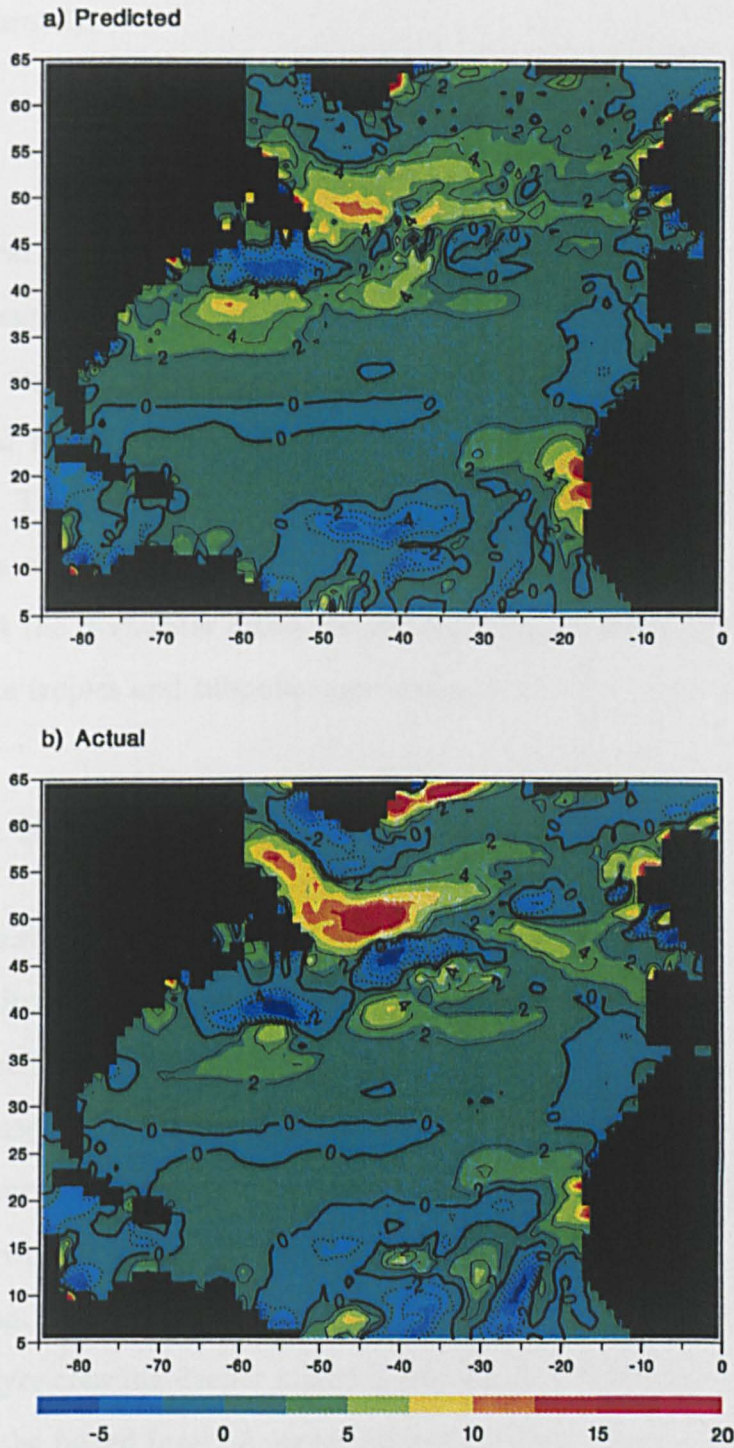
Figure 5.39: Annual mean Ekman nitrate supply (10^{-9} mol N m^{-2} s^{-1}) using a) the predicted mixed layer depths calculated from the heat flux; and b) the true mixed layer depths calculated from density data.

nitrate into the subtropical gyre from both the tropics and the subpolar gyre. The Ekman transports converge at ~ 30 °N. Below 20 °N, the transport is not predicted as accurately.

Conclusions

The climatological test shows that the method of predicting the mixed layer depth from the surface heat fluxes has an acceptable level of accuracy in the subtropical gyre region. The average difference between the predicted and the actual meridional Ekman nitrate transport is -0.16 $\times$ 10^{11} mol N yr^{-1} in the subtropical gyre. The method is less successful in the tropics and subpolar gyre. Freshwater fluxes are not included in the calculation of the mixed layer depth. It is possible that the freshwater fluxes are more important in setting the mixed layer depth in the tropics and subpolar gyre compared to the subtropical gyre.

5.5.5   Time Series of the Ekman Nitrate Transport

The method described in section 5.5.3 is used to calculate the annual mean Ekman flux of nitrate for the years 1945 to 1993. The general features of the time series of the annual mean Ekman nitrate flux can be explained by the variability associated with the North Atlantic Oscillation. The NAO is expected to have an influence on the Ekman flux of nitrate for two reasons. Firstly, the Ekman velocity will be greater in NAO+ years when the westerly winds are abnormally strong. Secondly, during NAO+ years, there is stronger convection in the subpolar gyre creating deeper mixed layers which will increase the nitrate concentration of the mixed layer. A larger nitrate concentration in the subpolar gyre will cause a greater horizontal flux across the intergyre boundary. The difference in the mixed layer depth and the inferred nitrate concentration during March for a typical NAO+ year (1989) and a NAO- year (1969) is shown in figure
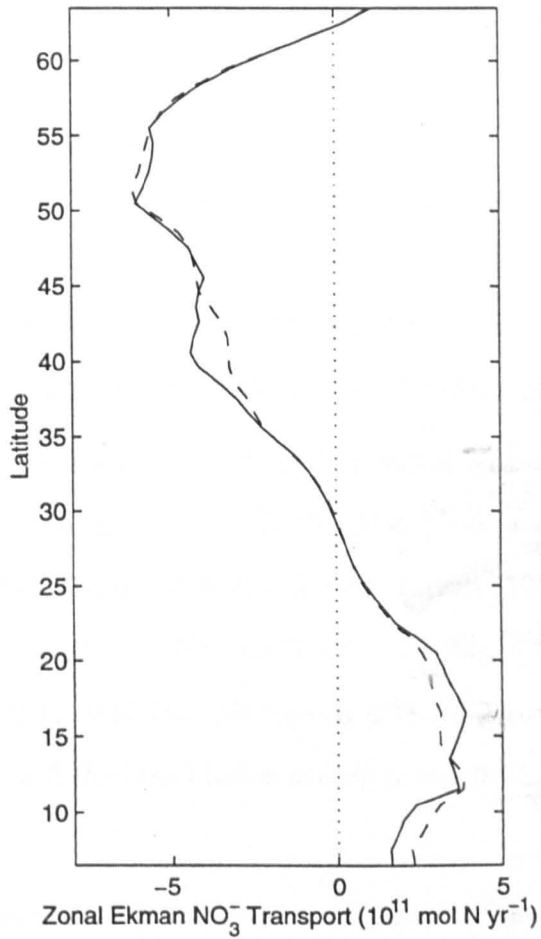
Figure 5.40: Annual mean meridional horizontal Ekman transport of nitrate (10^{11} mol N yr^{-1}) as a function of latitude, calculated using the predicted mixed layer depths (solid line) and the true mixed layer depths (dashed line).

5.41. The nitrate concentrations at the gyre boundary in March 1989 (NAO+) are as much as 2 μ mol N kg^{-1} higher than in March 1969 (NAO-).

The Ekman flux of nitrate for the years 1968-69 (NAO-) and 1988-89 (NAO+) is shown in figure 5.42. These can be compared with the nitrate fluxes calculated using the climatological heat flux (figure 5.39a). During 1968-69 the Ekman flux at the gyre boundary is lower than the climatological estimate, with a typical flux of 2 $\times$ 10^{-9} mol N m^{-2} s^{-1}. The opposite occurs during 1988-89 when the Ekman flux is larger than the climatological estimate with a typical flux of 8 $\times$ 10^{-9} mol N m^{-2} s^{-1}. The variability shown in figure 5.42 can be explained by the NAO. During 1988-89, the NAO index is positive and the westerly winds are strong (figure 5.37). Also the abnormal heat flux causes deeper mixed layers in the subpolar gyre and hence greater nitrate concentrations (figure 5.41).

Figure 5.43a shows the time series of the horizontal transport of nitrate into the subtropical gyre across 20 °N and 50 °N. Also plotted on the same figure is the North Atlantic Oscillation (NAO) index of Hurrell (1995). The transport ranges from 5.3 $\times$ 10^{11} to 13.4 $\times$ 10^{11} mol N yr^{-1}. During NAO+ years, there is a larger transport of nitrate into the subtropical gyre. The correlation coefficient between the transport and the NAO index is 0.60 which is significant at the 99% level.

The different effects of the NAO on the variability of Ekman nitrate flux are illustrated in figure 5.43b. The black line shows the anomalous Ekman transport taken from figure 5.43a. Also plotted is the anomalous Ekman transport calculated using climatological mean nitrate fields for each winter month (grey dashed line). Hence, the only variable component of the nitrate transport is the Ekman velocity. The difference between the black line and the grey line is caused by the effect of the variability of the nitrate concentrations on the Ekman nitrate flux. Therefore, it can be seen in figure 5.43b that it is the variable strength of the Ekman velocity that causes most of the interannual variability of the Ekman ni-

a) h difference

b) Nitrate difference
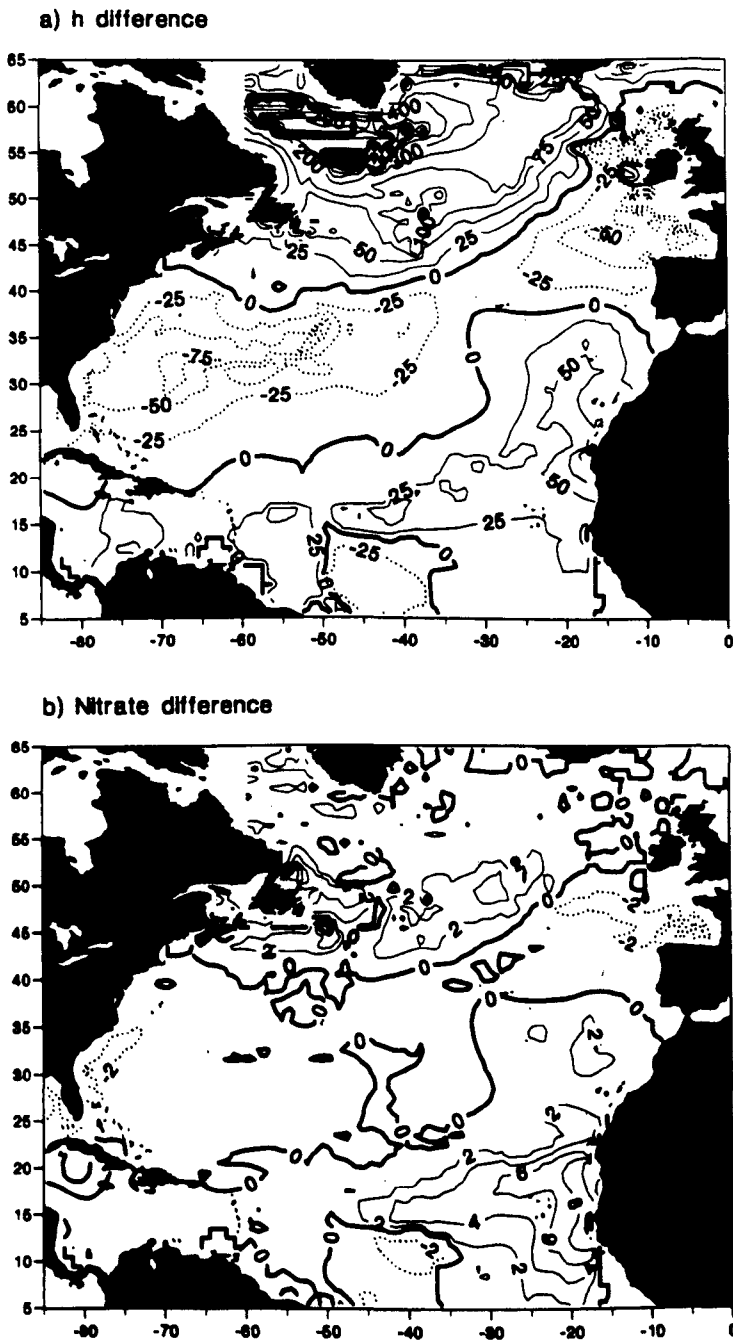
Figure 5.41: Difference between March 1989 and 1969 of: a) the depth of the mixed layer (m); and b) the mixed layer nitrate concentration (μ mol N kg^{-1}). Positive values indicate a deeper mixed layer or greater nitrate concentration during March 1989 (NAO+).
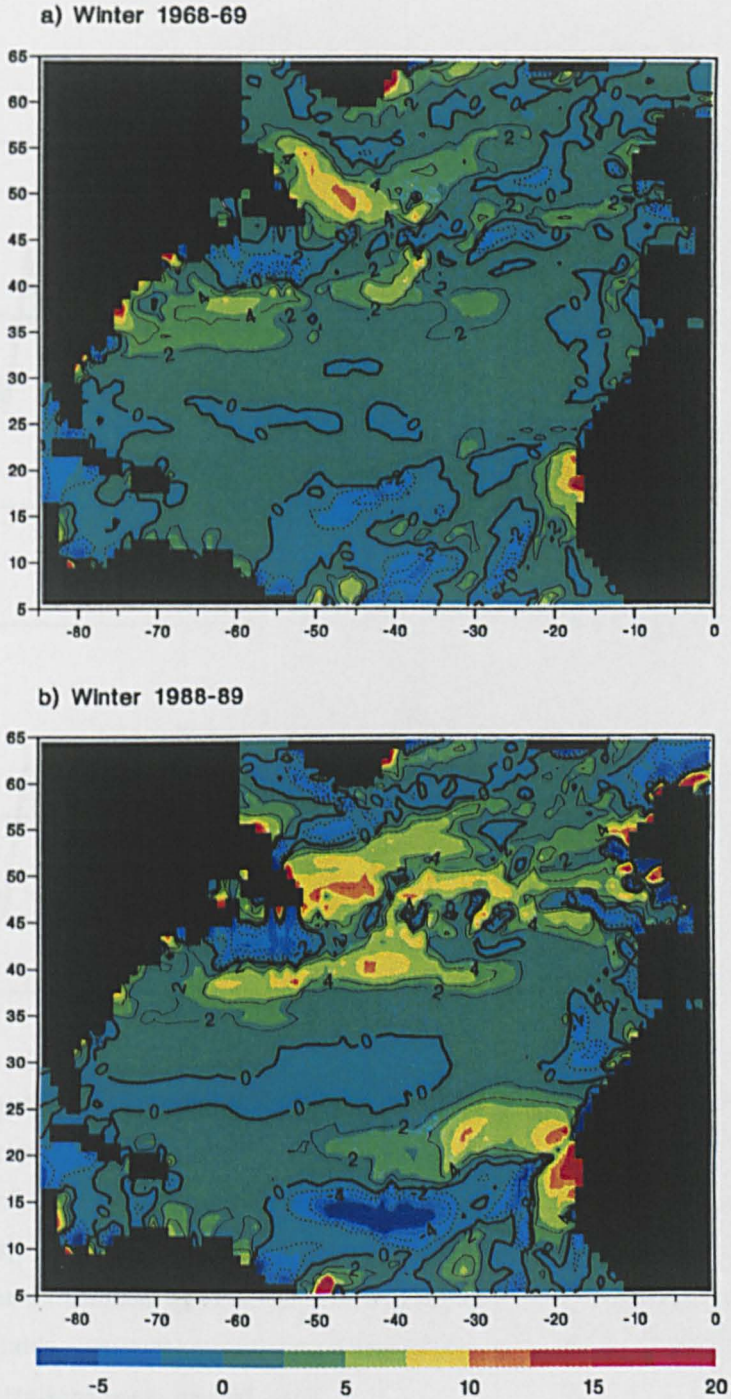
Figure 5.42: Annual mean Ekman supply of nitrate (10^{-9} mol N m^{-2} s^{-1}) during a) winter 1968-1969 (NAO-) and b) winter 1988-89 (NAO+). (The Ekman supply during the summer months is assumed to be negliable.)
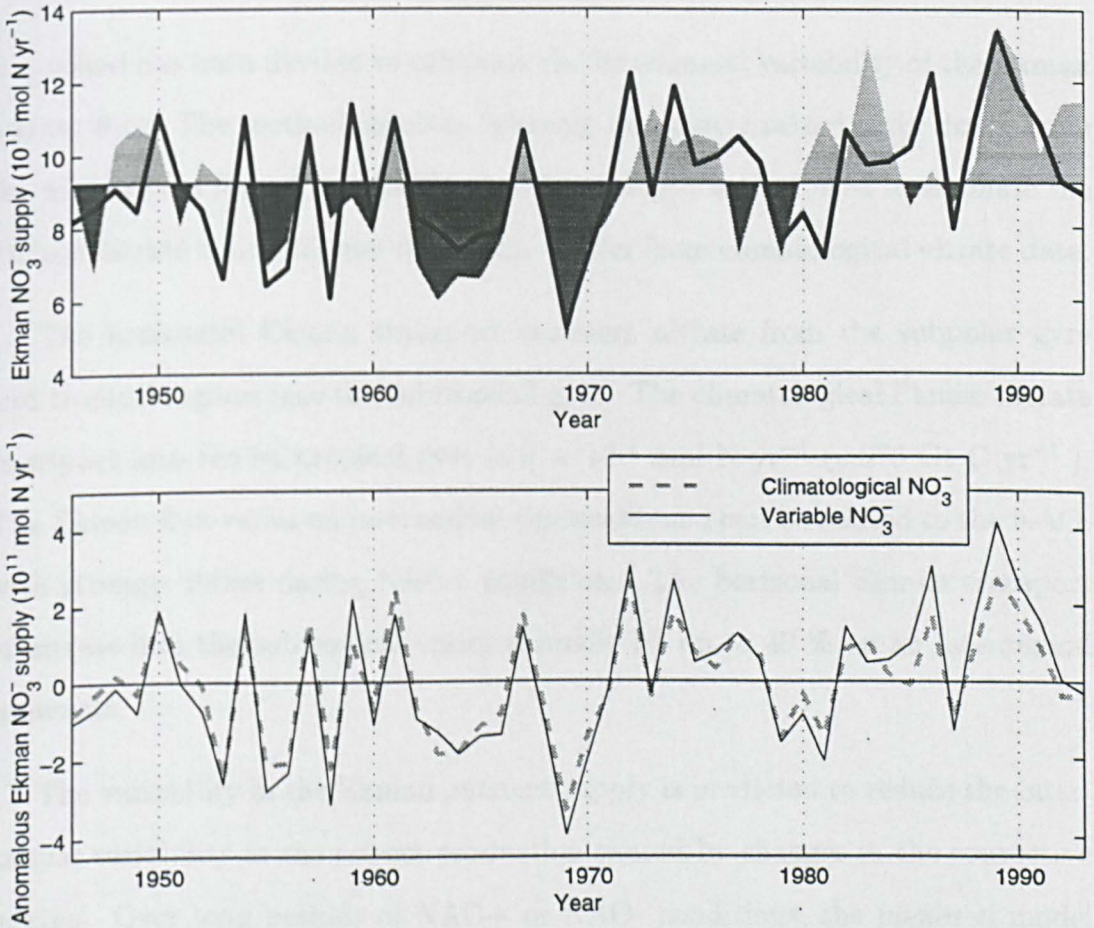
Figure 5.43: a) Annual mean horizontal Ekman transport of nitrate (10^{11} mol N yr^{-1}) into the subtropical gyre across 20 °N and 50 °N (black line) for 1945 to 1992. Plotted with the NAO winter index of Hurrell (1995) (grey shading : light grey for NAO+ years and darker grey for NAO- years). b) Anomalous annual mean horizontal Ekman transport nitrate (10^{11} mol N yr^{-1}) into the subtropical gyre across 20 °N and 50 °N (solid line) for 1945 to 1992. Calculated using variable nitrate concentrations (black line) and calculated using climatological mean nitrate concentrations (grey dashed line).

trate transport. However, in certain years (especially 1989), the variability of the nitrate concentration does affect the variability of the Ekman nitrate transport.

5.5.6 Conclusions

A method has been devised to calculate the interannual variability of the Ekman nitrate flux. The method involves inferring the winter mixed layer depth from the air-sea heat flux. The winter mixed layer depth is then used to estimate the surface nitrate concentration during the winter from climatological nitrate data.

The horizontal Ekman transport transfers nitrate from the subpolar gyre and tropical regions into the subtropical gyre. The climatological Ekman nitrate transport into the subtropical gyre is 9×10^{11} mol N yr^{-1} (0.076 Gt C yr^{-1}). The Ekman flux varies on interannual timescales and can be related to the NAO, with stronger fluxes during NAO+ conditions. The horizonal Ekman transport of nitrate into the subtropical varies annually by up to 40 % on an interannual timescale.

The variability in the Ekman nutrient supply is predicted to reduce the interannual variability in the export production caused by changes in the convective mixing. Over long periods of NAO+ or NAO- conditions, the idealised model experiments suggest that the anomalous Ekman nutrient supply will control the variability in the export production.

Chapter 6

Discussion

6.1 Solubility Pump

Watson *et al.*(1995) derived a relationship between that air-sea flux of CO_2 and heat that allowed the better known heat flux to be used to infer the physical CO_2 flux. In this relationship, it was assumed that the ocean stayed in equilibrium with the atmospheric CO_2 content. Watson *et al.*(1995) accepted that the ocean did not always stay in equilibrium in the atmosphere. However, they argued that during winter (when the CO_2 uptake occurs), the northern North Atlantic was 'reasonably close to saturation'.

The model experiments completed in this work show that the heat/CO_2 relationship of Watson *et al.*(1995) overestimates the net CO_2 uptake of an ocean basin. This result was also found for the Atlantic by Sarmiento *et al.*(1995) using a global general circulation model. The overestimation is caused by assuming that the air-sea CO_2 flux has the same timescale as the air-sea heat flux. The temperature exchange timescale is O(1 month) but the carbon exchange timescale is longer at O(1 year). Therefore, the air-sea CO_2 flux responds to temperature changes at a slower rate than the heat flux. However, the re-

lationship of Watson *et al.*(1995) does provide a useful upper limit on the net CO_2 flux.

A further heat/CO_2 relationship has been derived which predicts the CO_2 flux caused by one subduction period. This second heat/CO_2 relationship is effectively the relationship of Watson *et al.*(1995) scaled by the ratio of the carbon exchange timescale with a subduction timescale. This relationship gives a valuable lower limit on the net CO_2 flux of an ocean basin as the net flux will be determined by one or more subduction periods. In this work, the subduction timescale has been chosen to equal the temperature exhange timescale which is typically 2-3 months. However, different choices of the subduction timescale could be made and the results rescaled. The key difference between the two heat/CO_2 flux relationships is that the relationship of Watson *et al.*(1995) is appropriate over several years, whereas the second relationship is valid on seasonal timescales.

There are regions of the ocean where the air-sea heat flux is in the same direction as the CO_2 flux. This is caused by the delayed reaction of the CO_2 flux to changes in temperature. For example, in the models used in this work, the annual mean air-sea fluxes of heat and CO_2 are found to be in the same direction in the exit regions of the western boundary currents. The heat flux estimates of the CO_2 flux do not *locally* predict the delayed reaction of the CO_2 flux to the heat flux. However, the upper limit estimate effectively allows for the delayed reaction when integrated over large areas, but tends to overestimate the delayed reaction. The difference in the heat and CO_2 flux timescales has a reduced impact when the fluxes are integrated over a large area. The size of the area required to capture the CO_2 flux delayed reaction in the upper limit estimate depends on the speed of the circulation. The results of the one-dimensional Lagrangian model experiment, suggest that in the tropics, the distance that a water parcel travels in one year is a sufficient area. However, in the region of a western boundary current, a water parcel must travel for 7 years after exiting the current before

the upper limit estimate is accurate.

The lower limit heat flux estimate of the CO_2 flux is designed to be more accurate on short timescales as the estimate only allows for one subduction period. The lower limit relationship provides more accurate estimates of the local CO_2 flux in the western boundary currents than the equilibrium relationship of Watson *et al.*(1995) as the oceanic carbon concentration is not close to equilibrium with the atmosphere.

To summarize, the heat flux can be used to infer an upper and lower limit on the net CO_2 flux of an ocean region caused solely by changes in temperature. The heat flux estimates do not include any initial CO_2 fluxes occurring as the water enters or exits the region. Therefore, the ocean region in which the heat flux is used to infer the CO_2 flux must be selected thoughtfully. For example, the region 15°N to 50°N has been found to be a suitable region in which to use the heat flux method in the North Atlantic but not in the North Pacific. In the North Pacific at 15°N, the water entering the region has a large air-sea CO_2 flux associated with the large change in temperature that occurs in the equatorial region.

The heat flux method predicts the CO_2 uptake caused by the solubility pump to be between 0.18 to 0.68 Gt C yr^{-1} for the North Atlantic (25°N to 65°N) prior to the industrial revolution. The results of the global carbon transport model suggest that the actual CO_2 uptake value is in the middle of the upper and lower limit given by the heat flux. The heat flux estimate encompasses previous estimates of the net CO_2 uptake of the North Atlantic as discussed in chapter 4. Therefore, the North Atlantic CO_2 uptake is dominated by the solubility pump as has been found previously by Watson *et al.*(1995) and Keeling and Peng (1995).

This method of obtaining the air-sea CO_2 flux has both advantages and disadvantages relative to other methods that were described in chapter 2.

6.1.1 Advantages of the Heat Flux Method

The main advantage of the heat flux method over the direct methods of obtaining an estimate for the CO_2 flux is that no pCO_2 or $\sum CO_2$ data are required. Instead, only measurements of the heat flux are needed. The spatial coverage of heat flux measurements is much greater than pCO_2 or $\sum CO_2$ measurements. There is also full seasonal coverage of the heat flux data, unlike pCO_2 and $\sum CO_2$ data coverage which tends to be biased towards the summer. In addition, heat flux measurements have been taken over a longer time period than pCO_2 or $\sum CO_2$ measurements. Therefore, the heat flux method is able to provide an estimate on the temporal variability of the CO_2 flux which cannot be done using direct methods. Another advantage over methods that use the air-sea CO_2 flux equation is that no detailed knowledge of the gas exchange transfer velocity is needed. An average value of the transfer velocity is adequate in the calculation of the lower limit on the CO_2 uptake.

The heat flux method can provide some information of the spatial distribution of the annual air-sea CO_2 fluxes, in addition to an estimate of the net flux of a region. Some other methods of inferring the CO_2 flux can only provide an estimate for the net uptake (e.g. Keeling and Peng, 1995). Another advantage of the heat flux method is that the limitations of the method are known through the series of the model experiments undertaken in this work. The accuracy of some other methods is not always obvious, such as the sea surface temperature method of Stephens *et al.*(1995) which use empirical fits to temperature and pCO_2 observations.

6.1.2 Disadvantages of the Heat Flux Method

The heat flux method only provides an estimate of the CO_2 flux caused by the solubility pump. This can be seen as an advantage as it allows the complex system

to be divided into the different components. However, a method of inferring the CO_2 flux caused by the biological processes and changes in salinity and alkalinity is also required. The heat flux method is only appropriate for pre-industrial times during which it can be assumed that the atmospheric pCO_2 remained constant. Therefore, although the heat flux method is useful in gaining insight into past situations, it cannot be used to estimate the oceanic uptake of anthropogenic CO_2.

The heat flux is used to infer a range of possible CO_2 fluxes and cannot provide an exact estimate. However at present, there are no global methods with adequate data to provide an accurate map of the CO_2 air-sea flux. The accuracy of the heat flux predictions are reliant on the quality and quantity of the heat flux data. It has been shown that the heat flux data in the Southern Ocean are not reliable enough to be used to infer the CO_2 uptake.

6.1.3 Prediction of the Air-Sea Flux of Other Gases

This work has only considered the relationship between heat fluxes and the air-sea flux of CO_2. The physical component of the air-sea exchange of all gases will be related to the heat flux through the solubility. The heat flux method which provides the upper limit on the CO_2 flux is expected to provide a more accurate flux estimate for gases with the same equilibration timescale as heat. Oxygen has an exchange timescale of 1 month (Broecker and Peng, 1974), and, therefore, the heat flux could provide an accurate estimate of the air-sea O_2 exchange caused by temperature changes. Indeed, Keeling and Shertz (1992) used the heat flux to estimate the air-sea O_2 flux caused by seasonal temperature changes.

In a recent work by Holfort et al.(1998), observations of $\sum CO_2$ and O_2 were used to calculate the transport of carbon and oxygen in the South Atlantic Ocean. The calculated transports implied a convergence of carbon (650 kmols^{-1})

and oxygen (1180 kmols^{-1}) between 10ºS and 30ºS. The heat transport across the section implied a heat divergence of 0.24 PW. Holfort *et al.*(1998) used the heat/CO_2 relationship of Watson *et al.*(1995) to infer a sea to air CO_2 flux, caused by the heat divergence, of 480 kmols^{-1}. Similarly, the heat divergence was used to infer a sea to air O_2 flux of 360 kmols^{-1}. Holfort *et al.*(1998) noted that the inferred CO_2 flux was comparable to the observed carbon convergence, but the inferred O_2 flux was much less than the observed oxygen convergence. Holfort *et al.*(1998) suggested that the difference could be due to: 1) uncertainties in the transport terms and particularly the influence of seasonality; 2) a storage term for oxygen; or 3) some biological mechanism.

The global carbon transport model used in chapter 4 predicts a very small flux of CO_2 (50 kmols^{-1}) into the ocean between 10ºS and 30ºS. However, the model heat flux predicts a upper limit of 240 kmols^{-1} out of the ocean. Therefore, the model suggests that this is not a suitable ocean region in which to use the heat flux relationship to infer the CO_2 flux. The heat flux upper limit estimate is expected to be more accurate for the O_2 flux. Assuming that the thermally driven air-sea CO_2 flux is approximately zero and only a third of the O_2 flux is thermally driven, it is difficult to account for the observed convergences of carbon and oxygen in this region. Biological mechanisms will cause fluxes in difference directions for carbon and oxygen, so cannot account for the observed fluxes. It is suggested that the possible reasons for the unexplained convergences are the first two that Holfort *et al.*(1998) put forward.

6.2 Biological Pump

The experiments completed using the idealised 3-D model of Samelson and Vallis (1997b) have highlighted the importance of the Ekman horizontal transfer of nutrients into a subtropical gyre as earlier found by Williams and Follows (1998a).

In the model run with no DON, 34% of the export production in the subtropical gyre was supported by the lateral transfer of nutrients from the subpolar gyre into the region. However, the horizontal transfer is most important on the edge of the subtropical gyre and does not sustain export production in the centre of the gyre.

The model experiments have shown that the inclusion of DON in the system acts to increase export production in the subtropical gyre. The presence of DON increases the supply of inorganic nitrogen to the euphotic zone supporting a higher level of production. In particular, the lateral transfer of DON into the subtropical gyre and the subsequent remineralisation supplies inorganic nitrogen. The level of model export production is lower than observed rates, even with the inclusion of DON. This suggest that either the model is too simplified to produce realistic rates or that there most be additional sources of nutrients to the central gyre such as the supply due to eddies and nitrogen fixation. A range of parameters was used to model the creation and destruction of DON, as there are not sufficient DON observations available to accurately determine the parameters. Therefore, more DON observations are required before the exact contribution of dissolved organic nutrients to export production can be determined. The results of these model runs have shown the potential importance of DON.

6.3 Interannual Variability of the Air-Sea Flux of CO_2 in the North Atlantic

The interannual variability of the physical air-sea CO_2 flux in the North Atlantic has been quantified for the period 1960 to 1993. During this period, the variability is caused by natural and anthropogenic processes. An upper and lower limit on the natural variability is inferred from annual mean heat flux data. The

measure of interannual variability used by Lee *et al.*(1998) was 2σ, where σ is the standard deviation. Using this measure, the natural interannual variability inferred for the CO_2 uptake in the subpolar gyre is between 0.02 and 0.09 Gt C yr^{-1} for the period 1960 to 1993. The variability is related to the North Atlantic Oscillation, with stronger CO_2 uptake occurring during NAO+ years. The natural variability of the CO_2 uptake in the subtropical gyre is between 0.03 to 0.11 Gt C yr^{-1}. The natural variability of the annual mean CO_2 uptake over the whole of the subtropical gyre region (14°N to 50 °N) is not significantly correlated with the NAO. However, the CO_2 uptake of different areas of the defined region are related to the NAO, such as the CO_2 uptake in the Sargasso Sea which is negatively correlated to the NAO.

The anthropogenic component to the CO_2 uptake variability has been evaluated using the observed increase in atmospheric CO_2. The method involves inferring the change in oceanic pCO_2 with time from the atmospheric pCO_2. The method has been found to give accurate results when tested in an idealised 3-D model which was forced with a linearly increasing atmospheric carbon concentration. The results suggest that the variability in the CO_2 uptake of the North Atlantic is dominated by the natural variability. In the region 14°N to 65°N, the upper limit on the anthropogenic variability is only 0.08 Gt C yr^{-1} which is lower than the maximum natural variability of 0.15 Gt C yr^{-1} for the period. The combined natural and anthropogenic variability of the physical CO_2 uptake for the North Atlantic is predicted to be between 0.05 and 0.20 Gt C yr^{-1}. The pre-industrial climatological mean is predicted to be between 0.19 to 0.74 Gt C yr^{-1} for the period 1960 to 1990.

The natural variability of the CO_2 flux has been inferred using annual mean values. This assumes that the anomalous CO_2 flux response to the anomalous heat flux is independent of season. It is possible that anomalies during the winter period, when the CO_2 uptake is actually taking place, could be more influential

than summer anomalies on the net CO_2 flux variability over a year. However, the long equilibrium timescale of the CO_2 flux may remove any bias towards the winter. The inclusion of seasonality in the PGOM caused the net uptake to increase by only 9%. Therefore, the error caused by using annual mean values to calculate the interannual variability is expected to be small.

There has been a number of different estimates for the interannual variability related to the present day global oceanic uptake of anthropogenic CO_2. These variability estimates range from as high as 2.5 Gt C yr^{-1} (Francey et al., 1995) to lower values of 0.4 Gt C yr^{-1} (Lee et al., 1998) (both these values were quoted by Lee et al., 1998, using 2σ as the variability measure). The El Niño-Southern Oscillation (ENSO) has a big impact on the global variability with greater oceanic uptake occurring during ENSO events (e.g. Lee et al., 1998). Different methods have been used to evaluate the variability. For example, Keeling et al.(1995) analysed the interannual variability in the atmospheric CO_2 concentration and assessed the causes of the variability. Atmospheric measurements of $^{13}C/^{12}C$ were used to distinguish between the variability in the terrestrial and oceanic sources and sinks of carbon.

A more direct method of estimating the recent interannual variability of the oceanic CO_2 uptake was used by Lee et al.(1998). The air-sea CO_2 flux was estimated using the difference in pCO_2 between the atmosphere and ocean. The variability in the oceanic pCO_2 was inferred using sea surface temperature (SST) measurements and an empirical relationship between pCO_2 and SST. The empirical relationship was found using available pCO_2 and SST data with a horizontal resolution of 4^ox 5°. Lee et al.(1998) argue that changes in $\sum CO_2$ that affect pCO_2 are included in this empirical relationship, as processes that change $\sum CO_2$ also affect SST. For example, the deepening of the mixed layer is caused by the SST decreasing and leads to the surface $\sum CO_2$ increasing due to mixing with deeper water. The pCO_2 and SST relationships vary with location and sea-

son. In the subtropical zone, pCO_2 increases with SST, however, in other regions. pCO_2 decreases with SST due to changes in $\sum CO_2$. Stephens *et al.*(1995) found that using SST to predict pCO_2 was unsuccessful in the northern North Pacific. where changes in $\sum CO_2$ occurred. The method of Lee *et al.*(1998) also requires knowledge of the poorly-known gas transfer velocity which will also vary in time. Although, the variability in the gas transfer velocity was found to contribute less then 10% to the total air-sea CO_2 flux variability, except during ENSO years. where it contributed 20-30%.

The maximum anomaly in the CO_2 uptake of the ocean region north of 40°N estimated by Lee *et al.*(1998) is $\sim$ 0.05 Gt C yr^{-1} during 1982 to 1995. This estimate compares well with the heat flux estimate of the CO_2 uptake natural variability in the North Atlantic between 50°N to 65 °N of between 0.02 and 0.09 Gt C yr^{-1}. This supports the findings in chapter 4 that the present day variability is dominated by the natural variability. The method of using the heat flux to calculate the interannual variability of CO_2 uptake has advantages and disadvantages compared with the Lee *et al.*(1998) method. The limitations are known for the heat flux method, whereas, the errors in the Lee *et al.*(1998) method are more difficult to assess. Also the variability in the gas transfer velocity is partly included in the heat flux method as the heat flux will be similarly affected by changes in wind speed. The disadvantages of the heat flux method are that only the solubility pump variability is assessed and the heat flux method cannot assess the current day variability. An additional method has had to be devised to predict the anthropogenic component to the variability. In contrast, the method of Lee *et al.*(1998) implicitly includes the anthropogenic component.

Variability in the nutrient supply to the North Atlantic will modify the biological pump. The dynamical nutrient supply has been found to be sensitive to changes in the surface forcing of the ocean associated with the NAO. On interannual timescales, the export production responds to changes in the convective

nutrient supply as found by Follows and Marshall (1999). During NAO+ conditions, the convective nutrient supply is greater in the subpolar gyre but is less in the subtropical gyre. The anomalous advective nutrient supply is also greater in NAO+ conditions in the subpolar gyre, enhancing the change in export production created by the convective mixing. However, in the subtropical gyre, the advection is anomalously low in NAO- conditions, and therefore, the advection reduces the change in export production created by the convective mixing.

Over longer periods of abnormal forcings, the model experiments suggest that the anomalous export production is controlled by the advective nutrient supply. The Ekman component of the advective nitrate supply to the subtropical gyre has been calculated to vary by up to 40% from the climatological value. This component alone could cause a variability in the biological pump in the subtropical gyre of 0.03 Gt C yr^{-1} (using a Redfield ratio, C:N of 105:15). A change in the biological pump does not necessarily cause an anomalous air-sea flux of CO_2 , as the CO_2 required for the anomalous export production could be supplied by the anomalous circulation. Therefore, the change in the export production is viewed as an upper limit on the potential change on the biological air-sea CO_2 flux.

Overall, the CO_2 uptake in the subpolar gyre is expected to be stronger in NAO+ years due to both the solubility and biological pump. The solubility pump in the subtropical gyre has been found to be insignificantly related to the NAO. Hence, changes in the CO_2 uptake related to the NAO are only caused by the biological pump. On short timescales, the biological pump will increase during NAO- conditions and the CO_2 uptake is expected to be greater. However, after several years of anomalous NAO- forcing, the anomalous advective nutrient supply will become significant and the CO_2 uptake is expected to decrease.

Chapter 7

Conclusions

Two aspects of the air-sea flux of CO_2 have been investigated. Firstly, the relationship between the dynamically driven component of the air-sea CO_2 flux and the heat flux has been examined. This has led to using the heat flux to infer limits on the net CO_2 flux of an ocean region. Secondly, the dynamical supply of nutrients that help sustain the biological component of the air-sea flux of CO_2 has been analysed. Finally, the interannual variability of the physical air-sea CO_2 flux and the dynamical nutrient supply has been studied and some aspects have been quantified using available data. It is difficult to quantify the CO_2 flux variability directly from the available carbon measurements. Therefore, methods have been developed to infer the variability of the carbon pumps using other measured quantities.

Two methods of inferring the physical air-sea CO_2 flux from the heat flux have been derived. The methods differ in the timescales for which they are intended and the assumptions made during the derivation. One of these methods was first suggested by Watson *et al.*(1995). A series of model experiments was used to investigate the two different methods of inferring the CO_2 flux from the heat flux. The models ranged from a very basic non-seasonal one-dimensional

240

model to a highly complex global three-dimensional model. The results from this hierarchy of models have allowed a thorough understanding of the heat and CO_2 flux relationship to be built up. The model results showed that the heat flux can be used to provide an upper and a lower limit on the net CO_2 flux of an ocean region. The ocean region must be defined such that air-sea heat flux causing the CO_2 flux is included in that region. The size of the region is dependent on the speed of the circulation. A larger area is required for regions with fast circulations. An estimate of the spatial distribution of local air-sea CO_2 fluxes can be obtained from the heat flux. The heat flux method that provides the lower limit on the net flux gives good local estimates in fast moving regions. In slower moving regions, an upper and lower estimate of the local flux can be found using both heat flux methods. However, the local heat flux estimates can predict the incorrect sign of the air-sea CO_2 flux as the delayed response of the CO_2 flux to changes in temperature is not captured by a local heat flux estimate.

Climatological heat flux has been used to obtain upper and lower limits on the physical CO_2 uptake of different ocean regions. These limits have been compared to previous CO_2 uptake estimates and have been found to be feasible.

An idealised model has been used to study the dynamical supply of nutrients to the euphotic zone. In particular, the potential supply of dissolved organic nutrients to the subtropical gyre was examined. The inclusion of dissolved organic nitrogen (DON) in the model increased export production in the subtropical gyre. The model results stress the importance of the lateral transfer of nutrients into the subtropical gyre as found by Williams and Follows (1998a). The horizontal transfer of inorganic and organic nutrients by the Ekman transport was 37-50% of the total export production, depending on the DON parameters used in the model. The other important dynamical supply mechanisms to the subtropical gyre were found to be convective mixing and vertical diffusion. The lateral transfer of dissolved organic nutrients, and subsequent remineralisation,

increased export production in the central subtropical gyre. Despite this increase due to the presence of DON, the export production in the central subtropical gyre of the model was lower than observed rates. Therefore the model results suggest, that although DON is an important source of nutrients to the subtropical gyre, another mechanism is still needed to balance the nutrient budget. Other mechanisms that have been suggested include nitrogen fixation or transport by the time-varying circulation.

The variability of the dynamical nutrient supply caused by anomalous surface forcing has been examined in an idealised model. An increase in wind strength is found to increase export production through an increased dynamical supply of nutrients into the euphotic zone in steady state conditions. The variability in the individual dynamical supplies was investigated by modelling the response of an ocean basin to a 5 year period of anomalous forcing. The anomalous forcing was chosen to mimic the positive or negative phase of the North Atlantic Oscillation. The model experiments show that during NAO+ conditions, the stronger winds cause a greater advective supply of nutrients to the euphotic zone. In the subpolar gyre, the vertical upwelling increases, and in the subtropical gyre, the lateral transfer of nutrient increases. Therefore, during NAO+ conditions, anomalous advection acts to increase export production in both the subpolar and subtropical gyre. The change in the amount of heat lost to the atmosphere during NAO conditions affects the amount of convective mixing. In NAO+ conditions, convective mixing increases in the subpolar gyre but decreases in the subtropical gyre. Therefore, during NAO+ conditions, anomalous convection acts to decrease export production in the subtropical gyre but increase export production in the subpolar gyre. So the anomalous nutrients supplies due to advection and convection reinforce each other in the subpolar gyre, but oppose each other in the subtropical gyre during NAO conditions.

Follows and Marshall (1999) have previously shown that the interannual vari-

ability in export production in the North Atlantic was caused by the variability in the convective supply of nutrients. However, the idealised model experiments in this work suggest that after several years of anomalous forcing, it is the anomalous advection that controls the export production variability. The export production in the subtropical gyre is expected to decrease during the first year of NAO+ forcing, but after several years of NAO+ conditions, export production is expected to increase.

The variability of two components of the air-sea CO_2 flux in the North Atlantic have been quantified. Firstly, the variability in the CO_2 uptake of the North Atlantic caused by the solubility pump has been evaluated during 1960 to 1993. The heat flux method has been used to infer the natural interannual variability of the CO_2 uptake. An additional method has been devised to quantify the anthropogenic variability using the observed increase in atmospheric CO_2. The natural variability is found to dominate over the anthropogenic variability in the CO_2 uptake of the North Atlantic. In the region 14°N to 65°N, the upper limit on the anthropogenic variability is only 0.08 Gt C yr^{-1} which is lower than the maximum natural variability of 0.15 Gt C yr^{-1} for the period. The upper limit on the total variability in the subpolar gyre was inferred to be 0.10 Gt C yr^{-1}, with the pre-industrial climatological mean being 0.06 to 0.25 Gt C yr^{-1}. In the subtropical gyre, the pre-industrial climatological mean was estimated to be between 0.13 and 0.49 Gt C yr^{-1} with a maximum variability 0.13 Gt C yr^{-1}. The natural variability in the CO_2 uptake of the subpolar gyre is related to the NAO, with greater uptake occurring in NAO+ years. The natural variability in the subtropical gyre region as defined by 14°N to 50°N is not significantly related to the NAO. The local air-sea CO_2 flux anomalies caused by natural variability are predicted to as high as 0.6 mol C m^{-2} yr^{-1}.

A method was devised to quantify the variability in the Ekman advective supply of nutrients into the subtropical gyre using climatological nitrate and

monthly surface heat flux data. The Ekman supply in the North Atlantic subtropical gyre was found to vary by 40% from the climatological mean. This implies a variability in the biological carbon pump of 0.03 Gt C yr^{-1}. The variability was found to be mainly caused by the variable wind strength and not by variable nitrate concentrations. The Ekman nitrate supply is related to the NAO, with a larger horizontal transfer of nitrate occurring in NAO+ years. This Ekman nitrate flux variability is expected to counteract some of the convective nitrate flux variability on short timescales and become more important over longer timescales.

The interannual variability of the CO_2 uptake in the subpolar gyre is expected to be in phase with the NAO, with stronger CO_2 uptake in NAO+ years. Both the solubility pump and the biological pump are expected to increase during NAO+ conditions. In the subtropical gyre region, only the biological pump is related to the NAO. Over short timescales, the biological pump is expected to decrease in NAO+ years. However, if the NAO+ conditions persist for several years, the biological pump is expected to increase.

Overall, this work has highlighted the impact of the ocean circulation on the exchange of CO_2 between the ocean and atmosphere. The ocean circulation drives air-sea CO_2 fluxes directly be transporting carbon in and out of the surface layer. Air-sea CO_2 fluxes are also caused indirectly by the circulation , through the dynamic supply of nutrients which help sustain the biological carbon pump. Also, the variability in the surface forcing of the ocean has been found to cause changes in the circulation and carbon pumps.

7.1   Future Work

There are a number of aspects of this work that could be continued or improved. The global carbon transport model could be improved by using circulation fields

from a more recent version of the MIT general circulation model which is now available. In particular, the heat flux in the North Atlantic is more realistic in this improved GCM.

An additional analysis of the global carbon transport model would be to analyse the air-sea heat and CO_2 fluxes along water parcel trajectories. Trajectories could be calculated using the circulation fields and the fluxes monitored. This would provide more information on the size of the region that is required for the heat flux method to infer an accurate CO_2 flux. On a similar theme, there are some observational float data of the air-sea CO_2 and heat flux that is available that could be analysed.

The method used to assess the anthropogenic component of the variability of the CO_2 uptake in chapter 4 has been tested in an idealised 3-D model. This test would be improved if it was carried out in a more realistic model such as the global carbon transport model used in this work.

The increase in the amount of dissolved organic nutrient measurements being taken at sea will hopefully soon allow model parameters to be more realistically determined. This would allow more confidence to be placed in model predictions of the contribution of dissolved organic nutrients to sustaining export production in a subtropical gyre. More DON measurements could also make it possible to estimate the Ekman lateral supply of DON in the subtropical gyre.

The interannual variability in the convective nutrient supply has not be quantified in this work. The method used to infer the mixed layer depth from the heat flux (as described in section 5.5.1) could be used to assess the additional nutrient supply due to the mixed layer being anomalously deep.

Although the variability of the biological carbon pump has been investigated, it is not clear what effect this will have on the air-sea flux of CO_2 . This could be investigated with the Planetary Geostrophic Ocean Model which was used in

this work.

The important role of physical processes on the biogeochemical system of the ocean has long been accepted. However, there are still aspects of the biogeochemical system that are not fully understood. It is hoped that interdisciplinary studies, such as the future work suggested here, will improve our understanding of the complex ocean system.

Appendix A

Planetary-Geostrophic Ocean Model

This appendix contains a review of the ocean model of Samelson and Vallis (1997a, 1997b). The ocean model is used in this work to investigate the relationship between air-sea heat and CO_2 fluxes and to examine dynamical nutrient supplies. For further details of the ocean model see Samelson and Vallis (1997a, 1997b).

A.1   Model Formulation

A.1.1   Interior Equations

The interior equations are the planetary geostrophic equations described by Samelson and Vallis (1997a). The equations are nondimensional and in their cartesian form are,

$$-fv = -p_x - \varepsilon u$$

$$fu = -p_y - \varepsilon v$$

$$p_z + \rho = 0$$

$$u_x + v_y + w_z = 0$$

$$T_t + uT_x + vT_y + wT_z = \kappa_v T_{zz} + \kappa_h \nabla_h^2 T - \lambda \nabla_h^4 T$$

$$S_t + uS_x + vS_y + wS_z = \kappa_v S_{zz} + \kappa_h \nabla_h^2 S - \lambda \nabla_h^4 S$$

$$\rho = S - T$$

where

$$\nabla_h^2 = \frac{\partial^2}{\partial x^2} + \frac{\partial^2}{\partial y^2}.$$

u, v and w are the velocity in the x, y and z directions respectively. ρ, T and S are deviations of density, temperature and salinity from mean values. κ_h and κ_v are the horizontal and vertical diffusivities and λ is the biharmonic diffusivity. ε is a frictional parameter. The subscripts x, y, z and t denote partial derivatives.

The Coriolis parameter, f, is a linear function of y,

$$f = f_0 + \frac{\partial f}{\partial y}(y - y_0) \tag{A.1}$$

where f_0 is the Coriolis parameter at $y = y_0$.

The domain of the model is a rectangular box, with the lateral sides at $x = 0, 1$ and $y = 0, 1$ and a flat bottom at $z = 0$. The interior of the model extends to $z = 1$ and is overlaid by a Ekman layer of thickness δ_E, in which the circulation is governed by a different set of equations. The sea surface is therefore at $z = 1 + \delta_E$.

The model boundary conditions are no normal flow and no normal heat or salt diffusive flux through the lateral boundaries of the model. This implies that the temperature and salinity fields must satisfy two lateral boundary conditions. The set of internal equations allows these boundary conditions to be separately satisfied. No heat or salt flux is allowed through the base of the model. The model also involves a convective adjustment scheme, in which instabilities in the

vertical profile of density are removed. This is implemented at the end of each time step and involves vertically mixing the fluid.

The model integration is performed using centred space differencing, except at the upper boundary where an upwind scheme is used. A second-order Runge-Kutta algorithm is used for the timestepping. The same numerical schemes were used to include carbon, nitrogen and dissolved organic nitrogen (DON) in the PGOM, with the exception that upwind advection was used everywhere for nitrogen and DON.

A.1.2 The Ekman Layer

The Ekman layer is represented as a simple slab layer, which is forced by a wind stress and undergoes heat exchange with the atmosphere. The Ekman layer is of thickness δ_E and provides the upper boundary conditions for temperature and vertical velocity for the model interior.

Assuming the vertically integrated Ekman balance holds, the horizontal Ekman velocities in the x direction (u_E) and in the y direction (v_E) are

$$u_E = \tau^y / f \delta_E \qquad (A.2)$$

$$v_E = -\tau^x / f \delta_E, \qquad (A.3)$$

where $\tau = (\tau^x, \tau^y)$ is the surface wind stress. Using the continuity equation, the vertical velocity in the Ekman layer (w_E) is found using,

$$w_E = \delta_E(u_{Ex} + v_{Ey}). \qquad (A.4)$$

The temperature in the Ekman layer (T_E) is governed by a vertically integrated thermodynamic equation,

$$T_{Et} + (u_A T_E)_x + (v_A T_E)_y = (F_h - F_i)/\delta_E, \qquad (A.5)$$

where F_h is the air-sea heat flux and F_i is the heat flux through the base of the Ekman layer. Heat is transferred from the model interior to the Ekman layer by vertical advection and diffusion and F_i is given by

$$F_i = -w_{z=1}T_1 + \gamma_0 \frac{\kappa_v}{\delta_E}(T_E - T_{z=1}).$$

The advection is upwind, hence if $w_{z=1} > 0$, $T_1 = T_{z=1}$ otherwise $T_1 = T_E$. The temperature in the Ekman layer is relaxed to the imposed atmospheric temperature (T^*) with a time scale (γ_{T_*}), so that

$$F_h = -\gamma_{T_*}(T_E - T^*).$$

The advection velocities in equation (A.5) are defined as

$$(u_A, v_A) = (u_E, v_E) + (u, v,)_{z=1}.$$

This definition allows the western boundary current to advect warm water to the north. The salinity in the Ekman layer is governed by the same equations as temperature.

A.1.3 Dimensional Scales for the Model

The model is nondimensional but dimensional results can be obtained by multiplying the nondimensional quantity by the correct dimensional scale. The carbon chemistry scheme requires dimensional temperature and salinity values to calculate the equilibrium constants. The dimensional scales used to make the model results dimensional are shown in table A.1. These dimensional scales can then be used to derive dimensional scales for all the other quantities in the model (table A.2).

Quantity	Symbol	Dimensional scale
Length scale	L	5×10^6 m
Depth scale	H	5×10^3 m
Coriolis parameter	$f_* = f(35^oN)$	8.4×10^{-5} s^{-1}
Gravity	g	9.8 ms^{-2}
Vertical velocity	W	10^{-6} ms^{-1}
Mean density	ρ_0	1023 kg m^{-3}
Mean temperature	T_0	300 K
Mean salinity	S_0	35

Table A.1: Table of dimensional scales used to present the results of PGOM.

Quantity	Symbol	Derivation	Dimensional scale
Horizontal velocity	U	WL/D	1×10^{-3} m s^{-1}
Time	t_*	$D/W = L/U$	5×10^9 s $= 160$ yr
Density variations	ρ_*	$(\rho_0 f_* UL)/(gD)$	8.8×10^{-3} kg m$^{-3} \sim 0.01$ σ_θ
Temperature variations	T_D	$\rho_*/(\rho_0 \alpha_T)$	0.043 K
Vertical diffusivity	K_v	WD	5×10^{-3} m^2 s^{-1}
Horizontal diffusivity	K_h	UL	5×10^4 m^2 s^{-1}
Biharmonic diffusivity	Λ	UL^3	1.25×10^{17} m^4 s^{-1}
Frictional parameter	ε	f_*	8.4×10^{-5}s^{-1}
Air-sea flux coefficient	Γ_{T^*}	W	10^{-6}ms^{-1}

Table A.2: Table of derived dimensional scales. ($\alpha_T = 2 \times 10^{-4}$K^{-1} is used for the thermal expansivity of sea water).

251

A.1.4 Parameters used in the Model Run

The wind stress is purely zonal and has the form,

$$\tau^x = \tau_0(f(y)/f_0)sin(2\pi y),$$

where τ_0 is a constant and equals $-w_{E0}f_0/2\pi$. Therefore, using equations (A.2), (A.3) and (A.4) the horizontal and vertical Ekman velocities are

$$u_E = 0$$

$$v_E = -(\tau_0/f_0\delta_E)sin(2\pi y)$$

$$w_E = w_{E0}cos(2\pi y).$$

$we0$ is a constant and is equal to the maximum Ekman upwelling that occurs in the model. $we0$ is the input parameter to the model that controls the magnitude of the wind stress.

In the non-seasonal version of the model, the nondimensional atmospheric temperature is a linear function of y,

$$T^* = -520y, \quad \text{(i.e. 22.4K/5000km)}.$$

The surface salinity is relaxed to a non-seasonal salinity field that is a function of y only and is shown in figure A.1. The other model parameter are presented in table A.3.

The model is in the northern hemisphere centred on 35°N at $y = y_0 = 0.5$. The horizontal resolution of the model is 31 interior grid boxes in the x and y directions ($\Delta x = \Delta y = \sim 160$ km). The vertical resolution for the carbon model experiments is 16 interior levels, which are stretched to increase in resolution at the top of the domain. The vertical resolution in the euphotic zone is increased for the biological pump experiments.

The timestep used in the model runs was approximately 3 days. The model was generally run for 3000 years to allow the circulation to reach steady state.
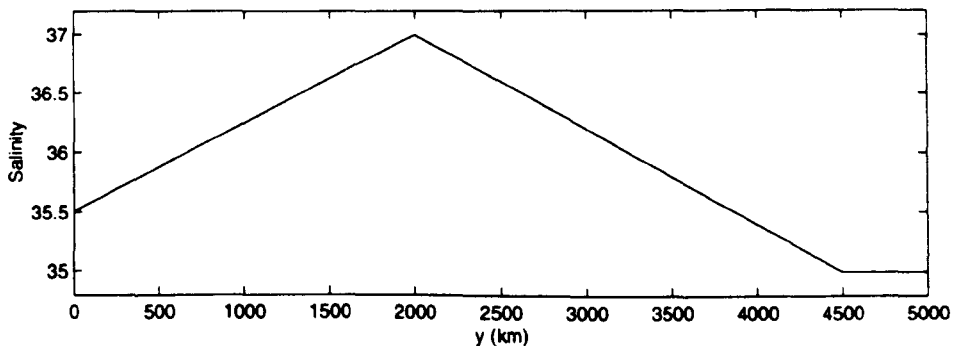
Figure A.1: Model relaxation salinity field against y (km). This field gives a surface salinity distribution comparable to the North Atlantic. Note that y=2500km is equal to 35 °N.

Parameter	Nondimensional value (Dimensional value)
f_0	1 (8.4 $\times 10^{-5}$ s^{-1}
$\partial f/\partial y$	1.1 (1.8 $\times 10^{-11}$ (ms)$^{-1}$
ε	0.02 (1.7 $\times 10^{-6}$ s^{-1}
κ_v	0.005 (0.25 cm^{2}s^{-1})
κ_h	0.04 (2 $\times 10^6$cm^{2}s^{-1})
δ_E	0.005 (25 m)
$\gamma_{T^\bullet} = \gamma_{S^\bullet}$	15 (1.3 m day^{-1})

Table A.3: Values of parameters used in PGOM runs.

A.1.5 Seasonal Model

The model of Samelson and Vallis (1997b) is non-seasonal. Seasonality is believed to be important in the transport of carbon (Follows *et al.*, 1996). Therefore, I added a seasonal cycle to the model. The atmospheric temperature was changed to be a function of time to create a realistic seasonal cycle in sea surface temperature and mixed layer depth.

The nondimensional atmospheric temperature in the seasonal model is a function of both y and t,

$$T^* = -520y + \frac{1}{T_D}(6y + 1)sin(\frac{2\pi t}{\tau_{year}})$$

where T_D is the dimensional scale for temperature and τ_{year} is the number of seconds in a year. Figure A.2 illustrates the seasonal atmospheric temperature cycle.

A.2 Model Fields

The results shown in this section are from a 6000 year model run with variable temperature and salinity with a maximum Ekman pumping 1×10^{-6} ms^{-1} ($we0 = 1$). (The velocity fields are presented in section 3.7.2.)

Cross sections of temperature and salinity during March are shown in figure A.3. A thermocline region forms below the subtropical gyre which shallows towards the tropics. In the tropics, cold water is upwelled to the surface causing the bowing of isotherms. Deep mixed layers in the north are formed at the end of winter. The deep ocean fills with very cold water, which is formed by convection at the northern boundary. An unrealistic feature of the model temperature field is the vertical stratification in the deep ocean which is too low.
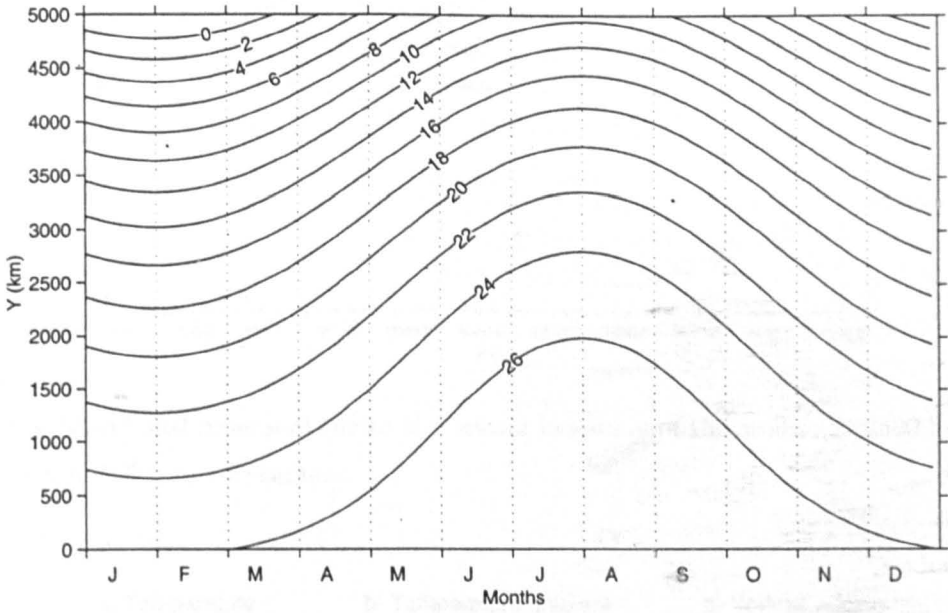
Figure A.2: Model atmospheric temperature cycle (^{o}C) as a function of time and latitude. Note that y=2500km is equal to 35 ^{o}N.
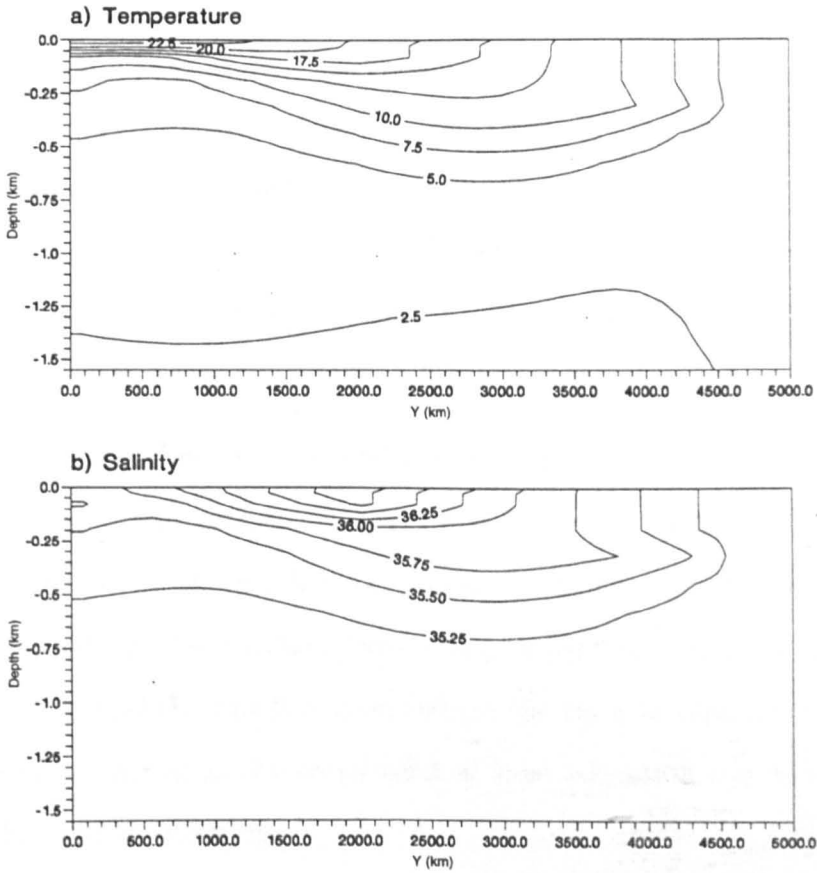
Figure A.3: Meridional cross sections at the central longitude of the model (x=2500 km) of: a) temperature ($^\circ$C); and b) salinity.
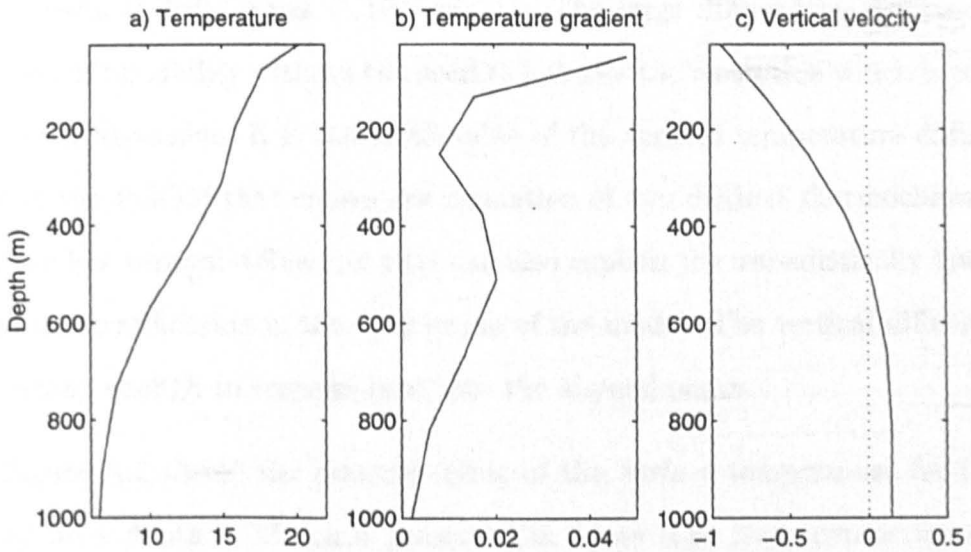
Figure A.4: Vertical profiles at the centre of the model basin for: a) temperature ($^\circ$C); b) $\partial T/\partial z$ ($^\circ$C m^{-1}); and c) vertical velocity (10^{-6}ms^{-1}).

Two thermoclines are formed in the model which are shown more clearly in figure A.4. The upper thermocline, the 'ventilated thermocline' is explained by the theory of Luyten *et al.*(1983). The thermocline is formed by the advection of the meridional surface temperature field down into the ocean by Ekman pumping. The horizontal advection of heat balances the vertical advection of heat in the Luyten *et al.*(1983) theory.

A second thermocline in the model temperature field forms at approximately 500m below the ocean surface. A shallow thermostad separates the two thermoclines. The lower thermocline or 'internal thermocline' is associated with an advective-diffusive heat balance and was proposed by Stommel and Webster (1962). The internal thermocline forms where the vertical velocity changes sign. This location is critical as the small vertical heat advection can be successfully balanced by vertical diffusion.

The vertical thermal diffusivity used in the model is $O(10^{-5}\text{m}^2\text{s}^{-1})$ which agrees with open ocean experiments (Ledwell *et al.*, 1993). However, the majority of ocean circulation models with more complicated governing equations, use larger vertical diffusivities $O(10^{-4}\text{m}^2\text{s}^{-1})$. The large diffusivities overcome the problem of instability without the need to increase the resolution which is computationally expensive. It is the small value of the vertical temperature diffusivity used in the PGOM that causes the formation of two distinct thermoclines. It is also the low vertical diffusivity that can also explain the unrealistically low temperature stratification in the deep ocean of the model. The vertical diffusivity is not strong enough to transfer heat into the abyssal ocean.

Figure A.5 shows the seasonal cycle of the surface temperature field. The mixed layer depth in March is presented in figure A.6. Deep convection occurs at sites on the northern boundary which mixes the entire water column. During summer, the mixed layer depth is equal to the Ekman layer depth (25m).
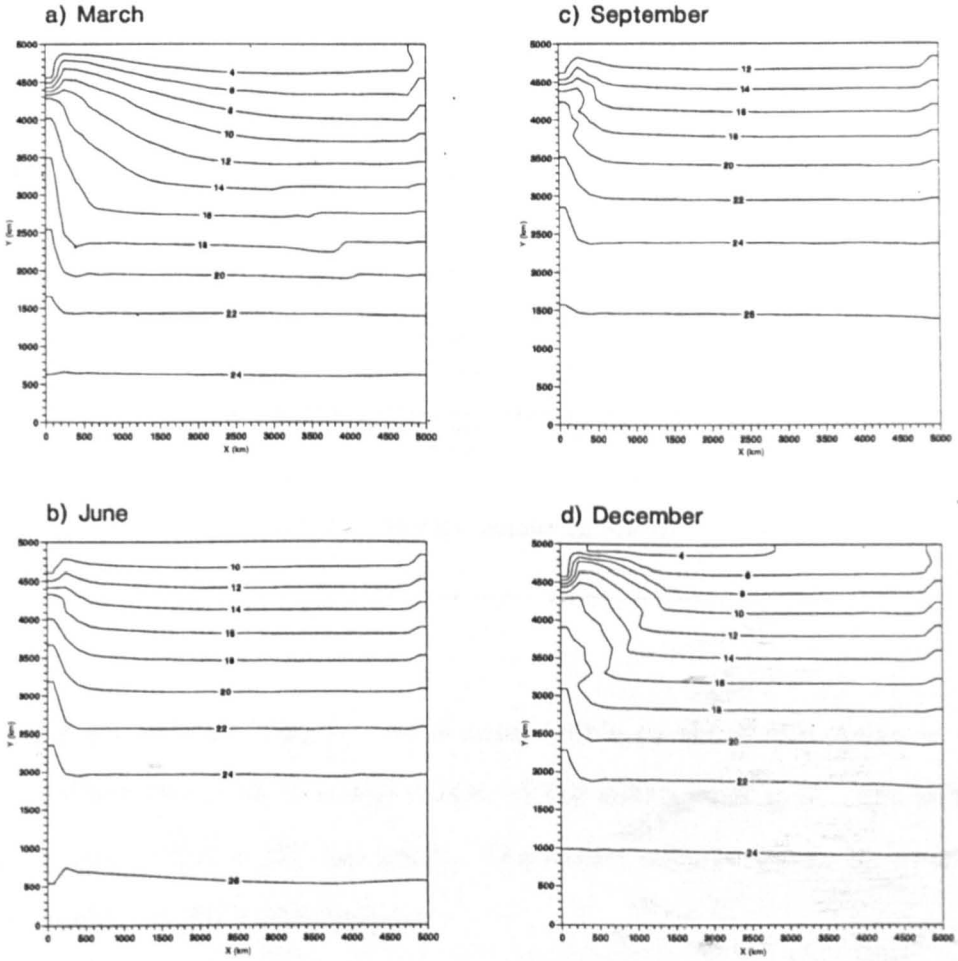
Figure A.5: Surface temperature (^oC) for: a) March; b) June; c) September; and d) December.
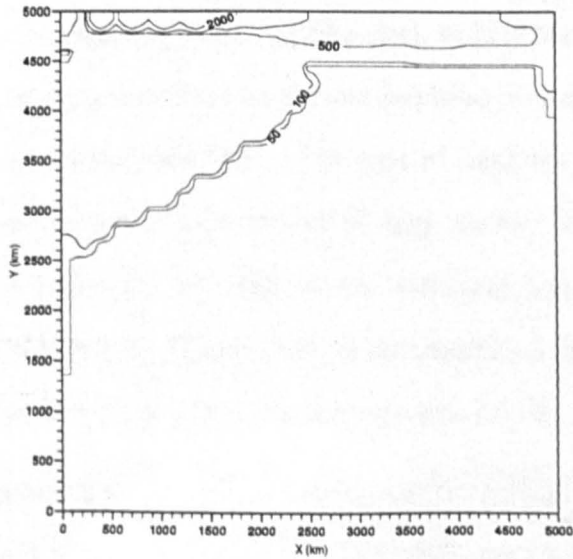
Figure A.6: Mixed layer depth (m) in March.

Figure A.7: Surface salinity in March.

The surface salinity (figure A.7) is comparable to the North Atlantic with salinities greater than 36.75 in the centre of the subtropical gyre. The salinity then decreases to the south and north. The lowest salinity values occur in the northern region of the model basin.

The annual mean air-sea heat flux is presented in figure A.8. The tropics gains heat from the atmosphere warming the deep cold water which upwells to the surface. The ocean transfers heat to the atmosphere in the western boundary current and in the northern boundary. The loss of heat to the atmosphere at the northern boundary causes the formation of deep water. Over the subtropical gyre, the heat flux is generally into the ocean, warming the water as it moves south. There is a small region of heat loss in the south of the subtropical gyre which is caused by the horizontal Ekman advection carrying warm water north.

The net northwards transport at $y = 1370$ km ($24\,°N$) is $0.22 \times 10^{15} W$. Ocean measurements of the heat transport of the North Atlantic reveal the northwards heat transport to be $O(10^{15} W)$ (Isemer *et al.*, 1989). Hence the heat trans-

Figure A.8: Annual mean air-sea heat flux (Wm^{-2}).

port of the model is too low. The discrepancy is primarily caused by the low vertical diffusivity used in the model runs. When deep water is formed in the northern latitudes, it must eventually return to the surface. The deep water must be warmed to rise back to the surface and complete the thermohaline circulation. In the PGOM, the deep water is not warmed at a sufficient rate to give a realistic northwards heat transport. Munk (1966) investigated the size of the vertical diffusivity needed to create the observed stratification using a simple 1-D advective-diffusive balance and found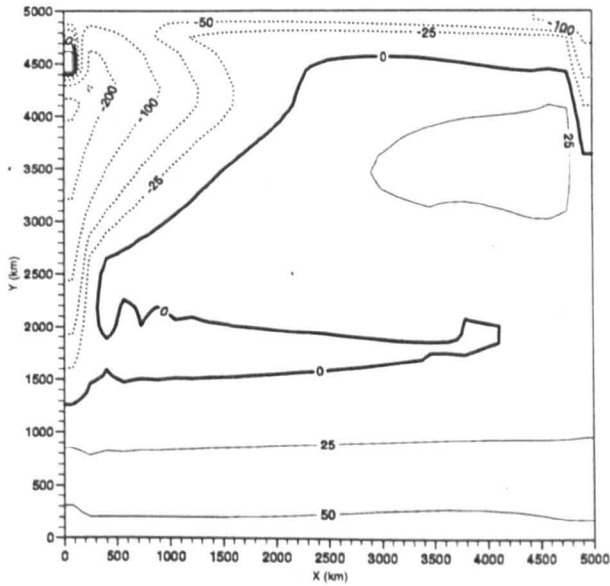 that a vertical diffusivity of $O(10^{-4}m^2s^{-1})$ was required. However, open ocean experiments have measured the vertical diffusivity to be $O(10^{-5}m^2s^{-1})$ (Ledwell et al., 1993) which appears to contradict the findings of Munk (1966). The apparent contradiction can be explained if the value found by Munk (1966) represents an average value. In the open ocean (away from topography) mixing is weak but in specific regions of the ocean mixing is greatly enhanced (Munk and Wunsch, 1998; Polzin et al., 1997). Samelson (1998) experimented with variable vertical diffusivity values in PGOM. If the vertical diffusivity was uniformly increased, Samelson (1998)

found that the deep stratification increased. Samelson (1998) also found that the deep stratification increased if the interior vertical diffusivity was kept realistically low ($O(10^{-5}\text{m}^2\text{s}^{-1})$) but the vertical diffusivity along the eastern boundary was greatly enhanced.

Appendix B

Global Carbon Transport Model

B.1 General Circulation Model

The global carbon model uses fields generated by the MIT model (Marshall *et al.*, 1997a,b). The MIT model is forced with monthly wind-stress and surface fluxes (from NCEP reanalysis). The heat and freshwater surface fluxes are equal to the observed flux plus a restoring term. The air-sea heat and freshwater fluxes are thus,

$$F_h = F_h{}^{obs} - z_0\rho_0 c_p \mathcal{K}_T(T - T^{obs}) \tag{B.1}$$

$$F_w = F_w{}^{obs} + \frac{z_0}{S_0}\mathcal{K}_S(S - S^{obs}). \tag{B.2}$$

where $F_h{}^{obs}$ is the climatological monthly mean air-sea heat flux and $F_w{}^{obs}$ is the climatological annual mean freshwater flux. T and S are the model surface temperature and salinity. T^{obs} and S^{obs} are the monthly surface temperature and salinity from Levitus and Boyer (1994) and Levitus *et al.*(1994). λ_T and λ_S are the inverse restoring timescales and both equal 1/75 days. z_0 is the depth of the top model layer (50 m) and S_0 is a reference salinity set to 35. The air-sea heat and freshwater fluxes used in this work were computed using the monthly mean surface temperature and salinity fields output from the GCM.

The monthly fields used in the carbon model were obtained over the last year of a GCM run which was initialised with Levitus climatology and run for 150 years. The temperature and salinity fields for January are shown in figure B.1. Convective mixing is parameterized in the GCM by vertical homogenisation when the density field becomes unstable or neutrally stable. A convective index was calculated from the GCM run to include the effect of convective mixing in the offline carbon model.

B.2   Carbon Transport Model

The subgridscale mixing processes were parameterized by Laplacian diffusion ($k_h = 10^3$ m^2 s^{-1} and $k_v = 10^{-5}$ m^2 s^{-1}) and the eddy parameterization scheme of Gent and McWilliams (1990). Convective mixing was included using the convective index output from the GCM. The convective index is equal to the frequency with which vertically adjacent cells were homogenised (with respect to tracer properties) by convective adjustment in the GCM. The index has a range of 0 (no mixing) to 1 (mixing at every timestep in the sampling period) and is stored as monthly three-dimensional fields. Statistics of the vertical mixing in the offline model are forced to be consistent with GCM mixing statistics at each pair of grid boxes. The carbon governing equation was integrated using Adams-Bashforth timestepping and centred space differencing. A timestep of one day was used.

The surface freshwater flux of the model should directly affect the surface concentration through changing the volume of water in the surface layer. However, the dilution effect was not included in the carbon transport model due to an apparent large freshwater loss from the GCM. The apparent freshwater loss is caused in the GCM by the magnitude of the relaxation term in the freshwater flux expression (equation B.2). The relaxation term is comparable to the obser-
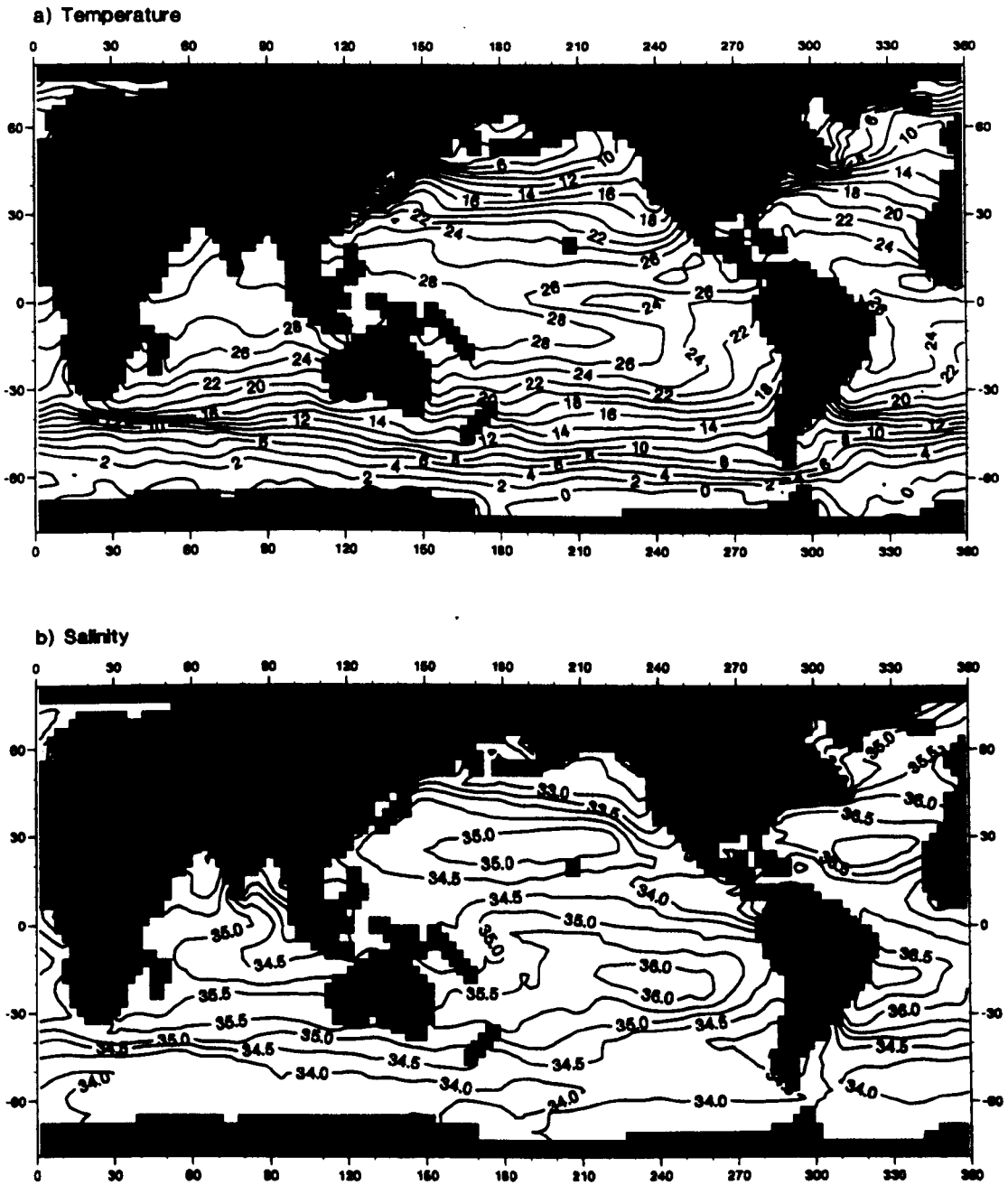
Figure B.1: Monthly mean fields from the MIT GCM run for January of: a) surface temperature ($^\circ$C); and b) salinity.

Region	F_w	$F_w{}^{obs}$	$\frac{z_0}{S_0}\mathcal{K}_S(S - S^{obs})$
N. Atlantic subarctic (north of 50 °N)	12.6	6.6	6.0
N. Atlantic gyre (14 °N to 50 °N)	-30.3	-50.9	20.6
N. Pacific gyre (14 °N to 50 °N)	-37.0	-8.6	-28.4
Equatorial (14 °S to 14 °N)	-52.3	51.4	-103.7
Southern gyres (50 °S to 14 °S)	-107.2	-65.0	-42.2
Southern Ocean (south of 50 °S)	29.8	40.3	-10.5

Table B.1: Annual freshwater fluxes (km^3 day^{-1}) and contributing terms for different ocean regions of the MIT GCM. The terms are defined as in equation (B.2).

vational flux in the freshwater fluxes (table B.1). The relaxation term causes a net flux of freshwater out of the ocean over a year at a rate of 184 km^3 day^{-1}. The air-sea heat flux of the GCM is dominated by the observational flux term in equation (B.1) and, therefore, does not suffer from the problem of a large apparent gain or loss of heat.

Appendix C

Modelling the Air-Sea Flux of CO_2

The air-sea flux of CO_2 is determined by the difference in partial pressures of carbon dioxide between the atmosphere and ocean,

$$F_{CO_2} = \kappa\alpha(pCO_2^{atmos} - pCO_2^{ocean}). \qquad (C.1)$$

Hence, the pCO_2 of the surface ocean needs to be calculated in a carbon model. In all of the models, pCO_2 is calculated by solving the full set of carbon equilibria equations using the scheme of Hoffert *et al.*(1979) as described in chapter 2.

A difficulty in modelling the air-sea flux of CO_2 is that the change in carbon concentration caused by the flux is dependent on pCO_2 , but in turn pCO_2 is dependent on the carbon concentration. To solve this problem an iterative process was used. The value of pCO_2^{ocean} used in equation (C.1) is an average of the pCO_2 values corresponding to the carbon concentration before and after the air-sea exchange. The Fortran code for calculating pCO_2 in the models was provided by Michael Follows at MIT.

In the simple models of chapter 3, a value of 20 cm hr^{-1} was used for κ. This is the gas exchange velocity found by Broecker *et al.*(1985) from the global

[14]Cbudget associated with a temperature of 20°C. It was also assumed that the quantity ($\kappa \alpha$) was independent of temperature. Hence, α evaluated at 20°C was used in the air-sea CO_2 flux equation.

In the MIT carbon model used in chapter 4, the gas exchange velocity was parameterized as a function of wind speed using the relationship of Wanninkhof (1992) (equation 2.17). The Schmidt number (S_c) was calculated using the following empirical relationship which was derived by Wanninkhof (1992) using the experimental data of Jähne et al.(1987) for a salinity of 35,

$$S_c = 2073.1 - 125.62T + 3.6276T^2 - 0.004317T^3$$

where T is temperature in °C. S_c for CO_2 in seawater is equal to 660 at 20 °C. The global annual mean gas transfer velocity of the model was 12.6 cm hr^{-1} at a temperature of 20 °C.

In the carbon chemistry scheme of all the models, a constant value of 409 μ mol kg^{-1} was assummed for $\sum B$. In the carbon model runs using PGOM, TA was modelled as a function of salinity using the empirical relationship found by Brewer et al.(1986) from North Atlantic observations,

$$TA = 547.05 + 50.560S,$$

where TA is in units of μ mol kg^{-1}and S is salinity in psu. In all other models, TA was defined as,

$$TA = 66S$$

with units of μmol kg^{-1}. This relationship was selected as a global representation of the TA and S relationships from GEOSECS data presented by Campbell (1983).

The solubility constant of CO_2 was calculated using the formula of Weiss (1974). The carbon equilibrium constants, k_1 and k_2, were computed using

the empirical relationships of Goyet and Poisson (1989) for the PGOM. The other carbon models used the empirical relationships of Dickson and Millero (1987) found using the data of Mehrbach *et al.*(1973). The formula of Brewer *et al.*(1986) was used for k_w, and k_b was evaluated using the relationship of Takahashi *et al.*(1981). All the equilibrium constants and the CO_2 solubility are functions of temperature and salinity.

References

Archer, D., E. T. Peltzer and D. L. Kirchman, 1997. A timescale for dissolved organic carbon production in equatorial Pacific surface waters. *Glob. Biogeochem. Cycles*, **11**, 435-452.

Bacastow, R. and E. Maier-Reimer, 1990. Ocean-circulation model of the carbon cycle. *Climate Dynamics*, **4**, 95-125.

Bacastow, R. and E. Maier-Reimer, 1991. Dissolved organic carbon in modelling oceanic new production. *Global Biogeochem. Cycles*, **5**, 71-85.

Baes, C. F., 1982. Effects of ocean chemistry and biology on atmospheric carbon dioxide. *Carbon Dioxide Review*. W.C.Clark ed. Oxford University Press.

Björkström, A., 1986. One-dimensional and two-dimensional ocean models for predicting the distribution of CO_2 between the ocean and the atmosphere. *The Changing Carbon Cycle. A Global Analysis*. J.R.Trabalka and D.E.Reichle, eds. Springer-Verlag, New York.

Brewer, P. G., A. L. Bradshaw and R. T. Williams, 1986. Measurements of total carbon dioxide and alkalinity in the North Atlantic Ocean in 1981. *The Changing Carbon Cycle: A Global Analysis.*, ed. J. R. Trabalka and D. E. Reichle, Springer-Verlag, New York, 592pp.

Brewer, P. G., C. Goyet and D. Dyrssen, 1989. Carbon dioxide transport by ocean currents at 25°N latitude in the Atlantic Ocean. *Science*, **246**, 477-479.

Brewer, P. G., 1991. UNEScO. As described in Watson *et al.*(1995).

Broecker, W. S., 1991. The great ocean conveyor. *Oceanogr.*,**4**, 79-89.

Broecker, W. S. and T-H. Peng, 1974. Gas exchange rates between air and sea. *Tellus*, **26**, 21-35.

Broecker, W. S. and T-H. Peng, 1982. *Tracers in the sea*. Eldigio Press, Lamont Doherty Geological Observations, Palisades, New York.

Broecker, W. S., T.-H. Peng, G. Ostlund and M. Stuiver, 1985. The distribution of bomb radiocarbon in the ocean. *J. Geophys. Res.*, **90**, 6953-6970.

Broecker, W. S. and T-H. Peng, 1992. Interhemisphere transport of carbon dioxide by the ocean circulation. *Nature*, **356**, 587-593.

Bunker, A. F., 1976. Computations of surface energy flux and annual air-sea interaction cycles of the North Atlantic Ocean. *Mon. Wea. Rev.*, **104**, 1122-1140.

Callendar, G. S., 1938. The artificial production of carbon dioxide and its influence on temperature. *Quart. J. Roy. Met. Soc.*, **64**, 223-240.

Campbell, J. A., 1983. Geochemical ocean sections study. *Chemical Oceanography*. eds. J. P. Riley and R. Chester. Academic Press.

Carlson, C. A., H. W. Ducklow and A. F. Michaels, 1994. Annual flux of dissolved organic carbon from the euphotic zone in the northwestern Sargasso Sea. *Nature*, **371**, 405-408.

Chen, G-T. and F. J. Millero, 1979. Gradual increase in oceanic CO_2. *Nature*, **277**, 205-206.

Conkright, M. E., S. Levitus, T. P. Boyer, 1994. World Ocean Atlas 1994, Vol. 1: Nutrients, NOAA Atlas NESDIS 1, U.S. Dept. of Commerce, Washington D.C., 150pp.

Craig, H., 1957. The natural distribution of radiocarbon and the exchange time of carbon dioxide between atmosphere and ocean. *Tellus*, **9**, 1-17.

Crane, A. J., 1988. The use of tracers in modelling the ocean uptake of carbon dioxide. *Phil. Trans. R. Soc. Lond.*, **A235**, 23-42. Denman, K. L., 1973. A time-dependent model of the upper ocean. *J. Phys. Oceanogr.*, **3**, 173-184.

Dickson, A. G. and F. J. Millero, 1987. A comparison of the equilibrium- constants for the dissociation of carbonic-acid in seawater media. *Deep-Sea Res. A - Oceanographic Research Papers*, **34**, 1733-1743.

Dickson, R., 1997. From the Labrador Sea to global change. *Nature*, **386**, 649-650.

Doney, S. C., 1997. The ocean's productive deserts. *Nature*, **389**, 905-906.

Doval, M. D., F. Fraga and F. F. Perez, 1997. Determination of dissolved organic nitrogen in seawater using Kjeldahl digestion after inorganic nitrogen removal. *Oceanologica Acta*, **20**, 713-720.

Dugdale, R. C. and J. J. Goering, 1967. Uptake of new and regenerated forms of nitrogen in primary productivity. *Limnol. Oceanogr*, **12**, 196-206.

Emerson, S., P. Quay, D. Karl, C. Winn, L. Tupas and M. Landry, 1997. Experimental determination of the organic carbon flux from open-ocean surface water. *Nature*, **389**, 951-954.

Fan, S., M. Gloor, J. Mahlman, S. Pacala, J. Sarmiento, T. Takahashi and P. Tans, 1998. A large terrestrial carbon sink in North America implied by atmospheric and oceanic carbon dioxide data and models. *Science*, **282**, 442-446.

Follows, M. J. and J. C. Marshall, 1999. Interannual variability of export production and the North Atlantic Oscillation. *Submitted to Deep-Sea Res.*

Follows, M. J., R. G. Williams and J. C. Marshall, 1996. The solubility pump of carbon in the subtropical gyre of the North Atlantic. *J. Mar. Res.*, **54**, 605-630.

Francey, R. J., P. P. Tans, C. E. Allison, I. G. Enting, J. W. C. White and M. Troller, 1995. Changes in oceanic and terrestrial carbon uptake since 1982. *Nature*, **373**, 326-373.

Friedli, H., H. Lotscher, H. Oeschger, U. Siegenthaler and B. Stauffer, 1986. Ice core record of the C^{13}/C^{12} ratio of atmospheric CO_2 in the past two centuries. *Nature*, **324**, 237-238.

Ganachaud, A. and C. Wunsch, 1998. Large scale oceanic nutrient and oxygen fluxes. *International WOCE Newsletter*, **32**, 12-15.

Gent, P. R. and J. C. McWilliams, 1990. Isopycnal mixing in ocean circulation models. *J. Phys. Oceanogr.*, **20**, 150-155.

Glover, D. M. and P. G. Brewer, 1988. Estimates of the wintertime mixed layer nutrient concentrations in the North Atlantic. *Deep-Sea Res.*, **35**, 1525-1546.

Goyet, C. and A. Poisson, 1989. New determination of carbonic acid dissociation constants in seawater as a function of temperature and salinity. *Deep-sea Res.*, **36**, 1635-1654.

Gruber, N. and J. L. Sarmiento, 1997. Global patterns of marine nitrogen fixation and denitrification. *Global Biogeochem. Cycles*, **11**, 235-266.

Hansell, D. A. and C. A. Carlson, 1998. Net community production of dissolved organic carbon. *Glob. Biogeochem. Cycles*, **12**, 443-453.

Hansell, D. A. and T. Y. Waterhouse, 1997. Controls on the distributions of organic carbon and nitrogen in the eastern Pacific Ocean. *Deep-Sea Res.*, **44**, 843-857.

Hoffert, M. I., Y-C. Wey, A. J. Callegari and W. S. Broecker, 1979. Atmospheric response to deep sea injections of fossil fuel carbon dioxide. *Climate Change*, **2**, 53-68.

Holfort, J., K. M. Johnson, B. Schneider, G. Siedler and D. W. R. Wallace, 1998. Meridional transport of dissolved inorganic carbon in the South Atlantic Ocean. *Glob. Biogeochem. Cycles*, **12**, 479-499.

Hurrell, J. W., 1995. Decadal trends in the North Atlantic Oscillation: Regional temperatures and precipitation, *Science*, **269**, 676-679.

Isemer, H-J., J. Willebrand and L. Hasse, 1989. Fine adjustment of large scale air-sea energy flux parameterizations by direct estimates of ocean heat transport. *J. Climate*, **2**, 1173-1184.

Jähne, B., G. Heinz and W. Dietrich, 1987. Measurement of the diffusion coefficients of sparingly soluble gases in water with a modified Barrer method. *J. Geophys. Res.*, **92**, 10767-10776.

Jenkins, W. J., 1998. Studying subtroipcal thermocline ventilation and circulation using tritium and He-3. *J. Geophys. Res.*, **103**, 15817-15831.

Jenkins, W. J., 1988. Nitrate flux into the euphotic zone near Bermuda. *Nature*, **331**, 521-523.

Jenkins, W. J., 1982. Oxygen utilization rates in North Atlantic subtropical gyre and primary production in oligotrophic systems. *Nature*, **300**, 246-248.

Jenkins, W. J., 1990. Tritium and ^{3}He in the Sargasso Sea. *J. Mar. Res.*, **38**, 533-569.

Jenkins, W. J. and J. C. Goldman, 1985. Seasonally oxygen cycling and primary production in the Sargasso Sea. *J. Mar. Res.*, **43**, 465-491.

Josey, S. A., E. C. Kent, D. Oakley and P. K. Taylor, 1996. A new global air-sea heat and momentum flux climatology. *International WOCE Newsletter*, **24**, 3-4.

Josey, S. A., E. C. Kent and P. K. Taylor, 1999. New insights into the ocean heat budget closure problem from analysis of the SOC air-sea flux climatology. J. Climate. In press.

Karl, D., R. Letelier, L. Tupas, J. Dore, J. Christian and D. Hebel, 1997. The role of nitrogen fixation in biogeochemical cycling in the subtropical North Pacific Ocean. *Nature*, **388**, 533-538.

Keeling, C. D. and M. Heimann, 1986. Meridional eddy diffusion model of transport of atmospheric carbon dioxide. 2. Mean annual carbon cycle. *J. Geophys. Res.*, **91**, 7782-7796.

Keeling, C. D., T. P. Whorf, M. Wahlen and J. van der Pilcht, 1995. Interannual extremes in the rate of rise of atmospheric carbon dioxide since 1980. *Nature*, **375**, 666-670.

Keeling, R. F. and T-H, Peng, 1995. Transport of heat, CO_2 and O_2 by the Atlantic's thermohaline circulation. *Phil. Trans. R. Soc. Lond.*, **B348**, 133-142.

Keeling, R. F. and S. R. Shertz, 1992. Seasonal and interannual variations in atmospheric oxygen and implications for the global carbon cycle. *Nature*, **358**, 723-727.

Kirchman, D. L., C. Lancelot, M. Fasham, L. Legendre, G. Radach and M. Scott, 1993. Dissolved organic matter in biogeochemical models of the ocean. In *Towards a Model of Ocean Biogeochemical Processes*, NATO ASI Series Vol. I 10. eds. G. T. Ecans and M. J. R. Fasham, pp. 209-225, Springer, Berlin.

Knap, A., T. Jickells, A. Pszenny and J. Galloway, 1986. Significance of an atmospheric-derived fixed nitrogen on productivity of the Sargasso Sea. *Nature*, **320**, 158-160.

Kortzinger, A., L. Mintrop and J. C. Duinker, 1998. On the penetration of anthropogenic CO_2 into the North Atlantic Ocean. *J. Geophys. Res.*, **103**, 18681-18689.

Kraus, E. B. and J. S. Turner, 1967. A one-dimensional model of the seasonal thermocline. II. The general theory and its consequences. *Tellus*, **19**, 98-105.

Ledwell, L., A. Watson and C. Law, 1993. Evidence for slow mixing across the pycnocline from an open-ocean tracer-release experiment. *Nature*, **364**, 701-703.

Lee, K., R. Wanninkhof, T. Takahashi, S. C. Doney and R. A. Feely, 1998. Low interannual variability in recent oceanic uptake of atmospheric carbon dioxide. *Nature*, **396**, 155-159.

Lefèvre, N., 1997. Objective mapping of the seasonal variability of ΔpCO_2 in the North Atlantic Ocean. *The Global Atmosphere and Ocean System*, *5*, 247-271.

Lefèvre, N. A. Watson, D. Cooper, R. Weiss, T. Takahashi and S. Sutherland, 1999. Assessing the seasonality of the oceanic sink of CO_2 in the northern hemisphere. *Glob. Biogeochem. Cycles*. In press.

Levitus, S. and T. P. Boyer, 1994. World Ocean Atlas 1994, Vol. 4: Temperature, NOAA Atlas NESDIS 4, U.S. Dept. of Commerce, Washington D.C., 117pp.

Levitus, S., R. Burgett and T. P. Boyer, 1994. World Ocean Atlas 1994, Vol. 3: Salinity, NOAA Atlas NESDIS 3, U.S. Dept. of Commerce, Washington D.C., 99pp.

Lewis, M. R., W. G. Harrison, N. S. Oakey, D. Hebert and T. Platt, 1986. Vertical nitrate fluxes in the oligotrophic ocean. *Science*, **234**, 870-873.

Lipschultz, F. and N. J. P. Owens, 1996. An assessment of nitrogen fixation as a source of nitrogen to the North Atlantic Ocean. *Biogeochem.*, bf 35, 261-274.

Liss, P. S. and L. Merlivat, 1986. *Air-Sea Gas Exchange Rates : Introduction and Synthesis*. The Role of Air-Sea Exchange in Geochemical Cycling. ed. P. Buat-Menard. D. Reidel, Hingham, Mass.

Lohrenz, S. E., G. A. Knauer, V. L. Asper, M. Tuel, A.F. Michaels and A. H. Knap, 1992. Seasonal variability in primary production and particle flux in the northwestern Sargasso Sea: U.S. JGOFS Bermuda Atlantic Time-series Study. *Deep-Sea Res.*, **39**, 1373-1391.

Luyten, J., J. Pedlosky and H. Stommel, 1983. The ventilated thermocline. *J. Phys. Oceanogr.*, **13**, 292-309.

Maier-Reimer, E. and K. Hasselmann, 1987. Transport and storage of CO_2 in the ocean - an inorganic ocean-circulation carbon cycle mode. *Clim. Dyn.*, **2**, 63-90.

Manabe, S. and R. J. Stouffer, 1993. Century-scale effects of increased atmospheric CO_2 on the ocean-atmosphere system. *Nature*, **364**, 215-218.

Marshall, J. C., A. Adcroft, C. Hill, L. Perelman and C. Heisey, 1997a. A finite-volume, incompressible Navier-Stokes model for studies of the ocean on parallel computers. *J. Geophys. Res.*, **102**, 5733-5766.

Marshall, J. C., C. Hill, L. Perelman and A. Adcroft, 1997b. Hydrostatic, quasi-hydrostatic and non-hydrostatic ocean modelling. *J. Geophys. Res.*, **102**, 5733-3752.

Marshall, J. C., A. J. G. Nurser and R. G. Williams, 1993. Inferring the subduction rate and period over the North Atlantic. *J. Phys. Ocean.*, **23**, 1315-1329.

Martin, J. H., G. A. Knauer, D. M. Karl and W. W. Broenkow, 1987. VERTEX: Carbon cycling in the northeast Pacific. *Deep-Sea Res.*, **34**, 267-285.

McGuillicuddy, JR, D. J. and A. R. Robinson, 1997. Eddy-induced nutrient supply and new production in the Sargasso Sea. *Deep-Sea Res.*, **44**, 1427-1450.

McGuillicuddy, J. R., D. J., A. R. Robinson, D. A. Siegel, H. W. Jannasch, R. Johnson, T. D. Dickey, J. McNeil, A. F. Michaels and A. H. Knap, 1998. New evidence for the impact of mesoscale eddies on biogeochemical cycling in the Sargasso Sea. *Nature*, **394**, 263-265.

Mehrbach, C., C. H. Culberson, J. E. Hawley and R. M. Pytkowicz, 1973. Measurement of the apparent dissociation constants of carbonic acid in seawater at atmospheric pressure. *Limn. and Ocean.*, **18**, 897-.907.

Michaels, A. F., A. H. Knap, R.L. Dow, K. Gundersen, R. J. Johnson, J. Sorenson, A. Close, G. A. Knauer, S. E. Lohrenz, V. A. Asper, M. Tuel and R. Bidigare, 1994. Seasonal patterns of ocean biogeochemistry at the U. S. JGOFS Bermuda Atlantic Time-series Study site. *Deep-Sea Res.*, **41**, 1013-1038.

Michaels, A. F., D. Olson, J. L. Sarmiento, J. W. Ammerman, K. Fanning, R. Jahnke, A. H. Knap, F. Lipschultz and J. M. Prospero, 1996. Inputs, losses and transformations of nitrogen and phosphorus in the pelagic North Atlantic Ocean. *Biogeochem.*, **35**, 181-226.

Munk, W., 1966. Abyssal recipes. *Deep-Sea Res.*, **13**, 707-730.

Munk, W. and C. Wunsch, 1998. The moon and mixing: Abyssal recipes II. *Deep-Sea Res. I*, **45**, 1977-2010.

Najjar, R.G., 1990. Simulations of the phosphorus and oxygen cycles in the world ocean using a GCM. Thesis, Princeton.

Najjar, R. G., J. L. Sarmiento and J. R. Toggweiler, 1992. Downward transport and fate of organic matter in the ocean: Simulations with a general circulation model. *Glob. Biogeochem. Cycles*, **6**, 45-76.

Neftel, A., E. Moor, H. Oeschger and B. Stauffer, 1985. Evidence from polar ice cores for the increase in atmospheric CO_2 . *Nature*, **315**, 45-47.

Oeschger, H., U. Siegenthaler, U. Schottener and A. Gugelmann, 1975. A box diffusion model to study the carbon dioxide exchange in nature. *Tellus*, **27**, 168-192.

Oschlies, A. and V. Garçon, 1998. Eddy-induced enhancement of primary production in a model of the North Atlantic Ocean. *Nature*, **394**, 266-269.

Peng, T-H, T. Takahashi and W. S. Broecker, 1987. Seasonal variability of carbon dioxide, nutrients and oxygen in the northern North Atlantic surface water : observations and a model. *Tellus*, **39B**, 439-458.

Peng, T-H, R. Wanninkhof, J. L. Bullister, R. A. Feely and T. Takahashi, 1998. Quantification of decadal anthropogenic CO_2 uptake in the ocean based on dissolved inorganic carbon measurements. *Nature*, **396**, 560-563.

Polzin, K. L., J. M. Toole, J. R. Ledwell and R. W. Schmitt, 1997. Spatial variability in turbulent mixing in the abyssal ocean. *Science*, **276**, 93-96.

Quay, P. D., B. Tilbrook and C. S. Wong, 1992. Oceanic uptake of fossil fuel CO_2 : Carbon-13 evidence. *Science*, **256**, 74-79.

Revelle, R. and H. E. Suess, 1957. Carbon dioxide exchange between atmosphere and ocean and the question of an increase of atmospheric CO_2 during the past decades. *Tellus*, **9**, 18-27.

Rintoul, S. R. and C. Wunsch, 1991. Mass, heat, oxygen and nutrient fluxes and budgets in the North Atlantic Ocean, *Deep-Sea Res. I*, **38**, Suppl. 1., S355-S377.

Robertson, J. E. and A. J. Watson, 1992. Thermal skin effect of the surface ocean and its implications for CO_2 uptake. *Nature*, **358**, 738-740.

Samelson, R. M., 1998. Large-scale circulation with locally enhanced vertical mixing. *J. Phys. Oceanogr.*, **28**, 712-726.

Samelson, R. M. and G. K. Vallis, 1997a. A simple friction and diffusion scheme for planetary-geostrophic basin models. *J. Phys. Oceanogr.*, **27**, 186-194.

Samelson, R. M. and G .K.Vallis, 1997b. Large-scale circulation with small diapycnal diffusion: The two-thermocline limit. *J. Mar. Res.*, **55**, 223-275.

Sanders, R. and T. Jickells, 1999. Dissolved organic nutrients in Drake passage. *Submitted to Deep-Sea Res. I.*

Sarmiento, J. L., T. M. C. Hughes, R. J. Stouffer and S. Manabe, 1998. Simulated response of the ocean carbon cycle to anthropogenic climate warming. *Nature*, **393**, 245-249.

Sarmiento, J. L., R. Murnane and C. Le Quere, 1995. Air-sea CO_2 transfer and the carbon budget of the North Atlantic.*Phil. Trans. R. Soc. Lond.*, B **348**, 211-219.

Sarmiento, J. L., J. C. Orr and U. Sigenthaler, 1992. A perturbation simulation of CO_2 uptake in an ocean circulation model. *J. Geophys. Res.*,**97**,3621-3645.

Sarmiento, J. L. and E. T. Sundquist, 1992. Revised budget for the oceanic uptake of anthropogenic carbon dioxide. *Nature*, **356**, 589-593.

Sarmiento, J. L. and J. R. Toggweiler, 1984. A new model for the role of the oceans in determining atmospheric P_{CO_2}. *Nature*, **308**, 621-624.

Sathyendranath, S., R. S. A. Longhurst, C. M. Caverhill and T. Platt, 1995. Regionally and seasonally differentiated primary production in the North Atlantic. *Deep-Sea Res. I*, **42**, 1773-1802.

Siegenthaler, U., 1983. Uptake of excess CO_2 by an outcrop-diffusion model of the ocean. *J. Geophys. Res.*, **88**, C6, 3599-3608.

Siegenthaler, U. and J. L. Sarmiento, 1993. Atmospheric carbon dioxide and the ocean. *Nature*, **365**, 119-125.

da Silva, A. M., C. C. Young and S. Levitus, 1994. Atlas of Surface Marine Data 1994, Volume 1: Algorithms and Procedures. *NOAA Atlas NESDIS4*, U.S. Department of Commerce, NOAA, NESDIS.

Stephens, M. P., G. Samuels, D. B. Olson, R. A. Fine and T. Takahashi, 1995. Sea-air flux of CO_2 in the North Pacific using shipboard and satellite data. *J. Geophys. Res.*, **100**, C7, 13571-13583.

Stommel, H., 1979. Determination of water mass properties of water pumped down from the Ekman layer to the geostrophic flow below.*Proc. Nat. Acad. Sci. U.S.*, **76**, 3051-3055.

Stommel, H. and J. Webster, 1962. Some properties of the thermocline equations in a subtropical gyre. *J. Mar. Res.*, **20**, 42-56.

Takahashi, T., W. S. Broecker and A. E. Bainbridge, 1981. The alkalinity and total carbon dioxide concentration in the world oceans. *Carbon Cycle Modelling.* B.Bolin ed. John Wiley & Sons, New York.

Takahashi, T., R. A. Feely, R. A. Weiss, R. H. Wanninkhof, D. W. Chipman, S. C. Sutherland and T. T. Takahashi, 1997. Global air-sea flux of CO_2 : An estimate based on measurements of sea-air pCO_2 difference. *Proc. Natl. Acad. Sci. USA*, **94**, 8292-8299.

Takahashi, T., J. Olafsson, J. G. Goddard, D. W. Chipman and S. C. Sutherland, 1993. Seasonal variation of CO_2 and nutrients in the high-latitude surface oceans : a comparative study. *Global Biogeochem. Cycles*, **7**, 843-878.

Takahashi, T., R. T. Williams and D. L. Bos, 1981. Carbonate Chemistry; in GEOSECS Atlantic Expedition. Vol.1. Hydrographic Data 1972-1973, National Science Foundation, Washington D.C.

Tans, P. P., I. Y.Fung and T. Takahashi, 1990. Observational constraints on the global atmospheric CO_2 budget. *Science*, **247**, 1431-1438.

Visbeck, M., J. Marshall and H. Jones, 1996. Dynamics of isolated convective regions in the ocean. *J. Phys. Oceanogr.*, **26**, 1721-1734.

Volk, T. and M. I. Hoffert, 1985. Ocean carbon pumps: Analysis of relative strengths and efficiences in ocean-driven atmospheric CO_2 changes. *The Carbon Cycle and Atmospheric CO_2 : Natural Variations Archaen to Present.* eds. E. T. Sundquist and W. S. Broecker. American Geophysical Union, Washington.

Wallace, J. M. and D. S. Gutzler, 1981. Teleconnections in the geopotential height field during the Northern Hemisphere winter. *Mon. Wea. Rev.*, *109*, 784-812.

Wanninkhof, R., 1992. Relationship between wind speed and gas exchange over the ocean. *J. Geophys. Res.*, **97**, 7373-7382.

Wanninkhof, R., J. R. Ledwell and W. S. Broecker, 1985. Gas exchange- wind speed relation measured with sulfur hexafluoride on a lake. *Science*, **227**, 1224-1226.

Watson. A. J., P. D. Nightingale and D. J. Cooper, 1995. Modelling atmosphere-ocean CO_2 transfer. *Phil. Trans. R. Soc. Lond.*, **B 348**, 125-132.

Watson, A. J., R. C. Upstill-Goddard and P. S. Liss, 1991a. Air-sea gas exchange in rough and stormy seas measured by a dual-tracer technique. *Nature*, **349**, 145-147.

Watson, A. J., C. Robinson, J. E. Robinson, P. J.le B. Williams and M. J. R. Fasham, 1991b. Spatial variability in the sink for atmospheric carbon dioxide in the North Atlantic. *Nature*, **350**, 50-53.

Watson, R. T. and H. Rodhe, H. Oeschger and U. Siegenthaler, 1990. Greenhouse gases and aerosols. *The IPCC Scientific Assessment.* Cambridge University Press.

Weiss, R. F., 1974. Carbon dioxide in water and seawater : The solubility of a non-ideal gas. *Mar. Chem.*, **2**, 203-215.

Williams, R. G., 1987. The influence of air-sea interaction on ocean synoptic-scale eddies. Ph.D. thesis, University of East Anglia, U.K.

Williams. R. G., 1988. Modification of ocean eddies by air-sea interaction. *J. Geophys. Res.*, **93**, 15523-15533.

Williams, R. G. and M. J. Follows, 1998a. The Ekman transfer of nutrients and maintenance of new production over the North Atlantic. *Deep-Sea Res.*, **45**, 461-489.

Williams, R. G. and M. J. Follows, 1998b. Eddies make ocean deserts bloom. *Nature, 'News and Views'*, **394**, 228-229.

Winn, C. D., F. T. MacKenzie, C. J. Carrilo, C. L. Sabrine and D. M. Karl, 1994. Air-sea carbon dioxide exchange in the North Pacific Subtropical Gyre : Implications for the global carbon budget. *Glob. Geochem. Cycles*, **8**, 157-163.

Yamanaka, Y. and E. Tajika, 1997. Role of dissolved organic matter in the marine biogeochemical cycle: Studies using an ocean biogeochemical general circulation model. *Glob. Biogeochem. Cycles*, **11**, 599-612.